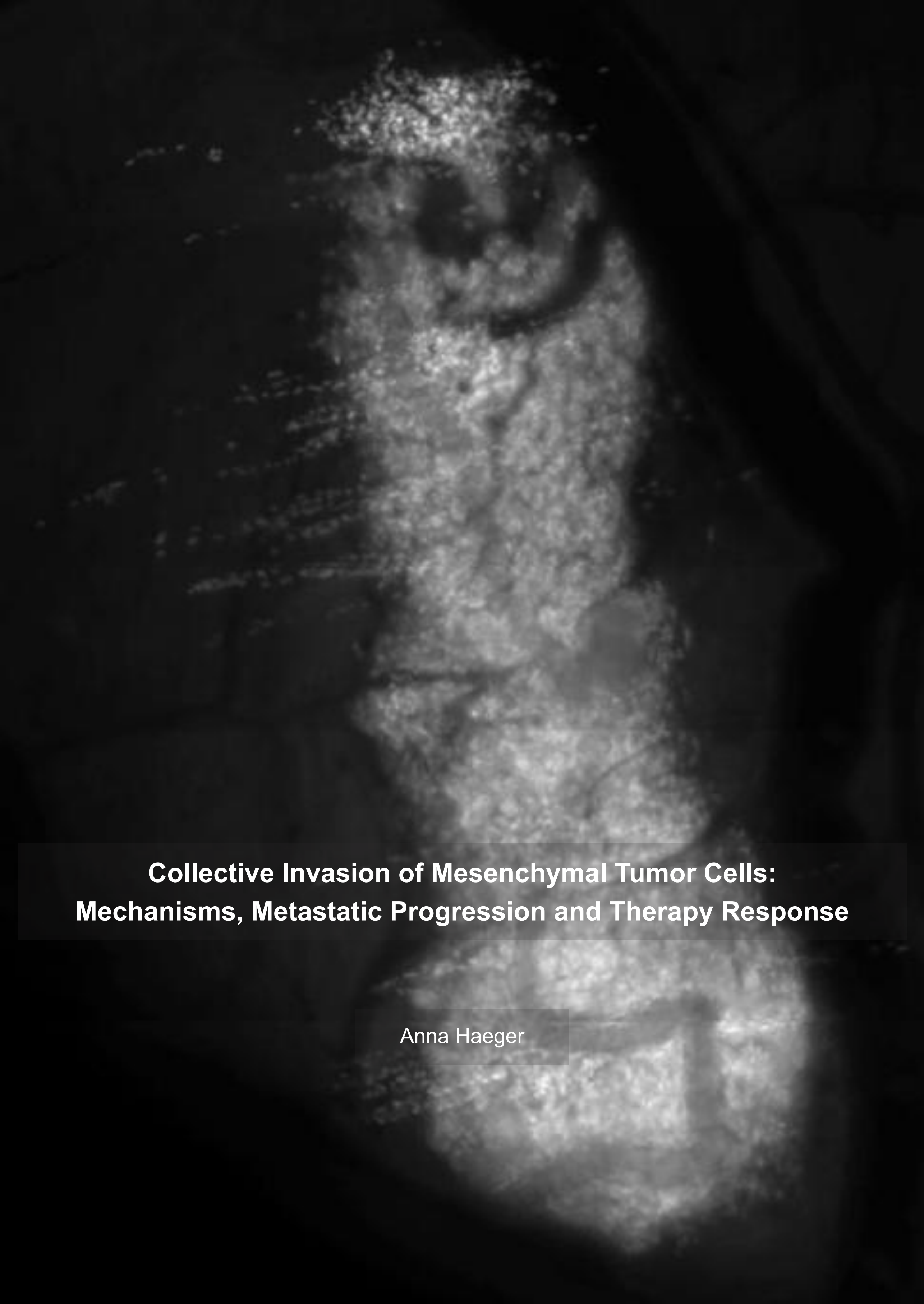

Collective Invasion of Mesenchymal Tumor Cells: Mechanisms, Metastatic Progression and Therapy Response

Anna Haeger

Collective Invasion of Mesenchymal Tumor Cells:

Mechanisms, Metastatic Progression and Therapy Response

Anna Haeger

Cover design: Anna Haeger
Layout and printing: Gildeprint – the Netherlands
ISBN: 978-94-92896-22-3

The research presented in this thesis was performed at the Department of Cell Biology, Radboud Institute for Molecular Life Sciences (RIMLS), Radboudumc, Nijmegen, the Netherlands.
The work was supported by the PhD fellowship program of the Radboudumc Nijmegen, the European Research Council (617430-DEEPINSIGHT), the Netherlands Science Foundation (NWO-Vici 918.11.626) and the Cancer Genomics Center (cancergenomics.nl).

Collective Invasion of Mesenchymal Tumor Cells:

Mechanisms, Metastatic Progression and Therapy Response

PROEFSCHRIFT

ter verkrijging van de graad van doctor
aan de Radboud Universiteit Nijmegen
op gezag van de rector magnificus prof. dr. J.H.J.M. van Krieken,
volgens besluit van het college van decanen
in het openbaar te verdedigen op dinsdag 8 mei 2018
om 10.30 uur precies

door
Anna Haeger
geboren op 13 januari 1986
te Bonn Duisdorf, Duitsland

Promotor:
Prof. dr. P. Friedl

Copromotor:
Dr. K. Wolf

Manuscriptcommissie:
Prof. dr. A.J. van Gool
Prof. dr. M. Vermeulen
Prof. dr. N. Cordes (Technische Universität, Dresden, Duitsland)

Für meine Eltern

Table of Content

Chapter 1

Introduction and Outline of the Thesis

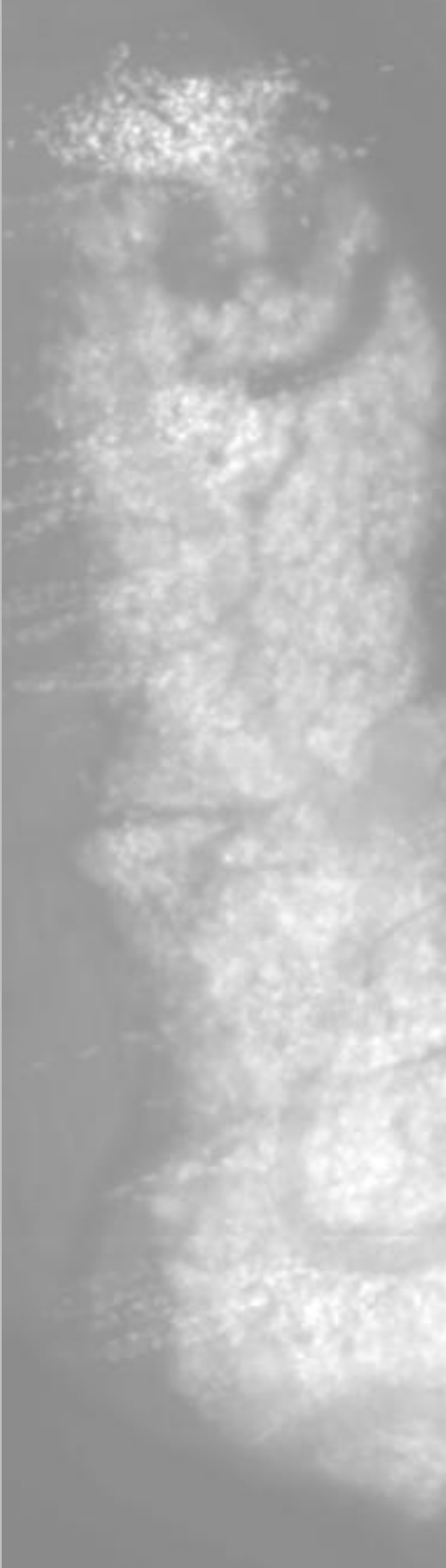

Fatal cancer disease accounts for a leading cause of deaths worldwide: approximately 1 in every 7 deaths is cancer-related[1,2]. Cancer progression occurs as a multi-step process which includes growth of a locally confined primary tumor, the onset of cancer cell invasion and subsequent dissemination to distant organs giving rise to metastatic lesions[3–5] (Fig. 1). 90% of cancer related deaths are caused by development of distant metastases, however the mechanisms of distant metastasis formation are poorly understood and preventive therapy to inhibit or delay metastatic cancer progression is lacking[6,7]. Studying the metastatic cascade and associated mechanisms underlying therapy failure is thus of utmost importance to gain the insight needed for development of efficient therapies for all cancer stages to decrease overall mortality rate. Focusing on this aim in this thesis mechanisms underlying progression and therapy response of two mesenchymal tumor types (i.e. soft tissue sarcoma and melanoma) were investigated, with a particular focus on integrins and their role in the metastatic cascade and as mediators of therapeutic resistance.

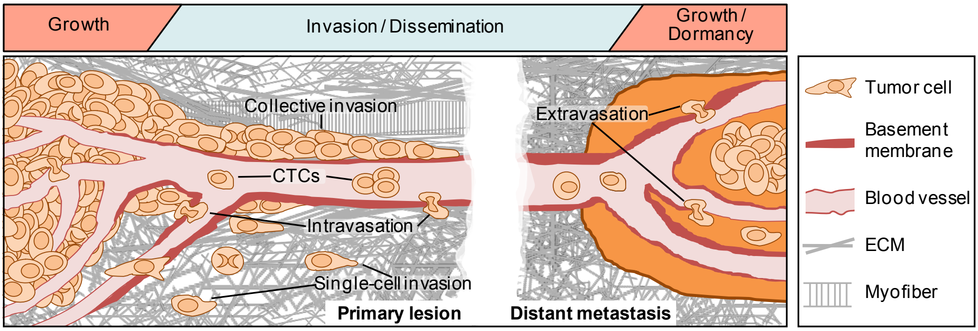

Figure 1. Steps of metastatic cancer progression.
At the primary site, invading cancer cells leave the growing tumor lesion eventually intravasating into local blood vessels. As CTCs in the blood stream cancer cells reach distant organs followed by extravasation. Outgrowth to macroscopic metastases is often preceded by a phase of growth arrest and persistence (dormancy).
Modified from: Alexander, S. & Friedl, P. Cancer invasion and resistance: Interconnected processes of disease progression and therapy failure. Trends Mol. Med. ***18,*** *13–26 (2012).*

Cancer development and progression as a multi-step process

Initiation of primary tumor growth

Underlying cause for the development of a primary tumor are genomic alterations, including either inherited mutations or newly acquired defects developed among others as consequence of aging, exposure to mutagens (e.g. UV irradiation, toxins, tobacco smoke) and/or secondary to chronic inflammation[8–12]. If these alterations affect proto-onco- and/or tumor suppressor genes, cellular pathways usually balancing survival, proliferation and apoptosis become deregulated, eventually resulting in an abnormally growing cell mass, which can arise from essentially every tissue type in the human body[13,14].

The most common cancer types are of epithelial or mesenchymal origin[15,16]. Epithelial tissue lining the body surface or cavities and glands is characterized by apical-basal polarization and strong cell-cell coherence[17]. In contrast, mesenchymal cells are individual, unpolarized and motile with a fibroblast-like shape and surrounded by an extracellular matrix (ECM) to constitute connective tissues including bone, cartilage and blood[18]. Primary tumors developing from these two tissue types initially maintain these basal characteristics, though with continuing progression and the onset of invasion dedifferentiation and phenotype switches may occur, shaping both, morphology of the primary lesion and the mode of invasion[19,20].

Cancer invasion

The onset of cancer invasion constitutes the first step of the metastatic cascade[4] (Fig. 1). Prerequisite for cancer cell invasion is that cells become mobile to detach and migrate out of the primary tumor into the surrounding tissue and, dependent on the environment and cancer type, the ability to remodel ECM and basement membrane in order to condition the tissue microenvironment, clear the migration path and penetrate the tissue[4,21]. Whereas mesenchymal cells intrinsically exhibit a motile phenotype and low cellular adhesion which facilitates invasion, for epithelial tumors it was assumed that upon exposure to extrinsic factors individual cells become reprogrammed and undergo an epithelial to mesenchymal transition (EMT) to lower cell-cell adhesion and gain motility for subsequent invasive behavior[22]. However, with the discovery of collective migration patterns and advanced expression profiling techniques it became clear that EMT is not a prerequisite for invasion and metastasis of epithelial cancer cells[23–25]. Thus currently cancer cell invasion modes are classified in two main categories i.e. individual cell migration and multicellular collective migration (Fig. 1,2), with or without EMT signature including partial EMT[20,26].

Cells lacking cell-cell adhesion invade as single cells using either mesenchymal or amoeboid migration strategies[20] (Fig. 2). During mesenchymal invasion cells are rather elongated or spindle-shaped caused by high levels of cell-ECM adhesion and the establishment of focal adhesions at the leading edge needed to propel the cell body forward[27] (Fig.2). In contrast, amoeboid cells appear rounded and are not dependent on cell-matrix adhesions but movement relies on cortical actomyosin contractility and the presence of a confined interface and sufficient space between tissue structures[27] (Fig.2).

Collective invasion is executed by cells retaining their cell-cell junctions, thus migrating as cohesive multicellular clusters or strands along or through tissue structures[20,28,29] (Fig.2). The migrating collective develops a polarized structure with pulling leader cells at the front and pushing follower cells in the rear part, facilitated by a supracellular organization of the actin cytoskeleton helping to generate protrusion and traction forces necessary for displacement of the cell cluster while maintaining cellular junctions[30–32]. **Chapter 2** describes which general guidance principles become employed during collective migration to efficiently coordinate processes like collective cancer invasion. Individual cells which are not or just transiently connected via stable cellular junctions but follow the same gradient or share the same migration path resemble a collective migration pattern. Though, unlike collectively invading cells, each cell is able to generate individual traction forces on the matrix and therefore this type of movement is described as multicellular streaming[20,33] (Fig. 2).

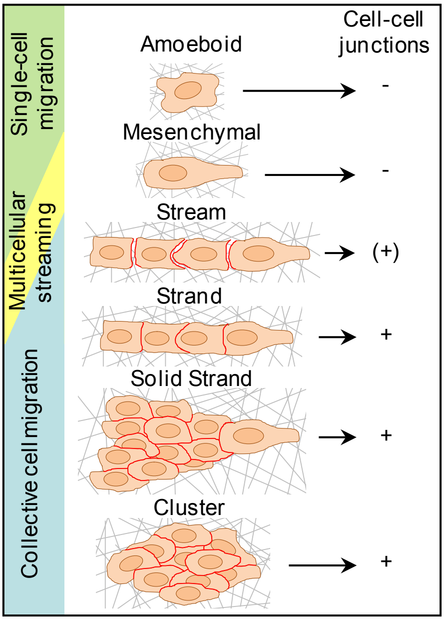

Figure 2. Modes of cancer cell invasion.
Whereas for single-cell migration modes junctions between cancer cells are dispensable, during multicellular streaming weak, transient junctions might form. In contrast, all collective migration modes rely on strong cell-cell cohesion between cancer cells. Red lines represent cellular junctions.
Modified from: Friedl, P., Locker, J., Sahai, E. & Segall, J. E. Classifying collective cancer cell invasion. Nat. Cell Biol. ***14,*** *777–83 (2012).*

Based on their intrinsic property of strong cell-cell cohesion, collective invasion is mainly attributed to epithelial cancers whereas mesenchymal tumor cells with a lower tendency to adhere to each other are expected to show a rather single cell invasion pattern or multicellular streaming[34]. However, as shown in *in vitro* and *in* vivo model systems as well as through histological analysis of patient samples[28,35–37], also these type of cancer cells are able to migrate collectively. In **chapter 3** the tissue determinants underlying this plasticity behavior were investigated *in vitro* using 3D collagen matrices, identifying ECM porosity and confinement as major factors determining the invasion mode of mesenchymal tumor cells. The switch to collective invasion went along with increasing ECM confinement, supporting the concept of cell jamming as mechanism underlying a collective migration pattern of mesenchymal cancer cells.

Metastasis formation

Regardless of whether invading individually or collectively, during metastatic cancer progression disseminating cancer cells will eventually enter the vasculature to circulate with the blood, where they can be detected as circulating tumor cells (CTCs)[38] (Fig. 1). CTCs are considered as indicator for ongoing dissemination of cancer cells and used as prognostic marker[39]. The rate-limiting steps between intravasation and metastatic outgrowth are (i) survival of cancer cells in the blood stream, (ii) adherence to the vessel wall and subsequent extravasation at a distant site and (iii) survival and onset of proliferation at the metastatic site[4]. Compared to single cells, collective invasion and subsequent dissemination of multicellular clusters (collective metastasis) clearly enhances the efficiency of metastatic seeding as it increases survival in the blood stream and in the “foreign” metastatic environment[40–42]. Furthermore, primary tumors have the ability of premetastatic conditioning: via secretion of tumor-derived factors and bone marrow-derived cells stimulated by the primary tumor, future metastatic sites become modified to create an environment that facilitates homing and thus survival and proliferation of disseminated cancer cells[3,43]. However, despite these adaptations of cancer cells to overcome the rate-limiting steps, just 0.1% of all CTCs succeed in efficient metastatic outgrowth[44,45] (Fig. 1). Thus, as such metastasis formation is a quite inefficient process but nevertheless the most fatal step in progressing cancer disease, especially because disseminated cancer cell can remain dormant for decades till growing out to form established metastatic lesions[46].

Sarcoma and melanoma cell lines

The findings described in this thesis focus on two types of malignant mesenchymal tumors i.e soft tissue sarcoma and melanoma, represented by the HT-1080 sarcoma and MV3 melanoma cell line.

HT-1080 sarcoma

Sarcoma comprise a class of malignant tumors originating from a mesenchymal cell type, likely a stromal stem cell[47]. The classification of this cancer type has recently been updated based on new and improved genetic and histological findings[48,49]. The HT-1080 sarcoma cell line has been generated in 1972 from a biopsy of a “poorly differentiated highly malignant fibrosarcoma” growing adjacent to the acetabulum[50]. While back then the term “fibrosarcoma” included any sarcoma containing fibroblasts which constituted 60-70% of all sarcoma diagnoses[51] based on the current WHO classification a “fibrosarcoma” excludes the presence of any other line or differentiation pattern but fibroblasts, making this diagnosis quite rare nowadays[49]. Therefore most likely the HT-1080 cell line is not derived from a “true” fibrosarcoma but rather needs to be classified as “undifferentiated high-grade pleomorphic sarcoma” according to the new guidelines[49]. Morphologically HT-1080 sarcoma cultures include typical mesenchymal elongated and spindle-shaped cells with a small subset of rounded cells[50]. The cells express wildtype TP53[52] which partially matches the status in human lesions where *TP53* alterations occur but are not obligatory[53,54]. Instead, growth of the tumor and cell line was/is driven by an activated NRAS oncogene[55], an alteration not frequently described for this type of sarcoma in which however generally no common driver mutations have been identified yet[53,54].

MV3 melanoma

A melanoma is a skin cancer which develops from the malignant transformation of melanocytes, the melanin-producing cells residing in the bottom layer (*stratum basale*) of the epidermis[56]. Melanocytes originate from the neural crest, a cell layer deriving from the neuroectoderm during embryonic vertebrate development giving rise to several cell lineages[57]. In the developing embryo, neural crest cells undergo an EMT to delaminate from the neuroectoderm and move towards the skin followed by melanocyte differentiation[58]. As part of the epidermis melanocytes reside between keratinocytes but upon malignant transformation they downregulate E-cadherin based cell-cell junctions and recapitulate the developmental EMT program; therefore invading melanoma is classified as a mesenchymal cancer type[59]. The MV3 melanoma cell line has been derived in 1990 from a human melanoma lymph node metastasis of which cells were subcutaneously implanted into a nude mouse and grown there for three passages before taking them into culture[60]. MV3 cells exhibit predominantly mesenchymal morphology with the presence of triangular and elongated cells and a small subset of rounded cells[60]. Genetically, MV3 melanoma cells are incompletely characterized; their TP53 status is wildtype[61] and they do not contain a BRAFV600E mutation[62] which is common to more than 50% of all melanoma cases[63], however whether they carry another type of BRAF mutation or belong to another melanoma suptype[63] has not been determined yet.

Genotoxic cancer therapy and resistance

In addition to metastasis formation, (disseminated) cancer cells which cope with and survive therapeutic approaches are a major factor accounting for cancer-related deaths[1,2,64]. The most broadly used anti-cancer therapies include genotoxic chemo- and radiotherapy which target the high proliferation rate of most cancer cells by damaging the DNA and/or interfering with DNA replication and proliferation such that cells eventually may undergo apoptosis[65–67]. However, either intrinsically before treatment or acquired during and after treatment (secondary resistance), a majority of cancers develop resistance to the applied therapy resulting in progressing or relapsing disease[68,69]. Therefore the study of cancer resistance mechanisms is of central importance to identify new therapeutic targets and improve current cancer therapy approaches.

Chemotherapy

Chemotherapeutic agents are non-specific poisons that are given systemically which has the advantage of principally reaching every cancer cell in the body though simultaneously also healthy cells may be harmed[66]. The four main types of chemotherapy include (i) alkylating agents (e.g. cisplatin) which directly damage DNA by covalently crosslinking the double strands, (ii) antimetabolites (e.g. methotrexate) inhibiting DNA and RNA synthesis, (iii) topoisomerase inhibitors (e.g. doxorubicin) precluding the removal of supercoils during DNA replication and (iv) anti-microtubule agents (e.g. taxanes) which interfere with either microtubule synthesis or disassembly and thereby inhibit completion of mitosis[70,71].

Radiotherapy

In contrast to chemotherapy which affects the process of proliferation at different levels, radiation therapy works by only introducing DNA double strand breaks of which the amount needs to be above a certain threshold to activate apoptosis signaling rather than DNA repair and subsequent cell survival[72]. However, as advantage compared to systemic chemotherapy, irradiation allows local application resulting in locally limited and reduced systemic adverse effects[65].

Therapeutic resistance

Numerous cell-intrinsic and acquired mechanisms accounting for cancer resistance to chemo- and radiotherapy have already been identified[68], among which (i) genomic alterations malignant cells might have acquired[73,74]; (ii) interaction with the tumor micro-environment including stromal cells (e.g. fibroblasts endothelial and immune cells), ECM components and chemical factors (e.g. growth factors or cytokines) and subsequent stimulation of (dependence) receptors like integrins, receptor tyrosine kinases or hormone receptors[75–80]; (iii) metabolic perturbation as consequence of hypoxia, which has been described as major mediator of radioresistance as cancer cells switch towards glycolysis leading to lactate production and hypoxia-inducible factor 1 (HIF-1) activation[81–83] and (iv) intratumor heterogeneity including the presence of slow-proliferating cells with stem cell-like properties often associated with EMT[84–89].

Eventually each resistance mechanism engages intracellular pathways and effector functions which confer survival advantages[68]. These include stimulation of pro-survival and proliferation pathways like the phosphatidylinositide 3-kinase (PI3K)-Akt cascade and overruling or silencing of pro-apoptotic signals, both often accompanied by deregulation of the DNA damage response with either enhanced repair or tolerance to DNA lesions and inactivation of cell cycle checkpoints, allowing proliferation despite damaged DNA or abnormal mitoses[68,69,90]. As consequence, cancer cell subsets may be sensitive to the cytotoxic treatment causing the tumor lesion to shrink, however the persistence of resistant subsets, or even individual cell clones, is sufficient to nullify therapy success when growing out as resistant cancer relapse[64,91,92].

Strategies to overcome resistance mechanisms are already included into current therapy regimens[67,93,94], among which the targeting of integrin adhesion receptors, which are considered as high potential target in cancer therapy[69,95,96]. **Chapter 4 and 5** in this thesis focus on this type of cell-matrix adhesion molecules, investigating their role in metastasis and radioresistance of mesenchymal tumor types.

Integrins and their role in cancer progression and therapeutic resistance

Cell adhesion to extracellular tissue structures is a substantial process underlying the development of tissue structures and organs[97]. Besides providing stable anchorage, cell-ECM interactions can be highly dynamic and undergo cyclic turnover during mesenchymal cell migration: the leading edge develops transient anchors needed to build up the traction force which eventually will propel the cell body forward[98,99]. Beyond their mechanical functions, cell-ECM adhesion systems provide important signaling functions stimulating cell growth, differentiation and survival[100,101]. Accordingly, cells lacking sufficient contact to ECM are prone to undergo apoptosis, a process called anoikis[102], unless they acquired the ability to survive independent of any anchorage. Anoikis resistance has been described as hallmark of (metastatic) cancer and is driven by the constitutive activation or suppression of survival and proapoptotic signaling respectively, mediated by e.g. oncongene expression, continuous growth factor stimulation or multicellular aggregate formation[101].

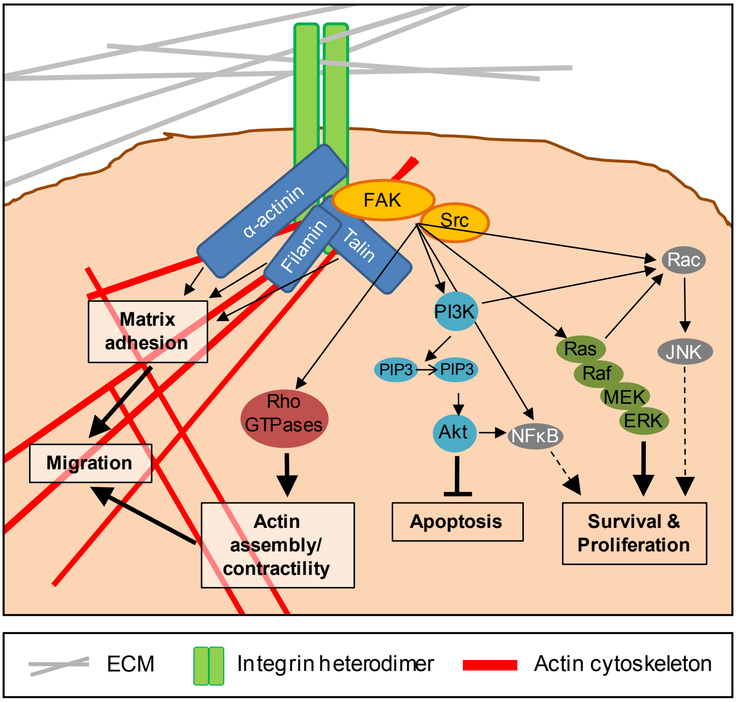

Figure 3. Pro-migratory and pro-survival signaling events initiated upon integrin-ECM interaction. The linker molecules α-actinin, filamin and talin directly connect the cytoplasmic integrin tail to the actin cytoskeleton ensuring strong adhesion to the matrix. Activated Rho GTPases stimulate actin assembly and contractility, altogether facilitating migration.
FAK becomes activated upon binding to the cytoplasmic integrin tail, recruiting and activating multiple signaling molecules eventually feeding into pro-survival pathways and inhibiting apoptosis.

Integrins as adhesion receptors and signaling hubs

Integrins are heterodimeric transmembrane receptors composed of an α- and β-subunit mediating attachment of cells to various ECM structures including the most abundant ECM components as well as cell surface receptors[103]. Different integrin subtypes show unique substrate preference with β1 and β3 integrins accounting for interaction with collagens, laminin, fibronectin and fibrillin, main constituents of interstitial ECM and basement membrane and thus important substrates during cancer cell dissemination[28,29,103–107].
After ligand binding, the short cytoplasmic integrin domain, which lacks any enzymatic function, is the center of integrin-mediated anchorage and outside-in signaling cascades, by recruiting various adaptor and signaling molecules[108,109] (Fig. 3). Via the linker proteins talin, alpha-actinin and filamin the cytoplasmic tail of integrin β subunits becomes connected to the actin cytoskeleton which is essential for the establishment of stable cell-ECM junctions[108,109] (Fig. 3). Integrin-dependent downstream signaling depends upon focal adhesion kinase (FAK), which becomes recruited and binds the β integrin cytoplasmic tail upon integrin ligand

engagement[108–110]. Subsequent conformational changes of FAK allow its autophosphorylation at tyrosine 397 followed by interaction with the SH2 domain of Src kinase and its activation[108–110]. The activated FAK/Src complex then serves as origin for diverging downstream signaling cascades including activation of Jun amino-terminal kinase (JNK), nuclear factor κB (NFκB), extracellular signal-regulated kinase (ERK), mitogen-activated protein kinase (MAPK), phosphatidylinositide 3-kinase (PI3K) and Rho-family GTPases[101,108–111]. Whereas Rho GTPases especially regulate the assembly and contractility of actin filaments[112], the other pathways, in particular ERK- and PI3K –mediated signaling, promote cell survival by activation of pro-proliferation targets or inhibition of pro-apoptotic signaling, both essential processes to counteract anoikis[108,113,114] (Fig. 3). Furthermore, lateral interactions between integrin heterodimers and growth factor receptors for ligands like epidermal growth factor (EGF), fibroblast growth factor (FGF) or vascular endothelial growth factor (VEGF) support activation of growth factor receptor tyrosine kinases and efficient stimulation of growth factor-mediated cell growth and proliferation[96,115]. Additionally, integrin engagement controls intricate signaling networks regulating cell functions like motility, shape, polarity, cell-cell adhesion and differentiation[116,117]. Thus beyond the formal appearance as cell-ECM adhesion molecules, integrins control a complex network of various signaling mechanisms feeding into numerous cellular pathways. Consequently, integrins constitute integral parts of the metastatic cascade and can function as mediators of therapeutic resistance[69,95,96,118–121].

Integrins and the metastatic cascade

Each step of the metastatic cascade depends on various types and strength of cellular adhesion to the surrounding matrix and survival cues, mediated by integrins and other adhesion receptors[118,120]. **Chapter 4** summarizes the known functions of integrin subsets for each step of the metastatic cascade, which subsequently were tested *in vivo* in sarcoma and melanoma xenografts in mice monitored by intravital microscopy, analysis of CTCs and the onset of spontaneous metastasis. The results show that growth of the primary and metastatic lesions was integrin dependent but that metastasis formation as such did not become abrogated after blocking all available integrin subsets. Rather integrin-independent dissemination was even more efficient relative to the tumor size, which contradicts the generally accepted notion that integrins are indispensable for cancer cell dissemination[120]. Thus, despite the dominant role of integrins probing individual steps of the metastatic cascade and their significance for tumor growth, interference with integrins may not suffice to block metastatic cancer cell dissemination.

Integrins as mediators of therapeutic resistance

Being often upregulated in various cancer types and based on their function in pro-survival and thus resistance signaling, integrins have been pursued as therapeutic targets in preclinical and clinical studies[100,117,121,122], which however failed to inhibit metastatic growth as endpoint[123,124]. **Chapter 5** describes the discovery of collective invasion-associated, integrin-dependent radioresistance in two mesenchymal xenograft models. To overcome this resistance phenotype, the study addresses compensation by alternative integrin subsets in providing partial resistance, a likely rate-limiting process typically not addressed in preclinical integrin targeting studies. As outcome, by interfering with the two most abundant integrin chains in mesenchymal cells, β1 and β3 integrins, previously resistant tumor fractions became fully sensitive to radiation therapy and successfully eliminated. These preclinical data suggest that therapeutic targeting of multiple integrins might increase the efficacy of integrin-targeted therapies.

Addressing lack of knowledge

The molecular adaptations resulting in metastatic plasticity and environment-induced resistance development are complex and likely depend upon local signals present in tissue niches[125]. Important insights on the signals involved in metastasis and resistance development were obtained by studies which systemically apply genomic and expression profiling to patient-derived cancer specimens[126,127]. As potential shortcoming, the samples used for these studies often contain only a small subset of the entire (metastatic) lesion making it difficult to assign tumor niches and the environmental context. Therefore experimental models are needed where each step of the metastatic cascade as well as therapeutic responses and stromal context can be monitored accompanied by simultaneous sampling for (epi)genomic and expression profiling. **Chapter 6** describes the establishment of a microscopy-based microdissection approach for live 3D tumor samples to separately isolate tumor core and invasion zone of sarcoma and melanoma xenografts, followed by differential expression profiling using RNAseq. This approach will be suited for detailed molecular characterization of the two tumor sub-regions to unravel mechanisms underlying integrin-independent invasion (**chapter 4**) and integrin-dependent, invasion-associated radioresistance (**chapter 5**), but also to generally identify microenvironemental re-programming events modulating therapy response and invasive properties. In addition to profiling of CTCs, image-based 3D microdissection of cells during metastatic progression will further help to define molecular changes during each step of the metastatic cascade, ideally using single-cell profiling techniques[128]. This strategy may facilitate the identification of new therapeutic targets to further improve therapy for sarcoma, melanoma and possibly other mesenchymal cancer types.

Chapter 7 summarizes results and emerging concepts described in this thesis and discusses their implications for understanding cancer cell dissemination resistance development.

References

1. American Cancer Society. Cancer Facts and Figures 2017. *Atlanta Am. Cancer Soc.* 53 (2017).
2. Siegel, R. L., Miller, K. D. & Jemal, A. Cancer statistics, 2017. *CA. Cancer J. Clin.* **67,** 7–30 (2017).
3. Fidler, I. J. The pathogenesis of cancer metastasis: the ‘seed and soil’ hypothesis revisited. *Nat. Rev. Cancer* **3,** 453–8 (2003).
4. Valastyan, S. & Weinberg, R. A. Tumor metastasis: Molecular insights and evolving paradigms. *Cell* **147,** 275–292 (2011).
5. Kang, Y. & Pantel, K. Tumor Cell Dissemination: Emerging Biological Insights from Animal Models and Cancer Patients. *Cancer Cell* **23,** 573–581 (2013).
6. Mehlen, P. & Puisieux, A. Metastasis: a question of life or death. *Nat. Rev. Cancer* **6,** 449–458 (2006).
7. Steeg, P. S. Targeting metastasis. *Nat. Rev. Cancer* **16,** 201–218 (2016).
8. Garber, J. E. & Offit, K. Hereditary Cancer Predisposition Syndromes. *J. Clin. Oncol.* **23,** 276–292 (2005).
9. Falandry, C., Bonnefoy, M., Freyer, G. & Gilson, E. Biology of Cancer and Aging: A Complex Association With Cellular Senescence. *J. Clin. Oncol.* **32,** 2604–2610 (2014).
10. D’Orazio, J., Jarrett, S., Amaro-Ortiz, A. & Scott, T. UV Radiation and the Skin. *Int. J. Mol. Sci.* **14,** 12222–12248 (2013).
11. Hecht, S. S. Lung carcinogenesis by tobacco smoke. *Int. J. Cancer* **131,** 2724–2732 (2012).
12. Scarpa, M. *et al.* Inflammatory colonic carcinogenesis: a review on pathogenesis and immunosurveillance mechanisms in ulcerative colitis. *World J. Gastroenterol.* **20,** 6774–85 (2014).
13. Hanahan, D. & Weinberg, R. A. The hallmarks of cancer. *Cell* **100,** 57–70 (2000).
14. Hanahan, D. & Weinberg, R. A. Hallmarks of cancer: the next generation. *Cell* **144,** 646–74 (2011).
15. Stewart, B. W. & Kleihues, P. World Cancer Report 2003. *World Heal. Organ.* (2003).
16. Schöffski, P., Cornillie, J., Wozniak, A., Li, H. & Hompes, D. Soft Tissue Sarcoma: An Update on Systemic Treatment Options for Patients with Advanced Disease. *Oncol. Res. Treat.* **37,** 355–362 (2014).
17. Roignot, J., Peng, X. & Mostov, K. Polarity in mammalian epithelial morphogenesis. *Cold Spring Harb. Perspect. Biol.* **5,** (2013).
18. Hay, E. D. The mesenchymal cell, its role in the embryo, and the remarkable signaling mechanisms that create it. *Dev. Dyn.* **233,** 706–720 (2005).
19. Gabbert, H., Wagner, R., Moll, R. & Gerharz, C.-D. Tumor dedifferentiation: An important step in tumor invasion. *Clin. Exp. Metastasis* **3,** 257–279 (1985).
20. Friedl, P., Locker, J., Sahai, E. & Segall, J. E. Classifying collective cancer cell invasion. *Nat. Cell Biol.* **14,** 777–83 (2012).
21. Wolf, K. & Friedl, P. Extracellular matrix determinants of proteolytic and non-proteolytic cell migration. *Trends Cell Biol.* **21,** 736–44 (2011).
22. Thiery, J. P. Epithelial-mesenchymal transitions in tumour progression. *Nat. Rev. Cancer* **2,** 442–454 (2002).
23. Christiansen, J. J. & Rajasekaran, A. K. Reassessing epithelial to mesenchymal transition as a prerequisite for carcinoma invasion and metastasis. *Cancer Res.* **66,** 8319–26 (2006).
24. Campbell, K. & Casanova, J. A common framework for EMT and collective cell migration. *Development* **143,** 4291–4300 (2016).
25. Revenu, C. & Gilmour, D. EMT 2.0: shaping epithelia through collective migration. *Curr. Opin. Genet. Dev.* **19,** 338–342 (2009).

26. Grigore, A., Jolly, M., Jia, D., Farach-Carson, M. & Levine, H. Tumor Budding: The Name is EMT. Partial EMT. *J. Clin. Med.* **5,** 51 (2016).
27. Sanz-Moreno, V. & Marshall, C. J. The plasticity of cytoskeletal dynamics underlying neoplastic cell migration. *Curr. Opin. Cell Biol.* **22,** 690–696 (2010).
28. Alexander, S., Koehl, G. E., Hirschberg, M., Geissler, E. K. & Friedl, P. Dynamic imaging of cancer growth and invasion: a modified skin-fold chamber model. *Histochem. Cell Biol.* **130,** 1147–54 (2008).
29. Weigelin, B., Bakker, G.-J. & Friedl, P. Intravital third harmonic generation microscopy of collective melanoma cell invasion: Principles of interface guidance and microvesicle dynamics. *IntraVital* **1,** 32–43 (2012).
30. Khalil, A. a & Friedl, P. Determinants of leader cells in collective cell migration. *Integr. Biol. (Camb).* **2,** 568–574 (2010).
31. Friedl, P. & Gilmour, D. Collective cell migration in morphogenesis, regeneration and cancer. *Nat. Rev. Mol. Cell Biol.* **10,** 445–57 (2009).
32. Haeger, A., Wolf, K., Zegers, M. M. & Friedl, P. Collective cell migration: Guidance principles and hierarchies. *Trends Cell Biol.* **25,** 556–566 (2015).
33. Patsialou, A. *et al.* Intravital multiphoton imaging reveals multicellular streaming as a crucial component of in vivo cell migration in human breast tumors. *IntraVital* **2,** e25294 (2013).
34. Theveneau, E. & Mayor, R. Collective cell migration of epithelial and mesenchymal cells. *Cell. Mol. Life Sci.* **70,** 3481–92 (2013).
35. Wolf, K. *et al.* Multi-step pericellular proteolysis controls the transition from individual to collective cancer cell invasion. *Nat. Cell Biol.* **9,** 893–904 (2007).
36. Eyden, B. P., Manson, C., Banerjee, S. S., Roberts, I. S. & Harris, M. Sclerosing epithelioid fibrosarcoma: a study of five cases emphasizing diagnostic criteria. *Histopathology* **33,** 354–60 (1998).
37. Clark, W. H., From, L., Bernardino, E. A. & Mihm, M. C. The histogenesis and biologic behavior of primary human malignant melanomas of the skin. *Cancer Res.* **29,** 705–27 (1969).
38. Haber, D. A. & Velculescu, V. E. Blood-Based Analyses of Cancer: Circulating Tumor Cells and Circulating Tumor DNA. *Cancer Discov.* **4,** 650–661 (2014).
39. Yap, T. A., Lorente, D., Omlin, A., Olmos, D. & de Bono, J. S. Circulating Tumor Cells: A Multifunctional Biomarker. *Clin. Cancer Res.* **20,** 2553–2568 (2014).
40. Cheung, K. J. *et al.* Polyclonal breast cancer metastases arise from collective dissemination of keratin 14-expressing tumor cell clusters. *Proc. Natl. Acad. Sci.* **113,** 201508541 (2016).
41. Cheung, K. J. & Ewald, A. J. A collective route to metastasis: Seeding by tumor cell clusters. *Science (80-.).* **352,** 167–169 (2016).
42. Aceto, N. *et al.* Circulating Tumor Cell Clusters Are Oligoclonal Precursors of Breast Cancer Metastasis. *Cell* **158,** 1110–1122 (2014).
43. Liu, Y. & Cao, X. Characteristics and Significance of the Pre-metastatic Niche. *Cancer Cell* **30,** 668–681 (2016).
44. Bidard, F.-C., Pierga, J.-Y., Vincent-Salomon, A. & Poupon, M.-F. A ‘class action’ against the microenvironment: do cancer cells cooperate in metastasis? *Cancer Metastasis Rev.* **27,** 5–10 (2008).
45. Chambers, A. F., Groom, A. C. & MacDonald, I. C. Dissemination and growth of cancer cells in metastatic sites. *Nat. Rev. Cancer* **2,** 563–72 (2002).
46. Alizadeh, A. M., Shiri, S. & Farsinejad, S. Metastasis review: from bench to bedside. *Tumor Biol.* **35,** 8483–8523 (2014).
47. Lye, K. L., Nordin, N., Vidyadaran, S. & Thilakavathy, K. Mesenchymal stem cells: From stem cells to sarcomas. *Cell Biol. Int.* **40,** 610–618 (2016).

48. Fletcher, C. D. M. The evolving classification of soft tissue tumours - an update based on the new 2013 WHO classification. *Histopathology* **64,** 2–11 (2014).
49. Doyle, L. A. Sarcoma classification: An update based on the 2013 World Health Organization Classification of Tumors of Soft Tissue and Bone. *Cancer* **120,** 1763–1774 (2014).
50. Rasheed, S., Nelson-Rees, W. A., Toth, E. M., Arnstein, P. & Gardner, M. B. Characterization of a newly derived human sarcoma cell line (HT-1080). *Cancer* **33,** 1027–33 (1974).
51. Enzinger, F., Lattes, R. & Torloni, H. Soft tissue sarcomas: Classification and natural history. *World Heal. Organ.* (1969).
52. Tarunina, M. & Jenkins, J. R. Human p53 binds DNA as a protein homodimer but monomeric variants retain full transcription transactivation activity. *Oncogene* **8,** 3165–73 (1993).
53. Barretina, J. *et al.* Subtype-specific genomic alterations define new targets for soft-tissue sarcoma therapy. *Nat. Genet.* **42,** 715–721 (2010).
54. Segal, N. H. *et al.* Classification and Subtype Prediction of Adult Soft Tissue Sarcoma by Functional Genomics. *Am. J. Pathol.* **163,** 691–700 (2003).
55. Paterson, H. *et al.* Activated N-ras controls the transformed phenotype of HT1080 human fibrosarcoma cells. *Cell* **51,** 803–12 (1987).
56. Herlyn, M. Human melanoma: development and progression. *Cancer Metastasis Rev.* **9,** 101–12 (1990).
57. Sommer, L. Generation of melanocytes from neural crest cells. *Pigment Cell Melanoma Res.* **24,** 411–421 (2011).
58. Theveneau, E. & Mayor, R. Neural crest delamination and migration: from epithelium-to-mesenchyme transition to collective cell migration. *Dev. Biol.* **366,** 34–54 (2012).
59. Braeuer, R. R. *et al.* Why is melanoma so metastatic? *Pigment Cell Melanoma Res.* **27,** 19–36 (2014).
60. van Muijen, G. N. *et al.* Establishment and characterization of a human melanoma cell line (MV3) which is highly metastatic in nude mice. *Int. J. cancer.* **48,** 85–91 (1991).
61. Houben, R. *et al.* High-level expression of wild-type p53 in melanoma cells is frequently associated with inactivity in p53 reporter gene assays. *PLoS One* **6,** e22096-1–7 (2011).
62. Schrama, D. *et al.* BRAFV600E mutations in malignant melanoma are associated with increased expressions of BAALC. *J. Carcinog.* **7,** 1 (2008).
63. Cancer Genome Atlas Network. Genomic Classification of Cutaneous Melanoma. *Cell* **161,** 1681–1696 (2015).
64. Li, S. *et al.* Model of Tumor Dormancy/Recurrence after Short-Term Chemotherapy. *PLoS One* **9,** e98021 (2014).
65. Baskar, R., Lee, K. A., Yeo, R. & Yeoh, K.-W. Cancer and Radiation Therapy: Current Advances and Future Directions. *Int. J. Med. Sci.* **9,** 193–199 (2012).
66. Fernando, J., Jones, R., Lyman, G. H. & al., et. The principles of cancer treatment by chemotherapy. *Surg.* **33,** 131–135 (2015).
67. Goldstein, M. & Kastan, M. B. The DNA Damage Response: Implications for Tumor Responses to Radiation and Chemotherapy. *Annu. Rev. Med.* **66,** 129–143 (2015).
68. Holohan, C., Van Schaeybroeck, S., Longley, D. B. & Johnston, P. G. Cancer drug resistance: an evolving paradigm. *Nat. Rev. Cancer* **13,** 714–726 (2013).
69. Eke, I. & Cordes, N. Focal adhesion signaling and therapy resistance in cancer. *Semin. Cancer Biol.* **31,** 65–75 (2015).
70. Jordan, M. A. & Wilson, L. Microtubules as a target for anticancer drugs. *Nat. Rev. Cancer* **4,** 253–265 (2004).
71. Cheung-Ong, K., Giaever, G. & Nislow, C. DNA-Damaging Agents in Cancer Chemotherapy: Serendipity and Chemical Biology. *Chem. Biol.* **20,** 648–659 (2013).

72. Lomax, M. E., Folkes, L. K. & O'Neill, P. Biological Consequences of Radiation-induced DNA Damage: Relevance to Radiotherapy. *Clin. Oncol.* **25,** 578–585 (2013).

73. Tan, S.-H. *et al.* High-Throughput Mutation Profiling Changes before and 3 Weeks after Chemotherapy in Newly Diagnosed Breast Cancer Patients. *PLoS One* **10,** e0142466 (2015).

74. Blagosklonny, M. V. Oncogenic resistance to growth-limiting conditions. *Nat. Rev. Cancer* **2,** 221–224 (2002).

75. Nakasone, E. S. *et al.* Imaging Tumor-Stroma Interactions during Chemotherapy Reveals Contributions of the Microenvironment to Resistance. *Cancer Cell* **21,** 488–503 (2012).

76. Eke, I. *et al.* β1 Integrin / FAK / cortactin signaling is essential for human head and neck cancer resistance to radiotherapy. *J. Clin. Invest.* **122,** 1529–1540 (2012).

77. Hirata, E. *et al.* Intravital imaging reveals how BRAF inhibition generates drug-tolerant microenvironments with high integrin beta1/FAK Signaling. *Cancer Cell* **27,** 574–588 (2015).

78. McMillin, D. W., Negri, J. M. & Mitsiades, C. S. The role of tumour-stromal interactions in modifying drug response: challenges and opportunities. *Nat. Rev. Drug Discov.* **12,** 217–28 (2013).

79. Barker, H. E., Paget, J. T. E., Khan, A. A. & Harrington, K. J. The tumour microenvironment after radiotherapy: mechanisms of resistance and recurrence. *Nat. Rev. Cancer* **15,** 409–425 (2015).

80. Mehlen, P. & Bredesen, D. E. The dependence receptor hypothesis. *Apoptosis* **9,** 37–49 (2004).

81. Manoochehri Khoshinani, H., Afshar, S. & Najafi, R. Hypoxia: A Double-Edged Sword in Cancer Therapy. *Cancer Invest.* **34,** 536–545 (2016).

82. Verduzco, D. *et al.* Intermittent hypoxia selects for genotypes and phenotypes that increase survival, invasion, and therapy resistance. *PLoS One* **10,** e0120958 (2015).

83. Bertout, J. A., Patel, S. A. & Simon, M. C. The impact of O2 availability on human cancer. *Nat. Rev. Cancer* **8,** 967–75 (2008).

84. Zheng, X. *et al.* Epithelial-to-mesenchymal transition is dispensable for metastasis but induces chemoresistance in pancreatic cancer. *Nature* **527,** 525–530 (2015).

85. Fischer, K. R. *et al.* Epithelial-to-mesenchymal transition is not required for lung metastasis but contributes to chemoresistance. *Nature* **527,** 472–476 (2015).

86. Bertolini, G. *et al.* Highly tumorigenic lung cancer CD133+ cells display stem-like features and are spared by cisplatin treatment. *Proc. Natl. Acad. Sci.* **106,** 16281–16286 (2009).

87. Shibue, T. & Weinberg, R. A. EMT, CSCs, and drug resistance: the mechanistic link and clinical implications. *Nat. Rev. Clin. Oncol.* (2017). doi:10.1038/nrclinonc.2017.44

88. Dean, M., Fojo, T. & Bates, S. Tumour stem cells and drug resistance. *Nat. Rev. Cancer* **5,** 275–284 (2005).

89. Colak, S. & Medema, J. P. Cancer stem cells - important players in tumor therapy resistance. *FEBS J.* **281,** 4779–4791 (2014).

90. Alexander, S. & Friedl, P. Cancer invasion and resistance: Interconnected processes of disease progression and therapy failure. *Trends Mol. Med.* **18,** 13–26 (2012).

91. Kottke, T. *et al.* Detecting and targeting tumor relapse by its resistance to innate effectors at early recurrence. *Nat. Med.* **19,** 1625–1631 (2013).

92. Martin-Padura, I. *et al.* Residual dormant cancer stem-cell foci are responsible for tumor relapse after antiangiogenic metronomic therapy in hepatocellular carcinoma xenografts. *Lab. Investig.* **92,** 952–966 (2012).

93. Kumar, S., Singh, R. K. & Meena, R. Emerging targets for radioprotection and radiosensitization in radiotherapy. *Tumor Biol.* **37,** 11589–11609 (2016).

94. Ronnekleiv-Kelly, S. M., Sharma, A. & Ahuja, N. Epigenetic therapy and chemosensitization in solid malignancy. *Cancer Treat. Rev.* **55,** 200–208 (2017).

95. Desgrosellier, J. S. & Cheresh, D. A. Integrins in cancer: biological implications and therapeutic opportunities. *Nat. Rev. Cancer* **10,** 9–22 (2010).

96. Blandin, A.-F. *et al.* β1 Integrins as Therapeutic Targets to Disrupt Hallmarks of Cancer. *Front. Pharmacol.* **6,** 279-1–10 (2015).

97. Rozario, T. & DeSimone, D. W. The extracellular matrix in development and morphogenesis: a dynamic view. *Dev. Biol.* **341,** 126–40 (2010).

98. Ridley, A. J. *et al.* Cell migration: integrating signals from front to back. *Science* **302,** 1704–1709 (2003).

99. Huttenlocher, A. & Horwitz, A. R. Integrins in Cell Migration. *Cold Spring Harb. Perspect. Biol.* **3,** a005074–a005074 (2011).

100. Xiong, J., Balcioglu, H. E. & Danen, E. H. J. Integrin signaling in control of tumor growth and progression. *Int. J. Biochem. Cell Biol.* **45,** 1012–1015 (2013).

101. Zhong, X. & Rescorla, F. J. Cell surface adhesion molecules and adhesion-initiated signaling: Understanding of anoikis resistance mechanisms and therapeutic opportunities. *Cell. Signal.* **24,** 393–401 (2012).

102. Paoli, P., Giannoni, E. & Chiarugi, P. Anoikis molecular pathways and its role in cancer progression. *Biochim. Biophys. Acta - Mol. Cell Res.* **1833,** 3481–3498 (2013).

103. Humphries, J. D., Byron, A. & Humphries, M. J. Integrin ligands at a glance. *J. Cell Sci.* **119,** 3901–3903 (2006).

104. Leitinger, B. & Hohenester, E. Mammalian collagen receptors. *Matrix Biol.* **26,** 146–155 (2007).

105. Mouw, J. K., Ou, G. & Weaver, V. M. Extracellular matrix assembly: a multiscale deconstruction. *Nat. Rev. Mol. Cell Biol.* **15,** 771–785 (2014).

106. Pickup, M. W., Mouw, J. K. & Weaver, V. M. The extracellular matrix modulates the hallmarks of cancer. *EMBO Rep.* **15,** 1243–53 (2014).

107. Gritsenko, P. G., Ilina, O. & Friedl, P. Interstitial guidance of cancer invasion. *J. Pathol.* **226,** 185–99 (2012).

108. Giancotti, F. G. & Ruoslahti, E. Integrin signaling. *Science (80-.).* **285,** 1028–1033 (1999).

109. Morse, E. M., Brahme, N. N. & Calderwood, D. A. Integrin Cytoplasmic Tail Interactions. *Biochemistry* **53,** 810–820 (2014).

110. Sulzmaier, F. J., Jean, C. & Schlaepfer, D. D. FAK in cancer: mechanistic findings and clinical applications. *Nat. Rev. Cancer* **14,** 598–610 (2014).

111. Juliano, R. L. Signal transduction by cell adhesion receptors and the cytoskeleton: functions of integrins, cadherins, selectins, and immunoglobulin-superfamily members. *Annu. Rev. Pharmacol. Toxicol.* **42,** 283–323 (2002).

112. Zegers, M. M. & Friedl, P. Rho GTPases in collective cell migration. *Small GTPases* **5,** e28997-1–10 (2014).

113. Mendoza, M. C., Er, E. E. & Blenis, J. The Ras-ERK and PI3K-mTOR pathways: cross-talk and compensation. *Trends Biochem. Sci.* **36,** 320–8 (2011).

114. Lien, E. C., Dibble, C. C. & Toker, A. PI3K signaling in cancer: beyond AKT. *Curr. Opin. Cell Biol.* **45,** 62–71 (2017).

115. Ivaska, J. & Heino, J. Cooperation Between Integrins and Growth Factor Receptors in Signaling and Endocytosis. *Annu. Rev. Cell Dev. Biol.* **27,** 291–320 (2011).

116. Deb, M., Sengupta, D. & Patra, S. K. Integrin-epigenetics: a system with imperative impact on cancer. *Cancer Metastasis Rev.* **31,** 221–34 (2012).

117. Seguin, L., Desgrosellier, J. S., Weis, S. M. & Cheresh, D. A. Integrins and cancer: regulators of cancer stemness, metastasis, and drug resistance. *Trends Cell Biol.* **25,** 234–240 (2015).

118. Bendas, G. & Borsig, L. Cancer cell adhesion and metastasis: Selectins, integrins, and the inhibitory potential of heparins. *Int. J. Cell Biol.* **2012,** 676731 (2012).

119. Weis, S. M. & Cheresh, D. A. AlphaV Integrins in Angiogenesis and Cancer. *Cold Spring Harb. Perspect. Med.* **1,** a006478–a006478 (2011).

120. Ganguly, K. K., Pal, S., Moulik, S. & Chatterjee, A. Integrins and metastasis. *Cell Adh. Migr.* **7,** 251–61 (2013).

121. Barkan, D. & Chambers, A. F. Beta1-integrin: A potential therapeutic target in the battle against cancer recurrence. *Clin. Cancer Res.* **17,** 7219–7223 (2011).

122. Dickreuter, E. & Cordes, N. The cancer cell adhesion resistome: mechanisms, targeting and translational approaches. *Biol. Chem.* **398,** 721–735 (2017).

123. Vehlow, A., Storch, K., Matzke, D. & Cordes, N. Molecular Targeting of Integrins and Integrin-Associated Signaling Networks in Radiation Oncology. *Mol. Radio-Oncology, Recent results cancer Res.* **198,** 89–106 (2016).

124. Bianconi, D., Unseld, M. & Prager, G. Integrins in the Spotlight of Cancer. *Int. J. Mol. Sci.* **17,** 2037 (2016).

125. Friedl, P. & Alexander, S. Cancer invasion and the microenvironment: plasticity and reciprocity. *Cell* **147,** 992–1009 (2011).

126. Yachida, S. *et al.* Distant metastasis occurs late during the genetic evolution of pancreatic cancer. *Nature* **467,** 1114–1117 (2010).

127. Van Allen, E. M. *et al.* The Genetic Landscape of Clinical Resistance to RAF Inhibition in Metastatic Melanoma. *Cancer Discov.* **4,** 94–109 (2014).

128. Grün, D. & van Oudenaarden, A. Design and Analysis of Single-Cell Sequencing Experiments. *Cell* **163,** 799–810 (2015).

Chapter 2

Collective Cell Migration:
Guidance Principles and Hierachies

Anna Haeger, Katarina Wolf,
Mirjam M. Zegers and Peter Friedl

Published in: Trends Cell Biol. 2015 Sep; 25(9):556-66

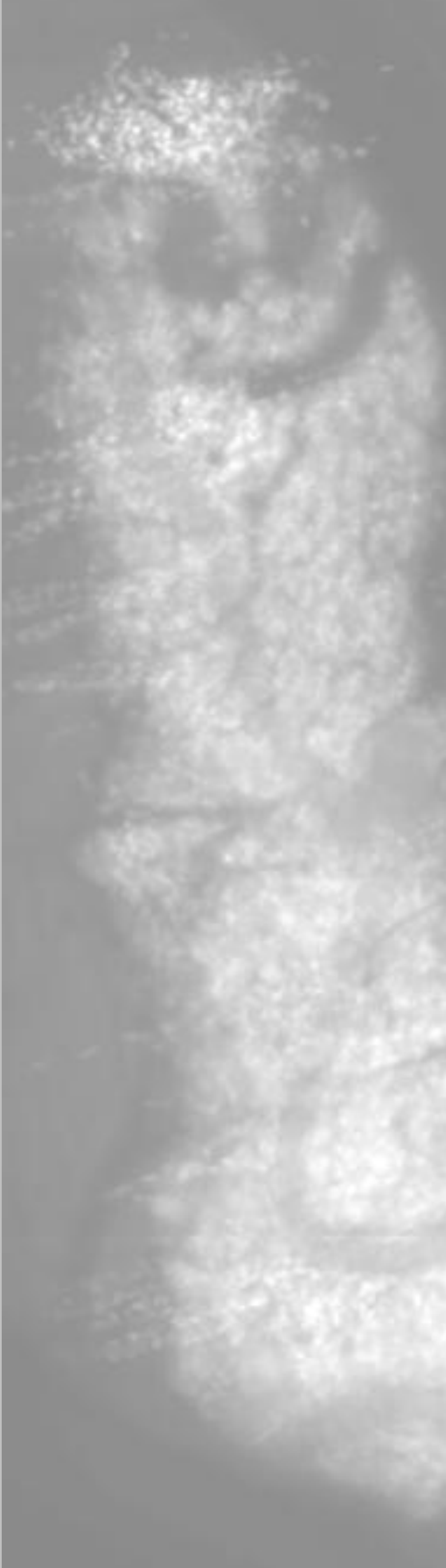

Collective cell migration results from the establishment and maintenance of collective polarization, mechanocoupling, and cytoskeletal kinetics. The guidance of collective cell migration depends on a reciprocal process between cell-intrinsic multicellular organization with leader-follower cell behavior and results in mechanosensory integration of extracellular guidance cues. Important guidance mechanisms include chemotaxis, haptotaxis, durotaxis and strain-induced mechanosensing to move cell groups along interfaces and paths of least resistance. Additional guidance mechanisms steering cell groups during specialized conditions comprise electrotaxis and passive drift. To form higher-order cell and tissue structures during morphogenesis and cancer invasion, these guidance principles act in parallel and are integrated for collective adaptation and shaping of varying tissue environments. We review mechanochemical and electrical inputs and multi-parameter signal integration underlying collective guidance, decision making, and outcome.

Moving cell groups

Collective cell migration is a fundamental process that enables the coordinated movement of groups of cells that remain connected via cell-cell junctions[1–3]. Collective cell movements support the formation and morphological re-shaping of larger tissue structures during the morphogenesis of ducts, glands and vessels, as well as epithelial homeostasis and regeneration[2,4,5]. In addition, when reinitiated in mature tissue during neoplasia, collective movements contribute to cancer invasion and, likely, metastasis[1,6–9].

During collective migration, cell-cell junctions secure supracellular adhesion, polarization, and mechanocoupling required to sense and integrate external guidance cues and further share signal processing and force transmission across the migrating collective (Box1). By connecting the actin cytoskeleton across multiple cell bodies, cell-cell junctions form the basis for integrating the forces generated by individual cells within groups and their supracellular front-rear polarity[10]. Furthermore, cell-cell coupling determines collective functions beyond migration, such as “purse-string” contraction and closure of epithelial gaps and tissue folding[11].

The mechanisms guiding individually migrating cells are well understood and include both chemical guidance by chemotactic soluble factors or haptotactic tissue-anchored factors and physical guidance[12–14]. These guidance mechanisms apply in principle also to collective movements. However, in addition to single-cell migration which results from processing of extracellular input within a single cell body, collective movement also involves intercellular integration of guiding signals to steer and maintain the migration of a cohesive cell group[15].

This includes cell-intrinsic prerequisites like the establishment of leader-follower polarization, supracellular mechanocoupling, and external mechanical, chemical and/or electrical stimuli to steer collective movements (Table 1). Here, we summarize cell-intrinsic and extracellular mechanisms of polarity and guidance in collective cell migration. The astounding variability of how different cell groups integrate converging and/or opposing guidance inputs in complex environments reveals collective cell migration as a versatile and adaptive example of multicellular decision making and plasticity.

Collective polarity by leader-follower behaviors

The guidance of collective migration often involves the coordination between two functionally distinct populations, leader and follower cells. Leader cells localize at the front of a moving group, where they receive guidance signals and instruct, with cell-cell junctions at their rear, follower cells into directional migration through chemical and/or mechanical signaling[16,17] (Fig. 1A). By acquiring a leading edge towards the substrate, including protruding actin-based structures like lamellipodia or filopodia, and specialized gene expression and signaling programs[17,18], leader cells secure front-rear polarity and guidance along or into tissue structures. Examples of well-defined leader cells are tip cells in the developing insect trachea or mammalian sprouting vessels[18]. As mechanism underlying tip-cell selection and collective sprouting, extracellular guidance signals by morphogens and chemokines induce receptor tyrosine kinase signaling. This causes tip cell selection in cell-subsets and inhibits tip-cell fate in adjacent cells, then called followers, by negative feedback signaling through Delta-Notch interaction[18]. Similar leader-follower segregation can be achieved in 2D cell sheets, where mechanical signals induce leaders cells at the front, which through subsequent Delta-dependent negative feedback signaling, inhibit leader formation in neighboring cells[17]. Leader cell functions may be also be adopted transiently, with yet-to-be-defined characteristics, such as in the developing mammary gland, where multicellular leaders rapidly exchange position[4]. The extracellular inputs and downstream intracellular signals that define and maintain leader cells are probably cell-type and tissue-context specific (Table 1). These include mitogen-activated protein kinase (MAPK) / extracellular signal-regulated kinase (ERK), focal adhesion kinase (FAK), phosphoinositide-3-kinase (PI3K)/Akt, Src kinases, Notch and Rho-GTPases. The early activation of these pathways contributes to the intrinsic bipolarity in leader cells [3,19–23]. As an example, the activation of Rho-GTPases (mainly Rac) at the anterior cell part regulates actin polymerization, actomyosin-based contractility, coupling and force transmission to stabilize integrin-mediated focal adhesions and thus defines leader cell motility[20,24,25]. Conversely, the rear of the leader cell retains cell-cell junctions and junction-derived signals, which locally silence Rho/Rock signaling and downregulate actomyosin contractility[26–29]. Compared with the formation of protrusions at the leader cell, near cell-cell junctions protrusions are usually minimized and mechanical coupling is secured in a process termed contact inhibition of locomotion (CIL)[3,30] (Table 1).

Table 1: Diversity of guidance cues and signaling in collective movements

Guidance principle	Cell type/ Environment	Steering mechanism	Refs.
Cell-intrinsic	Epithelial monolayer in scratch wound assay	Spatially constrained ERK activation in leader cells	19
	Epithelial monolayer on collagen I matrix	Activation of Rac, PI3K/upregula-tion of β1-integrin in leader cells	20
	Cranial neural crest cell migra-tion in developing *Xenopus*	N-cadherin mediated CIL and supracellular polarization	82
Contact guidance (1D)	Fibroblast streams on 1D fibrillar patterns	Uniaxial lamella, alignment of actin cytoskeleton (single cells)	54
Contact guidance (2D)	Epithelial monolayer in gap closure assay/single cells on micropatterned substrates	Interaction with substrate at free edge induces reorientation of cell polarity and front cell polarization	11,43
	MDCK[a] cells seeded on a fibronectin-coated cylindrical wire	Circumferential alignment of the actin cytoskeleton and multiple focal adhesions for movement along curved substrate	47

Contact guidance (3D)	Tumor cell spheroids in collagenI matrix	Generation of linear confined tracks by matrix degradation; haptokinesis	46,56,116,119,121
Contact guidance (1D-3D)	Melanoma invasion in mouse dermis	Movement along space defined by interfaces in tissue	50
Haptotaxis	Mammary epithelium organoids in different ECM	Guidance by fibrillar collagen but not amorphous Matrigel environment	136
	Epidermal wound healing	Guidance by laminin 5 newly deposited by leading keratinocytes onto dermal collagen	63
	Dictyostelium discoideum aggregation and migration	Slime sheath produced by leader cells that provides traction support for followers	137
Haptorepulsion	Neural crest and placodal cells in developing *Xenopus*	N-cadherin mediated repulsion between neural crest and placodal cells	69
Durotaxis	Spreading of sarcoma cells on substrates with varying rigidtity	Improved collective coordination on rigid substrates (by improved cell-cell cohesion)	75
Collective drift	Circulating tumor cell clusters in breast cancer metastasis	Passive drift with blood or interstitial fluid flow	6,76
Fluid-flow sensing	Pronephric cells in developing zebrafish	Migration against flow, sensing of shear stress probably by mechanosensitive focal adhesion proteins and Fak signaling	79,138
	Endothelial cells exposed to fluid flow *in vitro*	Migration with flow, sensing of shear stress probably by mechanosensitive focal adhesion proteins	78,139
Chemoattraction	Border cell migration in developing *Drosophila*	Leader cell induction by PVF1; Rac1 activation	110,140
	Endothelial cells in sprouting angiogenesis *in vitro*	VEGF-induced tip cell differentiation; ANG1[b] promoted cell-cell junctions	105
	Posterior line primordium in developing zebrafish	Self-generated SDF-1 gradient due to differential expression of activating CXCR4[c] in the front and CXCR7 decoy receptor in the rear	90–92
	B and T-cell lymphoma in flow chamber	Clustering and collective migration induced by CCL19[d] and SDF-1 gradient	93
Chemorepulsion	Gastrulation in chick embryo	Movement of mesendoderm cells out of primitive streak due to repulsive FGF8 signal	95,141
Electrotaxis	Epithelial monolayer	Electric field, migration towards anode or cathode	100,101,103

[a]Madin-Darby Canine Kidney, [b]Angiopoietin-1, [c]Chemokine receptor type 4, [d]Chemokine (C-C motif) ligand 19

Principles of force generation in collective guidance

The anterior traction forces generated by the leader cell towards the substrate are balanced by tensile forces at the cell-cell junctions with follower cells at the rear. Follower cells can also engage in cell-substrate traction forces, possibly as consequence of "cryptic lamellipodia" that protrude underneath the neighbor cell[31] and transmit forces across a longer distance and multiple cell bodies within moving cell sheets[32,33] (Fig. 1A). However, to what extent cryptic lamellipodia generate force to propel collective movement remains under debate[33,34]. Thus, both leader and, to lesser extent, follower cells generate traction force towards the substrate, which is balanced with the forces extending across cell-cell bodies. Collectively, an integrated mechanocoupling program within the leader cell reinforces outward polarization, cyclic actomyosin coupling, force transmission, and negative feedback signaling to follower cells to guide the cell group.

Beyond active pulling toward the substrate, mechanical pushing may be imposed by neighboring cells, either by volume increase after mitosis or when cells become jammed in a confined environment[9,35] (Fig. 1B). Together, pushing from the rear and pulling from the front synergize and contribute to collective coordination and displacement.

Alongside collective front-rear force transmission, moving cell groups process directional information by intra-and intercellular signaling. Along cell-cell junctions, signaling is exerted by the adhesion molecules themselves, including mainly cadherins[32,36,37] (Box 1). In addition, forces transmitted at cell-cell junctions may induce conformational changes in mechanoresponsive molecules, including vinculin or filamin and thereby trigger signaling events[38–40]. Lastly, moving cell groups maintain cell-cell communication via gap junction proteins (connexins); however, how signaling propagation via gap junctions contributes to polarity and mechanical connection between moving cells remains unclear[41].

Consequently, beyond leader-follower behavior, collective migration relies on integrated mechanocoupling and guidance throughout the cell group.

Topographic guidance

The structural and molecular organization of tissue provides important cues for collective guidance. Cell groups interact with the extracellular matrix (ECM) and molecules bound by the ECM and/or resident cells; thereby they sense, interpret and follow the topography of their environment, termed contact guidance or, when mediated by specific adhesion receptors, termed haptokinesis[42]. In the event that these physical and/or molecular cues are inhomogeneous and act as a gradient, directional sensing causes intracellular signal polarity and movement along the gradient, termed duro- or haptotaxis, respectively[43].

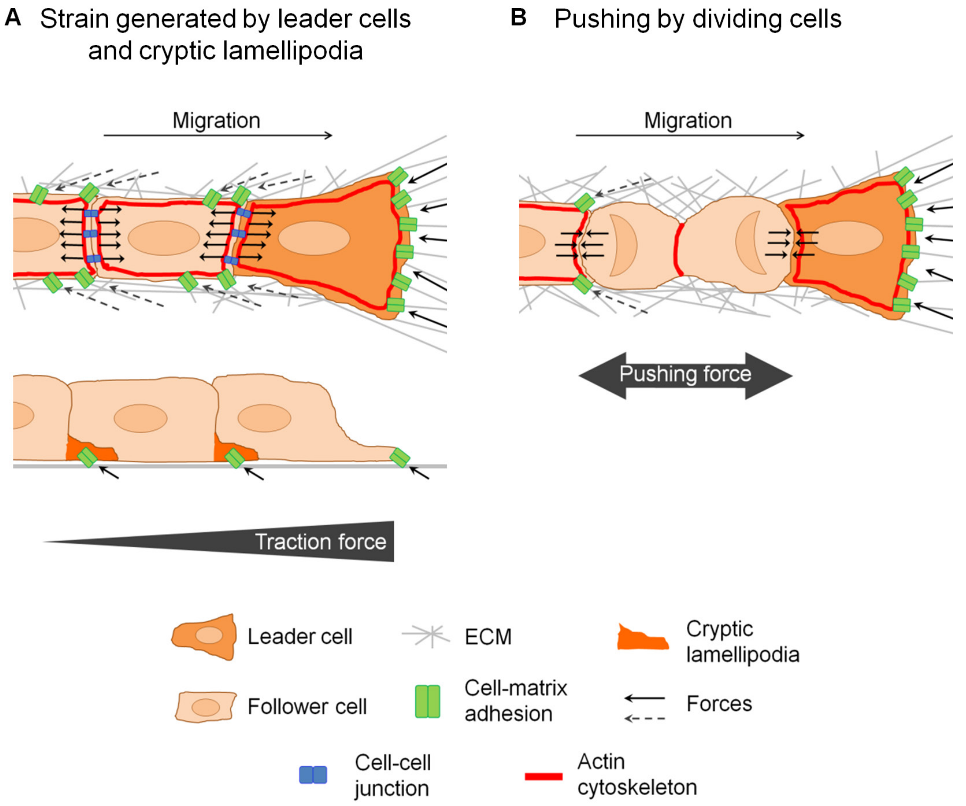

Figure 1. Cell-intrinsic mechanisms for collective cell guidance.
Leader-follower cell polarization and force generation/transduction in a migrating cell group. **A)** By interacting with and exerting pulling force on the ECM, leader cells generate a gradient of traction force toward the substrate and between neighbor cells (upper panel). Follower cells may form "cryptic lamellipodia" that anchor to the ECM and might contribute additional traction forces in the moving cell collective (lower panel). **B)** Cells undergoing mitosis can exert lateral pushing on neighboring cells, leading to cell displacement and eventually movement through group expansion, with forward pushing of leader cells and rearward pushing toward follower cells.

Contact guidance/haptokinesis

Contact guidance and haptokinesis result from cells orienting their length axis and movement along topographic cues provided by the anisotropy of the encountered environment[44,45]. To enable haptokinesis, adhesion-receptors engage with the substrate and thereby "sense" and mechanically couple to topographic cues[42,46]. These can be ECM components, including collagen fibers or basement membrane, or complex tissue structures such as nerve tracks, muscle fibers, or fat cells. To a varying degree, these structures are respected by moving cells and cell groups and therefore serve both a guiding and a barrier function shielding adjacent environments from moving cells[47–50]. Given the complexity of moving cell groups, it remains unclear when and which cell subsets exert active haptokinesis and when and which cells become passively dragged or carried along the restricted route.

The topography of the guiding structure, and hence the responding cytoskeletal organization, can be 1D, 2D, or 3D. Each topography supports alignment of adhesion sites in parallel orientation to the substrate, followed by longitudinal adaptation of the actin cytoskeleton and thus cell shape and migration direction[51,52]. 1D topography is provided by a spatially narrow ligand with near-linear orientation, such as a single collagen fiber or stripe-like ligand decorating a surface, which discourages cells to move next to each other. For 1D migration, cells are required to align their adhesion sites in a string-like fashion as narrow as the ligand, resulting in well-defined, usually chain-like movement along this single cue[53,54] (Fig. 2A and Table 1). A 2D surface, such as the plane of a cell culture dish *in vitro* or basement membrane lining a blood vessel *in vivo*, provides space for topographically unrestricted spreading of adhesion sites underneath the entire cell body and cell group, to perform 2D haptokinesis along the surface as multicellular sheet. Because the substrate provides lateral space, in contrast to 1D migration, moving cell sheets typically exhibit lateral turns and interspersed lateral rotational movements of cells within the group [34,47,55] (Fig. 2B and Table 1). Collective 3D haptokinesis occurs when cell groups follow 3D topographic cues, which provide both guidance and bi- or multi-lateral confinement. Examples of aligned 3D tissue include continuous sheet-like 2D interfaces present between muscle fibers or larger nerves and discontinuous networks formed by ECM fibrils or cell structures, such as neuronal filaments[50,56] (Fig. 2C,D and Table 1). As a “2.5D” intermediate, a groove or angled surface (e.g. along the edge of a cell culture dish) provides bilateral guidance whereby apical confinement is lacking [57,58] (Fig. 2E). Thus, in 1D, 2D, and 2.5D haptokinesis adhesion systems guide directionality, whereas 3D guidance additionally follows the path of least resistance defined by multilateral and space-confining extracellular structures[49].

Haptotaxis and repulsion

Whereas haptokinesis describes adhesion receptor-dependent migration along an isotropic substrate, haptotaxis combines principles of physical and chemical guidance by directing migration along a gradient of immobilized ligand[59]. Ligand gradients can result from different levels or distributions of ECM proteins including collagens, fibronectin, and laminins, matrix-bound cytokines and chemoattractants, and/or adhesion molecules present on encountered cells (e.g. cadherins, cell adhesion molecules (CAMs) (Box 1)). Cells usually orient their migration toward increasing availability of adhesion sites (Fig. 2F and Table 1); however, cell movement may also orient towards decreasing ligand density depending on the cell type and adhesion receptors involved[60,61].

With haptotaxis as the primary event, leader cells can reinforce or oppose collective haptotactic guidance at four levels: (i) sensing and responding to the guidance cue; (ii) deposition of ECM components and *de-novo* creation of adhesion sites[62,63]; (iii) removal of adhesion sites by matrix degradation[56,64]; and (iv) paracrine signaling via deposition of cytokines/chemokines while remodeling the matrix[65]. With the latter three, cell-derived tissue modifications, leader cells provide secondary guidance cues for the follower cells (Table 1).

Cell guidance away from an encountered structure is termed repulsion. Haptokinetic repulsion can be mediated through direct cell-cell communication, for instance by interaction of Eph receptor tyrosine kinase with membrane-bound associated ephrin ligands on neighboring cells[66,67], or through downstream signaling events of other cell-cell adhesion molecules, including N-cadherin[68,69] (Table 1). Repulsive downstream signaling leads to inhibition of Rac, disassembly of focal adhesions, and collapse of cell protrusions followed by reorientation of the cell in the opposite direction[69]. In addition, repulsion results from Rho-dependent contractility at cell boundaries, which prevents stable cell junctions and supports cell and tissue separation[68].

Box 1: Mechanocoupling along cell-cell junctions

Cell-cell connections in collectively migrating cell groups involve homophilic interactions mediated by cadherin adhesion receptors (adherens junctions) together with demosomal proteins, tight junction constituents, gap junctions, and homophilic or heterophilic interactions between immunoglobulin family members, including activated leukocyte adhesion molecule (ALCAM), neural cell adhesion molecule (N-CAM) or L1 cell adhesion molecule (L1-CAM) and Ephrins/Eph receptors[25,114,126–128]. Most, if not all, adhesion receptors contribute to cell-cell contact mediated signaling (e.g. PI3K/Akt, FAK, ERK, Rho-GTPases)[129–132]. Cadherins and desmosomal and tight junction proteins additionally provide stabilization of cell-cell connectivity[133]. In particular, these junctions form a mechano-transducing bridge to neighboring cells via cytoskeletal linkages at their cytoplasmic site, which underlies the supracellular organization of the actin cytoskeleton and actomysion cables that bridge across junctions[10,134]. It is likely that multiple adhesion mechanisms cooperate in a hierarchical manner to process guidance information and provide mechano-sensory integration and force coupling during collective migration. In addition, although cell-cell junctions provide mechanically stable connections, at the molecular level adhesion sites and cytoskeletal connections are dynamic and are constantly remodeled to secure both mechanical connection as well as junctional flexibility[135].

Durotaxis

The directional response of moving cells in response to a stiffness gradient of the substrate is termed durotaxis, with positive (i.e. toward high stiffness), negative (i.e. toward low stiffness), or perpendicular (i.e. along a corridor of unchanged stiffness) orientation and directionality[70,71] (Fig. 2G). Positive durotaxis is prevalent in fibroblasts that migrate towards regions of highest rigidity when placed on a matrix of varying stiffness[72] and results from graded mechanosensory signaling, including integrin-mediated focal adhesions and traction generation via myosin-II mediated contractility[73,74]. Suggestive of differential stiffness sensing, collective migration of sarcoma cell sheets is enhanced on stiffer substrates compared with soft substrates[75] (Table 1). However, the mechanisms by which cell groups integrate stiffness gradients for direction sensing remain to be explored.

Fluid flow and shear stress

Directional fluid flow, experienced by cell groups inside perfused vessels or in the urinary tract, can guide cells by several mechanisms. Collective drift occurs when cell groups enter perfused vessels, where detached cells can become passively dragged along in the direction of the flow and disseminate with blood or lymph flow or with fluids present in the peritoneal or pleural cavitiy[6,76] (Fig. 2H and Table 1).

Flow-imposed shear stress can also be translated by adherent cells into directional information through molecular sensors of shear stress. These sensors include mechanosensitive focal adhesion proteins, G-protein coupled receptors, transient receptor potential (TRP) ion channels, and primary cilia[77]. As a consequence, migrating cells may move with or against the flow[78,79] (Fig. 2I and Table 1).

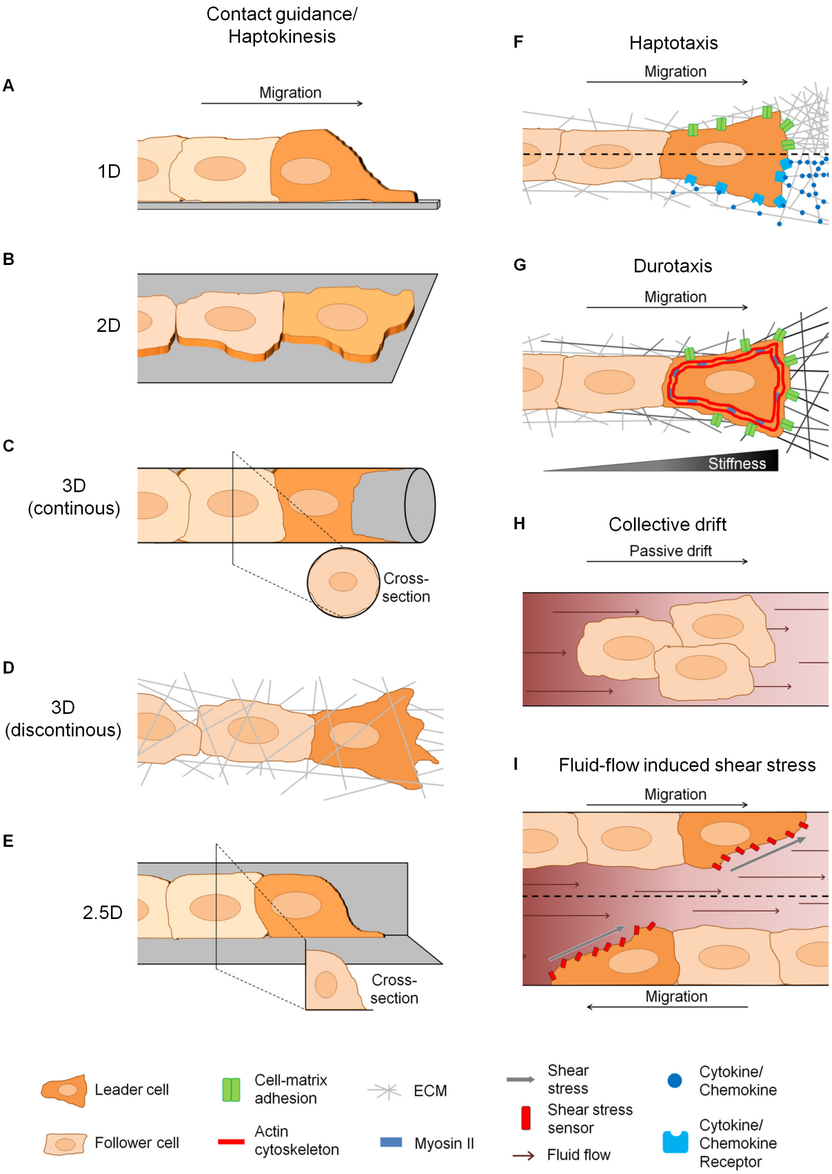

Figure 2. Collective guidance by topographic and mechanical cues.
Individual modules are displayed in which live-tissue context might occur concurrently. **(A-E)** Gui-dance dimensions of collective migration by substrate topography. Cell groups migrate via contact guidance/ haptokinesis along substrate of varying shape and order. **F)** Haptotaxis is induced by gradients of adhesion sites (upper panel) or substrate-bound molecules (mainly cytokines, lower panel), which combines principles of mechanical and chemical guidance in the same process. **G)** Cell groups may exert durotaxis and mechanically sense and follow gradients of matrix stiffness, a process dependent on adhesion signaling and actomyosin. **(H,I)** Collective guidance by fluid flow. Cell groups either undergo passive collective drift (H) or sense the fluid-flow imposed shear stress to steer migration either along (upper panel) or against the flow (lower panel) (I).

Chemical guidance through chemotaxis

Cell guidance via soluble chemical cues is termed chemotaxis and can be either attracting or repelling. Chemoattraction is the chemotactic movement along a gradient of soluble chemical stimuli including chemokines and cytokines but also altered pH or reactive oxygen species (ROS)[80]. Based on fluid drift and convection, this results in rapid but temporally limited molecular gradients, in contrast to the temporally and spatially more sustained signals provided by haptotaxis and haptorepulsion. Receptor binding and activation by chemotactic molecules induces local downstream signaling and cytoskeletal protrusions followed by cell polarization and movement toward the zone with the highest chemoattractant availability[81]. In response to a chemoattractant gradient, supracellular polarity is reinforced by preferential activation of signaling pathways in leading cell rows, which stimulates the pro-migratory signaling of leader cells and stabilizes cell polarity and cell-cell cohesion[82,83].

Collective chemoattraction is an essential guidance mechanism in developmental processes but also a powerful tool in experimental systems to direct collective migration[84]. Chemotaxis is typically a paracrine mechanism, through diffusive molecules secreted by other cells nearby[85,86], but also may be induced or maintained by the cells themselves[80,87] (Fig. 3A). Cell collectives can establish a self-generated chemokine gradient along the migrating group by (i) releasing a migration-enhancing factor near the front, which positively feeds-back on leader cells[88]; (ii) releasing chemokine-degrading enzymes that diffuse along the cell group and gradually clear chemokines along the length axis of the group[89]; and/or (iii) expressing migration-inducing receptors in the leading cell group and decoy receptors in the rear that bind, internalize, and thereby remove chemokines thus limiting their activity in follower and trailing cells[87] (Fig. 3A and Table 1). This self-generation of a chemotactic gradient induces supracellular polarity, which is required for directional migration of the zebrafish lateral line[90–92]. The scavenger chemokine receptor type 7 (CXCR7), which is preferentially expressed by the rear of the moving group, sequesters tissue-derived chemoattractant stromal cell derived factor-1 (SDF-1) and generates a front-rear SDF-1 gradient that guides collective migration through chemokine receptor type 4 (CXCR4) signaling[90–92].

Taking these findings together, collective chemotaxis includes a remarkable diversity of chemokine and signal processing across multiple cell bodies. Beyond guidance, chemotactic signaling can reinforce cell-cell adhesion and cell clustering, which can induce collective migration of cells that otherwise tend to migrate individually[93,94] (Table 1).

Chemorepulsion describes the movement away from a source of soluble chemical stimuli. Similar to chemoattraction, receptor binding by chemotactic molecules induces local signaling, whereby pro-migratory protrusions form at the pole of the cell, or cell group, opposed to receptor engagement[85,86]. Chemorepulsion in collective migration has important roles during embryonic development, where repulsion by morphogens like fibroblast growth factor (FGF)

8 and Wnt3a induce mesendodermal sheet migration away from the primitive streak during gastrulation[95]. However, whether the integration of signals controlling collective repulsion is similar to those in single cells[96,97] remains to be established.

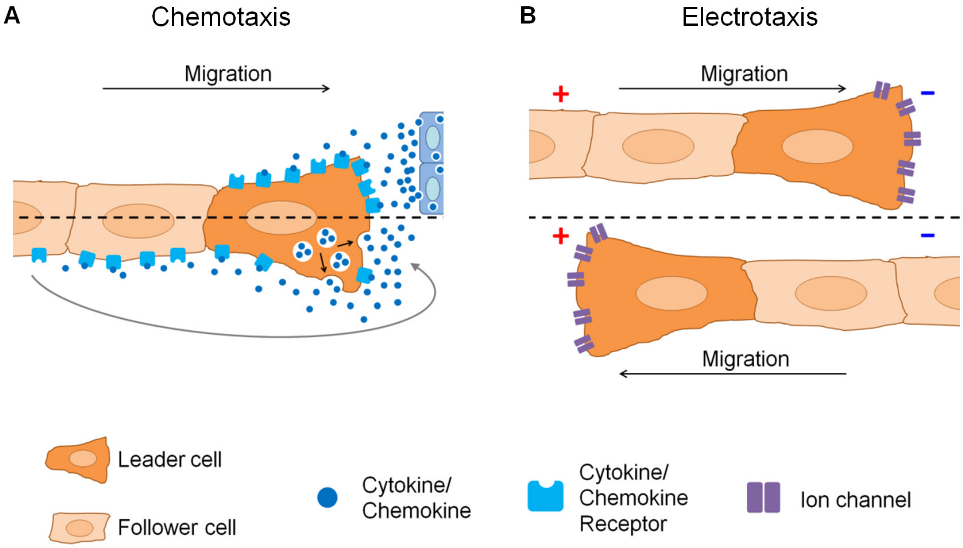

Figure 3. Chemical and electrical collective guidance.
Individual modules are displayed in which live-tissue context might occur concurrently. **A)** Chemo-tactic collective guidance. Chemoattractive cytokines are released by stromal cells and stimulate leader cells via paracrine signaling (upper panel) or leader cells stimulate themselves via autocrine signaling (self-generated gradient; lower panel).**B)** Collective guidance directed by an electric field. While sensing the electric field via ion channels, cells move toward the cathode (-) (upper panel) or the anode (+) (lower panel), which is dependent on the cell type and ion channels involved.

Electrical guidance

Electrotaxis (also known as galvanotaxis) is defined as directional migration of cells relative to a direct-current electric field with, depending on the cell type, orientation towards the cathode or the anode[14,98–101] (Fig. 3B and Table 1). As potential steering mechanisms, the electric field can open voltage-gated Ca^{2+} or Na^{+} ion channels, followed by intracellular influx of ions and downstream signaling through activation of ion transport proteins (e.g. Na/K-ATPase and sodium-hydrogen exchanger 3 (NHE3)) and cytoskeletal polarization[99,102]. In addition, migration-inducing cell surface receptors, including epidermal growth factor receptor (EGFR), acetylcholine receptor (AchR) and integrins were reported to respond to electric fields and locally activate PI3K/Akt and MAP/ERK signaling[99,101]. In epithelial sheets, electrotaxis appears to engage both leader and follower cells to generate oriented traction forces parallel with the electric field and adaptive reorientation with altered field polarity[100,103].

Electrotaxis has various effects including stimulation of the migration of many cell types such as fibroblasts, epithelial and endothelial cells, neurons, and immune cells as well as cancer cells[14]. Collective electrotaxis supports self-regeneration and wound healing. Disrupted epithelial cell sheets induce an endogenous gradient of weak electrical current that enhances migration into the open space for wound closure[101]. Besides the moving epithelium itself, endothelial and neuronal cells are also engaged to secure complete tissue regeneration[101,102]. These tissue-intrinsic effects can be clinically exploited and enhanced by external electrical stimulation, which accelerates the healing process [102,104].

In summary, collective movement is guided by numerous cell group-generated and external mechanical, chemical and electrical guidance cues. As a consequence, moving cell groups must interpret and hierarchically integrate such diverse signals for steering collective polarity, path finding, and decision making.

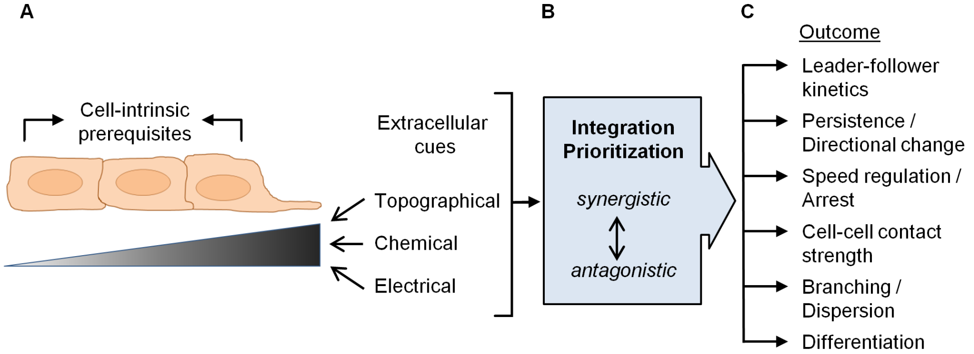

Figure 4. Collective processing of multiple guidance signals and response.
A) Cell-intrinsic interactions and directed extracellular cues act simultaneously on the cell group. **B)** Integration and prioritization of synergistic and opposing signals allows for prioritization and decision making. **C)** As an outcome, altered polarity, cell-cell cooperation, and additional para-meters including growth and differentiation determine persistent or altered direction or migration arrest.

Collective guidance in complex environments – multiscale integration

In tissues, physical and chemical guidance mechanisms act in parallel; therefore, migrating collectives need to integrate concurrent, potentially cooperative, or opposing inputs to make go or no-go decisions and adjust the direction of migration (Fig. 4A,B). In addition, integration of the input may impact cell-cell interaction strength and intercellular mechanocoupling and either support multicellular cohesion or permit dispersal and transition to single-cell migration[105]. Therefore, cell groups process and prioritize guidance cues for coordinated movements and cell-fate decisions (Fig. 4C).

In primordial or interim tissues, often comprising soft, amorphous ECM (e.g. the developing embryo, post-traumatic provisional fibrin network), chemical guidance by chemokines and growth factors dominates in attracting blood vessels and epithelial structures as part of tissue morphogenesis or repair[9]. Examples include the branching morphogenesis of the trachea induced by FGF, the lateral line forming the balance organ in Zebrafish in response to SDF-1, and vascular sprouting into a wound by vascular-endothelial growth factors (VEGFs) and FGF[90,105,106]. In these cases, chemoattraction initiates and guides collective movement, and ECM remodeling is a secondary element contributing to (re)shaping the tissue; for example by generating tube-like tissue tracks and deposition of a basement membrane[64,107].

Joint contributions of both chemical and physical guidance cues converge in a hierarchical manner in the collective movement of border cells moving in the ovary of developing *Drosophila* embryos. Initially, a single leader-cell is selected and further attracted by growth factors released from the oocyte in a paracrine fashion, which activate platelet-derived growth factor (PDGF) - and VEGF-related factor 1 (PVF1), EGFR and downstream Rac1 signaling followed by leader cell protrusion and guidance of the group[24,108–110]. Congruently, the haptokinetic path of the group is pre-defined in an adhesion receptor-dependent manner by a few confined trails of least resistance between the nurse cells of the ovary. Thereby, E-cadherin mediates interactions within the border cell group as well as between the border cell groups and the stationary nurse cells, which serve as an adhesion substrate and guiding scaffold for haptokinetic migration of the group[37]. Because ablation of EGFR signaling is sufficient to compromise guidance by the leader cell and deviate the group from its default track[111], the growth factor signal is likely to dominate leader cell function to prioritize one of a few available routes.

Hierarchy is further defined by the relative strength of guidance modalities. Migration of an epithelial monolayer closing a tissue defect follows the interface between the underlying substrate and cell-free space until the gap is closed and contact inhibition of migration overrules pro-migratory signaling[11,30]. However, on additional exposure to an electric field, electrotaxis overrides other guidance principles resulting in monolayers moving according to the current flow and in the opposite direction to open space or cells piling up at a barrier due to lack of contact inhibition of migration [102,103]. Similarly, endothelial cells following a haptotactic gradient initiate migration into the opposite direction when exposed to countercurrent and sufficiently strong fluid flow, whereas haptotaxis dominates at low levels of shear stress[78].

In mature tissue comprising ordered collagen architecture bordering functional tissue structures such as muscle fibers, blood vessels and nerve tracks, physical guidance cues are likely to dominate, with fine-tuning by chemical guidance. Such ordered tissue architecture creates pre-existing routes permissive for passenger leukocytes or invading tumor cell groups, which perform 2D and 3D contact guidance along small tissue interfaces (“tracks”)[47,50,56,112,113]. Due to lateral space limitations in 3D environments, the topographic confinement of invading cell groups leads to “jamming” - the promotion of cell-cell junction formation and supracellular mechanocoupling - and thereby reinforces cell-intrinsic collective polarity and guidance[35,114,115]. When particularly high tissue density or rigidity impedes or even ablates collective cell movement by physical constraints, initial leader cell protrusions may initiate proteolytic tissue remodeling, which enables and reinforces migration along the initial direction as well as branching of existing strands[49,116]. Thereby, intrinsic leader cell polarity and primary tissue remodeling cooperate to modify tissue and generate 3D haptokinetic collective guidance along the newly formed migration track[49,117]. Such 3D tracks may undergo further widening by lateral remodeling caused by follower cells, which reinforces a once established collective route[107,114,116]. Additionally, release or activation of chemotactic or haptotactic guidance signals by proteolytic cleavage of ECM and other proteins may act as a secondary cue[118,119].

The pathways downstream of the chemical or mechanical inputs discussed here share many common signaling intermediates. For example PI3K, FAK, Src, MAPKs, Rho GTPases and myosin II, which are prime candidates as major hubs for signal integration[99,101,120–122], may all contribute to sensing, transmitting, or dampening external guidance signals. However, how such guidance signals feed into the overall signal transduction networks and achieve collective cell-kinetic output remains largely unresolved.

Concluding remarks

The interdependence of self-organization within the cell groups and their communication with surrounding chemical, mechanical, electrical, and probably further tissue cues represent fascinating and challenging examples for multicellular signal processing and decision making in each individual cell as well as the group. To accommodate this complexity, multiparameter analysis at the intersection of physics and life sciences will be required. Technological trends to reach in-context analysis of highest-possible number of molecular and physical parameters through integration of multiparameter imaging require mechanical probing and the retrieval of molecular signatures from the same environmentally controlled sample[123]. This includes bioinformatic multiscale and meta-analysis of cell-derived datasets followed by integration of mathematical modeling to interpret and predict hierarchies of cues for collective guidance in complex environments[124].

Cell biological challenges to resolve both individual and collective cellular information processing and intercellular communication from the same sample, *in vitro* or *in vivo*, require single-cell reporter readout of signaling and mechanical states (“live-cell biochemistry”) and optogenetics to delineate functional heterogeneity and integration[24].

Beyond the analysis of collective migration, an integrated view on collective guidance signals and their cross-talk/overlap with other cell functions, including stemness and differentiation, growth and survival, and their implications for diagnostics and therapy will have to be established. This will include quantitative cell-resolved morphometry of tissue sections in tissue samples instead of arbitrary scoring and single-cell genomic and proteomic profiling of developing and diseased tissue. Principles delineated here may be being exploited in clinical routine; examples are diagnostic physical/molecular tissue probing in cancer[125], the integration of pro-migratory synthetic scaffold tracks for facilitated regeneration (e.g. to heal neuronal injury), and electrical stimulation to support closure of chronic wounds or ulcers[102,104]. Thus, understanding the hierarchies of collective guidance may foster concepts in both basic biology and application to steer or prevent collective cell migration for the purpose of applied tissue regeneration or intervention in progressing tumors.

Acknowledgements

This work was supported by the Dutch Cancer Foundation (KWF 2008-4031), NWO-VICI (918.11.626), and the Cancer Genomics Cancer, The Netherlands to PF; NWO-VIDI (917.10.364) to KW; and the European Comission FP7-PEOPLE-2011-IIF (302067) to M.Z.

References

1. Friedl, P., Locker, J., Sahai, E. & Segall, J. E. Classifying collective cancer cell invasion. *Nat. Cell Biol.* **14,** 777–83 (2012).
2. Montell, D. J. Morphogenetic cell movements: diversity from modular mechanical properties. *Science* **322,** 1502–5 (2008).
3. Zegers, M. M. & Friedl, P. Rho GTPases in collective cell migration. *Small GTPases* **5,** e28997-1–10 (2014).
4. Andrew, D. J. & Ewald, A. J. Morphogenesis of epithelial tubes: Insights into tube formation, elongation, and elaboration. *Dev. Biol.* **341,** 34–55 (2010).
5. Rørth, P. Collective cell migration. *Annu. Rev. Cell Dev. Biol.* **25,** 407–29 (2009).
6. Aceto, N. *et al.* Circulating Tumor Cell Clusters Are Oligoclonal Precursors of Breast Cancer Metastasis. *Cell* **158,** 1110–1122 (2014).
7. Friedl, P. & Alexander, S. Cancer invasion and the microenvironment: plasticity and reciprocity. *Cell* **147,** 992–1009 (2011).
8. Gray, R. S., Cheung, K. J. & Ewald, A. J. Cellular mechanisms regulating epithelial morphogenesis and cancer invasion. *Curr. Opin. Cell Biol.* **22,** 640–50 (2010).
9. Friedl, P. & Gilmour, D. Collective cell migration in morphogenesis, regeneration and cancer. *Nat. Rev. Mol. Cell Biol.* **10,** 445–57 (2009).
10. Trepat, X. & Fredberg, J. J. Plithotaxis and emergent dynamics in collective cellular migration. *Trends Cell Biol.* **21,** 638–46 (2011).
11. Anon, E. *et al.* Cell crawling mediates collective cell migration to close undamaged epithelial gaps. *Proc. Natl. Acad. Sci. U. S. A.* **109,** 10891–6 (2012).
12. Ridley, A. J. *et al.* Cell migration: integrating signals from front to back. *Science* **302,** 1704–1709 (2003).
13. Friedl, P. & Weigelin, B. Interstitial leukocyte migration and immune function. *Nat. Immunol.* **9,** 960–969 (2008).
14. Cortese, B., Palamà, I. E., D'Amone, S. & Gigli, G. Influence of electrotaxis on cell behaviour. *Integr. Biol. (Camb).* **6,** 817–30 (2014).
15. Rorth, P. Whence directionality: guidance mechanisms in solitary and collective cell migration. *Dev. Cell* **20,** 9–18 (2011).
16. Khalil, A. a & Friedl, P. Determinants of leader cells in collective cell migration. *Integr. Biol. (Camb).* **2,** 568–574 (2010).
17. Riahi, R. *et al.* Notch1-Dll4 signalling and mechanical force regulate leader cell formation during collective cell migration. *Nat. Commun.* **6,** 6556 (2015).
18. Weavers, H. & Skaer, H. Tip cells: master regulators of tubulogenesis? *Semin. Cell Dev. Biol.* **31,** 91–9 (2014).
19. Chapnick, D. a & Liu, X. Leader cell positioning drives wound-directed collective migration in TGFβ-stimulated epithelial sheets. *Mol. Biol. Cell* **25,** 1586–93 (2014).
20. Yamaguchi, N., Mizutani, T., Kawabata, K. & Haga, H. Leader cells regulate collective cell migration via Rac activation in the downstream signaling of integrin β1 and PI3K. *Sci. Rep.* **5,** 7656 (2015).
21. Han, J. *et al.* Epidermal growth factor stimulates human trophoblast cell migration through Rho A and Rho C activation. *Endocrinology* **151,** 1732–42 (2010).
22. Zhang, X., Moore, S. W., Iskratsch, T. & Sheetz, M. P. N-WASP-directed actin polymerization activates Cas phosphorylation and lamellipodium spreading. *J. Cell Sci.* **127,** 1394–405 (2014).
23. Benedito, R. *et al.* The notch ligands Dll4 and Jagged1 have opposing effects on angiogenesis. *Cell* **137,** 1124–35 (2009).

24. Wang, X., He, L., Wu, Y. I., Hahn, K. M. & Montell, D. J. Light-mediated activation reveals a key role for Rac in collective guidance of cell movement in vivo. *Nat. Cell Biol.* **12,** 591–7 (2010).

25. Hegerfeldt, Y., Tusch, M., Bröcker, E. B. & Friedl, P. Collective Cell Movement in Primary Melanoma Explants: Plasticity of Cell-Cell Interaction, Beta1-Integrin Function, and Migration Strategies. *Cancer Res.* **62,** 2125–2130 (2002).

26. Das, T. *et al.* A molecular mechanotransduction pathway regulates collective migration of epithelial cells. *Nat. Cell Biol.* **17,** 276–87 (2015).

27. Hidalgo-Carcedo, C. *et al.* Collective cell migration requires suppression of actomyosin at cell-cell contacts mediated by DDR1 and the cell polarity regulators Par3 and Par6. *Nat. Cell Biol.* **13,** 49–58 (2011).

28. Wennerberg, K. *et al.* Rnd proteins function as RhoA antagonists by activating p190 RhoGAP. *Curr. Biol.* **13,** 1106–15 (2003).

29. Reffay, M. *et al.* Interplay of RhoA and mechanical forces in collective cell migration driven by leader cells. *Nat. Cell Biol.* **16,** 217–23 (2014).

30. Mayor, R. & Carmona-Fontaine, C. Keeping in touch with contact inhibition of locomotion. *Trends Cell Biol.* **20,** 319–28 (2010).

31. Farooqui, R. & Fenteany, G. Multiple rows of cells behind an epithelial wound edge extend cryptic lamellipodia to collectively drive cell-sheet movement. *J. Cell Sci.* **118,** 51–63 (2005).

32. Bazellières, E. *et al.* Control of cell-cell forces and collective cell dynamics by the intercellular adhesome. *Nat. Cell Biol.* **17,** 409–420 (2015).

33. Trepat, X. *et al.* Physical forces during collective cell migration. *Nat. Phys.* **5,** 426–430 (2009).

34. Kim, J. H. *et al.* Propulsion and navigation within the advancing monolayer sheet. *Nat. Mater.* **12,** 856–63 (2013).

35. Sadati, M., Taheri Qazvini, N., Krishnan, R., Park, C. Y. & Fredberg, J. J. Collective migration and cell jamming. *Differentiation.* **86,** 121–5 (2013).

36. Desai, R. A., Gao, L., Raghavan, S., Liu, W. F. & Chen, C. S. Cell polarity triggered by cell-cell adhesion via E-cadherin. *J. Cell Sci.* **122,** 905–11 (2009).

37. Cai, D. *et al.* Mechanical feedback through E-cadherin promotes direction sensing during collective cell migration. *Cell* **157,** 1146–59 (2014).

38. Roca-Cusachs, P., Sunyer, R. & Trepat, X. Mechanical guidance of cell migration: Lessons from chemotaxis. *Curr. Opin. Cell Biol.* **25,** 543–549 (2013).

39. del Rio, A. *et al.* Stretching single talin rod molecules activates vinculin binding. *Science* **323,** 638–41 (2009).

40. Ehrlicher, A. J., Nakamura, F., Hartwig, J. H., Weitz, D. A. & Stossel, T. P. Mechanical strain in actin networks regulates FilGAP and integrin binding to filamin A. *Nature* **478,** 260–3 (2011).

41. Defranco, B. H. *et al.* Migrating cells retain gap junction plaque structure and function. *Cell Commun. Adhes.* **15,** 273–88 (2008).

42. Maheshwari, G. & Lauffenburger, D. A. Deconstructing (and reconstructing) cell migration. *Microsc. Res. Tech.* **43,** 358–368 (1998).

43. Théry, M. *et al.* Anisotropy of cell adhesive microenvironment governs cell internal organization and orientation of polarity. *Proc. Natl. Acad. Sci. U. S. A.* **103,** 19771–6 (2006).

44. Dunn, G. Contact guidance of cultured tissue cells: a survey of potentially relevant properties of the substratum. *Cell Behaviuor* 247–280 (1982).

45. Dickinson, R. B., Guido, S. & Tranquillo, R. T. Biased cell migration of fibroblasts exhibiting contact guidance in oriented collagen gels. *Ann. Biomed. Eng.* **22,** 342–56 (1994).

46. Dee, K. C., Anderson, T. T. & Bizios, R. Osteoblast population migration characteristics on substrates modified with immobilized adhesive peptides. *Biomaterials* **20,** 221–7 (1999).

47. Yevick, H. G., Duclos, G., Bonnet, I. & Silberzan, P. Architecture and migration of an epithelium on a cylindrical wire. *Proc. Natl. Acad. Sci.* **19,** 5944–5949 (2015).

48. Weiner, O. D., Marganski, W. A., Wu, L. F., Altschuler, S. J. & Kirschner, M. W. An actin-based wave generator organizes cell motility. *PLoS Biol.* **5,** e221 (2007).

49. Ilina, O., Bakker, G.-J., Vasaturo, A., Hofmann, R. M. & Friedl, P. Two-photon laser-generated microtracks in 3D collagen lattices: principles of MMP-dependent and -independent collective cancer cell invasion. *Phys. Biol.* **8,** 15010 (2011).

50. Weigelin, B., Bakker, G.-J. & Friedl, P. Intravital third harmonic generation microscopy of collective melanoma cell invasion: Principles of interface guidance and microvesicle dynamics. *IntraVital* **1,** 32–43 (2012).

51. Clark, P., Connolly, P., Curtis, a S., Dow, J. a & Wilkinson, C. D. Topographical control of cell behaviour. I. Simple step cues. *Development* **99,** 439–448 (1987).

52. Petrie, R. J., Doyle, A. D. & Yamada, K. M. Random versus directionally persistent cell migration. *Nat Rev Mol Cell Biol.* **10,** 538–549 (2009).

53. Doyle, A. D. *et al.* Micro-environmental control of cell migration - myosin IIA is required for efficient migration in fibrillar environments through control of cell adhesion dynamics. *J. Cell Sci.* **125,** 2244–2256 (2012).

54. Doyle, A. D., Wang, F. W., Matsumoto, K. & Yamada, K. M. One-dimensional topography underlies three-dimensional fibrillar cell migration. *J. Cell Biol.* **184,** 481–90 (2009).

55. Vitorino, P., Hammer, M., Kim, J. & Meyer, T. A steering model of endothelial sheet migration recapitulates monolayer integrity and directed collective migration. *Mol. Cell. Biol.* **31,** 342–50 (2011).

56. Gritsenko, P. G., Ilina, O. & Friedl, P. Interstitial guidance of cancer invasion. *J. Pathol.* **226,** 185–99 (2012).

57. Londono, C. *et al.* Nonautonomous contact guidance signaling during collective cell migration. *Proc. Natl. Acad. Sci. U.S.A.* **111,** 1807–1812 (2014).

58. Lawrence, B. D., Pan, Z. & Rosenblatt, M. I. Silk Film Topography Directs Collective Epithelial Cell Migration. *PLoS One* **7,** e50190-1–12 (2012).

59. Carter, S. B. Haptotaxis and the mechanism of cell motility. *Nature* **213,** 256–60 (1967).

60. Bauer, A. L., Jackson, T. L. & Jiang, Y. Topography of extracellular matrix mediates vascular morphogenesis and migration speeds in angiogenesis. *PLoS Comput. Biol.* **5,** (2009).

61. Chan, K. T. *et al.* LKB1 loss in melanoma disrupts directional migration toward extracellular matrix cues. *J. Cell Biol.* **207,** 299–315 (2014).

62. Stratman, A. N. & Davis, G. E. Endothelial cell-pericyte interactions stimulate basement membrane matrix assembly: influence on vascular tube remodeling, maturation, and stabilization. *Microsc. Microanal.* **18,** 68–80 (2012).

63. Nguyen, B. P., Ryan, M. C., Gil, S. G. & Carter, W. G. Deposition of laminin 5 in epidermal wounds regulates integrin signaling and adhesion. *Curr. Opin. Cell Biol.* **12,** 554–62 (2000).

64. Daub, J. T. & Merks, R. M. H. A Cell-Based Model of Extracellular-Matrix-Guided Endothelial Cell Migration During Angiogenesis. *Bull. Math. Biol.* **75,** 1377–1399 (2013).

65. Egeblad, M., Nakasone, E. S. & Werb, Z. Tumors as organs: complex tissues that interface with the entire organism. *Dev. Cell* **18,** 884–901 (2010).

66. Park, I. & Lee, H.-S. EphB/ephrinB Signaling in Cell Adhesion and Migration. *Mol. Cells* **38,** 14–19 (2015).

67. Sugiyama, N. *et al.* Epha2 cleavage by MT1-MMP triggers single cancer cell invasion via homotypic cell repulsion. *J. Cell Biol.* **201,** 467–484 (2013).

68. Fagotto, F., Rohani, N., Touret, A.-S. & Li, R. A Molecular Base for Cell Sorting at Embryonic Boundaries: Contact Inhibition of Cadherin Adhesion by Ephrin/Eph-Dependent Contractility. *Dev. Cell* **27,** 72–87 (2013).

69. Theveneau, E. *et al.* Chase-and-run between adjacent cell populations promotes directional collective migration. *Nat. Cell Biol.* **15,** 763–772 (2013).

70. Lo, C. M., Wang, H. B., Dembo, M. & Wang, Y. L. Cell movement is guided by the rigidity of the substrate. *Biophys. J.* **79,** 144–52 (2000).

71. Harland, B., Walcott, S. & Sun, S. X. Adhesion dynamics and durotaxis in migrating cells. *Phys. Biol.* **8,** 15011 (2011).

72. Wong, S., Guo, W.-H. & Wang, Y.-L. Fibroblasts probe substrate rigidity with filopodia extensions before occupying an area. *Proc. Natl. Acad. Sci.* **111,** 17176–17181 (2014).

73. Fouchard, J., Mitrossilis, D. & Asnacios, A. Acto-myosin based response to stiffness and rigidity sensing. *Cell Adhes. Migr.* **5,** 16–19 (2011).

74. Lange, J. R. & Fabry, B. Cell and tissue mechanics in cell migration. *Exp. Cell Res.* **319,** 2418–23 (2013).

75. Beaune, G. *et al.* How cells flow in the spreading of cellular aggregates. *Proc. Natl. Acad. Sci. U. S. A.* **111,** 8055–60 (2014).

76. Giuliano, M. *et al.* Circulating and disseminated tumor cells from breast cancer patient-derived xenograft-bearing mice as a novel model to study metastasis. *Breast Cancer Res.* **17,** 3 (2015).

77. Vasilyev, A. & Drummond, I. A. Fluid flow and guidance of collective cell migration. *Cell Adh. Migr.* **4,** 353–7 (2010).

78. Hsu, S., Thakar, R., Liepmann, D. & Li, S. Effects of shear stress on endothelial cell haptotaxis on micropatterned surfaces. *Biochem. Biophys. Res. Commun.* **337,** 401–409 (2005).

79. Vasilyev, A. *et al.* Collective cell migration drives morphogenesis of the kidney nephron. *PLoS Biol.* **7,** (2009).

80. Majumdar, R., Sixt, M. & Parent, C. a. New paradigms in the establishment and maintenance of gradients during directed cell migration. *Curr. Opin. Cell Biol.* **30,** 33–40 (2014).

81. Insall, R. H. Understanding eukaryotic chemotaxis: a pseudopod-centred view. *Nat. Rev. Mol. Cell Biol.* **11,** 453–458 (2010).

82. Theveneau, E. *et al.* Collective chemotaxis requires contact-dependent cell polarity. *Dev. Cell* **19,** 39–53 (2010).

83. Wan, P. *et al.* Guidance receptor promotes the asymmetric distribution of exocyst and recycling endosome during collective cell migration. *Development* **140,** 4797–806 (2013).

84. Shamloo, A. Cell-Cell Interactions Mediate Cytoskeleton Organization and Collective Endothelial Cell Chemotaxis. *Cytoskeleton* **512,** 501–512 (2014).

85. Bagorda, A. & Parent, C. A. Eukaryotic chemotaxis at a glance. *J. Cell Sci.* **121,** 2621–4 (2008).

86. Tessier-Lavigne, M. Axon guidance by diffusible repellants and attractants. *Curr. Opin. Genet. Dev.* **4,** 596–601 (1994).

87. Cai, D. & Montell, D. J. Diverse and dynamic sources and sinks in gradient formation and directed migration. *Curr. Opin. Cell Biol.* **30,** 91–8 (2014).

88. Kriebel, P. W., Barr, V. a., Rericha, E. C., Zhang, G. & Parent, C. a. Collective cell migration requires vesicular trafficking for chemoattractant delivery at the trailing edge. *J. Cell Biol.* **183,** 949–961 (2008).

89. Garcia, G. L., Rericha, E. C., Heger, C. D., Goldsmith, P. K. & Parent, C. A. The group migration of Dictyostelium cells is regulated by extracellular chemoattractant degradation. *Mol. Biol. Cell* **20,** 3295–304 (2009).

90. Donà, E. *et al.* Directional tissue migration through a self-generated chemokine gradient. *Nature* **503,** 285–9 (2013).

91. Venkiteswaran, G. *et al.* Generation and dynamics of an endogenous, self-generated signaling gradient across a migrating tissue. *Cell* **155,** 674–87 (2013).

92. Valentin, G., Haas, P. & Gilmour, D. The chemokine SDF1a coordinates tissue migration through the spatially restricted activation of Cxcr7 and Cxcr4b. *Curr. Biol.* **17,** 1026–31 (2007).

93. Malet-Engra, G. *et al.* Collective Cell Motility Promotes Chemotactic Prowess and Resistance to Chemorepulsion. *Curr. Biol.* **25,** 242–50 (2015).

94. Carmona-Fontaine, C. *et al.* Complement Fragment C3a Controls Mutual Cell Attraction during Collective Cell Migration. *Dev. Cell* **21,** 1026–1037 (2011).

95. Weijer, C. J. Collective cell migration in development. *J. Cell Sci.* **122,** 3215–23 (2009).

96. Jongbloets, B. C. & Pasterkamp, R. J. Semaphorin signalling during development. *Development* **141,** 3292–3297 (2014).

97. Larrieu-Lahargue, F., Thomas, K. R. & Li, D. Y. Netrin ligands and receptors: lessons from neurons to the endothelium. *Trends Cardiovasc. Med.* **22,** 44–7 (2012).

98. Wu, J. & Lin, F. Recent Developments in Electrotaxis Assays. *Adv. Wound Care* **3,** 149–155 (2013).

99. Liu, Q. & Song, B. Electric field regulated signaling pathways. *Int. J. Biochem. Cell Biol.* **55,** 264–8 (2014).

100. Li, L. *et al.* E-cadherin plays an essential role in collective directional migration of large epithelial sheets. *Cell. Mol. Life Sci.* **69,** 2779–89 (2012).

101. Zhao, M. *et al.* Electrical signals control wound healing through phosphatidylinositol-3-OH kinase-gamma and PTEN. *Nature* **442,** 457–60 (2006).

102. Zhao, M. Electrical fields in wound healing-An overriding signal that directs cell migration. *Semin. Cell Dev. Biol.* **20,** 674–682 (2009).

103. Cohen, D. J., Nelson, W. J. & Maharbiz, M. M. Galvanotactic control of collective cell migration in epithelial monolayers. *Nat. Mater.* **13,** 409–17 (2014).

104. Torkaman, G. Electrical Stimulation of Wound Healing: A Review of Animal Experimental Evidence. *Adv. wound care* **3,** 202–218 (2014).

105. Shin, Y. *et al.* In vitro 3D collective sprouting angiogenesis under orchestrated ANG-1 and VEGF gradients. *Lab Chip* **11,** 2175–2181 (2011).

106. Ghabrial, A. S. & Krasnow, M. A. Social interactions among epithelial cells during tracheal branching morphogenesis. *Nature* **441,** 746–9 (2006).

107. Gaggioli, C. *et al.* Fibroblast-led collective invasion of carcinoma cells with differing roles for RhoGTPases in leading and following cells. *Nat. Cell Biol.* **9,** 1392–400 (2007).

108. Bianco, A. *et al.* Two distinct modes of guidance signalling during collective migration of border cells. *Nature* **448,** 362–5 (2007).

109. McDonald, J. A., Pinheiro, E. M., Kadlec, L., Schupbach, T. & Montell, D. J. Multiple EGFR ligands participate in guiding migrating border cells. *Dev. Biol.* **296,** 94–103 (2006).

110. McDonald, J. A., Pinheiro, E. M. & Montell, D. J. PVF1, a PDGF/VEGF homolog, is sufficient to guide border cells and interacts genetically with Taiman. *Development* **130,** 3469–78 (2003).

111. Fernández-Espartero, C. H. *et al.* GTP exchange factor Vav regulates guided cell migration by coupling guidance receptor signalling to local Rac activation. *J. Cell Sci.* **126,** 2285–93 (2013).

112. Sroka, I. C. *et al.* The laminin binding integrin alpha6beta1 in prostate cancer perineural invasion. *J. Cell. Physiol.* **224,** 283–8 (2010).

113. Salmon, H. *et al.* Matrix architecture defines the preferential localization and migration of T cells into the stroma of human lung tumors. *J. Clin. Invest.* **122,** 899–910 (2012).

114. Haeger, A., Krause, M., Wolf, K. & Friedl, P. Cell jamming: Collective invasion of mesenchymal tumor cells imposed by tissue confinement. *Biochim. Biophys. Acta - Gen. Subj.* **1840,** 2386–2395 (2014).

115. Vedula, S. R. K. *et al.* Emerging modes of collective cell migration induced by geometrical constraints. *Proc. Natl. Acad. Sci.* **109,** 12974–12979 (2012).

116. Wolf, K. *et al.* Multi-step pericellular proteolysis controls the transition from individual to collective cancer cell invasion. *Nat. Cell Biol.* **9,** 893–904 (2007).

117. Friedl, P. & Wolf, K. Tube travel: the role of proteases in individual and collective cancer cell invasion. *Cancer Res.* **68,** 7247–9 (2008).

118. Tripathi, M. *et al.* Laminin-332 cleavage by matriptase alters motility parameters of prostate cancer cells. *Prostate* **71,** 184–96 (2011).

119. Schenk, S. *et al.* Binding to EGF receptor of a laminin-5 EGF-like fragment liberated during MMP-dependent mammary gland involution. *J. Cell Biol.* **161,** 197–209 (2003).

120. Chacón, M. R. & Fazzari, P. FAK: dynamic integration of guidance signals at the growth cone. *Cell Adh. Migr.* **5,** 52–5 (2011).

121. Theveneau, E. & Mayor, R. Integrating chemotaxis and contact-inhibition during collective cell migration: Small GTPases at work. *Small GTPases* **1,** 113–117 (2010).

122. Plotnikov, S. V, Pasapera, A. M., Sabass, B. & Waterman, C. M. Force fluctuations within focal adhesions mediate ECM-rigidity sensing to guide directed cell migration. *Cell* **151,** 1513–27 (2012).

123. Masuzzo, P. & Martens, L. An open data ecosystem for cell migration research. *Trends Cell Biol.* **25,** 55–8 (2014).

124. Stonko, D. P., Manning, L., Starz-Gaiano, M. & Peercy, B. E. A mathematical model of collective cell migration in a three-dimensional, heterogeneous environment. *PLoS One* **10,** e0122799 (2015).

125. Plodinec, M. *et al.* The nanomechanical signature of breast cancer. *Nat. Nanotechnol.* **7,** (2012).

126. Vitorino, P. & Meyer, T. Modular control of endothelial sheet migration. *Genes Dev.* **22,** 3268–81 (2008).

127. Lehembre, F. *et al.* NCAM-induced focal adhesion assembly: a functional switch upon loss of E-cadherin. *EMBO J.* **27,** 2603–2615 (2008).

128. Ikari, A. *et al.* Enhancement of cell-cell contact by claudin-4 in renal epithelial Madin-Darby canine kidney cells. *J. Cell. Biochem.* **113,** 499–507 (2012).

129. Parri, M. & Chiarugi, P. Rac and Rho GTPases in cancer cell motility control. *Cell Commun. Signal.* **8,** 23 (2010).

130. Matsubayashi, Y., Ebisuya, M., Honjoh, S. & Nishida, E. ERK activation propagates in epithelial cell sheets and regulates their migration during wound healing. *Curr. Biol.* **14,** 731–5 (2004).

131. Cavallaro, U. & Dejana, E. Adhesion molecule signalling: not always a sticky business. *Nat. Rev. Mol. Cell Biol.* **12,** 189–97 (2011).

132. Maness, P. F. & Schachner, M. Neural recognition molecules of the immunoglobulin superfamily: signaling transducers of axon guidance and neuronal migration. *Nat. Neurosci.* **10,** 19–26 (2007).

133. Peglion, F., Llense, F. & Etienne-Manneville, S. Adherens junction treadmilling during collective migration. *Nat. Cell Biol.* **16,** 639–51 (2014).

134. Maruthamuthu, V., Aratyn-Schaus, Y. & Gardel, M. L. Conserved F-actin dynamics and force transmission at cell adhesions. *Curr. Opin. Cell Biol.* **22,** 583–588 (2010).

135. Baum, B. & Georgiou, M. Dynamics of adherens junctions in epithelial establishment, maintenance, and remodeling. *J. Cell Biol.* **192,** 907–17 (2011).

136. Nguyen-Ngoc, K.-V. *et al.* ECM microenvironment regulates collective migration and local dissemination in normal and malignant mammary epithelium. *Proc. Natl. Acad. Sci.* **109,** E2595–E2604 (2012).

137. Palsson, E. & Othmer, H. G. A model for individual and collective cell movement in Dictyostelium discoideum. *Proc. Natl. Acad. Sci. U. S. A.* **97,** 10448–53 (2000).

138. Vasilyev, A., Liu, Y., Hellman, N., Pathak, N. & Drummond, I. A. Mechanical stretch and PI3K signaling link cell migration and proliferation to coordinate epithelial tubule morphogenesis in the zebrafish pronephros. *PLoS One* **7,** e39992 (2012).

139. Li, S. Analysis of endothelial cell migration under flow. *Methods Mol. Biol.* **294,** 107–21 (2005).

140. Poukkula, M., Cliffe, A., Changede, R. & Rørth, P. Cell behaviors regulated by guidance cues in collective migration of border cells. *J. Cell Biol.* **192,** 513–24 (2011).

141. Chuai, M., Hughes, D. & Weijer, C. J. Collective epithelial and mesenchymal cell migration during gastrulation. *Curr. Genomics* **13,** 267–77 (2012).

Chapter 3

Cell Jamming: Collective Invasion of Mesenchymal Tumor Cells Imposed by Tissue Confinement

Anna Haeger, Marina Krause,
Katarina Wolf and Peter Friedl

Published in:
Biochim Biophys Acta. 2014 Aug; 1840(8):2386-95

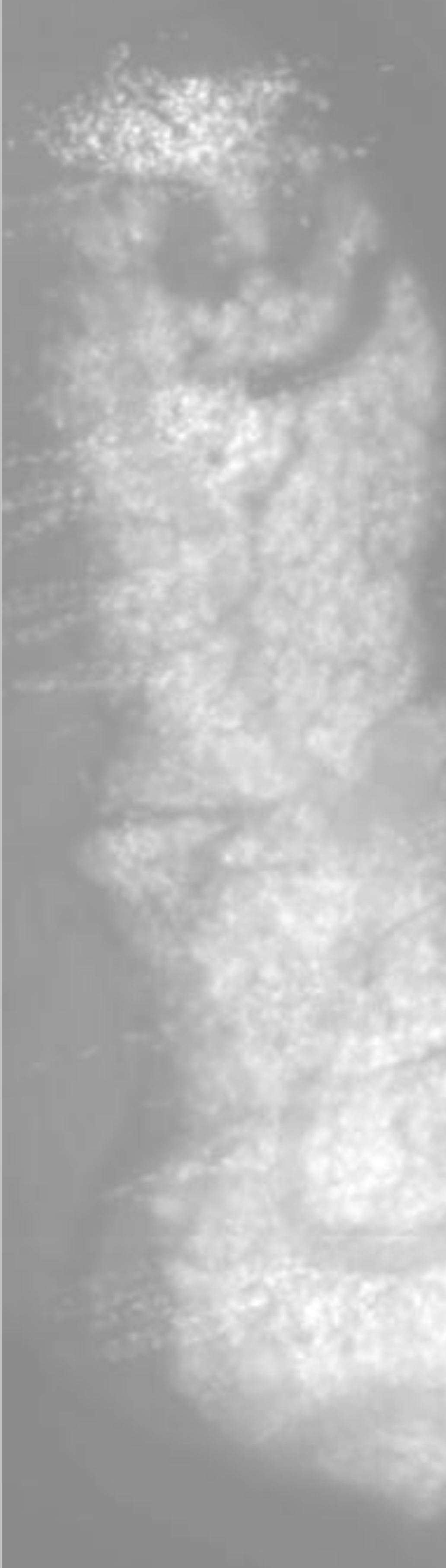

Cancer invasion is a multi-step process which coordinates interactions between tumor cells with mechanotransduction towards the surrounding matrix, resulting in distinct cancer invasion strategies. Defined by context, mesenchymal tumors, including melanoma and soft tissue sarcoma, develop either single-cell and collective invasion modes, however, the mechanical and molecular programs underlying such plasticity of mesenchymal invasion programs remain unclear. To test how tissue anatomy determines invasion mode, spheroids of MV3 melanoma and HT-1080 fibrosarcoma cells were embedded into 3D collagen matrices of varying density and stiffness and analyzed for migration type and efficacy with matrix metalloproteinase (MMP)-dependent collagen degradation enabled or pharmacologically inhibited. With increasing collagen density and dependent on proteolytic collagen breakdown and track clearance, but independent of matrix stiffness, cells switched from single-cell to collective invasion modes. Conversion to collective invasion included gain of cell-to-cell junctions, supracellular polarization and joint guidance along migration tracks. Thus, the density of the extracellular matrix (ECM) determines the invasion mode of mesenchymal tumor cells. Whereas fibrillar, high porosity ECM enables single-cell dissemination, dense matrix induces cell-cell interaction, leader-follower cell behavior and collective migration as an obligate protease-dependent process. These findings establish plasticity of cancer invasion programs in response to ECM porosity and confinement, thereby recapitulating invasion patterns of mesenchymal tumors *in vivo*. The conversion to collective invasion with increasing ECM confinement supports the concept of cell jamming as guiding principle for melanoma and sarcoma cells into dense tissue.

Introduction

Cancer invasion and dissemination into tissue is a multi-step process which balances mechanotransduction towards the ECM with cell-cell interactions between tumor cells. Tumor cell movement may result from distinct migration strategies determined by both, molecular properties of the tumor cells as well as mechanical and signaling input from the tumor microenvironment. Mesenchymal single-cell migration results from stringent adhesion sites linked to high actomyosin-mediated traction force and the capability to proteolytically degrade or remodel ECM[1,2]. Conversely, amoeboid single-cell migration is mediated by weak cell adhesion to ECM coupled to protrusive leading edge kinetics, including filopodia or blebs, and absence of structural ECM remodeling[3]. Distinct from single-cell movement, collective cell migration depends upon intact cell-cell junctions providing mechanical and signaling connection between tumor cells for supracellular polarization and coordination[4–6]. In collagen-rich 3D ECM, collective cell migration requires an integrin-based force generation and proteolytic cleavage of ECM to generate migration tracks that accommodate the moving cell group[1,7,8]. These cell migration programs are adaptive and interconvertible in response to cell-intrinsic and stroma-derived inputs[2].

As central mechanism for the conversion from multicellular to single-cell pattern, epithelial-mesenchymal transition (EMT) leads to the downregulation of stringent E-cadherin-based cell-cell junctions which releases individually migrating cells from multicellular epithelia[9–11]. Consistently, mesenchymal tumor cells migrate individually after experimental cell dissociation and exposure to 2D and 3D *in vitro* substrates, similar to migrating fibroblasts[12,13]. However, mesenchymal cells can also develop N-cadherin-based collective migration patterns in 3D models of multicellular invasion *in vitro* and mouse models of interstitial invasion[1,7,9,14–19]. Whereas molecular mechanisms of cell-cell junction regulation and cell patterning are well established, tissue determinants for single-cell versus collective migration modes remain unclear.

Depending on the type of tissue microenvironment, invading tumor cells are confronted with different extracellular structures and molecular patterns which jointly determine the biomechanics of cell-matrix interaction and migration efficacy. Physical, extracellular modulators of cell migration include: confinement, based on pore-size through which the cell migrates; geometry along which the cell-body aligns, determined by ECM alignment and dimensionality (2D vs. 3D); and stiffness which, depending on the composition, flexibility, density and cross-link status of ECM components, can vary greatly between tissue types and healthy or malignant tissue[20–22].

Collagen I, the main component of ECM in interstitial tissues, determines the spatial organization and stability of connective tissues. Natural patterns of collagen topography include low-density zones consisting of thick and thin collagen bundles forming a porous meshwork of random or aligned organization, or high-density zones, composed of tightly arranged and often aligned collagen bundles with micron-scale pore size. While loose connective tissue is usually located adjacent to epithelial layers, including the dermis or gut submucosa, densely packed collagen bundles dominate the desmoplastic peritumor stroma[17,20,23,24]. To recapitulate such heterogeneity of ECM topography and density, multi-scale approaches were developed to predict how moving cells integrate varying tissue organization by adjusting migration mode and efficacy[25].

Several types of adaptation were identified in moving cells in response to ECM heterogeneity. Contact guidance enables cells to take the path of least resistance when confronted with discontinuous environments, which supports preferential migration along ECM interfaces or aligned structures[17,25–30]. As fundamental biomechanical determinant, deformation of the cell body and nucleus maintains individual cell movement through narrow pores of mechanically challenging environments[31,32]. To overcome tissue constraints, cell deformation is further complemented by pericellular cleavage of ECM proteins through cell-derived MMPs, which increases space for facilitated single-cell and collective cell migration[1,8,20,33–35]. In addition, pericellular functionalization of ECM is achieved by paracrine deposition of ECM components which may increase ligand density and stiffness and thereby modulate mechanocoupling during migration[2,21,25,36–38]. These cellular responses cooperate and support a repertoire of adaptation responses to cope with heterogeneous tissue organization during migration.

Depending on the experimental model, mesenchymal cells, including fibroblasts, neural crest cells, sarcoma and melanoma cells, migrate either individually or as collective cell groups[1,7,12,18], however the environmental conditions enabling such diversity of migration mode are poorly understood. Using a systematic approach to modulate ECM density, stiffness and availability of MMP-dependent pericellular proteolysis, we here address how mechanical and molecular requirements govern the balance between single-cell and collective invasion of mesenchymal melanoma and sarcoma cells. The data show mesenchymal patterning and migration mode as a function of matrix porosity and support proteolytic track clearance followed by cell jamming as key steps to collective mesenchymal migration in confining environments.

Material and Methods

Cell culture

Human wild-type HT-1080 sarcoma (ACC315; DSMZ Braunschweig)[39] and human wild-type MV3 melanoma (provided by G. van Muijen, Dept. of Pathology, RadboudUMC Nijmegen, The Netherlands)[40] cells were cultured (37°C at 5% CO_2 humidified atmosphere) in Dulbecco's modified Eagle's medium (DMEM; Invitrogen) supplemented with 10% FCS (Sigma-Aldrich), penicillin (100 U/ml) and streptomycin (100 µg/ml; both PAA), L-glutamine (2 mM) and sodium pyruvate (1 mM; both Invitrogen). MMP function was inhibited by the broad-spectrum inhibitor GM6001 (ilomastat; EMD Millipore) at non-toxic concentration (20 µM)[13].

3D spheroid culture

Cells from subconfluent culture were detached with EDTA (1 mM) and trypsin (0.075%; Invitrogen), and multicellular spheroids were generated using the hanging-drop method[41]. In brief, cells were suspended in medium supplemented with methylcellulose (20%; Sigma) and incubated as droplets (25 µl) containing 7000 (MV3) or 4000 (HT-1080) cells for 24 h to ensure multicellular aggregation.

For 3D culture in collagen, spheroids were washed (PBS) and mixed with collagen solution consisting of non-pepsinized rat-tail collagen (BD Biosciences/Corning) at different concentrations (2.5 mg/mL to 8.0 mg/mL). Collagen-spheroid mixtures were either incorporated into a custom chamber or pipetted as a drop-matrix and polymerized at 37°C[31].

To generate collagen lattices with both high ligand and porosity, collagen polymerization in a custom chamber was performed at low temperature (21°C) which delayed polymerization and increased both fiber caliber and pore dimensions, as described[23,31]. (For reconstituting high-density matrices, the commercially available collagen stock solution was concentrated to 12.0 mg/mL using a Speed Vac Concentrator (Savant) prior to reconstitution to final concentration of 6.0 or 8.0 mg/mL.).

Spheroid-containing collagen lattices were maintained at 37°C for 24 h (HT-1080 cells) or 48 h (MV3 cells).

Time-lapse microscopy and cell tracking

Emigration from 3D spheroid cultures in 3D fibrillar collagen was monitored at 37°C using digital time-lapse, bright-field microscopy (20x / 0.30 NA air objective; Leica) connected to CCD cameras (Sentech) and Vistek software for up to 72 h at 4 min frame interval.

Cell tracking and quantification of the migration index was performed manually, using tracking plugin, area selection- and measurement tools in Fiji/Image J software (v1.48)[42].

Confocal fluorescence microscopy and quantification of matrix porosity and 3D invasion

Spheroids in 3D collagen matrices were fixed (4% Phosphate-buffered PFA), washed (PBS) and stained using the following reagents: mouse anti-ALCAM mAb (AZN-L50; IgG2A; Department of Tumor Immunology, Radboud Institute for Molecular Life Sciences (RIMLS), The Netherlands[43]); polyclonal rabbit anti-COL23/4C Ab (collagenI cleavage site) (Immunoglobe); secondary Alexa-Fluor-488-conjugated goat anti-rabbit or anti-mouse IgG (Invitrogen); Alexa-Fluor-488- or Alexa-Fluor-568-conjugated phalloidin (Invitrogen); DAPI (Roche). For COL23/4C staining, samples were pre-incubated with murine serum IgG (Sigma) to reduce non-specific background adsorption, followed by addition of primary antibody prior to fixation.

For multicolor detection of fluorescent spheroids inside collagen lattices, long working distance confocal microscopy was performed (Olympus FV1000 scanner; 20x / 0.50 NA water immersion objective). Z-stacks were obtained at 5 µm slice intervals. Migration analysis was performed on DAPI- and phalloidin-stained spheroids using high-content epifluorescence microscopy combined with automated multi-position image acquisition and stitching (Leica DMI6000B; 20x / 0.50 NA air objective; 25 µm slice interval). Maximum intensity z-projections were used to quantify the number of emigrated single cells, multicellular strands, area and length of strands and the angles between strand axis and mitotic planes using Fiji/Image J software (v1.48)[42] (Supplementary Fig. 1).

Pore size measurements of cell-free fibrillar collagen was performed in custom chambers also used for 3D spheroid invasion cultures. The reflectance signal from collagen fibers was obtained by confocal scanning (Olympus FV1000; 40x / 0.80 NA water immersion objective) as xy scans with 1 µm slice intervals and 30 µm z-depth from a central region of approximately 200 µm distance from the cover glass. Pore cross sections were measured from individual xz slices, as described[31].

Collagen stiffness measurement by atomic force microscopy (AFM)

Cell-free collagen matrices (~5 µl) were reconstituted in a WillCo-dish with PDMS insert, overlaid with PBS and probed in native state by AFM using a cantilever with an attached polystyrene microsphere (10 µm diameter) on a Catalyst BioScope (Bruker) coupled to a confocal microscope (TCS SP5 II; Leica)[31]. Bead attachment, calibration, measurements and data analysis (conversion of force-distance curves into force-indentation curves) (F-δ)) were performed as described[44]. Subsequently F-δ curves were fitted over the 0-0.6 nN range after baseline correction using in-house written Igor Pro 6 (WaveMetrics) algorithms kindly provided and written by Jonne Helenius (BSSE, ETH Zürich, Basel, Switzerland) and Joost te Riet (Department of Tumor Immunology, Radboud Institute for Molecular Life Sciences (RIMLS), The Netherlands) to calculate the stiffness with the Hertz model for spheres in contact with a flat surface[45]:

$$F = \frac{4E\sqrt{R_c}}{3(1-\nu^2)} \cdot \delta^{\frac{3}{2}}$$

Statistics

Statistical analysis was performed by the two-tailed unpaired Mann-Whitney test using GraphPad Prism 5 software.

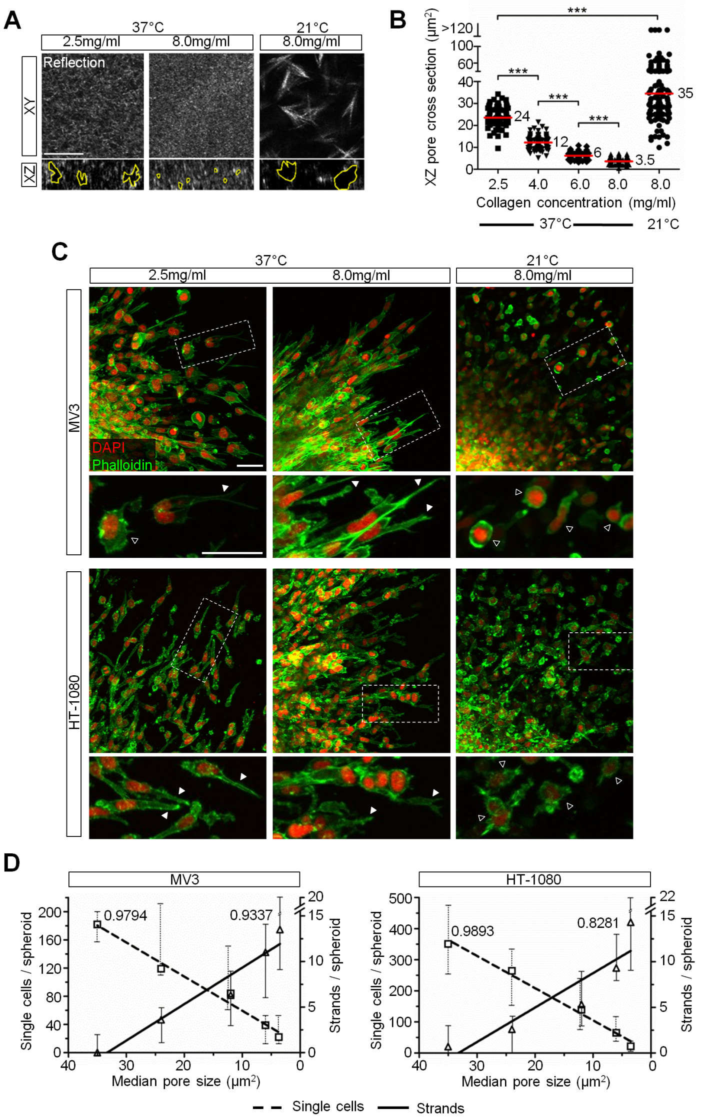

Figure 1. Matrix-density dependent switch from individual to collective cell migration in MV3 and HT-1080 cells.
A) Xy and xz confocal reflectance scans of rat-tail collagen matrices of different concentration and polymerization temperature and **B)** quantification of pore cross-sections (example pores outlined in xz-scan). $P < 0.0001$ from 3-4 independent experiments with measurements from ~12 different locations/gel. Red horizontal line, median. **C)** Emigration from spheroids 24h (HT-1080) and 48h (MV3) after embedding in collagen matrices of different density, detected as maximum intensity projection from confocal 3D stacks. Dashed rectangles, region of detail images. Black arrowheads, roundish, amoeboid cells. White arrowheads, elongated, mesenchymal shapes. **D)** Migration pattern as a function of median pore area. Frequency of single-cell or collective invasion from 30 to 70 spheroids/condition (3-5 independent experiments), shown as medians and 5th / 95th percentiles (whiskers) derived from Supplementary Fig. 2B. Approximate cell number per strand at the end-point was 15 (MV3) and 16 (HT-1080). R^2 values for regression lines are indicated in the graph. Scale bars, 10 µm (A); 50 µm (B).

Results

To identify matrix requirements and molecular determinants underlying collective invasion in mesenchymal tumor cells, we here used 3D multicellular spheroid cultures of MV3 melanoma and HT-1080 sarcoma cells in mechanically defined 3D collagen environments of varying density. We monitored invasion mode and efficacy as well as MMP-dependent ECM remodeling.

3D low- to high-density fibrillar collagen scaffolds were reconstituted from rat-tail type I collagen lattices and analyzed for porosity by 3D confocal backscatter reconstruction combined with image analysis of pore dimensions between fibers. With increasing collagen concentration matrix porosity was incrementally reduced, resulting in a median pore range between 24 µm^2 for low-density (2.5 mg/mL) and 3.5 µm^2 for high-density conditions (8.0 mg/mL) (Fig. 1A,B). This pore range is suited to accommodate efficient single-cell migration of individualized MV3[46] and HT-1080[31] cells in the absence of molecular interference.

To test for impact of collagen density on migration mode, multicellular spheroids of MV3 and HT-1080 cells were embedded inside 3D collagen matrices with varying density and monitored for the efficacy and type of cell invasion. Using both, bright-field time-lapse microscopy (Supplementary Fig. 1A) and 3D reconstructions of fixed and stained spheroid cultures (Fig. 1C, Supplementary Fig. 1B,C), the migration mode was quantified as the frequency of single-cell versus collective invasion pattern. Both cell types showed a significant discrimination of ECM density by invading as individual cells or loose chains without retaining cell-cell junctions in loose (2.5 to 4.0 mg/mL) and predominantly collective strands in dense fibrillar collagen (6.0 to 8.0 mg/mL) (Fig. 1C, Supplementary Fig. 2A). Concurrently, increasing collagen density impeded (collective) invasion, detected as decreased number of invading cells and reduced length or area of invasion strands (Supplementary Fig.2B,C), while inducing a gradual conversion from single-cell to collective invasion as a linear function with near-exclusive collective invasion reached at pore cross sections of ~4 µm^2 (Fig. 1D).

To address whether the physical matrix porosity, rather than altered content of collagen ligand and/or fibril thickness, controls ECM-imposed plasticity of invasion mode, 3D matrices of low porosity were generated by using high collagen concentration (8.0 mg/mL) with delayed polymerization speed at low temperature[31]. Compared with collagen matrices polymerized at 37°C, this altered polymerization regime led to lattices with nine-fold larger pores and increased fiber caliber (Fig. 1A,B). Concomitant to increased porosity, collective invasion reverted to the single-cell pattern in both cell types, reaching near-complete individual dispersion similar to low-density collagen matrices. (Fig. 1 C,D, Supplementary Fig. 1A and 2). An unexpected second-order morphological switch could be detected when comparing both high-porosity conditions: Whereas spindle-shaped, mesenchymal invasion with clearly visible actin-fibers was predominant in low-density microfibrillar conditions (2.5 mg/mL), single cells moving into macrofibrillar porous matrix (8.0 mg/mL, 21°C) showed near-exclusive rounded morphologies without profound actin-fibers, indicative of amoeboid migration (Fig. 1C)[2,3]. Thus, irrespective of collagen ligand density, the space between fibrils controls whether mesenchymally migrating single cells resort to the collective invasion pattern.

While single-cell migration, including multicellular streaming, lacks long-lasting adhesive junctions between moving cells, collective migration depends upon cell-cell interactions and supracellular communication, resulting in coordinated path structure and front-rear polarity[2,5,9]. Time-lapse analysis of cell position and path organization of collective strands invading high-density 3D collagen matrices showed a defined leader-follower behavior with a single tip-cell leading the strand as well as near-complete alignment of the migration tracks of cells composing the strand. Conversely, cells moving individually in low-density scaffolds lacked a dedicated follower behavior resulting in individualized tracks that did not, or rarely, overlapped with neighbor paths. (Fig. 2A,B). Thus, spatial confinement imposes "leader-follower" patterns and shared migration tracks.

To test whether ECM-induced alignment of migration tracks coincides with intact cell-cell junctions, invading spheroid cultures were stained for Activated Leukocyte Cell Adhesion Molecule (ALCAM/CD166), which provides homophilic cell-cell interactions and is highly expressed in MV3 and HT-1080 cells (data not shown). As expected, cell-cell junctions in the spheroid-body showed a linear colocalization of ALCAM and F-actin (Fig. 2C, region 1). Likewise, multicellular invasion strands retained linear ALCAM in colocalization with F-actin along cell-cell interactions for both, MV3 and HT-1080 cells, consistent with adhesive and functional collectivity (Fig. 2C, region 2).

Functional cell-cell cooperativity is further supported by a striking alignment of mitotic plane perpendicular (= angle of ~90°) to the length-axis of invasion (Fig. 2D). Thus, spatial confinement imposes central features of collective cell migration in mesenchymal tumor cells, including joint trails, linear cell-to-cell junctions with a cortical actin layer and collective front-rear polarization.

When monitored side-by-side and irrespective on cell-cell cooperativity, the net speed of invasion in both, MV3 and HT-1080 cells, was delayed with increased collagen density during both, early-onset and late invasion (Fig. 3A, Supplementary Fig. 1A).

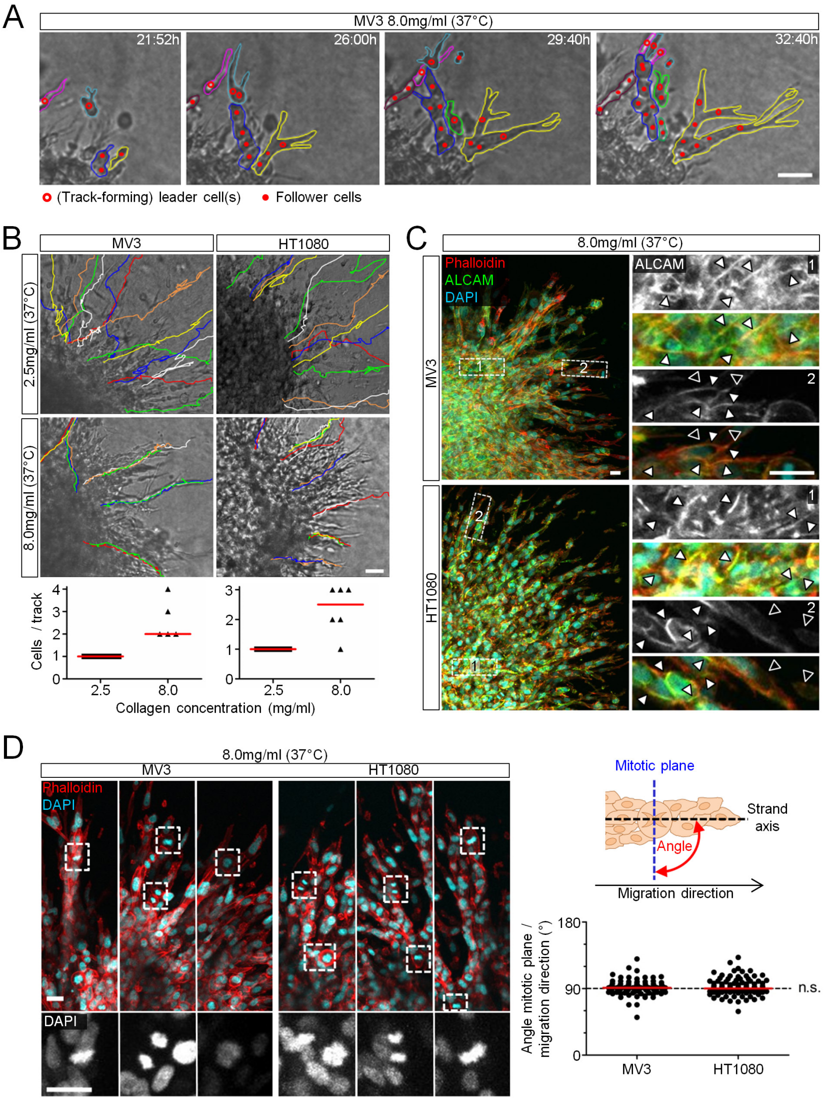

Figure 2. Multicellular path coordination, cell interactivity and polarity in MV3 and H-T1080 cells with ECM confinement.

A) Early-onset collective MV3 cell strands guided by individual leader cells. Frames taken from a time-lapse movie with individual invasion zones outlined in color. **B)** Positional alignment of cell tracks in fibrillar collagen of high (8.0 mg/mL) but not low density (2.5 mg/mL). 2D paths were taken from the center of individual cells and represented in orthotopic position. For quantification, cells were defined as following the same track if tracks showed a ± 10 μm overlay for at least 50% of the track length. **C)** F-actin and ALCAM-positive cell-cell contacts during collective invasion into dense collagen matrix. White arrowhead, linear ALCAM distribution along cell-cell junctions. Black arrowheads, relative ALCAM deficiency in the periphery of leader and follower cells. **D)** Orientation of mitotic planes in collective invasion strands. Angles were measured between longitudinal strand axis and mitotic plane axis as obtained from 3D confocal reconstructions (left panels) and displayed (right panel) (~110 mitotic figures from ~40 independent spheroids). Scale bars: 50 μm (A,B); 25 μm (C,D). Red horizontal line: median.

Collagenolysis mediated by MMPs is a prerequisite for *de-novo* track generation and collective invasion of tumor cells[1,26] or invasion-inducing fibroblasts[8], suggesting space restriction as a support principle for collective cell-cell cooperation. Consistent with MMP-dependent proteolytic collagen degradation and track generation, collective cell movement into high-, but not low-density collagen matrix was ablated by broad-spectrum MMP inhibitor GM6001 (Fig. 3B,C, Supplementary Fig. 3A,B). With MMPs inhibited, single-cell dissemination in low-density collagen was, however, associated with a more elongated and spindle-shaped morphology, indicating enhanced cell deformation as protease-independent rescue strategy to navigate through partly confining ECM (median pore size ~24 μm^2) (Fig. 3B,C). Despite the lack of MMP activity, time-lapse movies and F-actin staining revealed that cells in dense collagen were “trying hard” to exit the spheroid body. Especially for HT-1080 cells long, F-actin positive and DAPI negative, anuclear cell protrusions extended from the spheroid and, after disruption, moved into the collagen (Fig. 3B, Supplementary Fig. 3C). Such moving leading edges ripping apart from the main cell body followed by autonomous movement indicate high mechanical tension along the cell body, as described for single cells arrested in dense ECM[31]. Thus, proteolytic collagen breakdown is indispensable for collective invasion enforced by high-density ECM.

To directly show collagen cleavage and proteolytic track formation collagen degradation neoepitope (Col2¾C) was assessed for control and GM6001-treated samples. Pericellular collagen degradation was present along the periphery of both, single cells and collective strands with MMP activity unperturbed, and absent in the presence of GM6001 (Fig. 3D). Thus, cell extensions and migrating F-actin containing anuclear cell fragments were independent of collagen breakdown but, because of arrested position of the main cell body and nucleus, insufficient to establish multicellular invasion strands as consequence of space constraints (Fig. 3B, insets).

In addition to porosity, altered collagen matrix density impacts mechanical properties of the migration substrate. To test whether ECM stiffness independently controls invasion patterns[36,47], the elastic modulus of collagen scaffold types associated with single-cell or collective migration were probed by AFM (Fig. 4A). Constant force input was provided and downward movement of the cantilever together with the collagen surface was registered (Fig. 4B). ECM conditions associated with single-cell dissemination showed either high (8.0 mg/mL, 21°C) or low (2.5 mg/mL, 37°C) rigidity, whereas scaffold conditions favoring collective invasion (8.0 mg/mL, 37°C) showed an intermediate stiffness level (Fig. 4C). Thus, the single-cell to collective invasion switch was a function of ECM porosity (compare Fig. 1D) but not rigidity (Fig. 4C). This identifies matrix density as dominant modulator of migration plasticity.

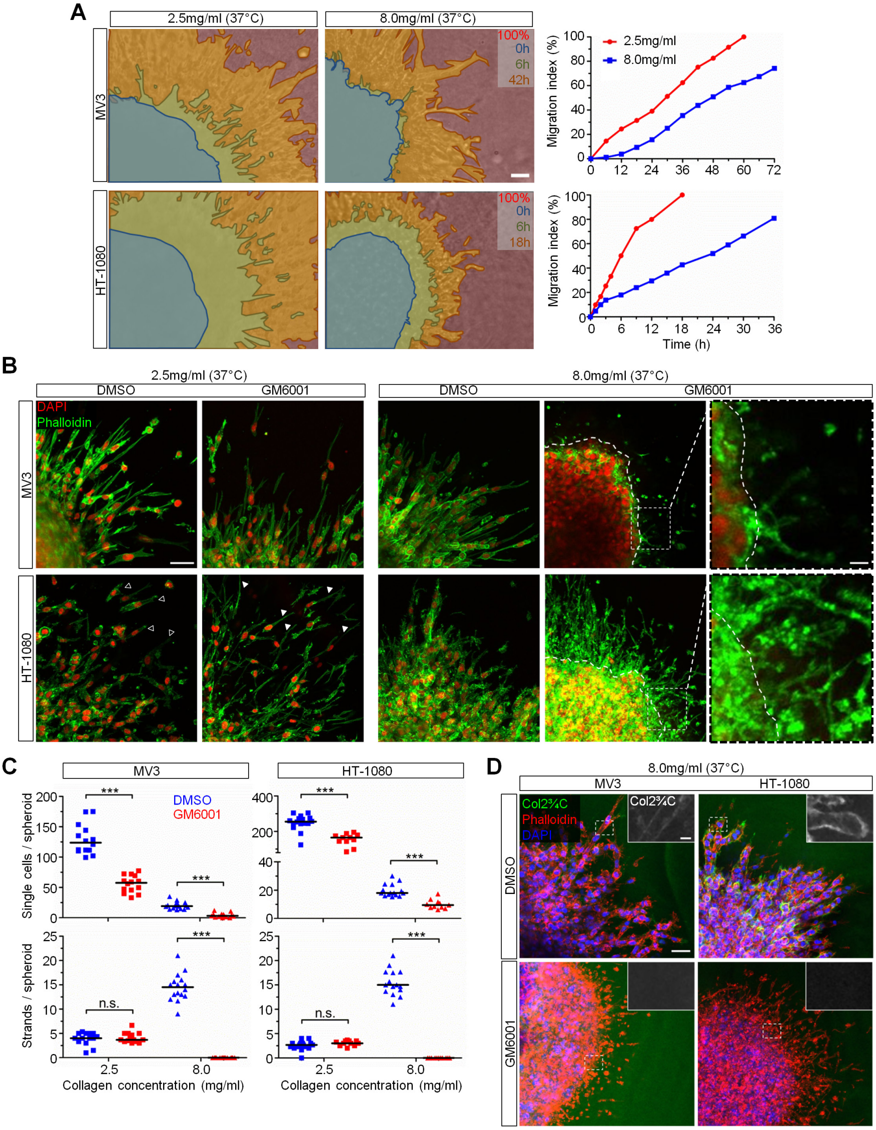

Figure 3. Emigration delay of MV3 and HT-1080 cells and proteolytic path clearance in dense ECM. A) Speed of emigration from spheroids embedded in collagen matrices of different density. The migration index was calculated from frames taken at different time points from time-lapse movies as the area covered with migrating cells minus initial spheroid area at 0 h (blue area). The 100% value corresponded to the maximum region covered by migrating cells at the end-point. **B)** Pattern and **C)** quantification of invasion efficiency of MV3 and HT-1080 cells from spheroids treated with DMSO or MMP inhibitor GM6001. Black arrowheads, mesenchymal protrusions. White arrowheads, thin, filament-like protrusions. ***, $P < 0.0001$ and $P = 0.0002$ for HT-1080 single cells 2.5 mg/ml DMSO vs. GM6001 and $P = 0.0007$ for HT-1080 and MVS strands 8.0 mg/ml DMSO vs. GM6001; ~30spheroids/condition (3-4 independent experiments). **D)** Pericellular collagen degradation along invasion strands in dense collagen matrix. Differences in absolute signal intensity in MV3 cells are caused by lower MMP-14 expression in MV3 compared to HT-1080 cells (data not shown). Scale bars, 50 µm; 10 µm (insets B,D). Red horizontal line, median.

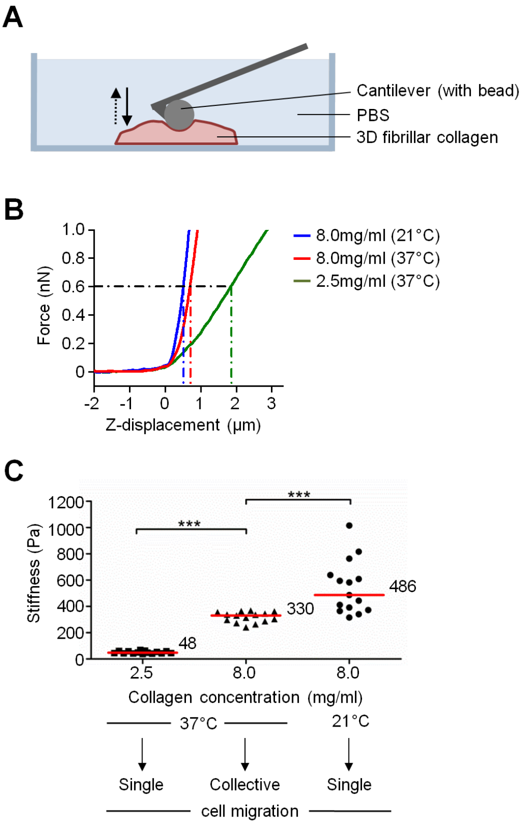

Figure 4. Lack of correlation between invasion pattern and matrix stiffness.
A) Principle of measuring collagen stiffness by atomic force microscopy (AFM). The cantilever was functionalized with a 10 µm bead to probe a 3D fibrillar collagen sample in PBS. **B)** Registration of Z-displacement while probing the surface of the collagen lattice by applying force with the bead-functionalized cantilever. The graph shows representative force curves of different collagen samples fitted with the Hertz deformation model. Dotted, vertical lines: deformation depth at 0.6 nN applied force. **C)** Stiffness for collagen matrices of different concentration and polymerization conditions. ***, $P < 0.0001$; measurements at 10-15 different positions (average of 3 repetitive probing cycles per position) from 3 independent experiments. Red horizontal line, median.

Discussion

Proteolytic tracks of least resistance generated by leader cells provide 3D space and an aligned interface which accommodate multiple cell bodies and guide collective migration. The transition from single-cell to collective invasion of mesenchymal MV3 melanoma and HT-1080 sarcoma cells in response to strong ECM confinement thus provides wet-lab evidence for cell jamming[48] as plasticity mechanism supporting collective cell migration in 3D tissue.

To probe the mechanisms balancing single-cell versus collective invasion of mesenchymal cells, we here used a type I collagen-based 3D model that matches the spectrum of tissue porosity and rigidity *in vivo.* Its pore-size range (0.5 to 170 μm^2) represents the estimated space between collagen fibers *in vivo* ranging from 2 to 30 μm diameter which reflects both upper and lower limits of interstitial tissue densities and, to the lower end, reaches strong confinement near the physical limit of cell migration[17,23,31,49]. Likewise, the initial diameter of proteolytic migration tracks established by leader cells amounts to 10-20 μm which corresponds to the space between collagen interfaces *in vivo*[2,17]. The stiffness range of *in vitro* generated collagen matrices (24 to 1160 Pa) corresponds to the stiffness of diverse tissues ranging from 20 Pa (adipose tissue) to 1000 Pa (interstitial tissue and tumor stroma)[22,50–53]. Other *in vitro* models provide similar confinement and rigidity, including microchannels of defined width[47,54–56] and stiffness[47], however, due to their synthetic polymer-based organization these models preclude cell-derived space adjustments by pericellular degradation or ECM remodeling[1,21,25,57]. 3D collagen matrices thus provide a reasonably physiological model for the biomechanics and susceptibility to cell-derived physicochemical modification of *in vivo* tissues. Beyond the biology of fibrillar collagen, additional modulation of cell-cell and cell-matrix interactions likely occurs in response to additional structural and molecular complexity not included in this study, including signals from collagen subtypes, fibronectin, laminins, and proteoglycans[21,58,59]. Thus, addressing additional microenvironmental modulation of cell patterning will require the use of polymorphous multimolecular ECM models that probe additional complexity of cell invasion, including cell adaptation and decision making when confronted with tissue heterogeneities.

Whereas collective cell migration is an established feature of normal epithelia and endothelia moving as cohesive sheets or tube-like strands across or through interstitial tissue[9,60–62], the ability of mesenchymal cells to move collectively remains controversial[5]. The plasticity response observed here confirms that constitutively mesenchymal tumor cells may readily switch between individual and collective migration strategies, depending on spatial confinement. Similar plasticity is observed in neural crest cells during development which, after EMT, adapt a variety of migration strategies, including single-cell migration, multicellular streaming and/or collective migration modes[63–67]. Likewise, invasive mesenchymal sarcoma or breast cancer cells after EMT generate single-cell or collective patterns, depending on the availability of ECM-degrading MMPs[1]. Several features identified here indicate that tissue confinement contributes to acquisition of collective cooperativity in mesenchymal cells. These include the precise use of joint trails, the maintenance of linear cell-to-cell junctions containing ALCAM and a cortical actin layer as well as collective front-rear polarization with leader-follower behavior[2,5,68]. Thus, by dictating a morphological pattern, plasticity of migration directly impacts intercellular communication and coordination. Beyond the here identified switch from single-cell to collective migration in mesenchymal cells, a transition from elongated, spindle-shaped to roundish, amoeboid morphologies was noted for migration conditions of highest porosity.

3D ECM ligand density and porosity variation thus likely impose such single-cell plasticity response by regulating cell adhesion strength and/or the dependence of cell translocation from protease engagement and proteolytic tissue remodeling[25,32]. Thereby, mesenchymal-to-amoeboid interconversion may represent a further response program to tissue-imposed confinement.

Multi-scale *in silico* computational modeling combining actomyosin dynamics and cell-matrix adhesion in the context of discontinuous or confined 3D matrix geometries retrieved no indication for the conversion from single-cell to collective migration of mesenchymal tumor cells[69]. A mechanically different monolayer-based *in silico* model combining cell density, amount of cell-cell adhesion and cell motility suggests the transition from individual-cell to sheet-like, collective movement as a function termed cell jamming phase diagram[48]. In this model, cell monolayers lack the stringent space confinement present in ECM-based 3D environments, however with increasing density ("jamming") cells gain cell-cell coordination during migration, thus representing a 2D variant of the here described matrix-density induced switch from single-cell to collective migration. In 3D environments, cell jamming occurs when space is limited and cells become increasingly confined, either in preexisting tissue tracks observed *in vivo*[16,17] or proteolytic *de novo* tracks generated by leader cells[1,8], which both provide space that approximates the width of single cells or small cell groups[23,26]. Because in high-density collagen lattices the pore cross-sections of the substrate and likely the boundaries of proteolytic tracks range below the physical limit of cell deformation (below 5-10 μm^2)[31], its inner lumen enables the jamming of follower cells which rather follow the track lining than breaking out laterally and establish new tracks.

The consequences of cell jamming on molecular cell functions, including cell-to-cell signaling and the molecular migration machinery, remain to be addressed. Mesenchymal tumor cells retain rather weak constitutive cell-cell adhesion, as indicated by spontaneous single cell dispersion in unconfined matrix conditions. However, cell jamming may impose contact-mediated secondary cell-to-cell signaling, altered protein-expression, -function and -localization, and eventually reinforce cell-cell junctions. In other mesenchymal cell models, cell-cell adhesion depends upon N-cadherin or adhesion receptors of the immunoglobulin family, including L1-CAM, NCAM, ALCAM, which may cooperate for multicellular interactivity and function[7,9,19,70,71]. Alternatively, in the absence of cell-cell adhesion engagement, confinement-imposed jamming may result in physical convolution of cell bodies which, despite high cell-cell proximity, maintain independent cytoskeletal activity and migrate as individual cells similar to mulitcellular streaming[2,5]. In other, microchannel-based models of cell migration, confined space causes a switch in molecular migration mechanisms, from actin-based kinetics to microtubule- or water-flux based, hydrostatic mechanisms of cell propulsion and transport[72,73]. Consequently, together with altered biomechanics, the impact of cell jamming on active versus passive cell-cell cooperation and, possibly, functionally inert, "agnostic" next-neighbor behaviors, will help to define subtypes of multicellular migration and associated cell-function states during migration in complex tissue.

These findings support the notion that mesenchymal cells with constitutively loose cell-cell adhesions[63,74,75] respond to ECM density by adjusting their cell-cell interactions, aggregation and protease dependence, and thereby transit from single-cell to collective invasion strategies, and vice versa. This plasticity response, albeit imposed by a physical mechanism that forces moving cells into and along confined tissue tracks, likely impacts the signals received from local cues, including organization of cell-matrix and cell-cell junctions. Future work will show whether the ECM-density induced collective pattern further induces cell-cell coupling by connexins, and altered signaling states, e,g. epithelium-like cell-cell junctions and apicobasal polarity reminiscent of mesenchymal-epithelial transition (MET)[9,10,75,76] and clarify the relevance of cell jamming in physiological and pathological contexts.

Acknowledgements

We gratefully acknowledge Joost te Riet (Department of Tumor Immunology, RIMLS, The Netherlands) for providing anti-ALCAM antibody. Work of AH was supported by the PhD fellowship program of the RadboudUMC (Nijmegen, The Netherlands). We further acknowledge support be the NWO-Vidi (917.10.364) to KW and by the European Research Council (617430-DEEPINSIGHT), NWO-Vici (918.11.626) and the Cancer Genomics Center (cancergenomics.nl) to PF. AFM work was supported by NWO Medium Sized Investment (NWO-ZonMW 91110007).

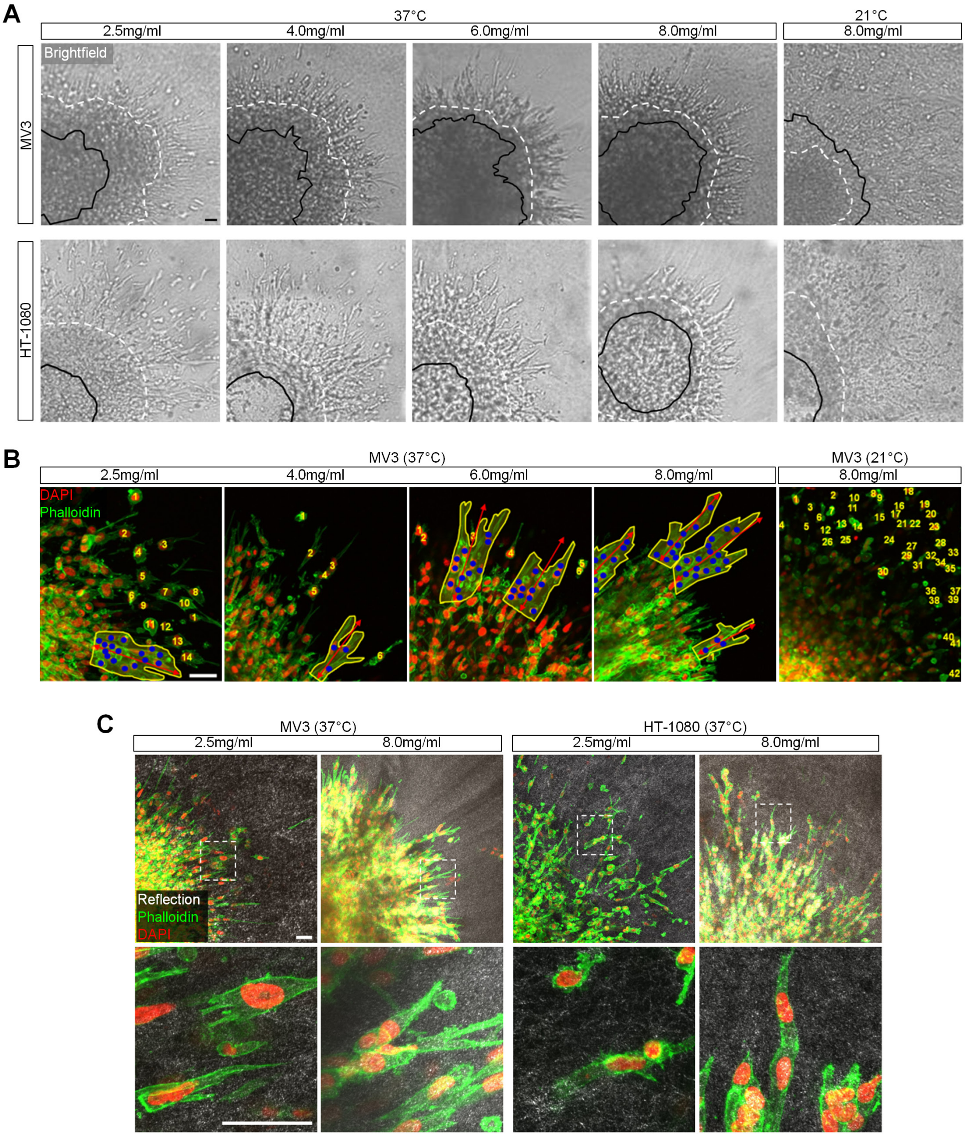

Supplementary Figure 1.

A) Extent of emigration from spheroids 24h (HT-1080) and 48h (MV3) after embedding in collagen matrices of different concentration and polymerization conditions. Bright-field images denote the tumor-collagen border at 0h (black line) and at the end-point (white dashed line). **B)** Quantification of the frequency of cells migrating individually (numbers) or collectively (blue dots within one strand). Yellow outline, area covered by a single strand. Red arrows, strand length. The sum of single cells and cells present in strands was used as total number of invading cells. **C)** Invasion pattern visualized in the context of the collagen reflection signal. Lower panels, 5x zoom highlighting cells and organization of the fibrillar network from regions indicated in the upper panel. Scale bars, 50 µm.

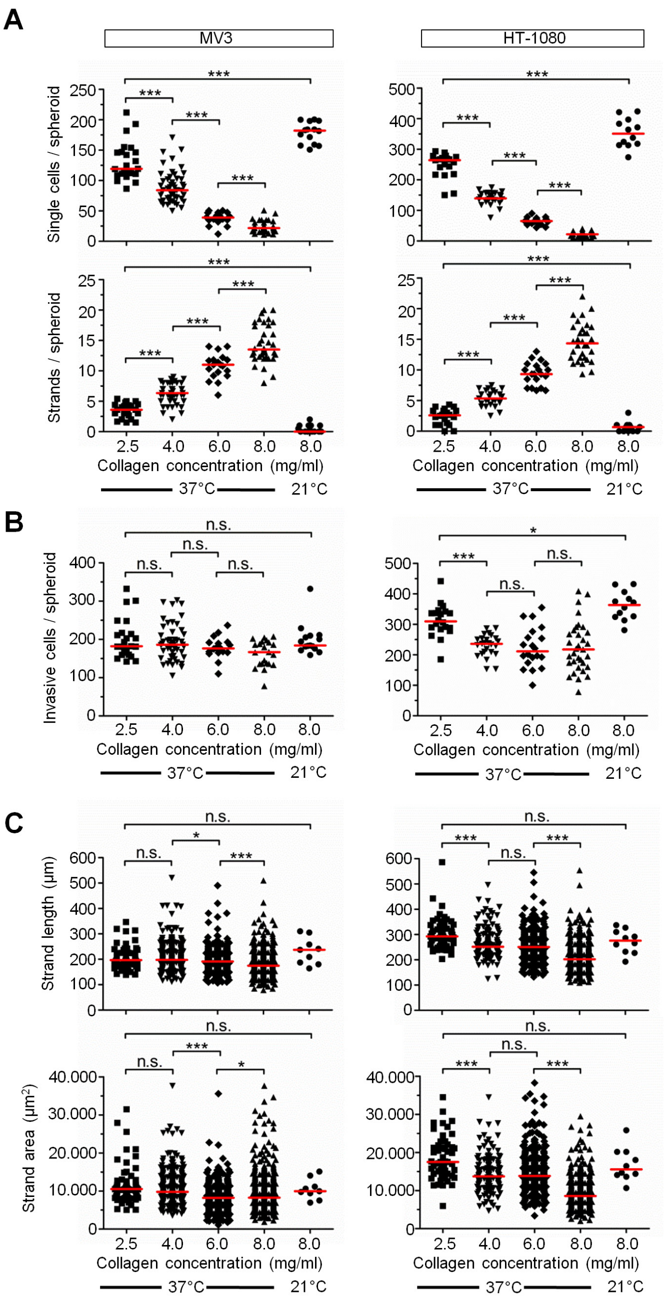

Supplementary Figure 2.

A-C) Quantification of single-cell and collective invasion using DAPI and phalloidin signal as described in Supplementary Fig. 1B (30-70 spheroids/condition from 3-5 independent experiments). ***P < 0.0001 and P = 0.0008 (HT-1080 strands 2.5 mg/mL vs. 8.0 mg/mL (21°C)); *P ≤ 0.0432. Red horizontal lines, median.

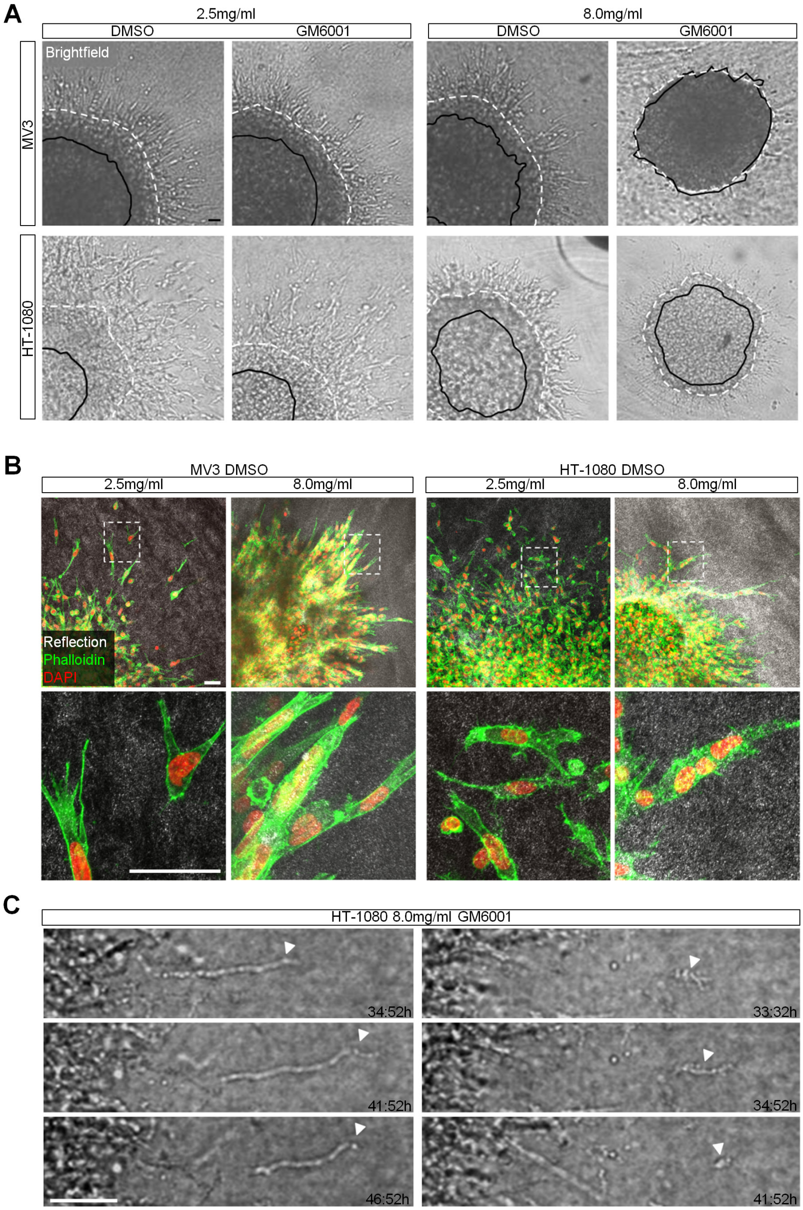

Supplementary Figure 3.
A) Extent of emigration from spheroids 24h (HT-1080) and 48h (MV3) after embedding in collagen matrices of different concentration in the presence of DMSO or MMP inhibitor GM6001. Bright-field images denote the tumor-collagen border at 0 h (black line) and at the end-point (white dashed line). **B)** Invasion pattern visualized in the context of the collagen reflection signal. Lower panels, 5x zoom highlighting cells and organization of the fibrillar network from regions indicated in the upper panel. **C)** Example of two anuclear actin-rich cell fragments (indicated by white arroheads) that moved for at least 48h in the absence of MMP activity in a dense matrix. Scale bars, 50 µm.

References

1. Wolf, K. *et al.* Multi-step pericellular proteolysis controls the transition from individual to collective cancer cell invasion. *Nat. Cell Biol.* **9,** 893–904 (2007).
2. Friedl, P. & Alexander, S. Cancer invasion and the microenvironment: plasticity and reciprocity. *Cell* **147,** 992–1009 (2011).
3. Lämmermann, T. & Sixt, M. Mechanical modes of ‘amoeboid’ cell migration. *Curr. Opin. Cell Biol.* **21,** 636–44 (2009).
4. Rørth, P. Fellow travellers: emergent properties of collective cell migration. *EMBO Rep.* **13,** 984–91 (2012).
5. Friedl, P., Locker, J., Sahai, E. & Segall, J. E. Classifying collective cancer cell invasion. *Nat. Cell Biol.* **14,** 777–83 (2012).
6. Trepat, X. & Fredberg, J. J. Plithotaxis and emergent dynamics in collective cellular migration. *Trends Cell Biol.* **21,** 638–46 (2011).
7. Hegerfeldt, Y., Tusch, M., Bröcker, E. B. & Friedl, P. Collective Cell Movement in Primary Melanoma Explants: Plasticity of Cell-Cell Interaction, Beta1-Integrin Function, and Migration Strategies. *Cancer Res.* **62,** 2125–2130 (2002).
8. Gaggioli, C. *et al.* Fibroblast-led collective invasion of carcinoma cells with differing roles for RhoGTPases in leading and following cells. *Nat. Cell Biol.* **9,** 1392–400 (2007).
9. Friedl, P. & Gilmour, D. Collective cell migration in morphogenesis, regeneration and cancer. *Nat. Rev. Mol. Cell Biol.* **10,** 445–57 (2009).
10. Nieto, M. A. Epithelial plasticity: a common theme in embryonic and cancer cells. *Science* **342,** 1234850 (2013).
11. Gheldof, A. & Berx, G. Cadherins and epithelial-to-mesenchymal transition. *Prog. Mol. Biol. Transl. Sci.* **116,** 317–36 (2013).
12. Maaser, K. *et al.* Functional hierarchy of simultaneously expressed adhesion receptors: integrin alpha2beta1 but not CD44 mediates MV3 melanoma cell migration and matrix reorganization within three-dimensional hyaluronan-containing collagen matrices. *Mol. Biol. Cell* **10,** 3067–79 (1999).
13. Wolf, K. *et al.* Compensation mechanism in tumor cell migration: Mesenchymal-amoeboid transition after blocking of pericellular proteolysis. *J. Cell Biol.* **160,** 267–277 (2003).
14. Bonaventure, J., Domingues, M. J. & Larue, L. Cellular and molecular mechanisms controlling the migration of melanocytes and melanoma cells. *Pigment Cell Melanoma Res.* **26,** 316–25 (2013).
15. Theveneau, E. & Mayor, R. Cadherins in collective cell migration of mesenchymal cells. *Curr. Opin. Cell Biol.* **24,** 677–84 (2012).
16. Alexander, S., Koehl, G. E., Hirschberg, M., Geissler, E. K. & Friedl, P. Dynamic imaging of cancer growth and invasion: a modified skin-fold chamber model. *Histochem. Cell Biol.* **130,** 1147–54 (2008).
17. Weigelin, B., Bakker, G.-J. & Friedl, P. Intravital third harmonic generation microscopy of collective melanoma cell invasion: Principles of interface guidance and microvesicle dynamics. *IntraVital* **1,** 32–43 (2012).
18. Miron-Mendoza, M., Lin, X., Ma, L., Ririe, P. & Petroll, W. M. Individual versus collective fibroblast spreading and migration: Regulation by matrix composition in 3D culture. *Exp. Eye Res.* **99,** 36–44 (2012).
19. Shih, W. & Yamada, S. N-cadherin-mediated cell-cell adhesion promotes cell migration in a three-dimensional matrix. *J. Cell Sci.* **125,** 3661–70 (2012).
20. Wolf, K. & Friedl, P. Extracellular matrix determinants of proteolytic and non-proteolytic cell migration. *Trends Cell Biol.* **21,** 736–44 (2011).

21. Karsdal, M. a *et al.* Extracellular matrix remodeling: the common denominator in connective tissue diseases. Possibilities for evaluation and current understanding of the matrix as more than a passive architecture, but a key player in tissue failure. *Assay Drug Dev. Technol.* **11,** 70–92 (2013).

22. Kraning-Rush, C. M. & Reinhart-King, C. A. Controlling matrix stiffness and topography for the study of tumor cell migration. *Cell Adh. Migr.* **6,** 274–9 (2012).

23. Wolf, K. *et al.* Collagen-based cell migration models in vitro and in vivo. *Semin. Cell Dev. Biol.* **20,** 931–41 (2009).

24. Provenzano, P. P. *et al.* Collagen density promotes mammary tumor initiation and progression. *BMC Med.* **6,** 11 (2008).

25. Friedl, P. & Wolf, K. Plasticity of cell migration: a multiscale tuning model. *J. Cell Biol.* **188,** 11–9 (2010).

26. Ilina, O., Bakker, G.-J., Vasaturo, A., Hofmann, R. M. & Friedl, P. Two-photon laser-generated microtracks in 3D collagen lattices: principles of MMP-dependent and -independent collective cancer cell invasion. *Phys. Biol.* **8,** 15010 (2011).

27. Nelson, C. M. & Bissell, M. J. Of extracellular matrix, scaffolds, and signaling: tissue architecture regulates development, homeostasis, and cancer. *Annu. Rev. Cell Dev. Biol.* **22,** 287–309 (2006).

28. Londono, C. *et al.* Nonautonomous contact guidance signaling during collective cell migration. *Proc. Natl. Acad. Sci.* (2014). doi:10.1073/pnas.1321852111

29. Bordeleau, F., Tang, L. N. & Reinhart-King, C. a. Topographical guidance of 3D tumor cell migration at an interface of collagen densities. *Phys. Biol.* **10,** 65004 (2013).

30. Provenzano, P. P., Inman, D. R., Eliceiri, K. W., Trier, S. M. & Keely, P. J. Contact guidance mediated three-dimensional cell migration is regulated by Rho/ROCK-dependent matrix reorganization. *Biophys. J.* **95,** 5374–84 (2008).

31. Wolf, K. *et al.* Physical limits of cell migration: control by ECM space and nuclear deformation and tuning by proteolysis and traction force. *J. Cell Biol.* **201,** 1069–84 (2013).

32. Wolf, K., Müller, R., Borgmann, S., Bröcker, E.-B. & Friedl, P. Amoeboid shape change and contact guidance: T-lymphocyte crawling through fibrillar collagen is independent of matrix remodeling by MMPs and other proteases. *Blood* **102,** 3262–9 (2003).

33. Mason, S. D. & Joyce, J. A. Proteolytic networks in cancer. *Trends Cell Biol.* **21,** 228–37 (2011).

34. Sabeh, F., Li, X.-Y., Saunders, T. L., Rowe, R. G. & Weiss, S. J. Secreted versus membrane-anchored collagenases: relative roles in fibroblast-dependent collagenolysis and invasion. *J. Biol. Chem.* **284,** 23001–11 (2009).

35. Friedl, P. & Wolf, K. Tube travel: the role of proteases in individual and collective cancer cell invasion. *Cancer Res.* **68,** 7247–9 (2008).

36. Miron-Mendoza, M., Seemann, J. & Grinnell, F. The differential regulation of cell motile activity through matrix stiffness and porosity in three dimensional collagen matrices. *Biomaterials* **31,** 6425–35 (2010).

37. Pelham, R. J. & Wang, Y. l. Cell locomotion and focal adhesions are regulated by substrate flexibility. *Proc. Natl. Acad. Sci. U. S. A.* **94,** 13661–5 (1997).

38. Vitorino, P. & Meyer, T. Modular control of endothelial sheet migration. *Genes Dev.* **22,** 3268–81 (2008).

39. Rasheed, S., Nelson-Rees, W. A., Toth, E. M., Arnstein, P. & Gardner, M. B. Characterization of a newly derived human sarcoma cell line (HT-1080). *Cancer* **33,** 1027–33 (1974).

40. van Muijen, G. N. *et al.* Establishment and characterization of a human melanoma cell line (MV3) which is highly metastatic in nude mice. *Int. J. cancer.* **48,** 85–91 (1991).

41. Del Duca, D., Werbowetski, T. & Del Maestro, R. F. Spheroid Preparation from Hanging Drops: Characterization of a Model of Brain Tumor Invasion. *J. Neurooncol.* **67,** 295–303 (2004).

42. Schindelin, J. *et al.* Fiji: an open-source platform for biological-image analysis. *Nat. Methods* **9,** 676–82 (2012).

43. Nelissen, J. M. D. T., Peters, I. M., de Grooth, B. G., van Kooyk, Y. & Figdor, C. G. Dynamic Regulation of Activated Leukocyte Cell Adhesion Molecule-mediated Homotypic Cell Adhesion through the Actin Cytoskeleton. *Mol. Biol. Cell* **11,** 2057–2068 (2000).

44. Krause, M., te Riet, J. & Wolf, K. Probing the compressibility of tumor cell nuclei by combined atomic force–confocal microscopy. *Phys. Biol.* **10,** 65002 (2013).

45. Lin, D. C., Dimitriadis, E. K. & Horkay, F. Robust strategies for automated AFM force curve analysis--I. Non-adhesive indentation of soft, inhomogeneous materials. *J. Biomech. Eng.* **129,** 430–40 (2007).

46. Friedl, P. *et al.* Migration of highly aggressive MV3 melanoma cells in 3-dimensional collagen lattices results in local matrix reorganization and shedding of alpha2 and beta1 integrins and CD44. *Cancer Res.* **57,** 2061–70 (1997).

47. Pathak, A. & Kumar, S. Independent regulation of tumor cell migration by matrix stiffness and confinement. *Proc. Natl. Acad. Sci. U. S. A.* **109,** 10334–9 (2012).

48. Sadati, M., Taheri Qazvini, N., Krishnan, R., Park, C. Y. & Fredberg, J. J. Collective migration and cell jamming. *Differentiation.* **86,** 121–5 (2013).

49. Stoitzner, P., Pfaller, K., Stössel, H. & Romani, N. A close-up view of migrating Langerhans cells in the skin. *J. Invest. Dermatol.* **118,** 117–25 (2002).

50. Butcher, D. T., Alliston, T. & Weaver, V. M. A tense situation: forcing tumour progression. *Nat. Rev. Cancer* **9,** 108–22 (2009).

51. Buxboim, A., Ivanovska, I. L. & Discher, D. E. Matrix elasticity, cytoskeletal forces and physics of the nucleus: how deeply do cells ‘feel’ outside and in? *J. Cell Sci.* **123,** 297–308 (2010).

52. Stein, A. M., Vader, D. A., Jawerth, L. M., Weitz, D. A. & Sander, L. M. An algorithm for extracting the network geometry of three-dimensional collagen gels. *J. Microsc.* **232,** 463–75 (2008).

53. Levental, K. R. *et al.* Matrix crosslinking forces tumor progression by enhancing integrin signaling. *Cell* **139,** 891–906 (2009).

54. Tong, Z. *et al.* Chemotaxis of cell populations through confined spaces at single-cell resolution. *PLoS One* **7,** e29211 (2012).

55. Balzer, E. M. *et al.* Physical confinement alters tumor cell adhesion and migration phenotypes. *FASEB J.* **26,** 4045–56 (2012).

56. Hung, W.-C. *et al.* Distinct signaling mechanisms regulate migration in unconfined versus confined spaces. *J. Cell Biol.* **202,** 807–24 (2013).

57. Xu, R., Boudreau, A. & Bissell, M. J. Tissue architecture and function: dynamic reciprocity via extra- and intra-cellular matrices. *Cancer Metastasis Rev.* **28,** 167–76 (2009).

58. Gritsenko, P. G., Ilina, O. & Friedl, P. Interstitial guidance of cancer invasion. *J. Pathol.* **226,** 185–99 (2012).

59. Nguyen-Ngoc, K.-V. *et al.* ECM microenvironment regulates collective migration and local dissemination in normal and malignant mammary epithelium. *Proc. Natl. Acad. Sci.* **109,** E2595–E2604 (2012).

60. Friedl, P. *et al.* Migration of Coordinated Cell Clusters in Mesenchymal and Epithelial Cancer Explants in Vitro. *Cancer Res.* **55,** 4557–4560 (1995).

61. Gray, R. S., Cheung, K. J. & Ewald, A. J. Cellular mechanisms regulating epithelial morphogenesis and cancer invasion. *Curr. Opin. Cell Biol.* **22,** 640–50 (2010).

62. Christiansen, J. J. & Rajasekaran, A. K. Reassessing epithelial to mesenchymal transition as a prerequisite for carcinoma invasion and metastasis. *Cancer Res.* **66,** 8319–26 (2006).

63. Wynn, M. L., Rupp, P., Trainor, P. A., Schnell, S. & Kulesa, P. M. Follow-the-leader cell migration requires biased cell-cell contact and local microenvironmental signals. *Phys. Biol.* **10,** 35003 (2013).

64. Theveneau, E. *et al.* Chase-and-run between adjacent cell populations promotes directional collective migration. *Nat. Cell Biol.* **15,** 763–72 (2013).

65. Theveneau, E. & Mayor, R. Neural crest delamination and migration: from epithelium-to-mesenchyme transition to collective cell migration. *Dev. Biol.* **366,** 34–54 (2012).

66. Theveneau, E. & Mayor, R. Can mesenchymal cells undergo collective cell migration? The case of the neural crest. *Cell Adh. Migr.* **5,** 490–8

67. Strobl-Mazzulla, P. H. & Bronner, M. E. Epithelial to mesenchymal transition: new and old insights from the classical neural crest model. *Semin. Cancer Biol.* **22,** 411–6 (2012).

68. Khalil, A. a & Friedl, P. Determinants of leader cells in collective cell migration. *Integr. Biol. (Camb).* **2,** 568–574 (2010).

69. Tozluoğlu, M. *et al.* Matrix geometry determines optimal cancer cell migration strategy and modulates response to interventions. *Nat. Cell Biol.* **15,** 751–62 (2013).

70. Shih, W. & Yamada, S. N-cadherin as a key regulator of collective cell migration in a 3D environment. *Cell Adh. Migr.* **6,** 513–7 (2012).

71. Kawauchi, T. Cell Adhesion and Its Endocytic Regulation in Cell Migration during Neural Development and Cancer Metastasis. *Int. J. Mol. Sci.* **13,** 4564–90 (2012).

72. Raman, P. S., Paul, C. D., Stroka, K. M. & Konstantopoulos, K. Probing cell traction forces in confined microenvironments. *Lab Chip* **13,** 4599–607 (2013).

73. Stroka, K. M. *et al.* Water permeation drives tumor cell migration in confined environments. *Cell* (2014).

74. da Rocha-Azevedo, B. & Grinnell, F. Fibroblast morphogenesis on 3D collagen matrices: the balance between cell clustering and cell migration. *Exp. Cell Res.* **319,** 2440–6 (2013).

75. Theveneau, E. & Mayor, R. Collective cell migration of epithelial and mesenchymal cells. *Cell. Mol. Life Sci.* **70,** 3481–92 (2013).

76. Ilina, O. & Friedl, P. Mechanisms of collective cell migration at a glance. *J. Cell Sci.* **122,** 3203–8 (2009).

Chapter 4

Integrin-Independent Invasion and Metastasis in Sarcoma and Melanoma Xenografts

Anna Haeger*, Stephanie Alexander, Sjoerd van Helvert,
Sarah Weischer, Manon Vullings, Fabian M. P. Kaiser,
Stephan Kissler, Micheal Weiger and Peter Friedl

Manuscript in preparation

*A.H. contributed to the study design, performed all *in vivo* work and analyzed experiments presented in Fig.1 and 5 and Supplementary Fig.2,3 and 7, prepared all (supplementary) figures and wrote this manuscript.

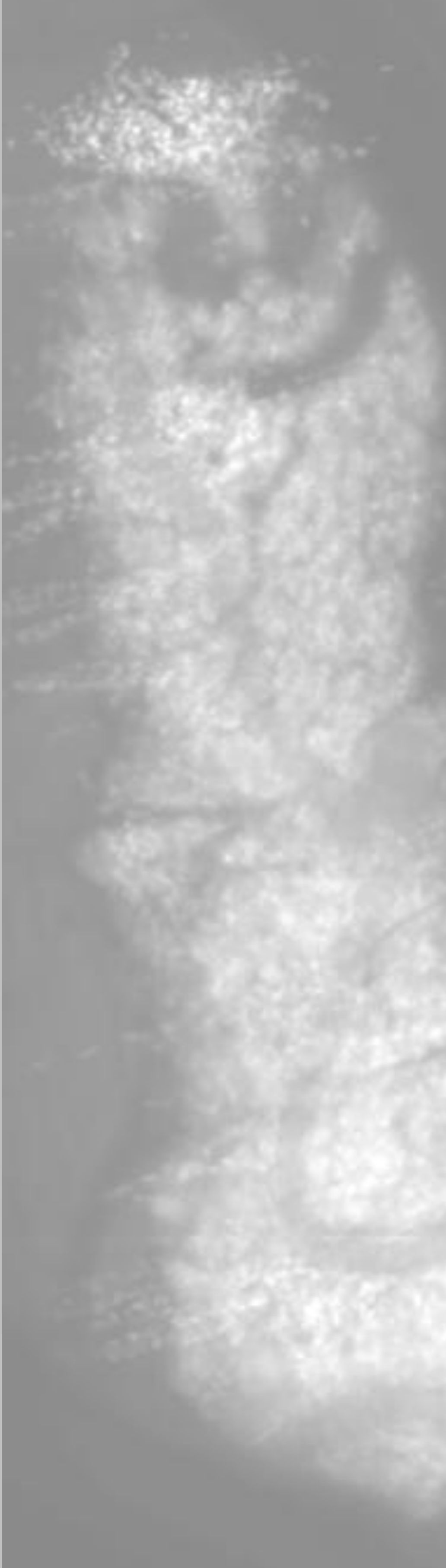

Cancer cell invasion followed by intravasation are rate-limiting steps contributing to systemic dissemination and distant metastasis. Adhesion receptors of the integrin family have been implicated in mediating cancer invasion and metastasis based on their critical function in mechanotransduction and migration. Accordingly, integrins are being considered as targets for anti-cancer therapy to inhibit tumor dissemination and progression. To assess the role of integrins in cancer metastasis, we monitored the growth and local tissue invasion of mesenchymal HT-1080 sarcoma and MV3 melanoma cells by intravital microscopy in orthotopic xenografts and followed their efficacy of systemic dissemination and distant metastasis. Integrins were targeted by stable shRNA-mediated knockdown of β1 and β3 integrins combined with adhesion-perturbing human-selective anti-β1/αV integrin antibody which reached >99% reduction of integrin availability without compensatory upregulation of other integrins or perturbing viability *in vitro*. In both models, integrin targeting caused a severe growth deficit leading to marginalization of local tumors. However migration, local tissue infiltration and emergence of circulating tumor cells were unperturbed and, when normalized to tumor burden, lung colonization and micrometastasis were enhanced. Invading cells *in vivo* showed switch behavior from predominantly collective to single-cell invasion, with diminished elongation and slightly reduced speed and persistence, and this plasticity response was confirmed *in vitro* using a 3D collagen interface assay. These data suggest that β1 and β3 integrins are indispensable for tumor growth and macrometastasis, but rather restrain cancer cell plasticity, local invasion and distant organ colonization. In conclusion, the metastatic cascade *in vivo* may be supported by low-adhesion, friction-based mechanisms suggesting that therapeutic targeting of integrins may bear the risk of enhancing metastatic dissemination.

Introduction

Systemic cancer metastasis results from a multi-step process which depends upon the interdependence of tumor cell migration, survival and growth. Tumor cells first detach and emigrate from the primary tumor lesion, infiltrate the surrounding tissue locally, intravasate into blood vessels, survive as circulating tumor cells in the vasculature, extravasate in secondary organs where, after a period of variable latency, they initiate metastatic outgrowth[1,2]. Whereas locally confined tumor growth usually results in a good prognosis, metastatic progression is the leading cause of cancer fatality[3]. Therefore, an ideal cancer therapy would target the entire metastatic cascade, including regression of the primary lesion but also inhibition and prevention of cancer cell dissemination. This however requires deep molecular and mechanistic insight into all steps underlying metastasis formation, which is currently still lacking[1,4].

For primary tumor growth and metastatic progression cancer cells rely on physical and chemical interaction with the surrounding environment, a prerequisite for the delivery of pro-survival signals and movement of cancer cells away from the main lesion[1,5,6]. Central mediators of this tumor-stroma interplay are integrins: comprising an α and a β chain they assemble into heterodimeric transmembrane adhesion receptors and interact with components of the extracellular matrix (ECM)[7]. Composition of the integrin heterodimer drives ligand specificity, where β1 and αV intgerin subfamilies serve as versatile receptors as they both interact with fibronectin and vitronectin and β1 integrin additionally with collagen and laminin, all abundant constituents of the ECM[7,8].

The short cytoplasmic tail of integrin molecules lacks enzymatic functions but through interactions with intracellular adaptors and signaling complexes integrins exert multiple functions. Talin-mediated coupling of integrins to the actin cytoskeleton stabilizes cell-ECM junctions which is necessary for mechanotransduction during adhesion-mediated migration[9]. Integrin-mediated activation of focal adhesion kinase (FAK) and various downstream signaling cascades, including phosphatidylinositide 3-kinase (PI3K)-Akt and mitogen-activated protein kinase (MAPK) stimulate cell survival, proliferation and counteract apoptosis[10–12] whereas activation of Rho-family GTPases promotes motility by protrusion formation and development of front-rear polarity[13]. Beyond this, lateral associations between integrins and growth factor receptors potentiate activity and downstream signaling of these receptor tyrosine kinases, again feeding into pro-survival pathways[14]. Thus, integrin-mediated cell-matrix junctions serve an important anchoring function and work as a hub for stimulating motility and survival, preventing anchorage-dependent cells from undergoing detachment-induced apoptosis, called anoikis[10,15].

Concordant with pro-survival and pro-invasive functions it has been shown that integrins play an important role in cancer growth and metastatic dissemination[14,16], making them also an important target in cancer therapy[17]. Studies comparing integrin expression in normal and malignant tissue revealed, that in cancer cells integrin expression often becomes deregulated and that expression of certain integrins correlates with metastatic disease such as upregulation of αVβ3 integrin in melanoma[18–20]. Similar correlations have been shown for β1 integrin, however here the interacting α chain co-determines effects: whereas α5β1 and α4β1 integrin expression have been associated with cancer progression in melanoma and ovarian carcinoma, α2β1 integrin was shown to be downregulated in breast cancer with reversal of malignant phenotypes upon re-expression[12,21,22]. Furthermore, also tumor-associated blood vessels or stromal fibroblasts show distinct expression of αVβ3 integrin and β1-containing integrin heterodimers, associated with ubiquitous integrin expression on blood cells and platelets[12,23–28]. Thus both, cancer cells themselves and associated tissue components exhibit distinct integrin expression, which has been shown to contribute to various steps of the metastatic cascade.

In the primary lesion integrin signaling stimulates cancer cell proliferation and neo-angiogenesis, which taken together underlie exponential tumor growth[29,30]. Upon initiation of invasion, integrin-mediated ECM adhesion, mechanocoupling and stimulation of cellular motility enable cancer cells to invade surrounding tissue either collectively or as individual, mesenchymal cells[13,31–33]. However, also cells lacking ECM adhesion are able to move via so-called amoeboid migration modes, although thus far these have been hardly observed during cancer cell invasion[34]. Beyond stimulation of migration and survival, integrin activation also mediates upregulation of matrix metalloproteinases (MMPs), necessary to degrade the basement membrane which facilitates transendothelial migration and thus entry of cancer cells into the vasculature[2,35,36]. The following haematogenous phase is most critical for disseminated cancer cells as the blood compartment lacks an ECM, the main substrate for integrin engagement and subsequent survival stimuli[1,14]. Therefore cancer cells undergo selectin- and integrin-mediated interactions with leukocytes and platelets, delivering survival stimuli to evade anoikis in the blood stream[27,37,38]. To overcome the endothelial barrier, cancer cells develop protrusions which has been shown to be dependent on β1 integrin expression and is further stimulated by the intgerin-based interactions with platelets[14,39–41]. Granulae released by platelets contain, among others, adhesive ligands and factors that decrease integrity of the endothelium, which further enhances transendothelial migration[41]. Generally, the process of extravastion constitutes the rate limiting step in the metastastic cascade as only cells that succeed in exiting the blood stream have a chance to colonize a distant organ[3]. The microenvironment and ECM composition of metastatic sites is usually quite distinct from the primary lesion and thus cancer cells are challenged to cope with this foreign stroma. In order to do so, primary tumors have the ability to create pre-metastatic niches at distant sites to facilitate homing of disseminated cancer cells[42,43]. Nevertheless, the integrin repertoire expressed by disseminated cancer cells and according ligand selectivity dictates whether they are able to “anchor” in the new environment and subsequently receive pro-proliferation signals for metastatic outgrowth[14]. However, initial incompatibility between ECM ligands and integrin expression profile on cancer cells does not mean that cells undergo immediate anoikis but they are able to remain quiescent till changes in the microenvironment provide stimuli upon which cancer cells re-enter the cell cycle[1,44].

Thus, overall there are several lines of evidence assuming an important role of integrins in cancer cell dissemination, including their function as important mechanotransducing system during invasion and source of growth and survival signals[2]. But, the relative contribution of both functions to metastatic outcome and relevance for integrin-targeted therapy remains unclear thus far. Using intravital analysis covering all steps of the metastatic cascade, we therefore investigated the role of integrins for distinct steps of metastatic cancer cell dissemination in a soft tissue sarcoma and melanoma model.

Materials and Methods

Cells and cell culture

Human HT-1080 sarcoma[45] and MV3 melanoma cells[46] were cultured in DMEM (Invitrogen) supplemented with 10% fetal calf serum (Sigma Aldrich), penicillin and streptomycin (both 100 µg/mL; PAA) at 37°C in a humidified 5% CO_2 atmosphere. Cell line identity was verified by SNP_ID Assay (Sequenom, MassArray System, Characterized Cell Line Core Facility, MD Anderson Cancer Center, Houston, TX, USA) and mycoplasma contamination was routinely excluded using the MycoAlert Mycoplasma Detection Kit (Lonza). Dual-color variants of HT-1080 and MV3 cells, expressing cytoplasmic DsRed2 and nuclear histone 2B (H2B)-EGFP[47] were cultured in medium additionally containing Hygromycin B (Invitrogen, 0.2 mg/mL) and G418 sulfate (Calbiochem, 0.2 mg/mL).

Generation of stable integrin knockdown cell lines by lentiviral shRNA

ShRNA sequences targeting ITGB1 (β1 integrin; AGCCACAGACATTTACATTAAA) and ITGB3 (β3 integrin; AAGTCACTTTCTTCTTCTTAAA) for gene silencing by RNA interference were cloned into the lentiviral vector pLBM containing a puromycin cassette and two shRNA integration sites (p-puro2). Lentiviral particles were produced and concentrated by ultracentrifugation, as described[48]. HT-1080 and MV3 dual-color cells were infected with empty p-puro2 pLBM viruses (empty vector (EV) controls), or with ITGB1/ITGB3 targeting p-puro2 pLBM viruses (β1/β3 integrin RNAi cells). For maintaining stable dual-color HT-1080 and MV3 control and knockdown cells medium was supplemented with puromycin (Sigma Aldrich, 5 µg/mL). Stability of knockdown was confirmed by Western Blot after 4-week culture and prior to implantation into mice.

To determine integrin expression profiles in HT-1080 and MV3 cells before and after integrin interference using flow cytometry, shRNA sequences targeting ITGB1 and were cloned into the pLBM vector containing either a puromycin (p-puro) or a neomycin (p-neo) cassette. After virus particle production, wildtype, non-dual-color HT-1080 and MV3 cells were consecutively infected with empty p-puro and p-neo pLBM viruses (p/n vector controls), or with ITGB1 (on p-puro) and ITGB3 targeting (on p-neo) pLBM viruses. Stably transduced cells were selected with puromycin (Sigma Aldrich, 5 µg/mL) and G418 sulfate (400 mg/mL). Stability of knockdown without antibiotics selection was confirmed after 4-week culture in antibiotic-free medium.

Animal experiments and experimental anti-integrin therapy

Animal procedures were approved by the Ethical Committee on Animal Experiments of the Radboud University, Nijmegen (The Netherlands) (RU-DEC 2013-074) and by the Institutional Animal Care and Use Committee (IACUC) of The University of Texas, M.D. Anderson Cancer Center (Texas, USA) (ACUF 07-11-07631, -07632). Animal experiments were performed in the Central Animal Laboratory of the Radboud University Nijmegen in accordance with the Dutch Animal Experimentation Act and the European FELASA protocol and at the University of Texas, M. D. Anderson Cancer Center (Texas, USA), Department of Genitourinary Medical Oncology Research, Division of Cancer Medicine in accordance with institutional guidelines.

To perturb integrin-mediated adhesion, monoclonal mouse anti-human β1 integrin antibody (clone 4B4, IgG1, Beckman Coulter, 6603113) and αV integrin antibody (clone 17E6, IgG1, Merck Serono, kindly provided by Simon Goodman, Department of Cellular Pharmacology - Oncology Platform, Merck KGaA, Darmstadt, Germany) were injected i.p. in mice bearing β1 and β3 integrin RNAi xenografts immediately after tumor implantation (day 0) and at day 3, 7, 11, 16 and 22 (before tumor removal) (Supplementary Fig. 3A). With a dosing of 5 mg/kg body weight (BW) a calculated antibody concentration of ~8 µg/mL in body fluids (60% of body weight)[49] could be pursued which ranged >2x above the minimum concentration required for 99% integrin epitope saturation *in vitro* (Supplementary Fig. 2D). Based on an IgG1 half-life of 6-8 days[50] a calculated antibody concentration of >3 µg/mL in a body fluids could be achieved for at least 6 days by a single injection and maintained by injection intervals of 3-6 days, sufficient to achieve >99% epitope saturation on HT1080 and MV3 cells (Supplementary Fig. 2D). Mice with EV control xenografts received mouse IgG1κ isotype (clone MOPC-21, Sigma Aldrich, M7894) at a dose of 10 mg/kg BW. Prior to application *in vivo*, NaN_3-containing antibody stocks (mAb 4B4, IgG1) were dialyzed against 0.9% NaCl solution (Braun). By using αV instead of β3 integrin blocking antibody we maintained proper αIIbβ3 integrin expression on platelets[51] and thereby prevented potential adverse effects of the *in vivo* integrin blocking treatment.

Intravital microscopy and image analysis
Polyethylene dorsal skin imaging windows were transplanted onto 10- to 14-week-old male athymic Balb/c nude mice (CANN.CG-FOXN1NU/CRL, Charles River), as described[52]. One day post-surgery tumor cells (~$5x10^5$ cells in 4 µl PBS) were implanted into the dermis by image-guided microinjection. $1x10^6$ cells of each implantation round were not injected but snap-frozen in liquid nitrogen or on dry-ice for subsequent protein lysate preparation to confirm integrin expression or presence of integrin knockdown.

For intravital microscopy, mice were anesthetized with isofluorane and stably mounted onto a temperature-controlled platform (37°C). Progression of dual-color tumors was monitored using longitudinal intravital multiphoton microscopy (MPM, LaVision BioTech)[53,54]. Epifluorescence overviews of xenografts and surrounding vascular network were obtained with a 4x objective (NA 0.3, Olympus) at day 1, 3, 8, 10, 15, 17 and 22 for HT-1080 xenografts and day 1, 4, 8, 11, 15, 18 and 22 for MV3 xenografts (Supplementary Fig. 3A). At day 7 (HT-1080 tumors) or day 8 (MV3 tumors) subcellular multiphoton time-lapse microscopy was performed of up to 4 invasion zones per tumor (Supplementary Fig. 3A), which were beforehand annotated in overview images. The emission ranges were 400/40 (blue), 535/50 (green), 605/70 (red), and 710/75 (far-red). Perfused blood vessels were visualized by i.v. injection of AlexaFluor-750-conjugated dextran (70 kD, Invitrogen, 1 mg/mouse). Sequential 4D image series (xyz & time) were recorded with a 20x objective (NA 0.95, Olympus) for up to 300 µm penetration depth at 7 µm step interval and 7 min time-interval for ~4 h. While obtaining image sequences mice were kept hydrated through s.c. injections of 0.9% NaCl solution (Braun).

Tumor volumes were derived from epifluorescence overview images by measuring length and width of the tumor core for each xenograft lesion along reference points (blood vessels, tumor shape) that were determined on the overview image acquired at day 1. Only coherent (parts of) lesions were measured while the presence of single-cell remnants was recorded without measurements. Eventually tumor volumes were calculated as $(\text{tumor width})^2$ x (tumor length) x π / 6 / 2. To determine the residual mass of tumor sub-regions (core vs. invasion zone) for β1 and β3 integrin interference xenografts, areas of sub-regions were measured using the freehand-selection tool in FIJI[55]. For HT-1080 tumors images obtained at day 3 and 10 were used to calculate the relative mass per sub-region of day 10 compared to day 3. For MV3 xenografts respective time-points were day 4 and 11. Area under the curve (AUC) of individual growth curves, needed to correct the number of metastatic lesions for tumor size, was analyzed using GraphPad Prism 5 software (per mouse AUCs of individual lesions were added up).

To analyze invasion in control and β1 and β3 integrin interference xenografts, 4D image sequences were corrected for tissue drift using the Correct 3D Drift plugin in FIJI[55,56] Specifically, the blood vessel (Alexa 750 Dextran) channel was used for registration. For cell tracking, a maximum projection spanning 3-10 z-slices (7 µm per slice, 21-70 µm thickness) was made of the nuclear channel (H2B-EGFP). Nuclei were tracked manually using the MTrackJ plugin in FIJI[55,57] and the nuclear/cell velocity was calculated based on nuclear displacement and acquisition rate. Migration modes were classified as collective, groups, and single cells based on the following criteria: strands are a continuous (from core/field) file of cells with a thickness of ≥ 1 cell, groups are cells in contact with more than 2 cells and 2 cells thick, single are cells not in contact with any neighboring cells and/or are displaying independent migration behavior. For migration mode classification, each tracked nuclei was located within the full 4D image sequence and spatial and temporally assessed for cell-cell association, dimensionality and motility and matched to the most consistent migration mode classification. Cellular elongation was measured in only single cells or leader cells with defined cytoplasmic DsRed2 fluorescent signal. The elongation factor was calculated to be the ratio of the longest chord defined by the cell cytoplasm and the longest chord approximately perpendicular to and still intersecting the cell nucleus (Supplementary Fig. 4B). Directionality of invasion was taken to be the ratio of the total displacement and the distance between the start and end nuclear position (Supplementary Fig. 4C).

Quantification of circulating tumor cells (CTCs)

To check for the presence of dual-color fluorescent CTCs, per xenograft model and group (control or β1 and β3 integrin interference) a fraction of mice was sacrificed at day 11 with prior total blood sampling through cardiac puncture[58]. In brief, mice were deeply anesthetized through a sublethal dose of isofluorane and subsequently fixed laying on the back onto a plastic tube with a slit, allowing to place the imaging window inside the tube. Cardiac puncture was performed using a 22G needle and 1 mL syringe, followed by immediate transfer of blood samples into Lithium Heparin microcuvettes (Sarstedt). Per mouse 300-800 µL blood were drawn. After removal of clots, blood samples were diluted with heparin sodium salt buffer (Sigma, H-3393, 2 units/mL) to a final concentration of 20 units per mL blood. To collect CTCs and leukocytes, blood-heparin solution was filtered through a microsieve with 5 µm pore size (Aquamarijn and Vycap), using a filtration system (Vycap) and applying 15-30 mBar pressure. In case the microsieve got clogged by blot clots, remaining solution was transferred to a second sieve.

Cells collected on the microsieve were washed 2x with phosphate-buffered saline (PBS), fixed with 2% Paraformaldehyde (PFA) for 10 min at room temperature (RT) and washed again 3x with PBS. To visualize leukocytes and counterstain all nuclei of cells captured on the sieve, cells were incubated with PBS supplemented with 10% normal goat serum (NGS, GIBCO Life Technologies, 30min RT), followed by primary antibody incubation (30 min RT) in PBS 10% NGS using rat anti-mouse CD45 antibody (clone 30-F11, BioLegend) at a final concentration of 2.5 µg/mL. After washing 3x with PBS, secondary antibody goat anti-rat Alexa Fluor 647 (Invitrogen, 4 µg/mL) and DAPI (Roche, 1 µg/mL) were diluted in PBS 10% NGS, added to the cells for incubation (30 min RT), succeeded by 3x washing with PBS and sealing the sieve and enclosed cells with FluoromountG (Southern Biotech) and a coverslip.

The entire surface of each microsieve was imaged using high-content epifluoresecence microscopy (DAPI, FITC, TRITC, Cy5 filter) combined with automated multi-position image acquisition and stitching (Leica DMI6000B, 10x HCX FL PLAN/0.25 NA air objective). Autofocus image plane was set based on the DAPI signal. Subsequently, every image was checked manually for the presence of potential CTSs, which were characterized by (partially) overlapping EGFP and DsRed2 signal. Nuclear area of potential CTCs was measured using FIJI[55], followed by exclusion of all cells with nuclei <300 μm^2. Remaining CTC candidates were further checked for overlapping DAPI and H2B-derived EGFP signal and absence of CD45 staining (Supplementary Fig. 6B). Cells fulfilling all criteria were counted as CTCs and categorized into single-cell CTCs or CTC clusters, the latter meaning two or more CTCs appearing connected to each other.

Analysis of spontaneous metastasis

Removal of the imaging window including xenografts or cellular remnants 22 days after tumor implantation was required due to animal welfare regulations and enabled us to separate the processes of cancer cell dissemination and metastatic outgrowth, thus metastasis outcome got not biased by continuous replenishment of disseminating cells. Instead it represents the fraction of cancer cells that successfully entered blood vessels when the primary lesion was present and gives a readout whether these disseminated cells were able to grow out or not after colonizing distant organs (Supplementary Fig. 3A).

Dorsal imaging windows were removed following a final overview image of the xenograft lesion. To check for a correlation between duration of tumor presence and metastasis outcome (Supplementary Fig. 7D), skin windows imposing almost an experimental humane endpoint (e.g. inflammation, necrosis, sideward flipping of the imaging window) prior to day 22 still were removed if the mouse was in an overall healthy condition. To remove the imaging window mice received ketamine/xylacine anesthesia and dorsal skin, including the imaging window, was disinfected with iodine solution (Meda Pharma (Betadine)), followed by cutting away the imaging window and excessive skin which formed due to stretching of the dorsal skin by the imaging window. The emerging wound was disinfected with a sterile gauze swab and iodine solution and subsequently sewed with a running percutaneous suture using absorbable filaments (Covidien (Caprosyn)), providing secure wound approximation for ~10 days. As analgesic treatment mice received buprenorphine hydrochloride (Schering-Plough (Temgesic), ~0.15 mg/kg BW i.m). Before waking up from anaesthesia, each mouse was subjected to whole-body fluorescence imaging (FluorVivo100, INDEC BioSystems, dorsal and ventral) to check for the presence of metastasis-derived fluorescence signal, especially in the thoracic area (Supplementary Fig. 7A).

After removal of the dorsal imaging window mice were followed up for 8 weeks with daily health monitoring and weight measurements minimum twice per week. Mice that were screened positive during whole-body fluorescence measurements after removing the imaging window, or mice showing symptoms like continuous weight loss or dyspnoea, were additionally imaged once per week to monitor potential metastasis progression. If severity of symptoms fulfilled humane end-point criteria, mice were sacrificed before completing the 8 week follow-up phase. Prior to euthanasia and metastasis screen, all mice were again subjected to whole-body fluorescence imaging. Immediately after sacrifice, lymph nodes (superficial cervical, brachial, inguinal), lung, liver and brain were isolated and submerged in PBS to keep the tissue hydrated. Organs were screened for the presence of superficial metastases using fluorescence stereomicroscopy (Leica MZFLIII, EL6000external light source, GFP Plus and DsRed filter sets). While we frequently observed cancer cells in the lungs, superficial and easily countable lesions in other organs were rarely detected. Therefore our eventual metastasis outcome focused on disseminated tumor cells in the lung. After counting metastatic lesions down to single-cell level, organs were embedded in O.C.T. compound (Sakura), deeply frozen using dry-ice or through swaying in liquid nitrogen and stored at -80°C. To validate that green fluorescence signal of lung metastases was derived from H2B-EGFP positive tumor cells, lungs were cut into 50-100 µm thick cryosections mounted on superfrost plus object slides. After fixation with 2% PFA (15 min, RT), lung tissue slices were rinsed with PBS and incubated in PBS containing 0.1% Triton X-100 (Sigma Aldrich) for permeabilization (20 min, RT), followed by incubation with DAPI (1 µg/mL) diluted in PBS 2% NGS, 0.1% cold water fish skin gelatin (CWFG, Sigma Aldrich) for 10 min at RT, washing with PBS and mounting in Fluoromount G. GFP positive tissue slices were subsequently imaged by confocal microscopy (Olympus FV1000) to verify colocalization of H2B-EGFP and DAPI signal. Selected lesions were scanned as 3D stacks using a 20x / 0.50 NA or 40x / 0.80 NA water immersion objective and 1 µm step size. Filters to additionally capture DsRed2 derived signal were activated, however signal was either blurred or lost due to freezing and fixation procedures.

In vitro interface migration assay

Multicellular spheroids (5000 cells per spheroid) were prepared from subconfluent cultures after detachment with EDTA (Invitrogen, 2 mM,) by 48h hanging-drop incubation[59] in the presence of 40% methylcellulose (Sigma) and bovine collagen-I (Advanced Biomatrix, 9.3 μg/mL final concentration).

Between two 6 mg/mL high-concentration collagen I layers we obtained the best defined interface and created a rather restrictive environment constraining the major part of migration along the interface to mimic the *in vivo* situation (Supplementary Fig. 5B,C). To prepare cell-free collagen-collagen interface gels, two 6 mg/mL rat-tail collagen-I (Corning) gels of each 50 μL were polymerized in in7x7x2 mm silicone isolators (Electron Microscopy Sciences), placed inside 24-well plates. The bottom layer was polymerized for 30 min at 37°C after which the upper layer was pipetted directly on top and polymerized similarly. For migration experiments, one spheroid was placed on the bottom gel after polymerization, prior to adding the upper layer of collagen. 0.75 mL culture medium containing 5 μg/mL puromycin was added per well after polymerization on top of the gel. Culture medium was supplemented with anti-β1 integrin monoclonal antibody (mAb) 4B4 and anti-αV integrin mAb 17E6 (both 10 μg/ml) for β1/β3 knock-down cells and IgG1κ isotype from murine myeloma (20 μg/mL) for EV control cells. Cells were allowed to migrate for 48 h followed by fixation with 4% PFA (1 h, RT).

PFA-fixed samples were washed twice with PBS followed by staining with mouse anti-ALCAM mAb (AZN-L50; IgG2A; kindly provided by Joost te Riet, Department of Tumor Immunology, Radboudumc Nijmegen, The Netherlands)[60], after over-day blocking in 0.1% bovine serum albumin (BSA, Aurion) at 4°C. Primary antibody was diluted in PBS 0.1% BSA and incubated overnight (o/n) at 4°C whilst gently agitating. Subsequently, samples were washed with PBS followed by o/n incubation with goat anti-mouse Alexa Fluor 405 and Phalloidin Alexa 633 (both Invitrogen, 4 μg/mL) in PBS 0.1% BSA (4°C) and washing with PBS. Eventually, stained collagen lattices were sealed into a PBS, 0.1% BSA, 0.05% sodim azide (Sigma Aldrich) containing self-made chamber on an object slide covered with a coverslip. Imaging was performed using a high-content epifluoresecence microscope (DAPI, FITC, Cy5 filter) combined with automated multi-position image acquisition and stitching (Leica DMI6000B, 10x HCX FL PLAN/0.25 NA air objective), generating z-stacks with 10 μm step-size. To obtain high-quality images, selected samples were subsequently re-imaged using confocal scanning microscopy (Olympus FV1000, 20×/0.5 NA and 40×/0.80 NA water immersion objectives, 5 and 1.38 μm step size respectively).

Analysis of migration modes was performed on a per spheroid basis, including only cells that were migrating into the collagen-collagen interface. To determine total area of the invasion zone as well as the fraction of cells migrating in a particular mode, outlines of 2D cohesive sheets connected to the spheroid, detached cells and cell clusters (>2 cells) were traced, assessing both brightfield and phalloidin signal for determining cellular detachment. Subsequently areas of each migratory fraction were measured and plotted as percentage of the total area of the invasion zone. Cellular elongation was determined from detached single cells by dividing the length of the longest possible straight line through the cell that intersects the nucleus by the longest possible line perpendicular to it (Supplementary Fig. 4B).

For time-lapse microscopy, samples were prepared with bicarbonate-free DMEM containing HEPES (Invitrogen, 20 mM). The 24-well plate containing the samples was placed in a heated chamber (Okolab; 37°C) with humidified gas supply, which was mounted on a motorized stage on an inverted microscope (Nikon Diaphot 300; 10× / 0.25 NA dry objective) equipped with a CCD Camera (Hamamatsu C8484-05G). Brightfield images were acquired every 10 min using Okolab time-lapse software for up to 48 h. Cell migration velocity and persistence were analyzed by manual tracking using the MTrackJ plugin for FIJI[55,57]. Persistence was calculated by dividing the distance from the first to the last measured point by the length of the track (Supplementary Fig. 4C).

Statistics

Statistical analysis was performed using GraphPad Prism 5 software. For data quantifying tumor growth or β1/β3 integrin knockdown two-tailed t-tests were performed, paired for intratumor comparison of tumor core and invasion zone, unpaired for all other cases. Migration analyses, amount of CTCs per mouse and metastasis outcome were analyzed using the two-tailed unpaired Mann–Whitney test. To evaluate differences between mice bearing CTCs and mice that were CTC negative, a Mantel-Cox Log-rank test performed. To adjust for multiple comparisons, p-value cutoffs were subjected to Bonferroni correction.

Results

To address the role of integrins for tumor progression and metastasis formation in HT-1080 sarcoma and MV3 melanoma xenografts we applied a preventive integrin interference approach prior to and during tumor implantation, aiming to minimize the availability of all integrin subtypes expressed by the cells. Both cell lines expressed β1 integrins at high and αV and β3 integrins at moderate to low levels, but lacked all other β integrin subsets (Supplementary Fig. 1). This integrin expression profile was consistent with mesenchymal cells, which lack integrins restricted to leukocytes (β2) or basement membrane interaction (β4-β8)[61,62]. Simultaneous downregulation of β1 and β3 integrins using shRNA resulted in respective 75-85% and 90-99% reduction of protein surface expression, without compensatory upregulation of other β chains (Supplementary Fig. 1, 2A,B). After integrin downregulation cells showed reduced mitotic activity but retained low frequency of apoptosis, indicating largely unperturbed survival without increased risk to select for anchorage-independent, anoikis-resistant clones[63] (Supplementary Fig. 2C). To improve targeting, adhesion of residual β1 and αVβ3 integrin epitopes was perturbed *in vitro* and *in vivo* by applying anti-β1 and -αV integrin antibodies (4B4 and 17E6, respectively) in HT-1080 and MV3 cells and xenografts expressing β1/β3 shRNA. Using 24h-exposure with both antibodies at a concentration of 3 µg/mL, as realistically achieved in body fluids *in vivo* with the applied dosing and application regime, surface β1 and β3 integrins were diminished to isotype control levels on HT-1080 and MV3 wild-type cells (Supplementary Fig. 2D). Consistently, HT-1080 β1/β3 integrin shRNAi xenografts growing in nude mice treated with mAb 4B4 and 17E6 showed efficient reversion of increased phospho-FAK signal to levels equal to the stromal background (Supplementary Fig. 2E).

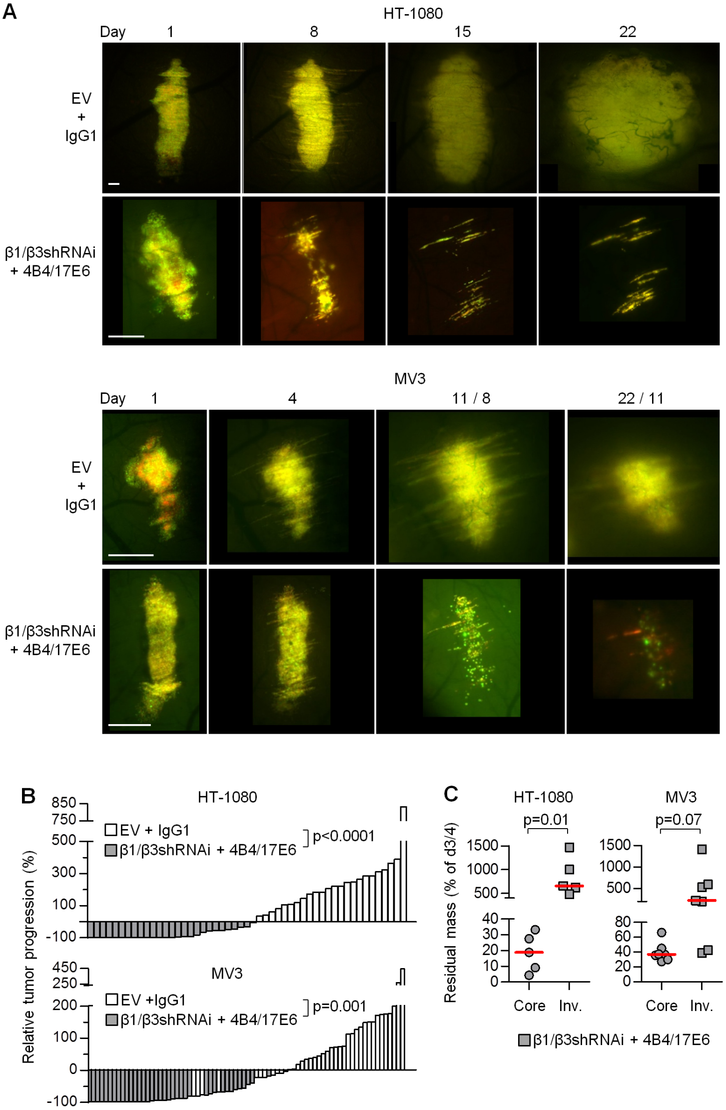

Figure 1. Tumor regression upon β1/αVβ3 integrin interference.
A) Time-dependent whole tumor morphology of HT-1080 and MV3 empty vector (EV) control xenografts treated with isotype and xenografts after shRNA-mediated RNAi for β1 and β3 integrin additionally treated with adhesion perturbing antibodies 4B4 (β1) and 17E6 (αVβ3). For MV3 tumors, last pictures of the series show the control lesion at day 22 and the integrin interference lesion at day 11. Beyond day 11 the β1/β3 shRNAi tumor had undergone complete regression. Scale bar, 200 µm. **B)** Relative tumor progression of individual control and β1/β3 integrin RNAi lesions at day 10 (HT-1080) or day 11 (MV3) compared to day 1, displayed as waterfall plots. Data include 25 (HT-1080, 13 mice) and 38 (MV3, 19 mice) control tumors and 26 (HT-1080, 13 mice) and 38 (MV3, 18 mice) integrin interference lesions. Statistics, unpaired t-test comparing tumor volumes of control or interference lesions at day 10/11 (see also Supplementary Fig. 3B). **C)** Median residual mass of core and invasion (Inv.) zone after β1/β3 integrin interference at day 10 compared to day 3 (HT-1080) or day 11 compared to day 4 (MV) from 5 (HT-1080) or 7 (MV3) independent tumors. Statistics, paired t-test.

To monitor how preventive integrin targeting affects spontaneous metastasis, HT-1080 and MV3 xenografts expressing nuclear H2B-EGFP and cytoplasmic DsRed2 were implanted intradermally and their growth and invasion were monitored using intravital microscopy. In addition, cells reaching the circulation were counted as CTCs after 11 days and metastatic outcome was quantified 11 weeks post-implantation (Supplementary Fig. 3A). *In vivo*, HT-1080 sarcoma and MV3 melanoma tumors expressing vector control, treated additionally with isotype antibody developed distinct growth behaviors: HT-1080 lesions grew exponentially whereas MV3 tumors were slowly progressing (Fig. 1A, Supplementary Fig. 3B). Despite this difference, HT-1080 and MV3 tumors were equally sensitive to integrin interference, reaching partial or complete regression within 3 weeks of observation (Fig. 1A,B, Supplementary Fig. 3B), confirming an essential role for integrins in mediating growth and survival of the primary tumor lesion.

When monitored by intravital MPM, HT-1080 and MV3 control tumors developed predominantly strand-like collective invasion with intact cell-cell junctions as described[52] (Fig. 1A, 2A,B, Supplementary Fig. 4A). Such collective migration patterns have been shown to depend on integrin-mediated cell-matrix adhesion, where especially the leader cells generate actin and integrin-mediated traction forces to propel the cell group forward and loss of integrin function goes along with a switch to amoeboid single-cell migration or abolished cellular migration[33,64,65]. Surprisingly, after multi-integrin targeting in HT-1080 and MV3 xenografts, collective invasion patterns persisted, however were accompanied by increased detachment of multicellular clusters and single cells (Fig. 2A,B). Decreased cellular elongation, especially in MV3 cells, further indicated a switch towards more amoeboid-like migration (Supplementary Fig. 4B). Independent of the migration mode, movement efficacy at single cell level was largely unperturbed after integrin targeting, showing only slightly reduced velocity and directionality (Fig. 2C, Supplementary Fig. 4C). Notably, compared to the tumor core, in both tumor types invasion zones of integrin-targeted xenografts were clearly more persistent and lagging behind in the regression process (Fig. 1A,C). Thus, in contrast to the tumor core, cells invading the deep dermis exhibited improved survival capacity upon blocking integrin function, accompanied by persisting integrin-independent invasion and enhanced migrational plasticity.

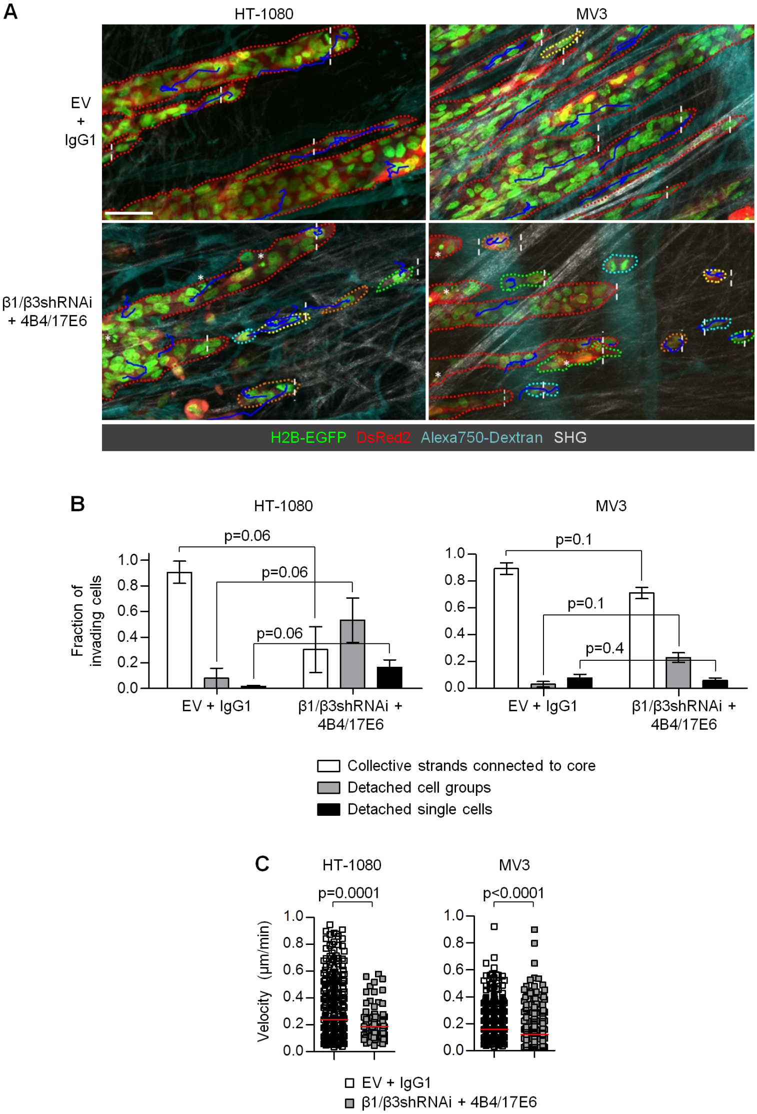

Figure 2. Persisting collective invasion and increased single-cell detachment after β1/αVβ3 integrin interference.
A) Invasion zones of HT-1080 or MV3 control or β1/β3 integrin interference xenografts. Tumor cells stably express nuclear H2B-EGFP and cytoplasmic DsRed2. Alexa Fluor 750-conjugated Dextran contrasts perfused blood vessels. Second harmonic generation (SHG) visualizes muscle and collagen fibers. Blue lines: migration tracks. Red dotted outlines: collective strands. Other dotted outlines: single cells and detached cell groups. Dashed lines: position strand tip or cell/cell group at start time-lapse sequence. * apoptotic cells. Scale bar, 50 µm. **(B,C)** Analysis of migration mode and velocity. **B)** Migration-mode based categorization and distribution of invading tumor cells displayed as mean fraction ± SEM. **C)** Median velocity derived from tracking 248 (HT-1080 EV), 112 (HT-1080 β1/β3 integrin RNAi) or ~480 (both MV3 conditions) individual cells. Migration mode and velocity data were analyzed from 2 (HT-1080) and 3 (MV3) mice for control conditions and 4 (HT-1080) and 3 (MV3) mice for interference conditions with 4-6 imaging positions per mouse. Statistics, Mann-Whitney test.

These findings were not consistent with the significant integrin dependence of HT-1080 and MV3 cells migrating into 3D fibrillar collagen matrices, which is strongly compromised by addition of anti-β1 integrin mAb 4B4[32,66]. We thus sought to reconcile this apparent *in vitro*/ *in vivo* inconsistency by analyzing the different environmental conditions. The deep mouse dermis is heterogeneously organized with interfaces provided by preexisting tissue structures including myofibers or blood vessels, interspersed with collagen fibers and other ECM components, altogether forming a track-like system guiding moving cells[67,68]. Conversely, the *in vitro* collagen I matrix is a dense network of randomly aligned fibers requiring proteolytic cleavage to form tracks of least resistance and enable cellular movement[69,70]. Following the concepts on adhesion-independent migration (i.e. “chimneying”) in 3D channel-like, confined environments[71–74], we hypothesized that guidance paths relative to space constraints dictate the differential requirement for integrin function and refined the 3D spheroid invasion model by introducing an interface between two high-density collagen matrices (6 mg/mL), serving as path of least resistance for invading cells (Supplementary Fig. 5A-B). When compared to engineered collagen-based models, using stamps to generate a “clean” interface[75,76], through two-step polymerization we secured a loose network of perpendicular collagen fibrils bridging the interface between both collagen compartments (Supplementary Fig. 5B), thus mimicking *in vivo* interfaces bordered by loose fibrillar structures[67,68].

Cells from HT-1080 and MV3 control spheroids embedded into this modified collagen I model invaded the interface collectively as cohesive 2D sheet with intact cell-cell junctions maintained (Fig. 3A,B, Supplementary Fig. 5C,D). After integrin interference, migration was clearly reduced but persistent with decreased velocity and collective sheets showing disintegration into smaller cell groups and single cells, which additionally displayed slightly less elongation compared to control cells (Fig. 3B,C, Supplementary Fig. 5E). Furthermore, especially in MV3 cells integrin interference impaired directional movement (Supplementary Fig. 5F). Overall, this unperturbed invasion and increased diversity of migration patterns obtained *in vitro* after integrin targeting recapitulated major patterns also observed *in vivo*, emphasizing the need of interfaces and track-like structures to enable integrin-independent movement.

To address whether multi-integrin interference affects intravasation and the occurrence of CTCs, blood samples from mice were analyzed ~2 weeks after tumor implantation using sensitive filter-based isolation procedure (Supplementary Fig. 6). The time of CTC analysis coincided with the phase of subtotal or complete regression in the majority of lesions after integrin targeting (compare Fig.1B and Supplementary Fig. 3A). In tumor-bearing control mice, 30-60% of the mice were CTC negative, whereas in the remaining mice either single-cell CTCs or in 10-20% of the mice CTC cluster and single-cell CTCs were detected (Fig. 4A-C). Notably, after integrin interference for both models fractions of CTC positive and negative mice as well as mice with single-cell CTCs and CTC clusters hardly changed (Fig. 4A,B). Additionally, normalized CTC counts revealed a moderate increase in CTC concentration after integrin function blocking, although not significant (Fig. 4C). Thus, the occurrence of both disseminating individual cells and CTC clusters was undiminished after integrin targeting, indicating that integrins are not required for intravasation and systemic dissemination.

To investigate whether integrins are required for distant metastasis, xenografts were allowed to progress for 3 weeks, then removed and after follow up of additional 8 weeks, typical target organs for metastasizing soft tissue sarcoma and melanoma including lung, liver, brain and draining lymphnodes[77–79] were subjected to fluorescence detection, with eventual metastasis outcome focusing on disseminated tumor cells in the lung (Fig.5A,B, Supplementary Fig. 7A). To account for all colonizing events, including macroscopically visible lesions, multicellular micrometastases and single cells, metastases were subsequently validated by DAPI counterstaining as being real cells rather than autofluorescent debris (Fig. 5A,B). To rule out that intradermal tumor cell injection caused accidental injury of blood vessels and passive entry of cancer cells into the blood stream followed by experimentally-induced metastasis, mice with detectable bleeding during tumor implantation were excluded from the analysis. To still rule out artificial dissemination in mice without detectable vascular damage during implantation, for a subset of mice the imaging window and tumor were removed 6h after tumor implantation, resulting in a negative metastasis outcome after 11 weeks (Supplementary Fig. 7D). Likewise, no early-onset of metastasis was detected, but rather the occurrence of metastatic lesions was strongly dependent on time after implantation (Supplementary Fig. 7D). These data rule out the likelihood that metastases were incurred by the implantation procedure but occurred through spontaneous dissemination.

For both, control and β1/β3 integrin targeted tumors in the HT-1080 and MV3 model, overall incidence of lung metastases was comparable (Fig. 5C). In absolute counts, both tumor models showed reduced numbers of multicellular micrometastases after integrin targeting, whereby HT-1080 control xenografts also developed macrometastases which were lacking upon integrin interference and were generally absent in the MV3 model (Supplementary Fig. 7B). The amount of single-cell lesions was similar for control and integrin-targeting conditions in the HT-1080 and MV3 model (Supplementary Fig. 7B). To exclude that this metastasis outcome was biased by escape behaviors, i.e. instability or loss of the β1/β3 integrin RNAi, we used β1 integrin mRNA expression as indicator to test reliability of the β1/β3 intgerin knockdown, which was possible because both β1 and β3 integrin shRNAs are expressed from the same vector. RNA was isolated from lung pieces containing fluorescent metastatic lesions derived from control or intgerin knockdown tumors obtained 11 weeks after tumor implantation, followed by cDNA generation and qPCR using human-specific β1 integrin and GFP specific primer to exclusively amplify tumor-cell derived cDNA, confirming maintenance of β1 integrin knockdown levels similar to *in vitro* cultured cells under antibiotics selection (Supplementary Fig. 7E).

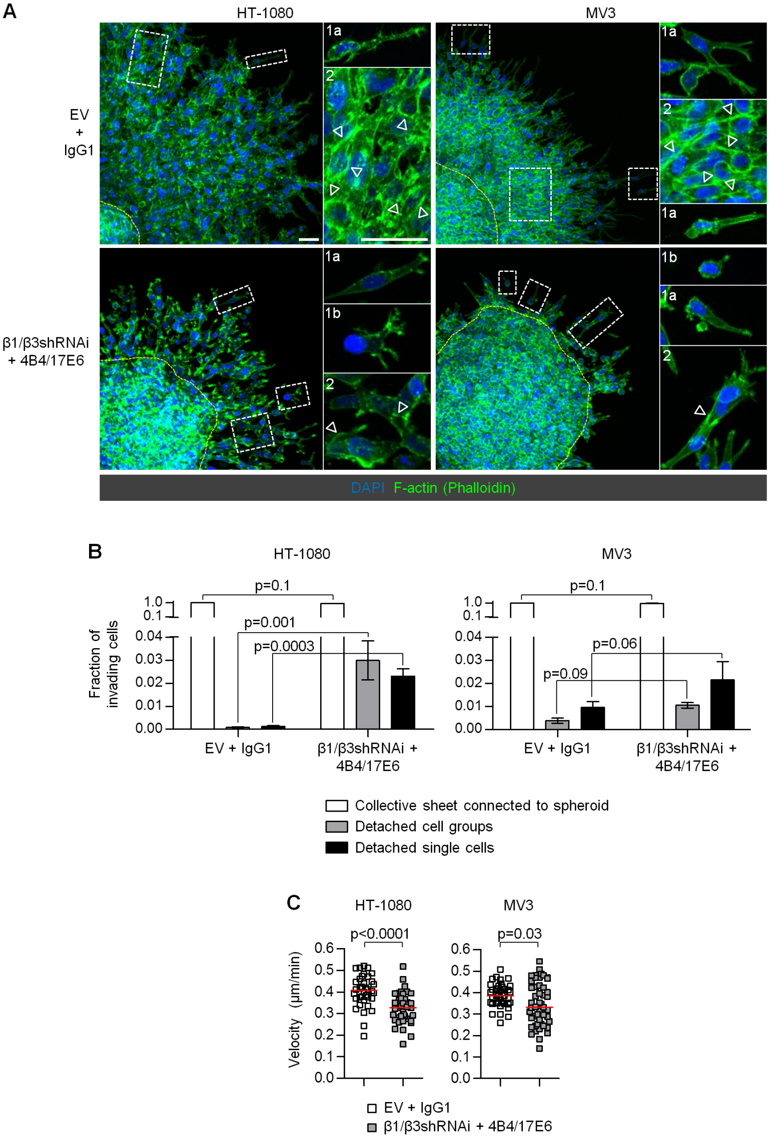

Figure 3. Interface-guided migration enables integrin-independent cellular movement *in vitro*. **A)** Interface-guided emigration from HT-1080 and MV3 control and β1/β3 integrin interference spheroids 48 h after embedding between two collagen matrices, displayed as maximum intensity projection from confocal 3D stacks. Dashed rectangles, region of detail images. 1, detached single cells (a, elongated, mesenchymal; b, roundish, amoeboid). 2, collective 2D sheets or cell groups. Arrowheads, cell-cell junctions. Scale bar, 50 µm (overview and zoom image). **(B,C)** Analysis of migration mode and velocity. **B)** Migration-mode based categorization and distribution of emigrating cells displayed as mean fraction ± SEM. **C)** Median velocity derived from tracking 91 (HT-1080 EV), 100 (HT-1080 β1/β3 integrin RNAi), 110 (MV3 EV) and 87 (MV3 β1/β3 integrin RNAi) individual cells. Migration mode and velocity data were analyzed from 3 independent experiments with 2-3 spheroids per experiment. Statistics, Mann-Whitney test.

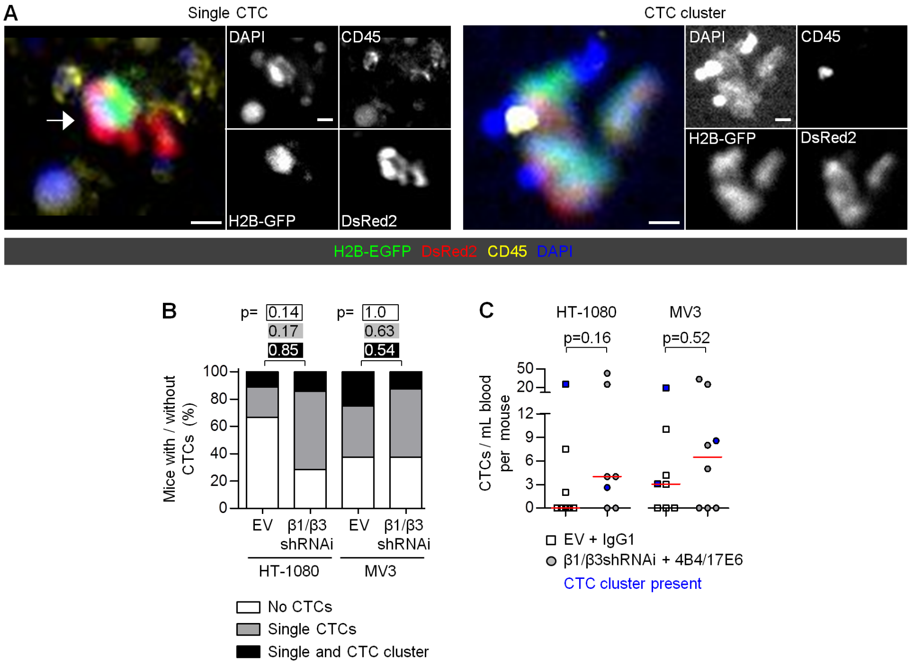

Figure 4. Unperturbed haematogenous dissemination of single cells and multicellular clusters upon β1/αVβ3 integrin interference.
A) Single-cell CTC and CTC cluster captured from blood samples on a microsieve. Tumor cells were identified based on (partial) colocalization of nuclear H2B-EGFP (overlapping with DAPI signal) and cytoplasmic DsRed2 signal. CD45 staining visualizes immune cells. Scale bar, 10 µm. **B)** Fractions of mice for HT-1080 and MV3 control and β1/β3 integrin interference xenografts, being either CTC negative or CTC positive with either exclusively single-cell CTCs or a combination of single-cell CTCs and CTC clusters. Blood samples were taken from 9 (HT-1080 EV), 7 (HT-1080 β1/β3 integrin RNAi), or 8 (both MV3 conditions) mice. Statistics, Log-Rank test. **C)** Normalized median amount of CTCs obtained per mouse. Total CTC numbers per mouse were counted with cases highlighted where multicellular clusters contributed to total CTC amount. Statistics, Mann-Whitney test.

Because growing control lesions comprised a 30-fold (HT-1080) and 20-fold (MV3) larger volume compared to regressing β1/β3 integrin RNAi lesions at day 10/11, individualized normalization of the amount of metastatic lesions relative to the time-integrated tumor mass was performed for each mouse (Supplementary Fig. 7C), to standardize metastatic outcome to tumor burden. Compared to absolute counts, this resulted in a significantly increased number of single cell and overall metastases for β1/β3 integrin interference xenografts of both models (Fig. 5D). For HT-1080 tumors even the normalized amount of micrometastases was enhanced after integrin targeting whereas for MV3 xenografts the number of micrometastases approximated for both conditions (Fig. 5D). Thus, after combined targeting of β1/β3 integrins by RNAi and adhesion-interfering antibodies, HT-1080 and MV3 xenografts developed an increased probability to colonize the lungs as single cells or small clusters which however lacked early onset outgrowth.

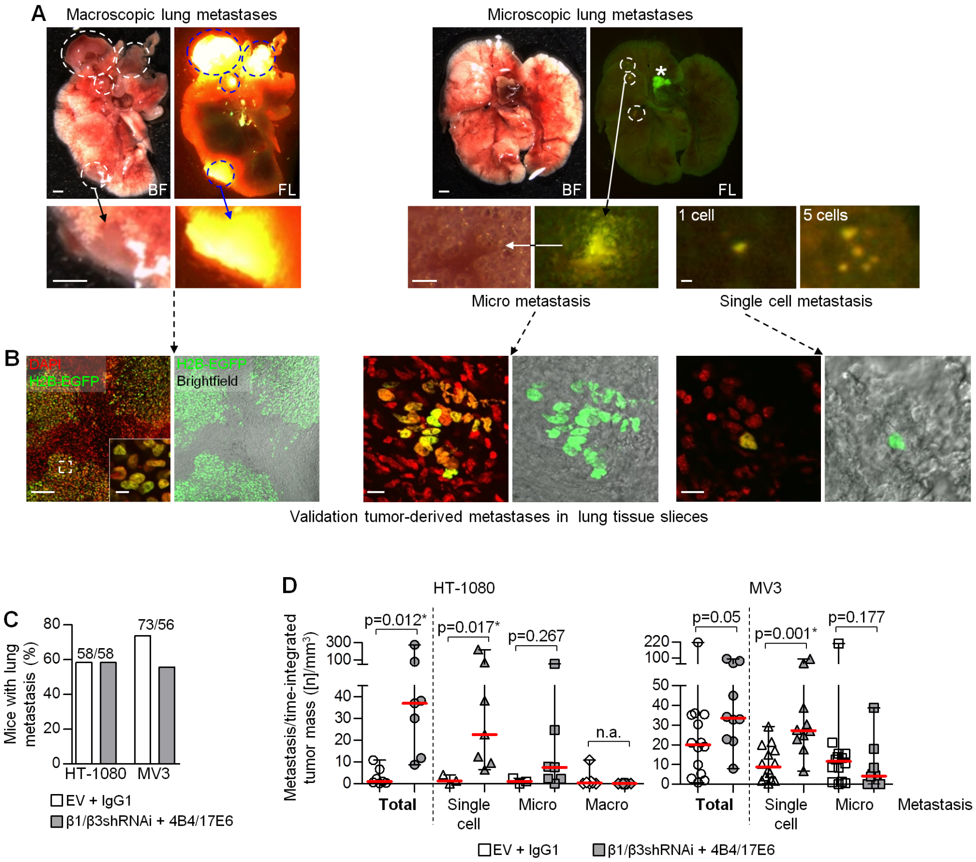

Figure 5. Enhanced metastatic seeding of cells after β1/αVβ3 integrin interference.
A) Categorization of metastatic lesions in the lung. Macroscopic lesions were visible by eye, micro metastasis could be detected in fluorescence overview images of whole lungs and constituted a homogeneous mass in contrast to countable single-cell lesions. Dashed circles, region of detail images.*, part of the highly autofluorescent esophagus. BF, brightfield image. FL, fluorescence signal. Scale bar, 1 mm (overview images and zoom macro metastasis), 100 µm (zoom micro metastasis), 10 µm (zoom single-cell metastasis). **B)** Metastatic lesions of different categories identified based on H2B-EGFP-derived green fluorescence colocalizing with nuclear DAPI signal displayed as maximum intensity projection from confocal 3D stacks of 50-100 µm tissue slices. Scale bars, 100 µm (macro metastasis), 10 µm (micro and single-cell metastasis). **C)** Fractions of mice for HT-1080 and MV3 control and β1/β3 integrin interference xenografts where lung metastases were detected. In total 13 (HT-1080 control and β1/β3 integrin RNAi), 19 (MV3 control) and 18 (MV3 β1/β3 integrin RNAi) mice were analyzed of which indicated percentages were metastasis positive. **D)** Median amount of lung metastases normalized for size of the primary lesion over time, determined as area under the curve (AUC). See also Supplementary Fig. 7 for absolute number of metastatic lesion and details on AUC analysis. Statistics, Mann-Whitney test. *, significant p value after Bonferroni correction (Bonferroni-corrected threshold was 0.017).

Discussion

The results of this work, investigating the relevance of integrins for all steps of the metastatic cascade *in vivo* by intravital imaging, confirmed that integrins function as important mediators of growth and survival signaling, showing that integrin targeting leads to a growth deficit in the primary tumor and diminished outgrowth after lung colonization with a dormancy-like phenotype[80]. However, unexpectedly and hardly anticipated by published *in vitro* results, our results also revealed that integrins are largely dispensable for local tissue invasion, intravasation and metastatic arrival at distant sites; instead integrin interference increased plasticity and efficiency of invasion and even enhanced metastatic dissemination when tumor load was taken into account. Thus, except for outgrowth of primary and metastatic lesions we could not identify any step in the metastatic cascade of mesenchymal sarcoma and melanoma xenografts to be significantly dependent on integrin function. This contradicts the common conclusion that integrins are indispensable for invasion and metastasis formation, mainly based on (i) *in vitro* models such as migration analysis on 2D ECM-coated surfaces or in 3D matrix models, transwell migration assays and microfluidics-based microvascular networks after integrin knockdown/blockade or overexpression[40,81–84], (ii) preclinical studies which either analyzed experimentally-induced metastasis or solely investigated growth of the primary and/or metastatic lesion[82,85–88] or (iii) studies showing correlations between (high) integrin expression and cancer progression[18,19,21,89]. Accordingly, our results emphasize the need for *in vivo* studies which longitudinally analyze the entire metastatic cascade in orthotopic models, including tumor sub-regions, while separating between survival and migration function of integrins.

During cell migration, integrins mediate attachment to the ECM and serve as linker between extracellular substrates and the actin cytoskeleton, necessary to generate traction forces to propel the cell body forward[90]. Despite this essential function of integrins in cell migration, we here show, that integrin-independent migration mechanisms contribute to cancer invasion and metastasis. Environments requiring adhesion-dependent migration include 2D substrates and dense, discontinuous 3D matrices without any pre-defined interface, where adhesion interference blocks migration and causes cells to round up[32,66,73,74]. Conversely, highly porous 3D matrices and confined 2.5D and 3D channel-like structures promote adhesion-independent migration, inducing cells to employ alternative mechanisms to build up traction forces[34,71–74]. The environmental conditions of disseminating cancer cells in the deep dermis include predefined tracks between tissue structures like endothelial cells or myofibers and offer such confined, channel-like structures[67]. They allow cells to adapt adhesion-independent migration modes such chimneying or friction-based migration where cells either exert pushing forces against the surrounding substrate or generate contractile flows of the actomyosin cortex to produce forward movement[34,91,92].

But, latest when reaching the basement membrane and crossing the endothelial barrier, disseminating cancer cells are thought to be forced to employ adhesion-dependent mechanisms combined with proteolytic ECM cleavage as transendothelial migration during in-and extravasation rather resembles migration in a discontinuous 3D matrix, similar to recirculating leukocytes which depend upon β1 and β2 integrins[93–95]. Accordingly, also for disseminating cancer cells integrins are the most prominent candidate to mediate attachment and facilitate proteolytic cleavage during intravasation[2,35,36]. However, our findings showing even increased CTC concentrations after integrin interference strongly contradict these assumptions but rather suggest alternative mechanisms to support transendothelial migration and crossing of the basement membrane. Essentially, both, the endothelial layer and space between individual endothelial cells and small capillaries which cause tumor cells to arrest, constitute a confined space comparable to the preexisting tissue tracks[1,3], which would allow employment of above-mentioned adhesion-independent migration mechanisms. Alternative, integrin-independent adhesion mechanisms which might facilitate dissemination include cell-cell adhesion-mediated interactions between cancer and stromal cells, such as N-cadherin- or selectin-based junctions that were shown to develop between cancer and endothelial cells or fibroblasts[96–99]. Although not shown yet experimentally for the process of intravasation but only as invasion-promoting mechanism, essentially also cancer-associated fibroblasts might contribute to basement membrane cleavage and blood vessel entry of cancer cells lacking integrin expression[100]. Furthermore, adhesion receptors of the discoidin domain receptor (DDR) family of transmembrane tyrosine kinases or CD44 are able to mediate alternative ECM interactions[101–104], with DDR signaling also inducing MMP upregulation to facilitate matrix cleavage[103,104].

Given these varying environmental topographies along the metastatic cascade, including both tissue invasion and passage through vessel walls, differential prerequisites for adhesion-dependent and independent migration in *in vivo*-inspired re-design of *in vitro* models used to probe defined aspects of metastatic cell migration, need to be considered. Using side-by-side analyses, we here modeled mechanisms observed *in vivo* by adjusting the randomly polymerized 3D collagen matrix towards an interface-based model which provides a confined, channel-like structure and consequently enabled *in-vivo*-like migration after stringent interference with integrin functions. Our combined *in vitro* and *in vivo* data thus indicate that all key steps of the metastatic cascade enable low integrin-based adhesion requirements to be efficiently accomplished.

Beyond fully unperturbed migration, lowering integrin availability in sarcoma and melanoma cells further induces plasticity of migration, switching from exclusively collective to collective and single-cell invasion with decreased cellular elongation after integrin interference. Known mechanisms of migrational plasticity include epithelial to mesenchymal or collective-amoeboid transition (EMT and CAT), both mainly described for epithelial models[105–108]. EMT is a molecular process resulting in down-regulation of cell-cell adhesion molecules with subsequent release of single cells[106,107]. During CAT, additional weakening or loss of cell-matrix interactions results in transition towards amoeboid crawling[105,109]. For mesenchymal cell types thus far matrix density has been identified as major regulator of migration plasticity, with loose matrix conditions favoring single-cell migration whereas confinement promotes a switch towards collective migration (chapter 3). Integrin-availability, as identified here, confirms a role for integrins in controlling migrational plasticity in mesenchymal cell types by directly or indirectly controlling cell adhesion. As consequence of integrin interference increased detachment of multicellular clusters and single cells is promoted *in vitro*[33] and shown here *in vivo*. Mechanistically, thus far no direct contribution of integrins to cell-cell junctions has been shown, however, several indirect mechanisms have been described. Via intercellular deposits of ECM components such as fibronection or laminin and integrin-mediated attachment to these matrix fibers, cells become indirectly linked to each other [110–112]. Furthermore, by undergoing so-called “adhesive crosstalk” with cadherins, integrins regulate cell-cell adhesion, whereby integrin-derived signals upregulate cadherins and subsequently (re)enforce cadherin-based cell-cell junctions[113–115]. Accordingly, similar to EMT, integrin interference might downregulate cadherins, destabilize cadherin-based junctions and stimulate a switch from collective to individual cell migration. By reducing cell-matrix adhesion and limiting cell spreading, reduced integrin availability then further promotes a rounded cell shape and amoeboid migration modes similar to CAT. Thus, through altering cell-cell and cell-matrix adhesion strength, lowering integrin levels releases tumor cells from multicellular units which constitutes a functionally critical plasticity step of migration in mesenchymal tumor cells *in vivo*.

Apart from integrin-independent migration, integrin interference initially did not affect survival of disseminating cells, whereas the tumor core and metastatic lesions instantly suffered from a survival deficit, which was consistent between both tumor types and across individual lesions. On the one hand these results confirm a critical function of integrins in cancer cell growth, however, initial anoikis resistance in the invasion zone suggests additional mechanisms which sustain survival despite integrin deficit. In contrast to the tumor core, which resembles a spheroid-like structure of densely packed tumor cells and blood vessels, hardly interspersed by ECM components[52], disseminating cancer cells reside in a ligand-rich environment containing various ECM components and numerous stromal cell-types, including fibroblasts, endothelial cells, myofibers, nerve cells and macrophages[6]. Either directly, through cadherin-based cell-cell junctions between stromal and cancer cells, or indirectly, via secretion of growth factors binding to receptor systems present on cancer cells, these microenvironmental components are able to activate pro-survival and anti-apoptotic pathways, including PI3K-Akt and MAPK signaling, similar to integrins, thereby promoting anoikis resistance[96,116–120]. Likewise, alternative cell-matrix adhesion systems such as DDRs induce downstream signaling events including PI3K-Akt and MAPK and thus might contribute to cell growth and survival[104]. Beyond these microenvironmental factors, cadherin-based homotypic cell-cell junctions between cancer cells themselves during collective migration display an important source to stimulate survival[96,117]. Upon integrin-interference, loss of integrin-based cadherin upregulation and release of single cells, former junction-mediated cell survival might be compensated by release of cytoplasmic adhesion adaptor proteins including beta-catenin and p120 catenin[121], which independently of cell junctions have been implicated in anoikis inhibition[122–125]. Thus, while infiltrating tissue, tumor cells may acquire largely integrin-independent survival strategies, mediated by both, external, environmental factors and cell-intrinsic mechanisms. It further suggests that, in case of abundant stroma- or cell-cell junction-derived survival stimuli, tumor lesions or sub-regions may not generally depend upon integrin-mediated survival stimuli, which becomes supported by heterogeneous patterns of integrin expression in tumor samples[126–128].

Overall our data show that a low integrin status agrees with efficient adhesion-independent invasion, increased migration plasticity and microenvironmentally-induced anoikis evasion, altogether promoting dissemination and resulting relative to tumor size in increased metastasis formation, however with a survival deficit of metastatic lesions as rate-limiting step. Growth and survival functions of integrins might stimulate rapid outgrowth of primary and metastatic lesions but become dispensable once tumor cells disseminate. Despite instant regression of the primary tumor and delayed regression of the invasion zone metastatic dissemination was not abrogated, ending up with metastatic disease but lacking primary tumor. Transferred to clinical observations, cancer of unknown primary site (CUP) is a common phenomenon observed in 3-5% of advanced cancers[129]. The etiology of CUPs may be diverse, thus investigation of mechanisms causing the primary lesion to spontaneously regress will be required and should include analysis of the integrin status.

Likewise, analysis of CTCs is currently becoming a valuable prognostic tool in the clinics[130], but thus far integrin expression in CTCs has been hardly investigated and does not show concordant correlations between integrin status of CTCs and metastasis outcome yet[131,132]. In our experiments, increased dissemination capacity after integrin downregulation became evident by both, increased relative CTC counts and enhanced single-cell metastasis relative to the tumor size. To reliably characterize correlations between integrin status and efficiency of metastatic seeding, similar parameters should be included in studies analyzing the integrin status of patient-derived CTCs in various cancer types, rather than focusing only on the sole presence of CTCs and clinically relevant, macroscopic, metastatic lesions. Eventually, extensive CTC profiling will help to reveal precise integrin-dependent and independent mechanisms that mediate metastatic dissemination and in particular transendothelial migration and survival in the blood stream.

Despite increased relative CTC concentrations after integrin interference, for both the sarcoma and melanoma model we detected single-cell and clustered CTCs of which proportions were remarkably not affected by the enhanced migration plasticity and cellular individualization observed upon integrin interference. Although not determined here which invasion mode and CTC type mainly contributed to metastasis formation, recent findings suggest collective invasion and multicellular CTCs to be more efficient in seeding metastatic lesions[133,134]. Therefore we assume that also in our models, the collective fraction majorly contributes to dissemination beyond intravasation, however experimental validation using experimental models as described is pending.

In summary, future preclinical studies on mechanisms of metastatic progression should analyze the entire metastatic cascade, rather than focusing on sub-stages like invasion, CTCs or metastatic lesions, including also single-cell analyses. To gain clinical insight into the status of integrin expression during metastasis formation, clinical studies should analyze integrin expression in tumor sub-regions and CTCs to identify potential niches and steps to metastasis with low integrin or integrin-ligand availability. Therapeutic approaches including blockade of integrin function should be seen with caution as it might have fatal outcome in patients, inducing cell release from the regressing local site and eventually macroscopic metastasis upon completion of integrin-targeted therapy. Instead, as delineated in Chapter 5 of this thesis, such mono-therapy approaches should be combined with a second lethal component to decrease the apoptosis threshold in integrin-low subsets and overcome initial anoikis resistance.

Acknowledgments

This work was supported by NWO-Vici (918.11.626), the European Research Council (617430-DEEPINSIGHT), and the Cancer Genomics Center (CGC.nl) to PF. Work of AH was supported by the PhD fellowship program of the Radboudumc, Nijmegen, The Netherlands.

We gratefully acknowledge Esther Wagena, Bettina Weigelin and Steve Alexander for expert technical assistance and logistic support and Simon Goodman, Joost te Riet and Bernhard Nieswandt for providing critical antibodies.

Supplementary Materials and Methods

Flow cytometry

The surface expression of adhesion molecules on HT-1080 and MV3 wild-type, vector control (p-puro or p-puro/p-neo) and stable knockdown (β1/β3RNAi) cells were obtained using cells from 3D matrix conditions after 24h-culture in 3D collagen lattices. Suspended cells were obtained by digestion with collagenase I (Sigma Aldrich, 1000 U/mL, 30 min, 37°C), pelleted and stained for 30 min on ice with the following monoclonal antibodies or isotypic control antibody: mouse anti-α1 integrin (clone TS2/7, Abcam), mouse anti-α2 (CD49b, clone AK-7), mouse anti-α3 integrin (CD49c, clone C3II.1, both BD Biosciences), mouse anti-α5 integrin (clone SAM-1, Millipore), rat anti-α6 integrin (CD49f, clone GoH3, BD Biosciences), mouse anti-αV (CD51, clone AMF7, Beckman Coulter), mouse anti-β1 (CD29, clone 4B4), mouse anti-β2 (CD18, clone 7E4), mouse anti-β3 integrin (CD61, clone SZ21, all Beckman Coulter), rat anti-β4 (CD104, clone 439-9B, BD Biosciences), mouse anti-β5 integrin (clone KN52, eBioscience), mouse anti-β6 (clone 437211, R&D), rat anti-β7 integrin (clone FIB504, BD Biosciences), mouse anti-β8 integrin (clone 416922, R&D); isotypic mouse IgG1κ (clone MOPC-21) and IgG2bκ (clone 27-35), rat IgG2aκ (clone R35-95) and IgG2bκ (clone A95-1) (all BD Biosciences). When primary antibody was unconjugated, secondary mouse IgG (H+L) antibodies conjugated to Alexa Fluor 488 (Invitrogen) were used for detection. Viability of cells was determined using propidium iodide exclusion.

To measure efficiency of integrin-blocking antibodies anti-β1 integrin 4B4 and anti-αV integrin 17E6, adherent HT-1080 and MV3 wild-type were cultured in the presence of either mouse IgG1κ isotype (6, 10 and 20 µg/mL) or 4B4/17E6 (2x 3, 5 and 10µg/mL) for ~18h. Prior to flow-cytometry measurements, cells were detached with 1mM EDTA (Thermo Fisher Scientific) and resuspended in culture medium supplemented with either 4B4/17E6 or isotype followed by incubation at 37°C for ~5h to compensate for potential loss of integrin blocking upon EDTA-mediated cell-detachment. Residual β1 and β3 integrin epitopes were subsequently stained using FITC-conjugated mouse anti-β1 mAb clone 4B4-FITC (Beckman Coulter, 6603109, 10 µg/mL) and rat anti-β3 integrin (kindly provided by Bernhard Nieswandt, Department of Experimental Biomedicine – Vascular Medicins, Rudolf Virchow Center Würzburg, Germany, 10 µg/mL) in combination with goat-anti-rat Alexa Fluor 647 (Invitrogen, 10 µg/mL). For isotype staining either mouse IgG1 negative control (Neormarker, NC-748-PABX, 10µg/mL) combined with goat-anti-rat Alexa Fluor 488 (Invitrogen, 10 µg/mL) or rat IgG (Thermo Fisher Scientifc, 02-9602, 10 µg/mL) were used. Cells were kept on ice during the staining procedure with 30 min incubation time each for primary and secondary antibodies. Viability of cells was determined using propidium iodide exclusion.

RNA isolation, cDNA generation and quantitative real-time PCR (qPCR)

RNA isolation from dual color HT-1080 and MV3 EV and β1/β3 integrin RNAi cells was performed using the RNeasy Miro kit (Qiagen) following the protocol “Purification of total RNA from animal and human cells (version 12/2007)”. Per cell line 250.000 cells were lysed using RLT buffer supplemented with β-mercaptoethanol and subsequently homogenized using a blunt 20G needle and syringe. DNase I digested RNA was eluted in a volume of 14 µL nuclease-free water. To extract RNA from metastatic lesions in the lung, samples frozen in O.C.T. compound were carefully thawed on ice in cold PBS. Tissue pieces containing fluorescent lesions were identified through fluorescence stereomicroscopy and then submerged in RNA*later* stabilization reagent (Qiagen). Prior to RNA isolation, RNA stabilization reagent was removed by squeezing tissue pieces between sterile filter paper (Whatman) followed by mincing them into smaller pieces which were put into a 2 cm^3 mortar. After adding 1 mL Trizol (Merck Millipore), tissue was homogenized with a pestle till no tissue pieces were left. The homogenate was transferred to a 1.5 mL tube, incubated at RT for ~5 min and then stored at -80°C for ~7 h to increase RNA yield. After thawing, per sample 200 µL Chloroform (Merck Millipore) were added. For phase separation, Trizol and Chloroform were mixed by inverting reaction tubes and centrifuged at 12,000 g for 15 min at 4°C after incubating samples at RT for 2-3 min. For RNA precipitation ~400 mL aqueous phase were transferred to 500 µL Isopropanol (Merck-Millipore), mixed by inverting reaction tubes, incubated at RT for 10 min and then at -80°C for 1 h. Thawed samples were centrifuged at maximum speed for 30 min at 4°C. Subsequently, RNA pellets were washed twice with 500 µL 80% Ethanol followed by centrifugation at maximum speed for 15 min at 4°C and air-drying the RNA pellet after the final washing step. For DNAse I treatment, RNA pellets were resuspended in 80 µL DNAse I solution and transferred onto a RNeasy spin column (Qiagen), which was incubated at RT for 15 min. The following steps were performed as described in the RNeasy Micro Handbook (version 12/2007) protocol ‘Purification of total RNA from animal and human tissues’ steps 9-12. After placing the spin column into a new 1.5 ml collection tube, RNA was eluted using 10 µL DNase/RNase-free water. Following application of nuclease-free water onto the filter of the column, collection tubes containing the column were incubated at 37°C for 1 min. After 1 min centrifugation at full speed for elution, RNA samples were immediately put on ice. Following the same procedure, RNA elution from the same spin column was repeated using a new collection tube, yielding in total ~16 µL RNA per sample.

After RNA concentration measurements (NanoDrop 1000, Thermo Fisher Scientific), for cell line samples 1 µg RNA and for metastasis samples 10µg RNA were used to generate cDNA using the iScript cDNA synthesis kit (BioRad), including per sample one reaction without reverse transcriptase. To check cDNA purity, per reaction 1 µL cDNA was added to a PCR amplifying human beta actin (forward (fw) primer GCGGGAAATCGTGCGTGACATT, reverse (rev) primer GATGGAGTTBGAAGGTAGTTTCGTG) resulting in specific bands (230 bp) for cDNA samples. Absence of any PCR product for reactions without reverse transcriptase indicated that RNA and cDNA were free of genomic DNA contamination.

qPCR was performed using iQ SYBR green Supermix (BioRad) and the following primer pairs: human specific β1 (fw: GAAGGGTTGCCCTCCAGA, rev: GCTTGAGCTTCTCTGCTGTT) and β3 integrin (fw: CCGTGACGAGATTGAGTCA, rev: AGGATGGACTTTCCACTAGAA) (specific amplification of only human β1 and β3 integrin was experimentally validated), GFP (fw: AAGCTGACCCTGAAGTTCATCTGC, rev: CTTGTAGTTGCCGTCGTCCTTGAA), human GAPDH (fw: TGATGACATCAAGAAGGTGGTGAA, rev: TCCTTGGAGGCCATGTGGGCCAT (only for cell line samples)) and human beta actin. For cell line samples, 1 μL cDNA was used for per reaction, whereas for metastasis samples 10 μL cDNA were added to pick up signal derived from human tumor cell metastatic lesions in a mouse tissue background. qPCR reactions were ran in a CFX96 Touch Real-Time PCR detection system (BioRad) with 40 cycles for cell line samples and 80 cycles for metastasis samples including generation of melt curves. For cell line derived cDNA, $2^{\Delta\Delta Ct}$ for β1 and β3 integrin normalized to GAPDH signal was calculated, while for metastasis samples GFP signal was used to normalize specifically for tumor-cell derived RNA. Overall, amounts of human tumor-cell derived RNA in metastasis samples were too low to measure β3 integrin expression, though as β1 and β3 integrin were targeted simultaneously by one vector, persistence of β1 integrin in metastatic lesion indirectly validates stability of β3 integrin knockdown.

Protein gelelectrophoresis and Western Blot

β1 integrin knockdown efficiency in dual-color HT-1080 and MV3 cells was detected by protein gel electrophoresis and Western blot analysis using complete cell lysates generated in TENT lysisbuffer[135]. β1 integrin was detected with rabbit anti-β1 integrin (Millipore, #04-1109 or AB4952) and GAPDH, as loading control, with rabbit anti-GAPDH (Sigma, #G9545). All protein samples were separated under reducing conditions on 8% SDS-PAGE and transferred onto a PVDF-FL (Immobilon) membrane, blocked with 5% milk– Tris-buffered saline 0.5% Tween (TBST, 1h, RT) incubated with primary antibody (~18 h, 4°C), washed with TBST, and incubated with fluorescence-labeled goat anti-rabbit antibody (Li-Cor, 1 h, RT). Protein bands were detected using an Odyssey CLX imaging system (Li-Cor).

Analysis of mitotic and apoptotic frequencies

To control for functional consequences after integrin knockdown *in vitro*, mitotic and apoptotic frequencies were determined from the H2B-EGFP label of dual-color HT-1080 cells incorporated in 3D collagen lattices for 48 h. Snapshots of cells (brightfield and FITC) were taken using a Zeiss Axiophot2 Fluorescence microscope with Axiocam MRm CCD camera (20×/0.30 NA air objective). Subsequently cell numbers and fractions of mitotic and apoptotic cells were determined manually using the "multi-point selection" tool in FIJI[55].

Immunohistological staining of tumor samples

Phospho-FAK signals were detected in tumors 5 days post-implantation into the imaging window. Tumor-containing tissue samples were cryopreserved as described above and processed as 10 µm thick cryosections mounted on superfrost plus object slides. After drying for ~18 h tissue slices were stored (-80°C) and prior to staining fixed (2% parafomaldehyde diluted in PHEM buffer, 15 min, RT), rinsed with phosphate-buffered saline (PBS) and incubated in PBS containing 0.1% Triton X-100 (Sigma Aldrich) for permeabilization (20 min, RT). To minimize background, samples were incubated in PBS supplemented with 5% NGS and 0.1% cold water fish skin gelatin (Sigma Aldrich; 30 min, RT), followed by staining with rabbit anti-phospho-Fak (pTyr397, Abcam, ab4803, 1:50) primary antibody, diluted in PBS supplemented with 2% NGS and 0.1% CWFG. Tissue slices were incubated with primary antibody solution (1 h, RT followed by ~18 h, 4°C), washed 8x 15 min (PBS), incubated with goat anti-rabbit IgG (H+L) Alexa Fluor 647 (Invitrogen, A-21245, 4 µg/mL) and DAPI (1 µg/mL), both diluted in PBS/NGS (2%)/CWFG (0.1%), washed (4x 15min, PBS) and mounted in Fluoromount G.

For the visualization of cell-cell junctions via ALCAM staining, untreated control tumor-bearing mice carrying the skin window were sacrificed on day 5 (HT-1080) or day 8 (MV3) after tumor implantation. Tumor-containing dorsal skin samples were cryopreserved with marked orientation of invasion strands and having the invasion status documented by intravital epifluorescence microscopy. Frozen tissue samples were cut into 50 µm thick cryosections (HM500OM Cryostat Microtome, Microm) which were immediately fixed in neutral buffered formalin (4%, formulation according to Lillie), incubated for ~18 h at room temperature and stored in phosphate buffer (0.1M, pH 7.4, 4°C). For staining, free aldehyde groups and unspecific epitopes were blocked using 0.15% glycine in Tris-buffered saline (30 min, RT), followed by incubation with TBS supplemented with 1% bovine serum albumin (Sigma Aldrich) and 15% normal goat serum (GIBCO Life Technologies, 30-60min, RT). After washing (TBS), endogenous mouse IgG in the tissue was blocked with unlabeled anti-mouse IgG Fab' fragments (Jackson ImmunoResearch, 15-007-003, ~18 h, 4°C) followed by washing (TBS). Mouse anti-ALCAM mAb (AZN-L50; IgG2A; kindly provided by Joost te Riet, Department of Tumor Immunology, Radboudumc Nijmegen, The Netherlands)[60] was biotinylated using biotin-SP (long-spacer) conjugated anti-mouse IgG Fab fragment (Jackson ImmunoResearch, 115-067-003, 1:2, 20 min, RT), followed by incubation in mouse serum (Biowest, 10 µl/1 µg Fab' biotin, 10 min, RT). Anti-ALCAM/biotin-Fab' complexes were diluted (1:15) in TBS/BSA (1%) and added to the tissue slices for incubation (~18 h, 4°C). After washing (TBS) tissue slices were overlaid with streptavidin-coupled Alexa 647 (Jackson ImmunoResearch, 016-600-084, 2 µg/mL) and DAPI (Roche, 1 µg/mL), in TBS/BSA (1%, 20 min, RT), washed (TBS) and mounted in Fluoromount G (Southern Biotech) on object slides for confocal microscopy.

Tissue samples stained for phosphor-Fak and ALCAM were analyzed by confocal microscopy (Olympus FV1000) as 3D stacks. Stainings of phosphor-FAK were scanned with a 40x / 0.80 NA water immersion objective and 3 µm step size to represent the whole 10 µm tissue slice using identical instrument settings for control and integrin interference conditions. ALCAM stainings were recorded using either a 20x / 0.50 NA water or 60x / 1.35 NA oil immersion objective with 3 or 1 µm step size respectively.

Visualization of collagen-collagen interface migration

To visualize the collagen-collagen interface by scanning electron microscopy (SEM), cell-free samples were fixed for 1 h at RT with 2% glutaraldehyde (Merck) in 0.1 M cacodylate buffer, followed by two washes in the same buffer. 1% osmium tetroxide (EMS) in 0.1 M cacodylate buffer was used as a secondary fixative with incubation for 1 h at RT. Cross sections of collagen-collagen interface gels were made by manually slicing the gel with a scalpel. Samples were then processed for SEM by dehydration through a graded series of ethanol followed by critical point drying using CO_2 and then sputtered with gold and imaged by SEM (JSM-6340F; JEOL).

To image tumor cell invasion from the spheroid along the collagen-collagen interface, cells were allowed to migrate for 48 h followed by fixation with 4% PFA and phalloidin staining as described above. Prior to embedding, cross sections of collagen samples were generated manually by an orthogonal cut through the collagen. Cross sections were imaged by confocal microscopy as described above, using a 20×/0.5 NA water immersion objective with 4µm z-steps, including record of the collagen reflectance signal.

Spiked CTC analysis

To determine the nuclear size cutoff to distinguish blood cells from CTCs, blood obtained from mice not having received any tumor cell injection was mixed with cell suspension of HT-1080 and MV3 dual color cells (10-60 tumor cells per 100-200 µL blood). Blood-cell solution was processed as above to capture both, blood and tumor cells on a microsieve followed by DAPI staining and imaging. Nuclear areas were measured using FIJI[55].

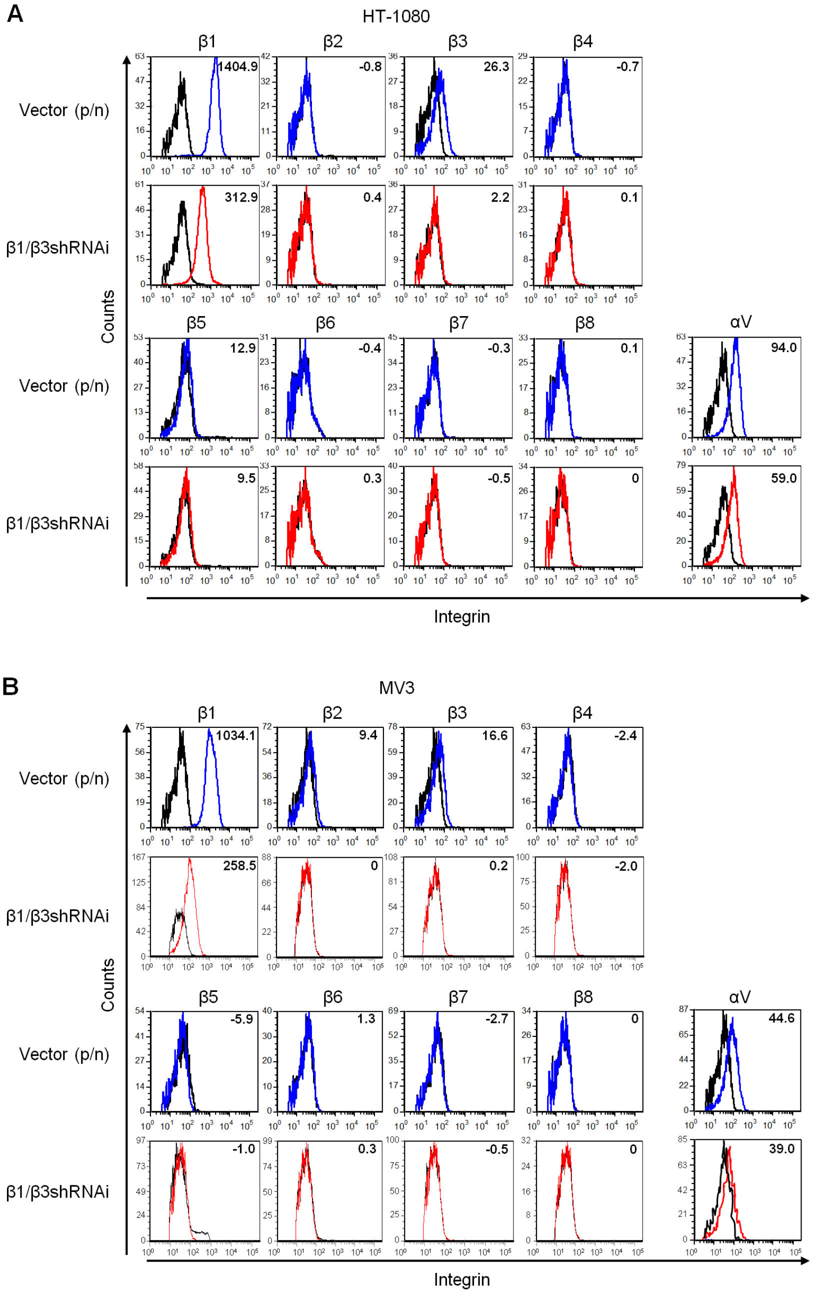

Supplementary Figure 1. Integrin expression profiles in HT-1080 and MV3 cells before and after β1/β3 integrin knockdown.
(A,B) Surface expression pattern of integrin β chains and αV integrin on HT-1080 **(A)** and MV3 **(B)** control cells (blue line) and after β1/β3 integrin shRNAi (red line) determined by flow cytometry. Black line, isotype control. Values, mean fluorescence (minus isotype values).

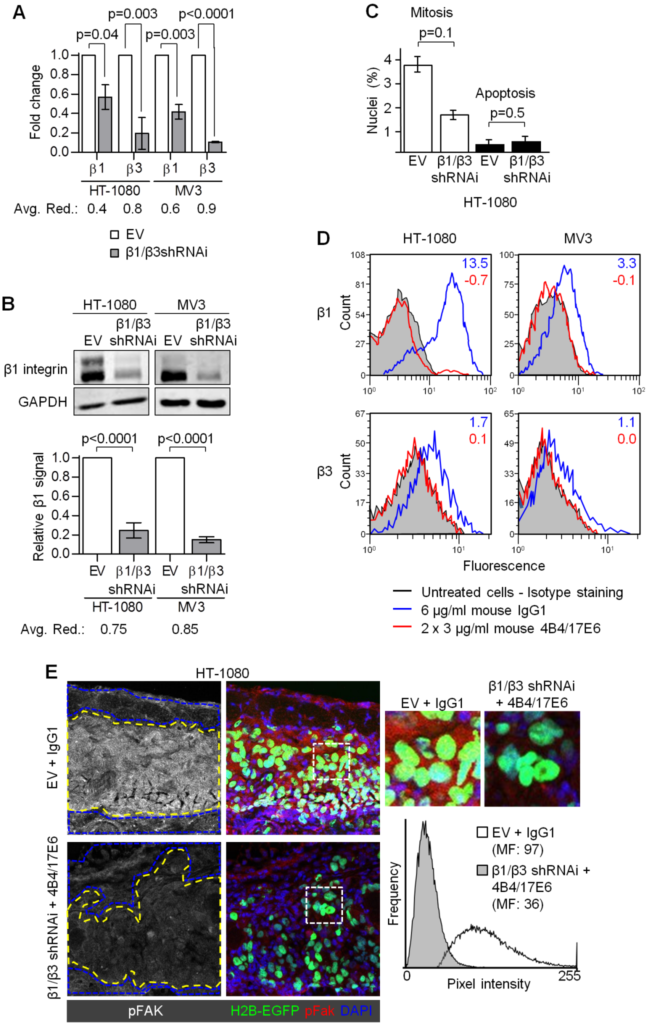

Supplementary Figure 2. RNAi and antibody-based integrin targeting in HT-1080 and MV3 cells. **A)** Relative β1 and β3 integrin expression in control cells and after β1/β3 integrin interference determined from cDNA by qPCR, displayed as mean ± SD (n=2-3). Statistics, unpaired t-test. **B)** β1 integrin protein levels in control cells and after β1/β3 integrin interference determined by whole-cell lysis and Western Blot. β1 integrin signal was normalized to GAPDH signal to calculate relative β1 integrin levels after β1 and β3 integrin RNAi displayed as mean ± SD (n=5 (HT-1080) or 7 (MV3)). Statistics, unpaired t-test. **C)** Mitotic and apoptotic frequencies of HT-1080 β1/β3 integrin RNAi cells compared to vector control cells after incorporated in 3D collagen lattices for 48h displayed as mean ± SD (3 visual fields of 500 cells were analyzed). Statistics, Mann Whitney test. **D)** Reduction of free, non-blocked β1 and β3 integrin adhesion epitopes after incubation with integrin-blocking antibodies 4B4 (unconjugated) and 17E6 or mouse isotype, detected by FITC-conjugated mAb 4B4 and rat anti-β3 integrin using flow cytometry. Blue line, integrin levels after isotype treatment. Red line, integrin levels after 4B4/17E6 treatment. Grey curve, isotype staining. Values, mean fluorescence (minus isotype values). **E)** Reduced phosphoFAK signal in HT-1080 β1/β3RNAi compared to HT-1080 control xenograft sections. Histograms show the mean pixel fluorescence (MF) intensity of AlexaFluor647-phosphoFAK calculated from tumor areas only (yellow dotted lines) normalized to stroma-derived signal (blue dotted lines). Dashed rectangle, region of detail image.

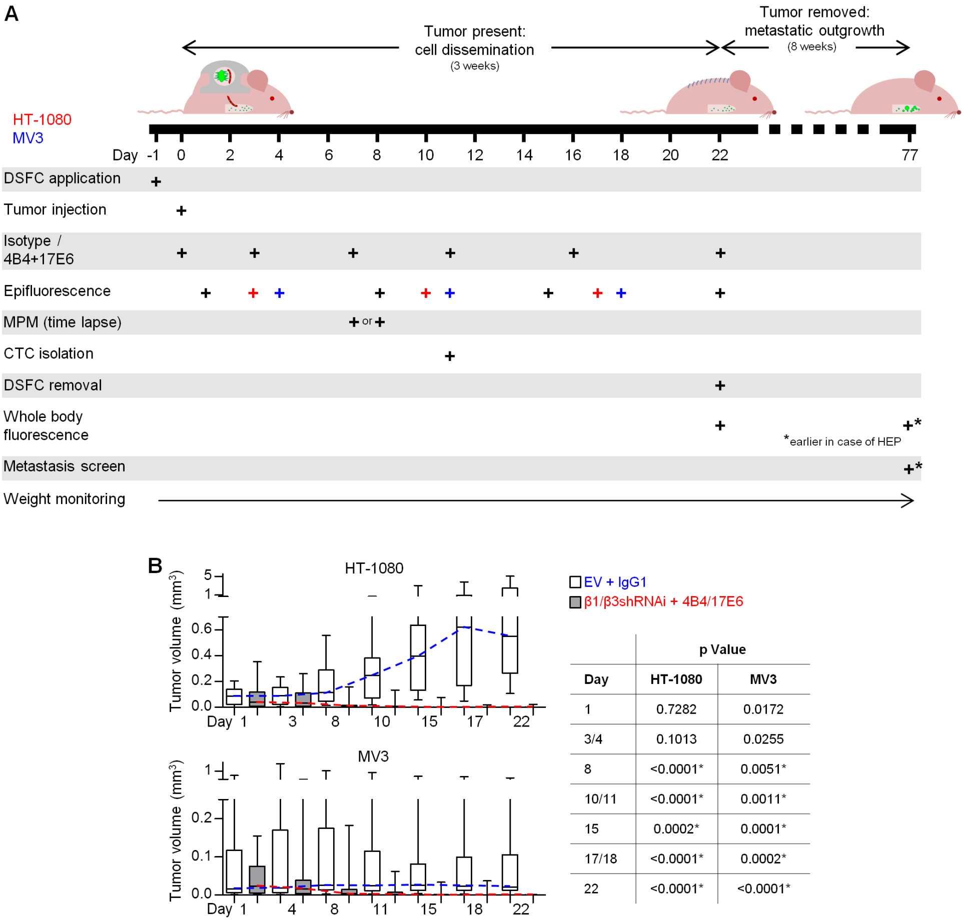

	p Value	
Day	HT-1080	MV3
1	0.7282	0.0172
3/4	0.1013	0.0255
8	<0.0001*	0.0051*
10/11	<0.0001*	0.0011*
15	0.0002*	0.0001*
17/18	<0.0001*	0.0002*
22	<0.0001*	<0.0001*

Supplementary Figure 3. Xenograft models and experimental approach to analyze role of integrins in the metastatic cascade.
A) Experimental set-up: Cancer cells were given three weeks to initiate dissemination and enter the vasculature, then the imaging window including the tumor lesion was removed and mice were kept for a maximum of 8 more weeks till metastasis development was analyzed. To check for the presence of circulating tumor cells (CTCs), at least 6 mice were subjected to total blood sampling after ~2 weeks of tumor development. DSFC, dorsal skin-fold chamber containing imaging window. HEP, humane end point. **B)** Tumor development of HT-1080 and MV3 control and β1/β3 integrin RNAi xenografts displayed as median, 25th/75th (box) and minimum/maximum (whiskers), corresponding to Fig. 1B. Blue and red dotted line, tumor growth curves based on median values. Statistics, unpaired t-test.

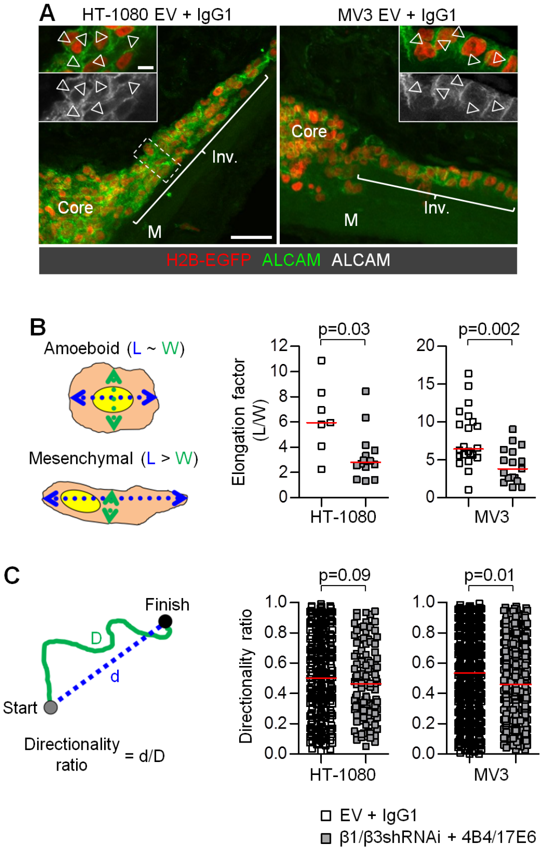

Supplementary Figure 4. Validation of cell-cell junctions in collective invasion and effects of β1/αVβ3 integrin targeting on invasion *in vivo*.

A) Distribution of ALCAM along cell-cell junctions (arrowheads) in invading tumor strands (Inv.) of HT-1080 and MV3 control cells. Maximum intensity projections (overview) and individual sections (insets) from confocal 3D stacks. Background fluorescence originates from myofibers (M). Dashed rectangle, region of detail image. Scale bars, 50 µm (overview) and 10 µm (insets). **(B,C)** Median cellular elongation **(B)** and median directionality **(C)** of invading HT-1080 and MV3 control and β1/β3 integrin shRNAi cells. Cell shape was determined as ratio of cellular width and length. To analyze directionality of invasion, ratio of shortest and actual distance was identified. Statistics, Mann-Whitney test.

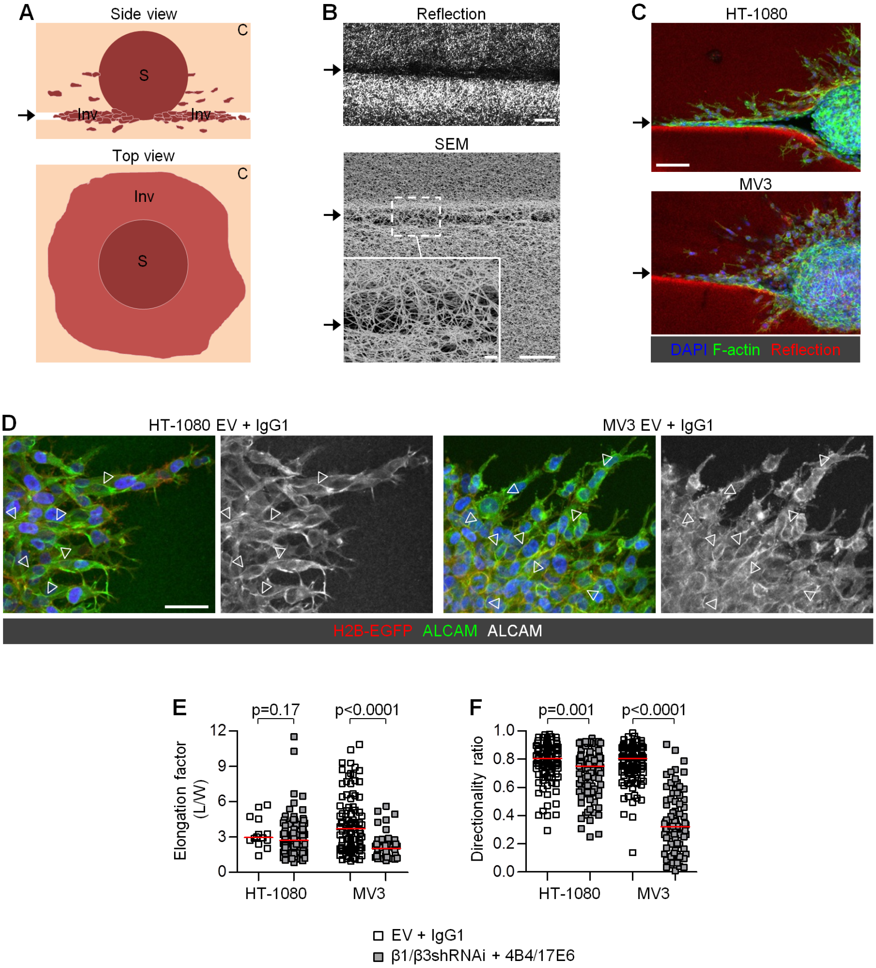

Supplementary Figure 5. Characterization of *in vitro* interface migration and effects of β1/αVβ3 integrin targeting.
A) Principle of interface-guided invasion (Inv.) between two high-density collagen (C) layers. Beyond migration along the interface (arrow) as track of least resistance, proteolytically-active cells will also, though to a lesser extent, migrate directly through the collagen matrix. S, spheroid. **B)** Visualization of the collagen-collagen interface (arrow) in cross-sections of the collagen-collagen layer through confocal reflection microscopy (top) or SEM (bottom). Zoomed SEM image shows single collagen fibers interspersing the interface. Scale bars, 10 µm (reflection and SEM overview), 1 µm zoom SEM. **C)** HT-1080 and MV3 dual-color control cells primarily migrating along the collagen-collagen interface (arrow) accompanied by scattered single-cell migration inside the collagen matrix, displayed as maximum intensity projection from confocal 3D stacks. Collagen matrix visualized by reflection imaging. Scale bar, 100 µm. **D)** Distribution of ALCAM along cell-cell junctions (arrowheads) in collective 2D sheets and strands of HT-1080 and MV3 control cells migrating along the collagen-collagen interface, displayed as maximum intensity projection from confocal 3D stacks. Scale bar, 50 µm. **(E,F)** Median cellular elongation **(E)** and median directionality **(F)** of HT-1080 and MV3 control and β1/β3 integrin RNAi cells migrating in the collagen-collagen interface model. See also Supplementary Fig. 4 B,C. Statistics, Mann-Whitney test.

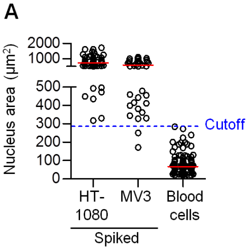

	Spiked cell type		
	HT-1080	MV3	Blood cells
Minimum	317.7	172.4	21.12
25% Percentile	552.6	414.9	45.63
Median	731.5	580.2	67.18
75% Percentile	1057	863.6	99.92
Maximum	1720	1110	283.9
5% Percentile	420.3	246.2	25.22
95% Percentile	1619	1051	201.5

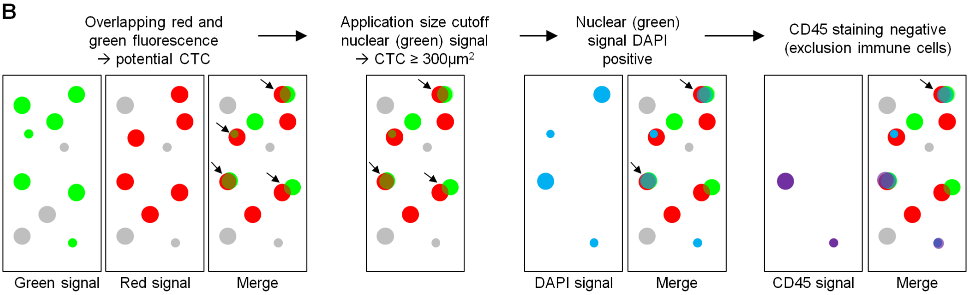

Supplementary Figure 6. Capture and detection of CTCs.
A) Nuclear size measurements of dual-color HT-1080 and MV3 control cells collected together with mouse blood cells on a microsieve. A cutoff of 300 μm² was determined to distinguish human tumor cells and mouse blood cells Red line, median. **B)** Work-flow for identification of dual-color labeled CTCs in mouse blood. CTCs were identified based on their fluorescent markers (H2B-EGFP (green signal) and DsRed2 (red signal)) combined with a nuclear area ≥300μm², positive DAPI and negative CD45 staining. Arrows point towards potential CTCs matching criteria of the analysis work-flow.

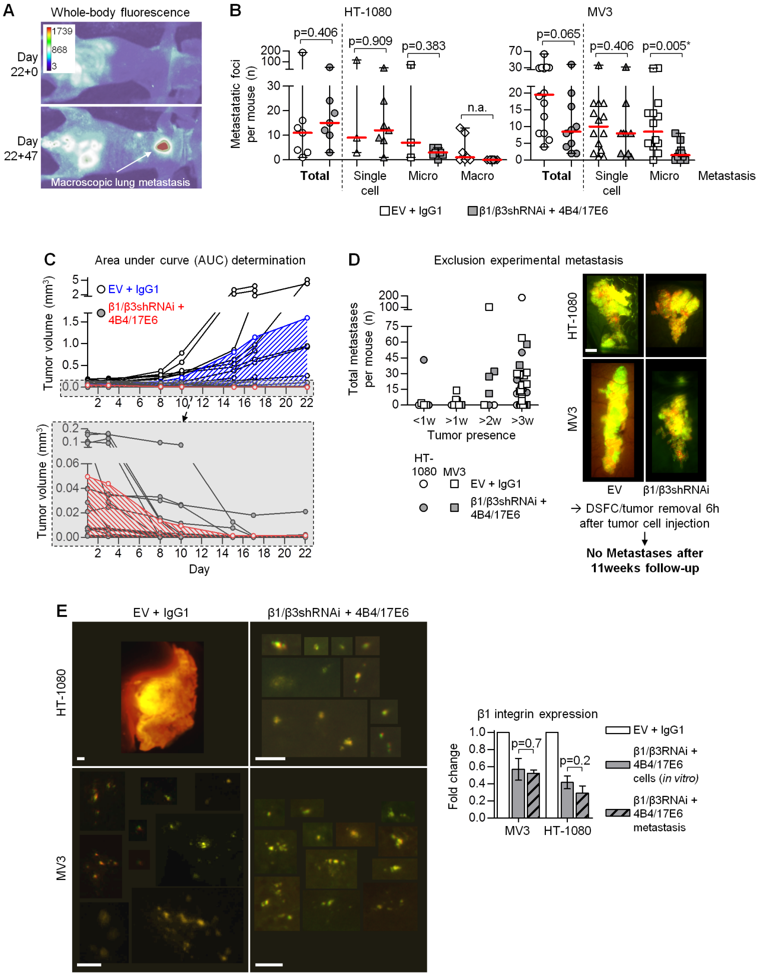

Supplementary Figure 7. Quantification and analysis of metastatic lesions. **A)** Development of fluorescent lung macrometastasis (arrow) visualized by whole-body fluorescence imaging. Day 22+0 corresponds with removal of the imaging window and tumor lesion. Mouse suffered from clinical symptoms and was terminated before reaching end of the 8-week follow-up phase. Calibration bar, minimum and maximum grey value. **B)** Median amount of lung metastases detected per category and mouse for HT-1080 and MV3 control and β1/β3 integrin shRNAi xenografts. Statistics, Mann-Whitney test. *, significant p value after Bonferroni correction (Bonferroni-corrected threshold was 0.017). **C)** Growth curves of individual HT-1080 control and β1/β3 RNAi tumors to exemplify determination of the area under the curve (AUC), which was needed to correct numbers of metastatic lesions for tumor size. Dashed areas represent average AUC for HT-1080 xeongrafts of both conditions. **D)** Number of metastatic lesions detected per mouse approximately correlate with tumor presence which excludes experimentally-induced metastasis formation due to tumor cell injection (left panel). Additionally, in mice where tumors were removed 6 h after injection (right panel) no metastatic lesions were detected after 11 weeks (per group 3 mice were included). Scale bar, 100 µm. **E)** Maintenance of β1 RNAi in HT-1080 and MV3 metastases. Left panel: metastatic lesions isolated from one mouse lung of either the HT-1080 and MV3 control or β1/β3 integrin RNAi group to validate presence of β1 RNAi. Scale bars, 100 µm. Right panel: relative β1 integrin expression of β1/β3 integrin RNAi metastasis samples or *in vitro* cultured cells normalized to levels obtained for control metastases, analyzed from cDNA by qPCR and displayed as mean ± SD. Statistics, unpaired t-test.

References

1. Valastyan, S. & Weinberg, R. A. Tumor metastasis: Molecular insights and evolving paradigms. *Cell* **147,** 275–292 (2011).
2. Ganguly, K. K., Pal, S., Moulik, S. & Chatterjee, A. Integrins and metastasis. *Cell Adh. Migr.* **7,** 251–61 (2013).
3. Chambers, A. F., Groom, A. C. & MacDonald, I. C. Dissemination and growth of cancer cells in metastatic sites. *Nat. Rev. Cancer* **2,** 563–72 (2002).
4. Alizadeh, A. M., Shiri, S. & Farsinejad, S. Metastasis review: from bench to bedside. *Tumor Biol.* **35,** 8483–8523 (2014).
5. Pickup, M. W., Mouw, J. K. & Weaver, V. M. The extracellular matrix modulates the hallmarks of cancer. *EMBO Rep.* **15,** 1243–53 (2014).
6. Hui, L. & Chen, Y. Tumor microenvironment: Sanctuary of the devil. *Cancer Lett.* **368,** 7–13 (2015).
7. Humphries, J. D., Byron, A. & Humphries, M. J. Integrin ligands at a glance. *J. Cell Sci.* **119,** 3901–3903 (2006).
8. Hynes, R. O. & Naba, A. Overview of the matrisome--an inventory of extracellular matrix constituents and functions. *Cold Spring Harb. Perspect. Biol.* **4,** a004903 (2012).
9. Sun, Z., Guo, S. S. & Fässler, R. Integrin-mediated mechanotransduction. *J. Cell Biol.* **215,** 445–456 (2016).
10. Giancotti, F. G. & Ruoslahti, E. Integrin signaling. *Science (80-.).* **285,** 1028–1033 (1999).
11. Juliano, R. L. Signal transduction by cell adhesion receptors and the cytoskeleton: functions of integrins, cadherins, selectins, and immunoglobulin-superfamily members. *Annu. Rev. Pharmacol. Toxicol.* **42,** 283–323 (2002).
12. Desgrosellier, J. S. & Cheresh, D. A. Integrins in cancer: biological implications and therapeutic opportunities. *Nat. Rev. Cancer* **10,** 9–22 (2010).
13. Zegers, M. M. & Friedl, P. Rho GTPases in collective cell migration. *Small GTPases* **5,** e28997-1–10 (2014).
14. Seguin, L., Desgrosellier, J. S., Weis, S. M. & Cheresh, D. A. Integrins and cancer: regulators of cancer stemness, metastasis, and drug resistance. *Trends Cell Biol.* **25,** 234–240 (2015).
15. Paoli, P., Giannoni, E. & Chiarugi, P. Anoikis molecular pathways and its role in cancer progression. *Biochim. Biophys. Acta - Mol. Cell Res.* **1833,** 3481–3498 (2013).
16. Bendas, G. & Borsig, L. Cancer cell adhesion and metastasis: Selectins, integrins, and the inhibitory potential of heparins. *Int. J. Cell Biol.* **2012,** 676731 (2012).
17. Goodman, S. L. & Picard, M. Integrins as therapeutic targets. *Trends Pharmacol. Sci.* **33,** 405–412 (2012).
18. Albelda, S. M. *et al.* Integrin distribution in malignant melanoma: association of the beta 3 subunit with tumor progression. *Cancer Res.* **50,** 6757–64 (1990).
19. Hieken, T. J., Ronan, S. G., Farolan, M., Shilkaitis, A. L. & Das Gupta, T. K. Molecular prognostic markers in intermediate-thickness cutaneous malignant melanoma. *Cancer* **85,** 375–82 (1999).
20. Nip, J., Shibata, H., Loskutoff, D. J., Cheresh, D. A. & Brodt, P. Human melanoma cells derived from lymphatic metastases use integrin alpha v beta 3 to adhere to lymph node vitronectin. *J. Clin. Invest.* **90,** 1406–1413 (1992).
21. Danen, E. H. *et al.* Emergence of alpha 5 beta 1 fibronectin- and alpha v beta 3 vitronectin-receptor expression in melanocytic tumour progression. *Histopathology* **24,** 249–56 (1994).
22. Zutter, M. M., Santoro, S. A., Staatz, W. D. & Tsung, Y. L. Re-expression of the alpha 2 beta 1 integrin abrogates the malignant phenotype of breast carcinoma cells. *Proc. Natl. Acad. Sci. U. S. A.* **92,** 7411–5 (1995).

23. Avraamides, C. J., Garmy-Susini, B. & Varner, J. A. Integrins in angiogenesis and lymphangiogenesis. *Nat. Rev. Cancer* **8,** 604–617 (2008).

24. Brooks, P. C., Clark, R. A. & Cheresh, D. A. Requirement of vascular integrin alpha v beta 3 for angiogenesis. *Science* **264,** 569–71 (1994).

25. Meyer dos Santos, S. *et al.* The integrin antagonist, cilengitide, is a weak inhibitor of αIIbβ3 mediated platelet activation and inhibits platelet adhesion under flow. *Platelets* **26,** 59–66 (2015).

26. Zhu, C.-Q. *et al.* Integrin alpha 11 regulates IGF2 expression in fibroblasts to enhance tumorigenicity of human non-small-cell lung cancer cells. *Proc. Natl. Acad. Sci. U. S. A.* **104,** 11754–9 (2007).

27. Tesfamariam, B. Involvement of platelets in tumor cell metastasis. *Pharmacol. Ther.* **157,** 112–119 (2016).

28. Zhang, Y. & Wang, H. Integrin signalling and function in immune cells. *Immunology* **135,** 268–275 (2012).

29. Xiong, J., Balcioglu, H. E. & Danen, E. H. J. Integrin signaling in control of tumor growth and progression. *Int. J. Biochem. Cell Biol.* **45,** 1012–1015 (2013).

30. Ellison, T. S. *et al.* Suppression of β3-integrin in mice triggers a neuropilin-1-dependent change in focal adhesion remodelling that can be targeted to block pathological angiogenesis. *Dis. Model. Mech.* **8,** 1105–19 (2015).

31. Hood, J. D. & Cheresh, D. A. Role of integrins in cell invasion and migration. *Nat. Rev. Cancer* **2,** 91–100 (2002).

32. Maaser, K. *et al.* Functional hierarchy of simultaneously expressed adhesion receptors: integrin alpha2beta1 but not CD44 mediates MV3 melanoma cell migration and matrix reorganization within three-dimensional hyaluronan-containing collagen matrices. *Mol. Biol. Cell* **10,** 3067–79 (1999).

33. Hegerfeldt, Y., Tusch, M., Bröcker, E. B. & Friedl, P. Collective Cell Movement in Primary Melanoma Explants: Plasticity of Cell-Cell Interaction, Beta1-Integrin Function, and Migration Strategies. *Cancer Res.* **62,** 2125–2130 (2002).

34. Paluch, E. K., Aspalter, I. M. & Sixt, M. Focal Adhesion-Independent Cell Migration. *Annu. Rev. Cell Dev. Biol.* **32,** 469–490 (2016).

35. Bauer, K., Mierke, C. & Behrens, J. Expression profiling reveals genes associated with transendothelial migration of tumor cells: A functional role for αvβ3 integrin. *Int. J. Cancer* **121,** 1910–1918 (2007).

36. Baum, O. *et al.* Increased invasive potential and up-regulation of MMP-2 in MDA-MB-231 breast cancer cells expressing the beta3 integrin subunit. *Int. J. Oncol.* **30,** 325–32 (2007).

37. Felding-Habermann, B. *et al.* Integrin activation controls metastasis in human breast cancer. *Proc. Natl. Acad. Sci.* **98,** 1853–1858 (2001).

38. Li, J. & King, M. R. Adhesion receptors as therapeutic targets for circulating tumor cells. *Front. Oncol.* **2,** 79 (2012).

39. Stoletov, K. *et al.* Visualizing extravasation dynamics of metastatic tumor cells. *J. Cell Sci.* **123,** 2332–2341 (2010).

40. Chen, M. B., Lamar, J. M., Li, R., Hynes, R. O. & Kamm, R. D. Elucidation of the roles of tumor integrin β1 in the extravasation stage of the metastasis cascade. *Cancer Res.* **76,** 2513–2524 (2016).

41. Weber, M. R. *et al.* Activated tumor cell integrin alphaVbeta3 cooperates with platelets to promote extravasation and metastasis from the blood stream. *Thromb. Res.* **140,** S27–S36 (2016).

42. Liu, Y. & Cao, X. Characteristics and Significance of the Pre-metastatic Niche. *Cancer Cell* **30,** 668–681 (2016).

43. Alphonso, A. & Alahari, S. K. Stromal cells and integrins: conforming to the needs of the tumor microenvironment. *Neoplasia* **11,** 1264–71 (2009).

44. Ghajar, C. M. *et al.* The perivascular niche regulates breast tumour dormancy. *Nat. Cell Biol.* **15,** 807–17 (2013).

45. Rasheed, S., Nelson-Rees, W. A., Toth, E. M., Arnstein, P. & Gardner, M. B. Characterization of a newly derived human sarcoma cell line (HT-1080). *Cancer* **33,** 1027–33 (1974).

46. van Muijen, G. N. *et al.* Establishment and characterization of a human melanoma cell line (MV3) which is highly metastatic in nude mice. *Int. J. cancer.* **48,** 85–91 (1991).

47. Yamamoto, N. *et al.* Cellular dynamics visualized in live cells in vitro and in vivo by differential dual-color nuclear-cytoplasmic fluorescent-protein expression. *Cancer Res.* **64,** 4251–6 (2004).

48. Kissler, S. *et al.* In vivo RNA interference demonstrates a role for Nramp1 in modifying susceptibility to type 1 diabetes. *Nat. Genet.* **38,** 479–83 (2006).

49. Chapman, M. E., Hu, L., Plato, C. F. & Kohan, D. E. Bioimpedance spectroscopy for the estimation of body fluid volumes in mice. *Am. J. Physiol. Renal Physiol.* **299,** F280-3 (2010).

50. Vieira, P. & Rajewsky, K. The half-lives of serum immunoglobulins in adult mice. *Eur. J. Immunol.* **18,** 313–316 (1988).

51. Hodivala-Dilke, K. M. *et al.* Beta3-integrin-deficient mice are a model for Glanzmann thrombasthenia showing placental defects and reduced survival. *J. Clin. Invest.* **103,** 229–38 (1999).

52. Alexander, S., Koehl, G. E., Hirschberg, M., Geissler, E. K. & Friedl, P. Dynamic imaging of cancer growth and invasion: a modified skin-fold chamber model. *Histochem. Cell Biol.* **130,** 1147–54 (2008).

53. Andresen, V. *et al.* Infrared multiphoton microscopy: subcellular-resolved deep tissue imaging. *Curr. Opin. Biotechnol.* **20,** 54–62 (2009).

54. Weigelin, B. *et al.* Focusing and sustaining the antitumor CTL effector killer response by agonist anti-CD137 mAb. *Proc. Natl. Acad. Sci. U. S. A.* **112,** 7551–6 (2015).

55. Schindelin, J. *et al.* Fiji: an open-source platform for biological-image analysis. *Nat. Methods* **9,** 676–82 (2012).

56. Parslow, A., Cardona, A. & Bryson-Richardson, R. J. Sample Drift Correction Following 4D Confocal Time-lapse Imaging. *J. Vis. Exp.* **12,** 51086 (2014).

57. Meijering, E., Dzyubachyk, O. & Smal, I. Methods for Cell and Particle Tracking. *Methods Enzymol.* **504,** 183–200 (2012).

58. Hoff, J. Methods of blood collection in the mouse. *Lab Anim. (NY).* **29,** 47–53 (2000).

59. Del Duca, D., Werbowetski, T. & Del Maestro, R. F. Spheroid Preparation from Hanging Drops: Characterization of a Model of Brain Tumor Invasion. *J. Neurooncol.* **67,** 295–303 (2004).

60. Nelissen, J. M. D. T., Peters, I. M., de Grooth, B. G., van Kooyk, Y. & Figdor, C. G. Dynamic Regulation of Activated Leukocyte Cell Adhesion Molecule-mediated Homotypic Cell Adhesion through the Actin Cytoskeleton. *Mol. Biol. Cell* **11,** 2057–2068 (2000).

61. Pinon, P. & Wehrle-Haller, B. Integrins: versatile receptors controlling melanocyte adhesion, migration and proliferation. *Pigment Cell Melanoma Res.* **24,** 282–294 (2011).

62. Barczyk, M., Carracedo, S. & Gullberg, D. Integrins. *Cell Tissue Res.* **339,** 269–80 (2010).

63. Cerezo, A. *et al.* The absence of caveolin-1 increases proliferation and anchorage- independent growth by a Rac-dependent, Erk-independent mechanism. *Mol. Cell. Biol.* **29,** 5046–59 (2009).

64. Friedl, P., Hegerfeldt, Y. & Tusch, M. Collective cell migration in morphogenesis and cancer. *Int. J. Dev. Biol.* **48,** 441–449 (2004).

65. Grose, R. *et al.* A crucial role of beta 1 integrins for keratinocyte migration in vitro and during cutaneous wound repair. *Development* **129,** 2303–15 (2002).

66. Wolf, K. *et al.* Compensation mechanism in tumor cell migration: Mesenchymal-amoeboid transition after blocking of pericellular proteolysis. *J. Cell Biol.* **160,** 267–277 (2003).

67. Weigelin, B., Bakker, G.-J. & Friedl, P. Intravital third harmonic generation microscopy of collective melanoma cell invasion: Principles of interface guidance and microvesicle dynamics. *IntraVital* **1,** 32–43 (2012).

68. Weigelin, B., Bakker, G.-J. & Friedl, P. Third harmonic generation microscopy of cells and tissue organization. *J. Cell Sci.* **129,** 245–55 (2016).

69. Haeger, A., Krause, M., Wolf, K. & Friedl, P. Cell jamming: Collective invasion of mesenchymal tumor cells imposed by tissue confinement. *Biochim. Biophys. Acta - Gen. Subj.* **1840,** 2386–2395 (2014).

70. Wolf, K. *et al.* Multi-step pericellular proteolysis controls the transition from individual to collective cancer cell invasion. *Nat. Cell Biol.* **9,** 893–904 (2007).

71. Lämmermann, T. *et al.* Rapid leukocyte migration by integrin-independent flowing and squeezing. *Nature* **453,** 51–5 (2008).

72. Pinner, S. E. & Sahai, E. Integrin-independent movement of immune cells. *F1000 Biol. Rep.* **1,** 67 (2009).

73. Toyjanova, J., Flores-Cortez, E., Reichner, J. S. & Franck, C. Matrix confinement plays a pivotal role in regulating neutrophil-generated tractions, speed, and integrin utilization. *J. Biol. Chem.* **290,** 3752–3763 (2015).

74. Liu, Y. J. *et al.* Confinement and low adhesion induce fast amoeboid migration of slow mesenchymal cells. *Cell* **160,** 659–672 (2015).

75. Bordeleau, F., Tang, L. N. & Reinhart-King, C. a. Topographical guidance of 3D tumor cell migration at an interface of collagen densities. *Phys. Biol.* **10,** 65004 (2013).

76. Carey, S. P. *et al.* Comparative mechanisms of cancer cell migration through 3D matrix and physiological microtracks. *Am. J. Physiol. - Cell Physiol.* **308,** C436–C447 (2015).

77. Damsky, W. E., Theodosakis, N. & Bosenberg, M. Melanoma metastasis: new concepts and evolving paradigms. *Oncogene* **33,** 2413–2422 (2014).

78. Billingsley, K. G. *et al.* Pulmonary metastases from soft tissue sarcoma: analysis of patterns of diseases and postmetastasis survival. *Ann. Surg.* **229,** 602–10 (1999).

79. Mazeron, J.-J. & Suit, H. D. Lymph nodes as sites of metastases from sarcomas of soft tissue. *Cancer* **60,** 1800–1808 (1987).

80. Sosa, M. S., Bragado, P. & Aguirre-Ghiso, J. A. Mechanisms of disseminated cancer cell dormancy: an awakening field. *Nat. Rev. Cancer* **14,** 611–622 (2014).

81. Poschau, M. *et al.* EGFR and β1-integrin targeting differentially affect colorectal carcinoma cell radiosensitivity and invasion. *Radiother. Oncol.* **116,** 510–6 (2015).

82. Eberlein, C. *et al.* A human monoclonal antibody 264RAD targeting alphaV beta6 integrin reduces tumour growth and metastasis, and modulates key biomarkers in vivo. *Oncogene* **32,** 4406–4416 (2012).

83. Cantor, D., Slapetova, I., Kan, A., McQuade, L. R. & Baker, M. S. Overexpression of αvβ6 Integrin alters the colorectal cancer cell proteome in favor of elevated proliferation and a switching in cellular adhesion that increases invasion. *J. Proteome Res.* **12,** 2477–2490 (2013).

84. Wilisch-Neumann, A. *et al.* The Integrin Inhibitor Cilengitide Affects Meningioma Cell Motility and Invasion. *Clin. Cancer Res.* **19,** 5402–5412 (2013).

85. Bretschi, M. *et al.* Cilengitide inhibits metastatic bone colonization in a nude rat model. *Oncol. Rep.* **26,** 843–51 (2011).

86. Kimura, H. *et al.* Imaging the inhibition by anti-β1 integrin antibody of lung seeding of single osteosarcoma cells in live mice. *Int. J. Cancer* **131,** 2027–2033 (2012).

87. Parvani, J. G., Galliher-Beckley, A. J., Schiemann, B. J. & Schiemann, W. P. Targeted inactivation of β1 integrin induces β3 integrin switching, which drives breast cancer metastasis by TGF-β. *Mol. Biol. Cell* **24,** 3449–59 (2013).

88. Liu, H. *et al.* MYC suppresses cancer metastasis by direct transcriptional silencing of αv and β3 integrin subunits. *Nat. Cell Biol.* **14,** 567–574 (2012).
89. Diaz, L. K. *et al.* β4 integrin subunit gene expression correlates with tumor size and nuclear grade in early breast cancer. *Mod. Pathol.* **18,** 1165–1175 (2005).
90. Huttenlocher, A. & Horwitz, A. R. Integrins in Cell Migration. *Cold Spring Harb. Perspect. Biol.* **3,** a005074–a005074 (2011).
91. Hawkins, R. J. *et al.* Pushing off the Walls: A Mechanism of Cell Motility in Confinement. *Phys. Rev. Lett.* **102,** 58103 (2009).
92. Bergert, M. *et al.* Force transmission during adhesion-independent migration. *Nat. Cell Biol.* **17,** 524–529 (2015).
93. Reymond, N., d'Água, B. B. & Ridley, A. J. Crossing the endothelial barrier during metastasis. *Nat. Rev. Cancer* **13,** 858–870 (2013).
94. Sherwood, D. R. Cell invasion through basement membranes: an anchor of understanding. *Trends Cell Biol.* **16,** 250–256 (2006).
95. Friedl, P. & Weigelin, B. Interstitial leukocyte migration and immune function. *Nat. Immunol.* **9,** 960–969 (2008).
96. Li, G., Satyamoorthy, K. & Herlyn, M. N-cadherin-mediated intercellular interactions promote survival and migration of melanoma cells. *Cancer Res.* **61,** 3819–25 (2001).
97. Apostolopoulou, M. & Ligon, L. Cadherin-23 Mediates Heterotypic Cell-Cell Adhesion between Breast Cancer Epithelial Cells and Fibroblasts. *PLoS One* **7,** e33289 (2012).
98. Chen, C.-C. *et al.* The Endothelin-Integrin Axis Is Involved in Macrophage-induced Breast Cancer Cell Chemotactic Interactions with Endothelial Cells. *J. Biol. Chem.* **289,** 10029–10044 (2014).
99. Richter, U. Small-Cell Lung Cancer (SCLC) Cell Adhesion on E- and P-Selectin Under Physiological Flow Conditions. *Methods Mol. Biol.* **1070,** 47–56 (2014).
100. Gaggioli, C. *et al.* Fibroblast-led collective invasion of carcinoma cells with differing roles for RhoGTPases in leading and following cells. *Nat. Cell Biol.* **9,** 1392–400 (2007).
101. Schmidt, S. & Friedl, P. Interstitial cell migration: integrin-dependent and alternative adhesion mechanisms. *Cell Tissue Res.* **339,** 83–92 (2010).
102. Ponta, H., Sherman, L. & Herrlich, P. A. CD44: From adhesion molecules to signalling regulators. *Nat. Rev. Mol. Cell Biol.* **4,** 33–45 (2003).
103. Leitinger, B. Discoidin domain receptor functions in physiological and pathological conditions. *Int. Rev. Cell Mol. Biol.* **310,** 39–87 (2014).
104. Fu, H.-L. *et al.* Discoidin Domain Receptors: Unique Receptor Tyrosine Kinases in Collagen-mediated Signaling. *J. Biol. Chem.* **288,** 7430–7437 (2013).
105. te Boekhorst, V. & Friedl, P. Plasticity of Cancer Cell Invasion-Mechanisms and Implications for Therapy. *Adv. Cancer Res.* **132,** 209–264 (2016).
106. Thiery, J. P. Epithelial-mesenchymal transitions in tumour progression. *Nat. Rev. Cancer* **2,** 442–454 (2002).
107. Nieto, M. A., Huang, R. Y.-J., Jackson, R. A. & Thiery, J. P. EMT: 2016. *Cell* **166,** 21–45 (2016).
108. Nieto, M. A. Epithelial plasticity: a common theme in embryonic and cancer cells. *Science* **342,** 1234850 (2013).
109. Lehmann, S. *et al.* Hypoxia Induces a HIF-1-Dependent Transition from Collective-to-Amoeboid Dissemination in Epithelial Cancer Cells. *Curr. Biol.* **27,** 392–400 (2017).
110. Salmenperä, P. *et al.* Formation and activation of fibroblast spheroids depend on fibronectin–integrin interaction. *Exp. Cell Res.* **314,** 3444–3452 (2008).
111. Belvindrah, R., Hankel, S., Walker, J., Patton, B. L. & Muller, U. Beta 1 Integrins Control the Formation of Cell Chains in the Adult Rostral Migratory Stream. *J. Neurosci.* **27,** 2704–2717 (2007).

112. Blandin, A.-F. *et al.* Glioma cell dispersion is driven by α5 integrin-mediated cell–matrix and cell–cell interactions. *Cancer Lett.* **376,** 328–338 (2016).

113. Mui, K. L., Chen, C. S. & Assoian, R. K. The mechanical regulation of integrin-cadherin crosstalk organizes cells, signaling and forces. *J. Cell Sci.* **129,** 1093–100 (2016).

114. Weber, G. F., Bjerke, M. A. & DeSimone, D. W. Integrins and cadherins join forces to form adhesive networks. *J. Cell Sci.* **124,** 1183–1193 (2011).

115. Epifano, C. & Perez-Moreno, M. Crossroads of integrins and cadherins in epithelia and stroma remodeling. *Cell Adh. Migr.* **6,** 261–73 (2012).

116. Zhong, X. & Rescorla, F. J. Cell surface adhesion molecules and adhesion-initiated signaling: Understanding of anoikis resistance mechanisms and therapeutic opportunities. *Cell. Signal.* **24,** 393–401 (2012).

117. Ko, H. *et al.* Protein Kinase Casein Kinase 2-Mediated Upregulation of N-Cadherin Confers Anoikis Resistance on Esophageal Carcinoma Cells. *Mol. Cancer Res.* **10,** 1032–1038 (2012).

118. Zeng, Q. *et al.* Hepatocyte Growth Factor Inhibits Anoikis in Head and Neck Squamous Cell Carcinoma Cells by Activation of ERK and Akt Signaling Independent of NFκB. *J. Biol. Chem.* **277,** 25203–25208 (2002).

119. Luey, B. C. & May, F. E. B. Insulin-like growth factors are essential to prevent anoikis in oestrogen-responsive breast cancer cells: importance of the type I IGF receptor and PI3-kinase/Akt pathway. *Mol. Cancer* **15,** 8 (2016).

120. Hilmi, C. *et al.* IGF1 Promotes Resistance to Apoptosis in Melanoma Cells through an Increased Expression of BCL2, BCL-X(L), and Survivin. *J. Invest. Dermatol.* **128,** 1499–1505 (2008).

121. Harris, T. J. C. & Tepass, U. Adherens junctions: from molecules to morphogenesis. *Nat. Rev. Mol. Cell Biol.* **11,** 502–514 (2010).

122. Yang, F., Zeng, Q., Yu, G., Li, S. & Wang, C. Y. Wnt/Beta-catenin signaling inhibits death receptor-mediated apoptosis and promotes invasive growth of HNSCC. *Cell. Signal.* **18,** 679–687 (2006).

123. Li, H., Ray, G., Yoo, B. H., Erdogan, M. & Rosen, K. V. Down-regulation of death-associated protein kinase-2 is required for beta-catenin-induced anoikis resistance of malignant epithelial cells. *J. Biol. Chem.* **284,** 2012–2022 (2009).

124. van de Ven, R. a. H. *et al.* Nuclear p120-catenin regulates the anoikis resistance of mouse lobular breast cancer cells through Kaiso-dependent Wnt11 expression. *Dis. Model. Mech.* **8,** 373–384 (2015).

125. Schackmann, R. C. J. *et al.* Cytosolic p120-catenin regulates growth of metastatic lobular carcinoma through Rock1-mediated anoikis resistance. *J. Clin. Invest.* **121,** 3176–88 (2011).

126. Seguin, L. *et al.* An integrin β3–KRAS–RalB complex drives tumour stemness and resistance to EGFR inhibition. *Nat. Cell Biol.* **16,** 457–468 (2014).

127. Peltonen, J. *et al.* Localization of integrin receptors for fibronectin, collagen, and laminin in human skin. Variable expression in basal and squamous cell carcinomas. *J. Clin. Invest.* **84,** 1916–1923 (1989).

128. Schittenhelm, J. *et al.* Comparing the expression of integrins αvβ3, αvβ5, αvβ6, αvβ8, fibronectin and fibrinogen in human brain metastases and their corresponding primary tumors. *Int. J. Clin. Exp. Pathol.* **6,** 2719–32 (2013).

129. Greco, F. A. Cancer of unknown primary site: still an entity, a biological mystery and a metastatic model. *Nat. Rev. Cancer* **14,** 3–4 (2014).

130. Alix-Panabieres, C. & Pantel, K. Clinical Applications of Circulating Tumor Cells and Circulating Tumor DNA as Liquid Biopsy. *Cancer Discov.* **6,** 479–491 (2016).

131. Oh, B.-Y., Kim, K. H., Chung, S. S., Hong, K. S. & Lee, R.-A. Role of β1-Integrin in Colorectal Cancer: Case-Control Study. *Ann. Coloproctol.* **30,** 61 (2014).

132. Mishra, D. K., Scott, K. L., Wardwell-Ozgo, J. M., Thrall, M. J. & Kim, M. P. Circulating tumor cells from 4D model have less integrin beta 4 expression. *J. Surg. Res.* **193,** 745–753 (2015).

133. Aceto, N. *et al.* Circulating Tumor Cell Clusters Are Oligoclonal Precursors of Breast Cancer Metastasis. *Cell* **158,** 1110–1122 (2014).

134. Cheung, K. J. *et al.* Polyclonal breast cancer metastases arise from collective dissemination of keratin 14-expressing tumor cell clusters. *Proc. Natl. Acad. Sci.* **113,** 201508541 (2016).

135. Kim, T. *et al.* Aspartate-glutamate-alanine-histidine box motif (DEAH)/RNA helicase A helicases sense microbial DNA in human plasmacytoid dendritic cells. *Proc. Natl. Acad. Sci. U. S. A.* **107,** 15181–6 (2010).

Chapter 5

Collective Cancer Invasion – An Integrin-dependent Radioresistant Niche

Anna Haeger[#,*], Stephanie Alexander[#], Manon Vullings,
Fabian M. P. Kaiser, Cornelia Veelken, Uta Flucke,
Gudrun E. Koehl, Markus Hirschberg, Michael Flentje,
Robert M. Hoffman, Edward K. Geissler,
Stephan Kissler and Peter Friedl

Manuscript in revision

#contributed equally

*A.H. contributed to the study design, performed and analyzed experiments presented in Fig.3 and 6 and Supplementary Fig.3 and 8, prepared according (supplementary) figures and wrote this manuscript.

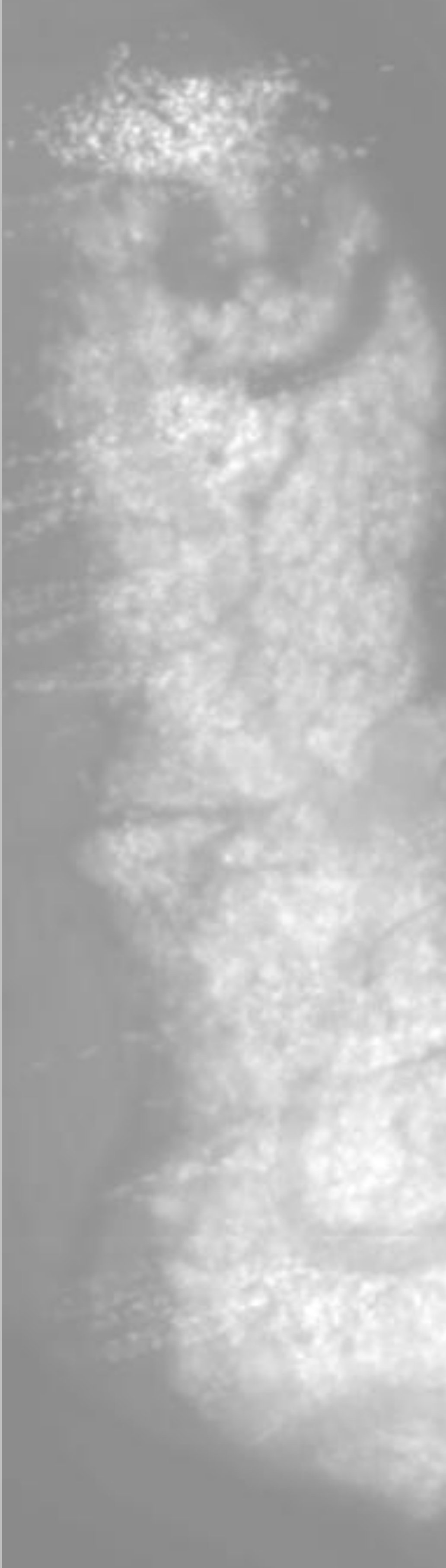

Cancer fatalities are caused by two often concurrent events, metastatic dissemination of neoplastic cells and resistance to therapy. To visualize these processes and dissect their interdependence *in vivo*, we have used longitudinal intravital microscopy on sarcoma and melanoma xenografts and demonstrate that these mesenchymal tumors invade collectively. Radiotherapy induced apoptosis and regression preferentially in the tumor core, whereas the collective invasion niche showed accelerated DNA damage repair and survived. Thus, collective invasion mediates radioresistance. Invading sarcoma and melanoma cells engage β1 and β3 integrins, and integrins support metastatic progression and resistance signaling, yet therapeutic targeting of individual integrins has met limited clinical success. Consistently, β1 or αVβ3 integrin monotargeting achieved incomplete radiosensitization, whereas dual-interference with β1/αVβ3 integrins ablated invasion-associated radioresistance, spontaneous metastasis and secured tumor eradication long-term. Collectively invading cancer cells thus withstand radiation therapy and DNA damage by β1/αVβ3 integrin crosstalk which can be overcome by dual-integrin targeted therapy.

Introduction

Metastatic progression of cancer depends upon neoplastic cells migrating from the primary tumor into the surrounding tissue[1]. To initiate and maintain invasion, cancer cells receive tumor stroma-derived signals which enhance both their invasion and survival potential[2–4]. Stroma-derived tumor cell invasion and survival programs are mediated by hypoxia-related and/or metabolic stress and signaling from adhesion to extracellular matrix and growth factor receptors[3,5,6]; these environmentally controlled signals often cooperate and generate functionally complex networks supporting cancer progression[2,7].

Cancer invasion occurs through individual or collective cell migration[1,8]. Moving single cells detach from the primary site and deliver high numbers of circulating tumor cells which retain only limited probability to survive the metastatic cascade[9,10]. Alternatively, collective metastasis empowers grouped and cooperating cells to invade, circulate and efficiently colonize distant organs[10,11]. While the particular ability of collective cancer cell behaviors for metastatic progression is becoming appreciated, their significance for the response to anti-cancer therapy remains unclear.

During invasion, tumor cells engage a range of mechano-chemical systems, and integrin-based adhesion systems have been identified as central mediators of cell interaction with the surrounding matrix to enhance collective invasion[12], antagonize apoptosis (anoikis) by providing anchorage[13] and mediate radiation resistance, among many other functions[14–16]. Accordingly, integrins or their downstream signaling networks are considered as important targets for overcoming cancer resistance[3,14–17]. Single-agent targeting of integrins, however, has failed to reach clinical endpoints in delaying advanced cancer disease even in continuous or antibody-based delivery schemes alone or in combination with cytotoxic therapy[17,18] or, consistent with partial inefficacy, to eradicate established lesions in preclinical tumor models which express multiple and likely redundant integrin systems[14,16]. Integrins possess overlapping ligand-dependent and -independent functions, coordinate multiple and plastic signaling cascades dependent on cell type and context, and support distinct important tumor-promoting functions, including survival, proliferation and DNA damage repair[19–22]. While several integrin-dependent signaling hubs and functions are suited for therapeutic intervention[23], their crosstalk in solid tumors may also limit the efficacy of single-agent based integrin targeting.

To address these potential caveats limiting therapeutic efficacy, we here aimed to identify the lesional sub-regions responsible for integrin-dependent tumor cell survival upon radiation therapy, and probe whether multiple integrin systems confound stringent integrin-based targeting. By combining preclinical intravital microscopy with *in situ* cytometry and long-term survival analysis, we identify the collective invasion niche as primary zone for an efficient DNA damage response and integrin-dependent radiation resistance and the requirement of dual-β1/αVβ3 integrin targeting to achieve efficient sensitization and elimination of cancer disease.

Materials and Methods

Cells and cell culture

Human HT-1080 sarcoma[24] and MV3 melanoma cells[25] were cultured in DMEM (PAN Biotech GmbH or Invitrogen) supplemented with 10% fetal calf serum (Aurion or Sigma Aldrich), penicillin and streptomycin (both 100 µg/mL; PAN Biotech GmbH or PAA) at 37°C in a humidified 5% CO_2 atmosphere. Identity of the cells was verified by SNP_ID Assay (Sequenom, MassArray System, Characterized Cell Line Core Facility, MD Anderson Cancer Center, Houston, TX, USA) and lack of contamination with mycoplasma was routinely verified using the MycoAlert Mycoplasma Detection Kit (Lonza). Dual-color variants of HT-1080 and MV3 cells, expressing cytoplasmic DsRed2 and nuclear histone 2B (H2B)-EGFP[26] were cultured in medium additionally containing Hygromycin B (Invitrogen, 0.2 mg/mL) and G418 sulfate (Calbiochem, 0.2 mg/mL).

Generation of stable knockdown cell lines by lentiviral shRNA

ShRNA sequences targeting ITGB1 (β1 integrin; AGCCACAGACATTTACATTAAA) and ITGB3 (β3 integrin; AAGTCACTTTCTTCTTCTTAAA) for gene silencing by RNA interference were cloned into the lentiviral vector pLBM either containing a puromycin (p-puro) or a neomycin (p-neo) cassette, and lentiviral particles were produced and concentrated by ultracentrifugation, as described[27]. HT-1080 dual-color cells were infected with p-puro or p-neo viruses (vector controls), or with ITGB1 (on p-puro) or ITGB3 targeting (on p-neo) pLBM viruses. For generation of double knockdown cells, HT-1080 p-puro or HT-1080 β1RNAi cells were additionally infected with ITGB3 targeting or p-neo viruses, respectively. For maintaining stable HT-1080 knockdown cells medium was supplemented with puromycin (Sigma Aldrich, 5 µg/mL) for single transfectants (single vector control, β1RNAi) or puromycin and G418 sulfate (400 mg/mL) for dual-transfectants (dual vector control, β1/β3RNAi). Stability of knockdown without antibiotics selection was confirmed after 4-week culture in antibiotic-free medium and prior to implantation into mice.

Skin window model, intravital microscopy and image analysis

Dorsal skin imaging windows were transplanted onto 10- to 14-week-old male athymic Balb/c nude mice (CANN.CG-FOXN1NU/CRL, Charles River), as described[28]. One day post-surgery tumor cells (~5x10^5 cells in 4 µl PBS) were implanted into the dermis by image-guided microinjection. Tumor progression and therapy response were typically monitored for up to 14 days using a titanium window. In selected experiments, monitoring for 26 days was achieved using a polyethylene window. Tumors used for histological analysis of the DNA damage response were harvested 4 or 5 days after implantation, representing the time point of radiation therapy initiation. Dual-vector control xenografts showed no significant differences in growth and invasion parameters compared with wild-type tumors and thus were used interchangeably as controls. For intravital microscopy, live mice were anesthetized with isofluorane and stably mounted onto a temperature-controlled platform (37°C). Progression of dual-color tumors was monitored using longitudinal multiphoton microscopy (LaVision BioTech)[29,30]. By taking overview images of the entire tumor and surrounding vascular network prior to subcellular multiphoton microscopy, regions of interest for detailed image acquisition could be repetitively annotated and traced over multiple days and measurements. The emission ranges were 400/40 (blue), 535/50 (green), 605/70 (red), and 710/75 (far-red). Epifluorescence overviews of xenografts were obtained with a 4x objective (NA 0.3) and subcellular-resolved multiphoton microscopy with a 20x objective (NA 0.95, both Olympus). Sequential 3D stacks were obtained for up to 300 µm penetration depth at 5 µm step interval. Perfused blood vessels were visualized by i.v. injection of AlexaFluor-660-conjugated dextran (70 kD, Invitrogen, 1 mg/mouse).

Images obtained during intravital microscopy were 3D reconstructed, stitched and analyzed using ImageJ 1.40g (W. Rasband, NIH), ImSpector 3.4 (LaVision BioTec GmbH), Photoshop CS 8.0.1 (Adobe Systems Inc.), and Volocity 4.0.1 (Improvision). Unless indicated otherwise, multiphoton micrographs represent z-projections of 120 to 250 µm imaging depth. Migration velocities were obtained by computer-assisted cell tracking of invasion strand tips (Autocell software, Universities of Bremen and Würzburg). Tumor volume from epifluorescence overview images was calculated as (tumor width)^2 x (tumor length) x π / 6 / 2. Mitotic and apoptotic fractions were determined from the morphology of tumor cell nuclei identified by H2B-EGFP from 5-30 multiple visual fields (dependent on analyzable cell amounts) representing ~100 cells each from 3 to 5 independent tumors. The orientation of mitotic planes was expressed as angle relative to the length axis of the invasion strand, measured in invading cells and the adjacent core of the lesion. The extent of residual invasion after treatments was measured as the area covered by invading cells at day 13 normalized to day 6 of the same lesion using stitched high-resolution overviews from 3D projections obtained by multiphoton microscopy (Supplementary Fig.2G).

Long-term monitoring of intradermal tumors

Intradermal xenograft lesions without imaging window were injected along the dorsal mid-line (~1x10^4 cells in 20µl PBS, 30G needle, two tumors per mouse) sparing rostral and caudal zones. Correct intradermal positioning of growing tumors was verified by high frequency ultrasound (DermaScan, Cortex Technology). Tumor development and therapy response were monitored by whole-body fluorescence imaging (FluorVivo100, INDEC BioSystems) and caliper measurements of macroscopic nodules. Treatment of tumors was initiated at day 6 (HT-1080) or day 13 (MV3) (Supplementary Fig. 8A), to secure a macroscopically visible tumor stage and equal size distribution between different groups. Inclusion criteria for treatment were at least one macroscopic, fluorescence-positive and exponentially growing tumor lesion per mouse not exceeding a volume of 35 mm^3 (HT-1080) or 40 mm^3 (MV3). Prior to and during therapy, tumor development was monitored every second day. After therapy was completed monitoring frequency was adjusted to the progression rate ranging from 3x / week (growing tumor) to 2x / month (complete regression) for up to 180 days. Humane end-point criteria were a tumor size of 2 cm^3, ulceration, weight loss or poor overall condition due to internal metastasis. Each sacrificed animal was screened for the presence of tumor remnants in the dorsal dermis, lymph nodes (superficial cervical, brachial, inguinal), lung, liver and brain using fluorescence stereomicroscopy (Leica MZFLIII, EL6000external light source, GFP Plus and DsRed filter sets). Tumor material and organs were embedded in O.C.T. compound (Sakura), deeply frozen using dry-ice or through swaying in liquid nitrogen, stored at -80°C and analyzed for the presence or absence of tumor cells or invasion status from 10 to 50 µm thick cryosections (M500 or HM500OM Cryostat Microtome, Microm) by epifluorescence microscopy (Leica DMRA fluorescence microscope, Leica DFC340 FX CCD camera, Cytofluor software; 2.5x to 40x objectives). A fixed monolayer of HT-1080 or MV3 dual-color cells from *in vitro* culture served as positive control to discriminate specific fluorescence from autofluorescence.

Antibody treatment

Adhesion-perturbing mouse anti-human β1 (clone 4B4, IgG1, Beckman Coulter, 6603113) and αV integrin (clone 17E6, IgG1, Merck Serono, kindly provided by Simon Goodman, Department of Cellular Pharmacology - Oncology Platform, Merck KGaA, Darmstadt, Germany) monoclonal antibody (mAb) or mouse IgG1κ isotype (clone MOPC-21, Sigma Aldrich, M7894) were injected i.p. at 5 mg/kg or 10 mg/kg body weight, respectively, to reach a calculated antibody concentration of ~8 µg/mL in body fluids (60% of body weight) [31] which ranges >2x above the minimum concentration required for 99% integrin epitope saturation *in vitro* (Supplementary Fig. 5D and data not shown). Based on an IgG1 half-life of 6-8 days[32] a calculated antibody concentration of >3 µg/mL in a body fluids is achieved for at least 6 days by a single injection, sufficient to achieve >99% epitope saturation on HT1080 cells (Supplementary Fig.5D). To additionally secure sufficient availability during the therapy phase antibody was administered every 2-3 days starting with a boost (2 injections at 2 subsequent days). For application *in vivo*, NaN_3-containing antibody stocks (mAb 4B4, IgG1) were dialyzed against 0.9% NaCl. In mice carrying the imaging window antibody was administered at days 3, 4, 7 and 10 as therapeutic intervention in established tumors after the onset of invasion (Supplementary Fig. 7A). Mice carrying established tumors without imaging window received antibody on days 6 (before irradiation), 7, 9, 11 and 13 (HT-1080) or days 13 (before irradiation), 14, 16, 18 and 20 (MV3) after tumor implantation (Supplementary Fig. 8A).

Irradiation procedures

Tumors in mice carrying the imaging window were irradiated either locally with a focused beam of 2 cm in diameter using a RT 50 (X-ray) source (Philips Medical Systems) at a dose-rate of 4.9 Gy/min or with a wide-field beam using an X-ray tube (X-RAD 320ix, Precision X-Ray) with 0.75 mm tin, 0.25 mm copper and 1.5 mm aluminum filter for beam conditioning, 30 cm source-skin distance (SSD), 320 KV output voltage with 12.5 mA for a dose rate of 3.6 Gy/min. To shield the mouse body but expose the tumor and peritumor tissue to the wide-field radiation beam, the mouse was placed inside a 6 mm lead-coated tube, while the tumor in the skin-fold window was exposed through a slit. To irradiate tumors in imaging window-free mice using the non-focused beam, the mouse was positioned inside the shielding tube and the skin-fold containing the tumor was gently extended through the slit, fixed by surgical tape and exposed to the radiation field. By varying the duration of exposure, radiation doses ranging from 2 to 10 Gy per session were applied. For tumors growing in the imaging window, a fractionation scheme with cumulative doses of 40 Gy for HT-1080 tumors (daily fractionation from day 4 to 8) or 50 Gy for MV3 tumors (day 4, 5, 7, 8, 11) was used, to reach detectable response curves within a 2-week period for intravital microscopy. Tumors used for the analysis of DNA damage markers received a single dose of either 8 Gy (HT-1080) or 10 Gy (MV3) at day 4. Intradermal tumors in imaging window-free mice used for long-term follow-up obtained a fractionated scheme with adjusted individual doses of 2 Gy from day 6 to 10 (HT-1080) or 3 Gy at day 13, 14, 16, 17 and 20 (MV3) after tumor implantation, amounting to cumulative 10 Gy (HT-1080) or 15 Gy (MV3) (Supplementary Fig. 8A). This mid-dose scheme was established by dose-escalation and long-term monitoring to yield relapse frequencies between 60 and 80% for detecting the long-term effects of radiosensitization by integrin-targeted combination therapy (data not shown).

Immunohistological stainings

For the visualization of cell-cell junctions via ALCAM staining, untreated tumor-bearing mice carrying the skin window were sacrificed on day 5 (HT-1080) or day 8 (MV3) after tumor implantation. Tumor-containing dorsal skin samples were cryopreserved as described above, with marked orientation of invasion strands and invasion status documented by intravital epifluorescence microscopy. Frozen tissue samples were cut into 50 μm thick cryosections (HM500OM Cryostat Microtome, Microm) which were immediately fixed in neutral buffered formalin (4%, formulation according to Lillie), incubated for ~18 h at room temperature (RT) and stored in phosphate buffer (0.1M, pH 7.4, 4°C). For staining, free aldehyde groups and unspecific epitopes were blocked using 0.15% glycine in Tris-buffered saline (TBS, 30 min, RT), followed by incubation with TBS supplemented with 1% bovine serum albumin (BSA, Sigma Aldrich) and 15% normal goat serum (NGS, GIBCO Life Technologies, 30-60min, RT). After washing (TBS), endogenous mouse IgG in the tissue was blocked with unlabeled anti-mouse IgG Fab' fragments (Jackson ImmunoResearch, 15-007-003, ~18 h, 4°C) followed by washing (TBS). Mouse anti-ALCAM mAb (AZN-L50; IgG2A; kindly provided by Joost te Riet, Department of Tumor Immunology, Radboudumc Nijmegen, The Netherlands)[33] was biotinylated using biotin-SP (long-spacer) conjugated anti-mouse IgG Fab fragment (Jackson ImmunoResearch, 115-067-003, 1:2, 20 min, RT), followed by incubation in mouse serum (Biowest, 10 µl/1 µg Fab' biotin, 10 min, RT). Anti-ALCAM/biotin-Fab' complexes were diluted (1:15) in TBS/BSA (1%) and added to the tissue slices for incubation (~18 h, 4°C). After washing (TBS) tissue slices were overlaid with streptavidin-coupled Alexa 647 (Jackson ImmunoResearch, 016-600-084, 2 µg/mL) and DAPI (Roche, 1 µg/mL), in TBS/BSA (1%, 20 min, RT), washed (TBS) and mounted in Fluoromount G (Southern Biotech) on object slides for confocal microscopy.

For analysis of DNA damage response (DDR) markers, non-irradiated or irradiated tumors (day 4 or 5) grown in the imaging window were obtained before or 30-60 min and 23-24 h after irradiation. Tumor-containing skin samples were cryopreserved with marked invasion status as described above. Frozen tissue samples were cut into 10 µm cryosections (HM500 Cryostat Microtome, Microm), mounted on superfrost plus object slides and screened to determine tumor sub-region as core or invasion zone. After drying for ~18 h tissue slices were stored (-80°C) and prior to staining fixed (2% parafomaldehyde diluted in PHEM buffer, 15 min, RT), rinsed with phosphate-buffered saline (PBS) and incubated in PBS containing 0.1% Triton X-100 (Sigma Aldrich) for permeabilization (20 min, RT). To minimize background, samples were incubated in PBS supplemented with 5% NGS and 0.1% cold water fish skin gelatin (CWFG, Sigma Aldrich; 30 min, RT), followed by staining with the following primary antibodies: rabbit anti-γH2AX (pSer139, Novus Biologicals, NB-100-384, 1:10,000), rabbit anti-phosphoChk2 (pThr68, Abcam, ab85743, 1:1,000) or rabbit anti-phospho(Ser/Thr)-ATM/ATR-substrates (4F7, Cell Signaling, 2909, 1:1,000), all diluted in PBS supplemented with 2% NGS and 0.1% CWFG. Tissue slices were incubated with primary antibody solution (1 h, RT followed by ~18 h, 4°C), washed (PBS), incubated with goat anti-rabbit IgG (H+L) Alexa Fluor 647 (Invitrogen, A-21245, 4 µg/mL) and DAPI (1 µg/mL), both diluted in PBS/NGS (2%)/CWFG (0.1%), washed and mounted in Fluoromount G. For reliable intratumor comparison of sub-regions all slices per tumor sample and staining were processed and recorded in parallel.

Hypoxia and phospho-p44/42-MAPK signals were detected in tumors 7 days post-implantation from window-bearing mice. As hypoxia probe, pimonidazole (Hypoxyprobe-1 Kit, Hypoxyprobe Inc.) was applied i.p. (60 mg/kg body weight) and tissue was harvested 60 min thereafter. Tumor-containing samples were cryopreserved with marked invasion status and processed as 10 µm thick cryosections. Fixation, staining and mounting were performed as described for immunohistological analysis of DDR markers using primary rat anti-CD31 (clone MEC13.3, BD Biosciences, blood vessel staining), mouse anti-pimonidazole adducts (Hypoxyprobe-1 Kit, staining hypoxic cells) and rabbit anti-phospho-p44/42-MAPK antibody (Thr202/Tyr204, Cell Signaling, 9101, 1:50, phospho-Erk1/2 signal) and secondary goat anti-rat, anti-rabbit or anti-mouse IgG (H+L) Alexa Fluor 488 or 647 (Invitrogen) antibodies.

Image acquisition and analysis

Tissue samples stained for ALCAM and DDR markers were analyzed by confocal microscopy (Olympus FV1000) as 3D stacks. ALCAM stainings were recorded using either a 20x / 0.50 NA water or 60x / 1.35 NA oil immersion objective with 3 or 1 µm step size respectively. Stainings of DDR markers were scanned with a 40x / 0.80 NA water immersion objective and 3 µm step size to represent the whole 10 µm tissue slice using identical instrument settings for each tumor sample and staining. Hypoxia and phosphoErk staining were scanned as z-stacks (2 µm step depth) on a LSM 510 META confocal microscope (Zeiss).

Using Fiji/Image J software (v1.48)[34], DDR staining in tumor sub-regions was analyzed from average intensity projections of ~10µm 3D stacks, followed by image segmentation using the H2B-EGFP signal to identify and mark the edges of tumor nuclei (Supplementary Fig. 3C). Compared to maximum intensity projections, the mean intensity projection resulted in cleaner image segmentation with less regions of interest (ROIs) $\leq 1\ \mu m^2$ incurred from irrelevant particles and background noise signal (data not shown). The mean gray value representing an individual DDR signal was quantified for large nuclear segments ($\geq 38\ \mu m^2$) representing intact, non-apoptotic nuclei, and the values were corrected for the background signal measured in non-nuclear regions (Supplementary Fig. 3C,D). Because image acquisition was optimized to identify intratumor heterogeneity, direct comparison of data points from different time-points was obsolete.

Statistics

For comparative analysis of DDR markers in tumor sub-regions, data were log-transformed and a longitudinal analysis in the form of a mixed model ANOVA was performed using the lmer function of the R package lme4[35]. Per DDR marker and time point (before/after IR) differences between the variables “tumor sample” and “sub-region” (i.e. core versus invasion zone) were analyzed. Due to the high number of data points and high inter-tumor variability, each comparison between tumor sub-regions resulted in statistically significant differences, even when independent replicates of the same condition were compared based on quantitatively minor sample-to-sample variation with typically inconsistent trends (Supplementary Fig. 3G**,** left panel). To separate biologically relevant effects from background variability, comparisons showing inconsistent data trends were considered non-significant, whereas analyses with consistent trends (i.e. similar slope and direction of mean of log values between tumor sub-regions) (Supplementary Fig. 3G**,** right panel) were considered biologically significant with p-values displayed.

Survival of tumor-bearing mice during long-term follow-up was analyzed using the Mantel-Cox Log-rank test. For all other statistical analyses the two-tailed Mann-Whitney U-Test for independent and Student's T-test for paired samples were used. To adjust for multiple comparisons, Bonferroni correction was performed. Unless mentioned otherwise, GraphPad Prism 5 or 6 software was used.

Study approval

All animal procedures were approved by the German regional government (Regierung von Unterfranken) (TVA_AZ 54-2531.01-47_06), the Ethical Committee on Animal Experiments of the Radboud University, Nijmegen (The Netherlands) (RU-DEC 2011-124, 2011-230, 2013-008, 2013-125), both in accordance with the respective German and Dutch Animal Experimentation Acts and the European FELASA protocol, and by the Institutional Animal Care and Use Committee (IACUC) of The University of Texas, M.D. Anderson Cancer Center (Texas, USA) (ACUF 07-11-07631, -07632), performed according to the institutional guidelines for animal care and handling.

Results

To identify tumor sub-regions of therapy resistance as well as whether invasion and survival programs coincide, we monitored fluorescent orthotopic HT-1080 sarcoma and MV3 melanoma xenografts in the mouse dermis using longitudinal intravital microscopy[28]. Originating from the growing tumor, both sarcoma and melanoma lesions developed deep dermis invasion (mean velocity 100 µm/day) (Supplementary Fig. 1A-C), with >98% of the cells moving collectively, either as continuous strands connected to the tumor core or detached clusters (Fig. 1A-C). Intact junctions and collective polarity were verified from (i) linear enrichment of the homophilic adhesion receptor ALCAM (CD166) between invading HT-1080 and MV3 cells (Fig. 1D), (ii) collective front-rear polarity with mitotic planes aligned perpendicular to the invasion direction (Supplementary Fig. 1D) and (iii) multicellular orientation along tissue landmarks, including collagen bundles, myofibers (Fig. 1D) and perfused blood vessels (Fig. 1B)[36]. These collective patterns obtained in the mouse model recapitulated the typical strands and nest-like organization of invasion zones in clinical sarcoma and melanoma specimens (Supplementary Fig. 1E,F)[37,38].

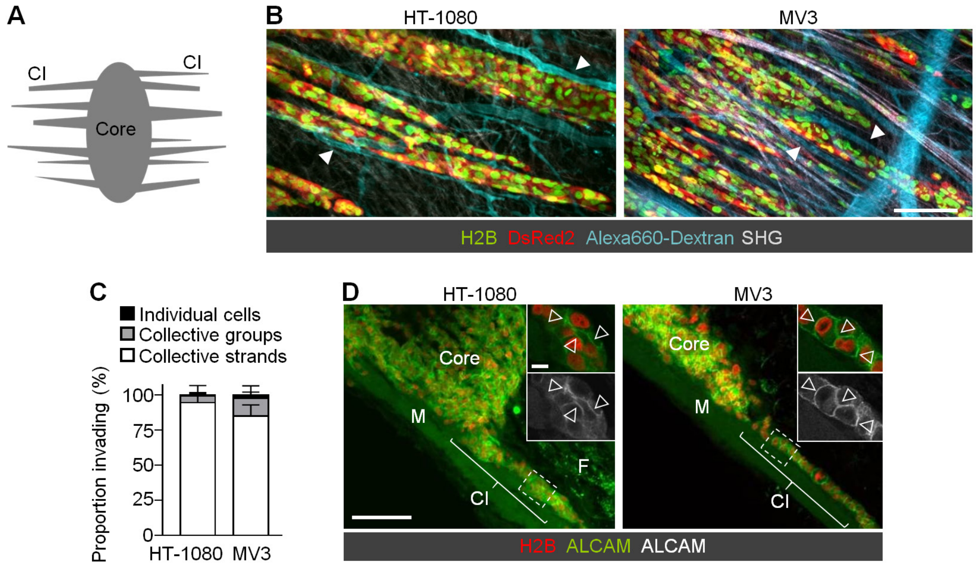

Figure 1. Collective invasion as primary invasion pattern in sarcoma and melanoma xenografts. **A)** Schematic view defining tumor core and collective invasion zone (CI) of tumors growing in the deep dermis of the mouse monitored intravitally through an imaging window. **B)** Collective invasion strands of human HT-1080 sarcoma (left; day 7) and MV3 melanoma xenografts (right; day 8). Tumor cells stably express nuclear H2B-EGFP and cytoplasmic DsRed2. Alexa Fluor 660-conjugated Dextran contrasts perfused blood vessels. Second harmonic generation (SHG) visualizes muscle and collagen fibers. Arrowheads, alignment of invasion strands with perfused blood vessels. Scale bar, 100 µm. **C)** Prevalence of invasion types, including individual cells, detached clusters or collective strands connected to the core (day 5-7). Data represent the means and standard deviation from 5 (HT-1080) and 3 tumors (MV3). **D)** Distribution of ALCAM along cell-cell junctions (arrowheads) in invading tumor strands. Maximum intensity projections (overview) and individual sections (insets) from confocal 3D stacks. Diffuse background fluorescence originates from fat (F) and myofibers (M). Scale bars, 100 µm (overview) and 10 µm (insets).

Rather than approaching the therapy response of the tumor as a homogeneous entity[14,16], we next addressed whether tumor sub-regions, including the collective invasion niche, retain differential sensitivity to genotoxic therapy. In disseminated clinical sarcoma and melanoma DNA damaging radiotherapy is highly effective, with patient subsets nonetheless developing detrimental resistance[39,40]. To reach homogeneous and sustained exposure across all tumor regions, isometric whole-field irradiation (IR) and fractionation were applied in invading tumors after the angiogenic switch (Supplementary Fig. 2A-C). Irradiation thus avoids varying compound delivery to tumor sub-regions caused by heterogeneous vascular perfusion or pressure distribution which may confound systemic chemotherapy[41]. Fractionated IR induced mitotic arrest within hours in both the tumor core and the invasion zone followed by apoptosis induction (Fig. 2A,B, Supplementary Fig. 2D,E) and substantial tumor regression a few days later (Fig. 2C,D, Supplementary Fig. 2F). Despite an overall reliable response, apoptosis induction identified by three-dimensional intravital reconstruction and single-cell cytometry identified significant variance of the radiation response between tumor sub-regions. Collectively invading cells showed a mild, approximately 2-fold apoptotic increment, whereas apoptosis in the tumor core was elevated 4-fold and higher (Fig. 2A-C, Supplementary Fig. 2E). Consistently, over time the collective invasion niche largely survived whereas the core regressed (Fig. 2E). Thus, collective invasion conveys relative radioresistance in an otherwise radiosensitive tumor.

Irradiation induces DNA double-strand breaks (DSBs) followed by a DNA damage response (DDR) with DNA repair or apoptosis induction as outcomes[42,43]. To address whether the tumor core and the invading niche differ in their DDR, we performed quantitative sub-region analysis of central DDR effectors in untreated and irradiated lesions (Fig. 3A, B, Supplementary Fig. 3A- E). Both HT-1080 and MV3 cells express wildtype p53[44,45] and thus are competent to undergo cell cycle arrest and DNA repair after DNA damage[42]. 30-60 min post-IR, the general DSB marker γH2AX[46] was induced with equal (HT-1080) or mildly increased levels (MV3) in the invasion zone relative to the core (Fig. 3C,D, Supplementary Fig. 3F), indicating uniform initiation of the DDR in all tumor sub-regions. The low γH2AX baseline in invading cells rules out preset DSB elevation induced by mechanical damage of the nucleus during invasion[47] or other microenvironmental assault. Chk2 activation which controls DDR outcome[43], was similar in all tumor regions 30-60 min after IR but declined in the collective invasion zone one day later, while phosphoChk2 levels remained elevated in the tumor core (Fig. 3C,D, Supplementary Fig. 3F,G). Consistently after IR the phosphorylation of phosphoATM/ATR substrates, which also include Chk2[43], remained significantly increased in the tumor core but decreased in the invasion zone of HT-1080 lesions (Fig. 3D), verifying completion of the DDR at multiple levels. By inducing cell cycle arrest Chk2 kinase enables DSB repair or mediates apoptosis when damage is irreparable[43]. Thus, timely phosphoChk2 normalization followed by cell survival indicates efficient repair in the collective invasion niche. Conversely, persisting Chk2 activation and ongoing apoptosis beyond day 13 in the tumor core reveal sustained but eventually ill-fated attempts of DNA repair.

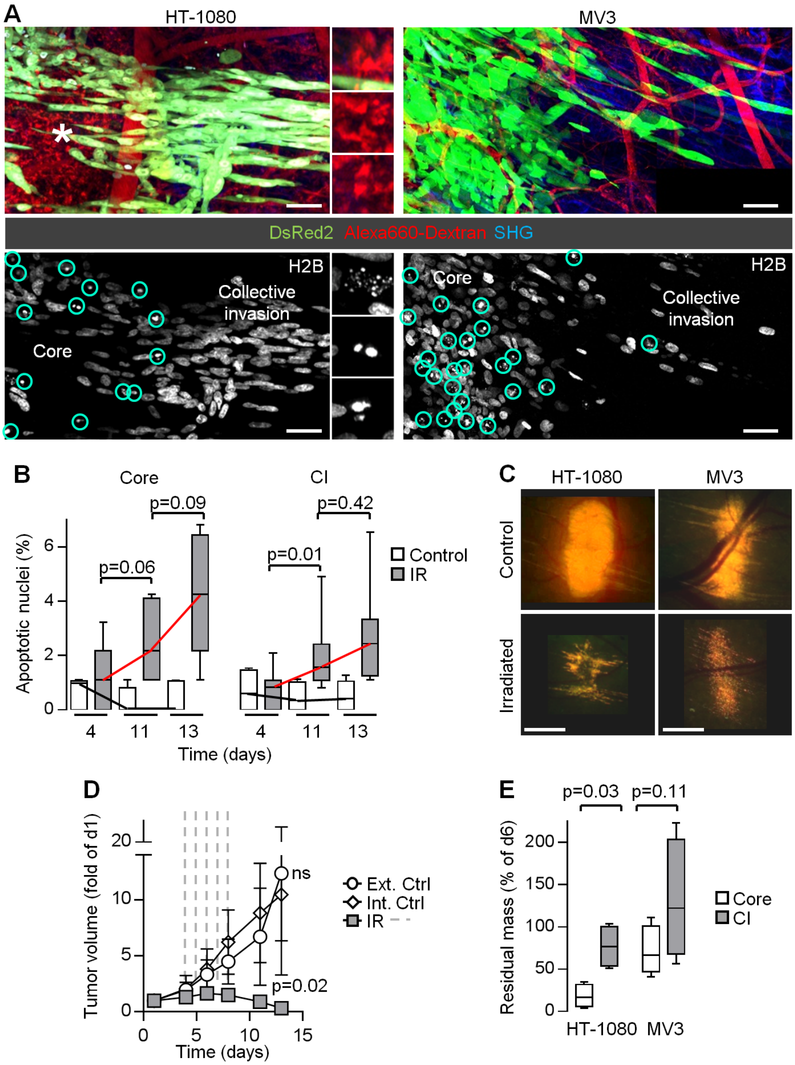

Figure 2. Collective invasion niche mediates radioresistance.
A) Differential response to radiation therapy in invasion strands and tumor core. Multiphoton microscopy images show the borders between core and collective invasion zone (day 13). Asterisk, regressing tumor core. Insets upper panel, infiltrating dextran-positive macrophages. Circles and insets lower panel, apoptotic nuclear fragmentation used for quantification. Scale bars, 100 µm. **B)** Frequency of apoptotic nuclei in HT-1080 tumor cores and collective invasion strands. Data represent the medians, 25th/75th (box) and 5th/95th percentiles (whiskers) from 5 to 20 fields/tumor from 3-4 independent mice. Statistics, Mann-Whitney test. **C)** Epi-fluorescence overviews of whole-tumor topology in untreated and irradiated HT-1080 (5 x 8 Gy) and MV3 (5 x 10 Gy) lesions (day 13). Scale bar, 1 mm. **D)** HT-1080 tumor growth before, during (dashed lines; 5 x 8 Gy) and after irradiation, compared to untreated tumors in independent mice (Ext Ctrl) or non-irradiated contralateral tumors in the same mouse (Int Ctrl). Means ± standard deviation (3 to 9 independent tumors). P value, significant difference between irradiated and control tumors at the end-point (day 13). Statistics, Mann-Whitney test. **E)** Extent of tumor regression in core and invasion zone of irradiated tumors. Data show median residual areas, 25th/75th (box) and 5th/95th percentiles (whiskers) of day 13 normalized to day 6 from 4 independent tumors. Statistics, paired t-test.

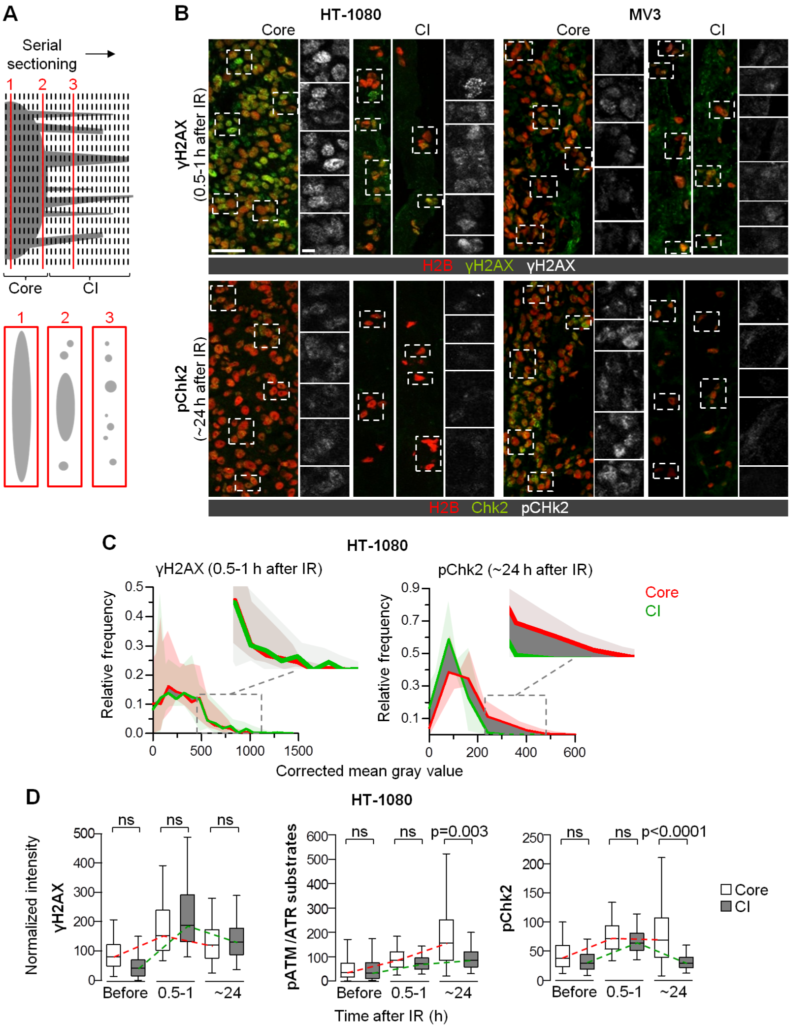

Figure 3. Differential DNA damage response in tumor core and collective invasion niche. **A)** Strategy for differential immunohistological analysis of DNA damage response in tumor core and collective invasion (CI) zone. Upper panel, serial sectioning of the entire tumor; lower panels, resulting cross-sectioned patterns. **B)** γH2AX and pChk2 signal in tumor core and collective invasion zone detected at early (≤1h) and late (24h) time-point after a single-dose irradiation. Maximum intensity projections from confocal 3D stacks. Dashed rectangles indicate representative tumor nuclei for single-channel display of γH2AX or pChk2 signal. H2B, H2B-EGFP (tumor nuclei). Scale bars, 50 µm (overview), 25 µm (inset). Examples for non-irradiated samples are shown in Supplemental Figure 3e. **C)** Intensity distribution of DDR signals in HT-1080 tumors after a single-dose irradiation. Data show the mean gray value after background correction (lines) and signal range (filled areas, lowest to highest values) from 3 independent tumors. Dark grey shaded area, difference between core and collective invasion zone. **D)** Quantification of γH2AX, pATM/ATR substrates and pChk2 signal intensity after single-dose irradiation. Data represent the median gray value per nucleus after background correction, with 25th/75th (box) and 5th/95th percentiles (whiskers) from 3 independent tumors. ~150-600 nuclei per invasion zone and tumor and ~1,000-6,000 representative nuclei per core and tumor were analyzed. Dashed lines visualize approximate dynamics of DNA damage response. Statistics, mixed model ANOVA (see methods section for details).

When probed for vascular integrity by intravascular dextran retention (Fig. 1B,E) or for tissue oxygenation using pimonidazole staining (Supplementary Fig. 1G), we found that invading sarcoma and melanoma cells engaged with morphologically intact, well-perfused and metabolically unperturbed dermal stroma. These results exclude hypoxia-mediated resistance[5]. We therefore tested whether integrins, which are expressed and preferentially engaged during collective invasion[12] and have been implicated in mediating radiation resistance[14–16], orchestrate cell survival during invasion *in vivo*. HT-1080 and MV3 cells expressed high levels of β1 and moderate levels of β3 integrin, but lacked other β integrin sub-types (Supplementary Fig. 4) and thus provide a system for probing the relative function of multiple integrins. To test the role of both integrin systems in enhancing survival during collective invasion, β1 integrin alone or, to account for potential compensation, both β1 and β3 integrins were stably downregulated in HT-1080 cells by RNAi (Supplementary Fig. 5A-C). To maximize interference strength but minimize cell reprogramming towards anchorage independence[48], mice carrying shRNA expressing tumors additionally received anti-β1 integrin antibody 4B4, and this regimen repressed the β1 adhesion epitope by 99.5% (Supplementary Fig. 5D,E). In non-irradiated HT-1080 tumors, single- and dual-integrin interference were both sufficient to compromise tumor growth by arresting mitosis and enhancing apoptosis in the tumor core (Fig. 4A-C). Mitogen-activated protein kinase (MAPK) signaling which supports cell growth and survival downstream of integrins[20], was diminished after integrin targeting to levels slightly below the stromal background (Supplementary Fig. 5F). Notably after dual-integrin targeting, similar to the radiation response, the tumor core regressed, whereas the collective invasion zone retained ongoing low-level mitotic activity and persisted (Fig. 4A,D,E). This indicates that the collective invasion niche withstands anoikis induction after integrin deprivation, reminiscent of an overarching anchorage-independent survival advantage[13,49].

However, when combined with radiotherapy, β1 integrin targeting induced significant disruption and shrinkage of collective invasion strands (Supplementary Fig. 6A,C). This effect was further enhanced by dual-targeting of β1 and β3 integrins, reaching effective regression of both the tumor core and collective invasion niche (Supplementary Fig. 6). As dual β1/β3 integrin targeting was superior to β1 integrin mono-targeting in radiosensitization of HT-1080 tumors, these results suggested that β1 and β3 integrins cooperate to enhance cancer cell survival after IR in collectively invading cells.

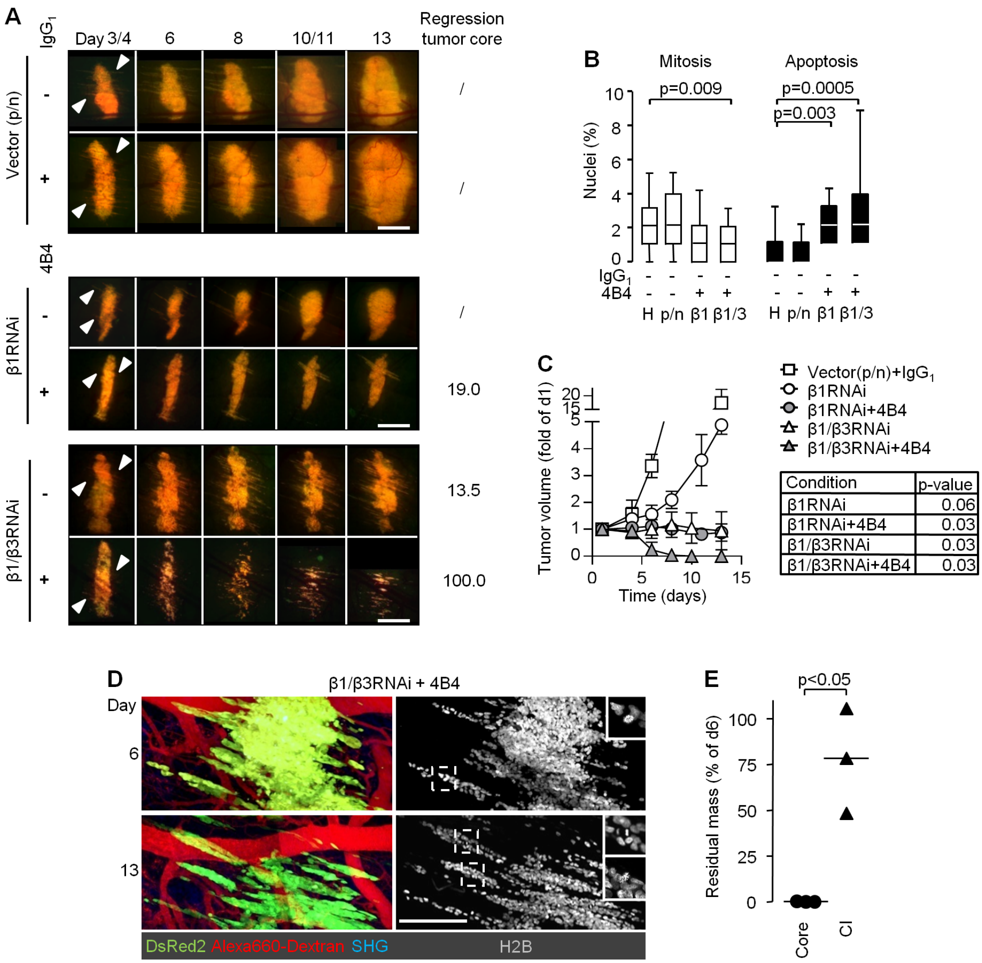

Figure 4. Compromised tumor integrity and persistence of the invasion niche by RNAi- and antibody-based targeting of β1/β3 integrins in HT-1080 tumors.
A) Time course of tumor growth or regression in control tumors transduced with empty vectors (p-puro/p-neo), β1RNAi or β1/β3RNAi in the absence or presence of IgG1 or anti-β1 integrin mAb 4B4. White arrowheads, onset of collective invasion. Numbers (right column), percent mean regression of the tumor core (day 13 compared to day 6) from 3 to 4 independent tumors. Scale bars, 1 mm. **B)** Mitotic and apoptotic fractions from the tumor core for different interference schemes displayed as medians, 25th/75th (box) and 5th/95th percentiles (whiskers) from 20 independent fields from 3 to 4 independent tumors. Statistics, Mann-Whitney test. **C)** Tumor development in response to the indicated interference procedures. Data show the means ± standard deviation from 3 to 4 independent tumors, with p-values for comparing treated tumors with vector controls (Bonferroni-corrected threshold was p=0.0125). Statistics, Mann-Whitney test. **D)** Preferential survival of invading collective strands after combined β1/β3 integrin targeting. Z-projections of the same tumor region. Insets, mitotic figures in collective strands. Scale bar, 250 µm. **E)** Median residual volume of tumor core and collective invasion (CI) zones after β1/β3RNAi combined with mAb 4B4 (day 13 compared to day 6) from 3 independent tumors. Statistics, paired t-test.

To validate these findings using a translational approach for both HT-1080 and MV3 lesions, dual-integrin targeting was performed by antibody-based systemic therapy prior to and during radiotherapy (Supplementary Fig. 7A). To target β3 integrins, but spare αIIbβ3 integrin expressed by platelets[50], we used anti-αV integrin antibody 17E6 which interferes with αVβ3 integrin[51]. When combined with fractionated IR, antibody-based β1/αV integrin targeting induced severe apoptosis followed by regression of the entire lesion in both tumor types (Fig. 5A,B, Supplementary Fig. 7B,C,E,F). By day 7 post-IR, HT-1080 tumor remnants consisted of few individualized non-dividing and slowly regressing cells in perivascular position, of which few cells persisted until day 28, when intravital monitoring had to be terminated for reasons of animal welfare (Fig. 5A,C, Supplementary Fig. 7B,D,H). Likewise, both tumor core and invasion strands of MV3 lesions effectively regressed with mitotically inactive scattered cells as remnants (Fig. 5A,C, Supplementary Fig. 7E,G). This notable difference in regression kinetics between both tumor models replicates the higher radiation sensitivity of clinical sarcoma compared to melanoma[39,40]. These data indicate that combining antibody-based β1 and αVβ3 integrin targeting overcomes invasion-associated radiation resistance and effectively shrinks the invasion niche.

To verify the curative impact of single- vs. dual-integrin targeting combined with IR, fluorescent HT-1080 and MV3 tumors were directly implanted into the dermis of mice, without an imaging window using ultrasound-controlled implantation, and followed up for 180 days (Fig. 6A, Supplementary Fig. 8A,B). Mice bearing emerging macroscopic tumors were treated with antibodies 4B4 and 17E6, individually or combined, and irradiated using an adjusted dosing scheme to model relapsing disease (Supplementary Fig. 8A). To account for minimal residual and disseminated disease, the tumor implantation site and distant organs were dissected at the end-point and scored for the presence of tumor cells (Supplementary Fig. 8C,D,E). Tumors in window-free mice developed collective invasion as a primary pattern (Fig. 6B), ruling out artifacts caused by the imaging window. Dual-integrin targeting drastically improved the efficacy of the radiation response and resulted in relapse-free follow-up in 80% (HT-1080) and >90% (MV3) of the mice with elimination of the lesions locally and at metastatic sites, whereas individual targeting of either β1 or αV integrins was less efficient (Fig. 6C,D and Table 1,2). This outcome indicates that dual-integrin targeting is required to maximize the radiation sensitivity of experimental sarcoma and melanoma lesions.

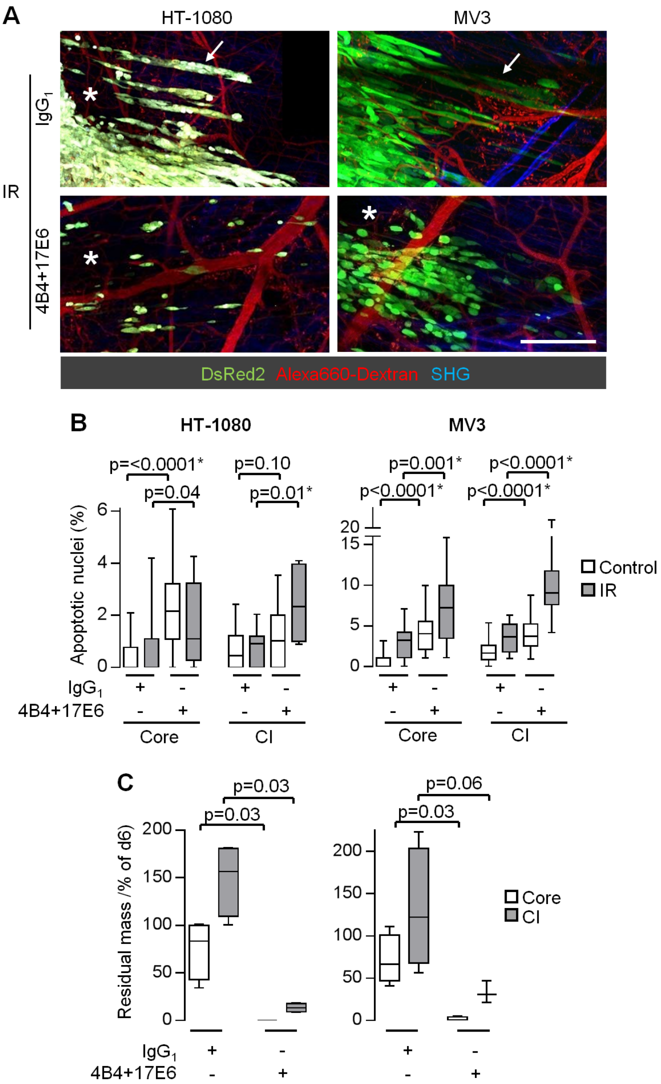

Figure 5. Dual-integrin targeting abrogates radioresistance in the collective invasion niche.
A) Radiation response of tumor core and collective invasion zone after combined treatment with mAbs 4B4 and 17E6 compared to IgG1-treated control (day 13). Asterisks, areas of regression. Arrows, persisting invasion strands. Alexa Fluor 660-conjugated Dextran, perfused blood vessels. Second harmonic generation (SHG) originates from muscle and collagen fibers. Scale bar, 250 µm. **B)** Frequency of apoptotic figures in core and collective invasion (CI) zone after antibody-based integrin targeting and/or irradiation (day 6). Data show the medians, 25th/75th (box) and 5th/95th percentiles (whiskers) from 4 to 5 tumors reflecting a total of 9 to 28 different microscopic fields. *, significant p-value after Bonferroni correction for multiple comparisons (Bonferroni-corrected threshold was $p=0.0125$). Statistics, Mann-Whitney test. **C)** Extent of tumor regression in core and collective invasion zone of irradiated tumors combined with or without integrin targeting. Data show median residual areas, 25th/75th (box) and 5th/95th percentiles (whiskers) of day 13 normalized to day 6 from 4 independent tumors. Statistics, Mann-Whitney test.

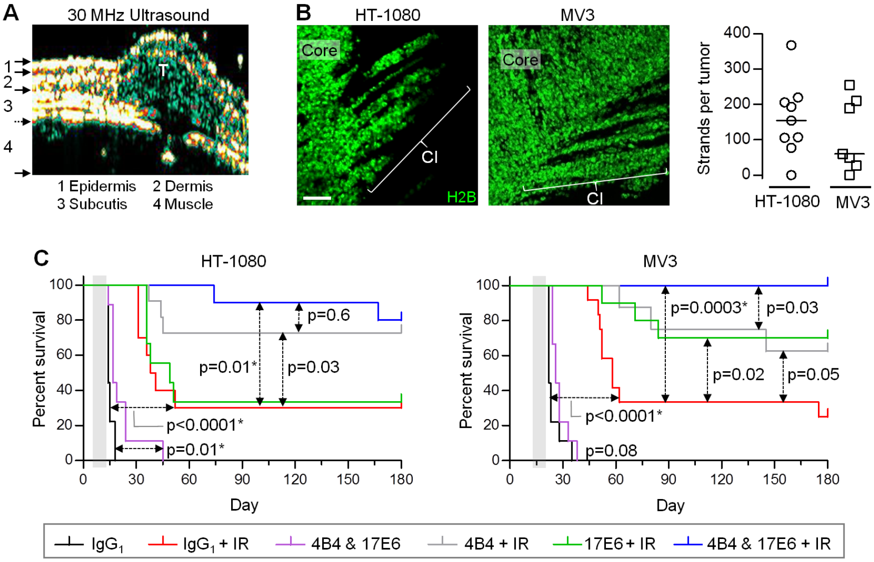

Figure 6. Dual-targeted but not individual anti-integrin therapy to enhance radiation response, tumor eradication and long-term survival.
A) Tumor lesion (T) after implantation in imaging window-free mouse. Intradermal localization was confirmed by high-frequency ultrasound. **B)** Collective invasion (CI) pattern in intradermal tumors in imaging window-free dermis (maximum intensity projections). Number of multicellular strands per tumor was counted from 50 µm thick tumor sections from 9 (HT-1080) and 7 (MV3) tumors. Scale bar, 100 µm. **C)** Tumor-free long-term survival of mice after application of treatment, including fractionated irradiation without and with individual and dual-targeted integrin inhibition with antibodies 4B4 and/or 17E6. Mice were sacrificed after 180 days or earlier, upon humane endpoint criteria. See Table 1 for details on mouse numbers (8-12 mice per group), metastasis formation and tumor remnants. Grey-shaded area, therapy phase. *, significant p-value after Bonferroni correction for multiple comparisons (Bonferroni-corrected thresholds were p=0.01 (HT-1080) and p=0.008 (MV3)). Statistics, Log-rank survival analysis.

Table 1. Survival rates and tumor outcome for long-term follow up experiments on integrin-targeted and IR (combination) therapy in HT-1080 sarcoma xenografts.

Treatment	Negative[A]		Growing primary lesion[B]	Macroscopic tumor relapse[C]	Minimal residual lesion[D]	Metastatic disease[E]
IgG1	0 / 9	0%	9 / 9	0 / 9	0 / 9	0 / 9
4B4 & 17E6	0 / 9	0%	9 / 9	0 / 9	0 / 9	3 / 9
IR + IgG1	3 / 10	30%	6 / 10	1 / 10	0 / 10	7 / 10
IR + 17E6	2 / 9	22%	5 / 9	1 / 9	1 / 9	6 / 9
IR + 4B4	8 / 11	72%	1 / 11	2 / 11	0 / 11	3 / 11
IR + 4B4 & 7E6	8 / 10	80%	0 / 10	1 / 10	0 / 10	1 / 10[F]

Table 2. Survival rates and tumor outcome for long-term follow up experiments on integrin-targeted and IR (combination) therapy in MV3 melanoma xenografts.

Treatment	Negative[A]		Growing primary lesion[B]	Macroscopic tumor relapse[C]	Minimal residual lesion[D]	Metastatic disease[E]
IgG1	0 / 9	0%	9 / 9	0 / 9	0 / 9	0 /9
4B4 & 17E6	0 / 9	0%	9 / 9	0 / 9	0 / 9	0 / 9
IR + IgG1	1 / 12	8%	8 / 12	1 / 12	2 / 12	8 / 12
IR + 17E6	6 / 10	60%	3 / 10	0 / 10	1 / 10	2 / 10
IR + 4B4	3 / 8	38%	1 / 8	1 / 8	2 / 8	3 / 8[F]
IR + 4B4 & 7E6	10 / 11	91%	0 / 11	0 / 11	1 / 11	0 / 11

[A] Lack of growing primary lesion, relapse, minimal residual lesion or metastasis.

[B] Persisting and increasing fluorescence signal at the tumor implantation site reaching endpoint tumor burden.

[C] Recurring and increasing fluorescence signal at the implantation site after a period of absence of signal (transient regression).

[D] Absence of detectable tumor or fluorescence signal until the end point, but presence of H2B-EGFP positive cells in the dermis.

[E] Presence of fluorescent lesions detected by microscopic screening of lungs and lymph nodes.

[F] 1mouse with complete regression of primary lesion but distant metastasis.

Discussion

Using single-cell and time-resolved preclinical intravital microscopy we here show that, beyond other emergent properties of multicellular behaviors including collective chemotactic and stiffness sensing[52,53] and boosted metastatic seeding[10,11], collective invasion empowers sarcoma and melanoma cells to better withstand DNA damaging radiotherapy. In contrast to metabolically perturbed, hypoxic resistance niches[5], the invasion niche is normoxic and co-engages β1 and αVβ3 integrins interacting with the ligand-rich microenvironment of the deep dermis containing collagens, laminins and fibronectins[36,54]. Integrin-mediated growth and survival signaling comprises a complex network originating from integrin-dependent activation of focal adhesion kinase (FAK), Src and other components of the integrin adhesome (e.g. integrin-linked kinase (ILK), PINCH1); this membrane-proximal platform synergizes with receptor tyrosine kinase activation and other receptor systems including CD63/TIMP1 interaction to engage MAPK and phosphoinositide 3-kinase (PI3K) signaling and downstream effectors, including Myc and NF-κB[15,16,19–23]. Several integrin-dependent pathways were reported to accelerate clearance of DSBs and regulate cell cycle checkpoints, including FAK/c-Jun N-terminal kinase 1 (JNK1) and PI3K signaling combined with nuclear actin delivery[22,55,56] and hence might account for enhanced DNA damage repair and subsequent resistance in the collective invasion niche. By directly targeting integrin receptors upstream of the signaling network, even moderate radiation doses (cumulative 10 to 15 Gy) were sufficient to achieve eradication of the entire tumor, including the invasion zone as sub-region of highest survival ability, and further to eliminate distant metastasis. Thus, direct interference with β1/αVβ3 integrin receptors may reach particular stringency in perturbing integrin-dependent signaling as most direct and arguably robust strategy to dampen integrin functions, besides interfering with signaling intermediates (e.g. FAK, Src, MAPK) which may suffer from compensatory network rewiring and resistance development[3,17,57].

In aggregate, we propose that antibody-based clinical integrin receptor targeting in solid tumors requires reconsideration, with emphasis on (i) prior profiling of expressed integrin subsets to select the most appropriate antibody combination, (ii) pre- or post-operative intervention of surgically challenging, non-curable and recurrent invasive lesions, and/or (iii) persisting lesions exhibiting clinical radiation resistance. Future work is required to secure the tolerability of combined β1 and αV integrin targeting in patients. αVβ3 integrin antagonists (Etaracizumab, Cilengitide) are clinically well tolerated[17], whereas targeting of β1 integrin, due to its ubiquitous expression, may require particular care to minimize leukocyte malfunction or wound healing defects[58]. Intermittently applied, dual- or multi-integrin targeted therapy may thus (re)gain clinical relevance to improve efficacy of DNA damaging therapy and eradicate niches of tumor resistance.

Acknowledgements

We gratefully acknowledge Dirk Vordermark, Thomas Krieger, Thierry Felkers and Justyna van Hiel-Mordaka for providing access to irradiation infrastructure and expert support; Huib Croes, Katharina Hermann, Monika Kuhn, Margit Ott, Magdalena Pruszko, Eva Riedel, Liying Jiang and Esther Wagena for expert experimental and logistic support; Willeke Blokx for providing clinical melanoma samples; Joost te Riet for providing ALCAM antibody; Simon Goodman (Merck KGaA, Darmstadt, Germany) for providing 17E6 antibody and helpful discussions; and Wiebe Pestman and Johannes Braegelmann for support with statistical analyses.

This work was supported by the Deutsche Forschungsgemeinschaft (DFG) (FR1155/8-1, 8-2 and 8-3 SPP-1190); an infrastructure grant to the Rudolf Virchow Center (FZ82); NWO-Vici (918.11.626), the European Research Council (617430-DEEPINSIGHT), and the Cancer Genomics Center (CGC.nl) to PF. Work of AH was supported by the PhD fellowship program of the Radboudumc, Nijmegen, The Netherlands and EG by the DFG (GE 1188/3-1, as part of research group 2127).

Supplementary Material and Methods

Immunohistochemistry

Human tissue was fixed in 4% PBS-buffered formalin, routinely processed and paraffin-embedded. Mouse dorsal skin was cryopreseved as described in the Material and Methods section. 2 to 4 μm thick sections of human tissue and 10 μm thick sections of mouse tissue were routinely stained with hematoxylin and eosin and subsequently immuno-histochemically stained by HRP reaction using mouse monoclonal anti-human α-smooth muscle actin (clone 1A4, DAKO) or rabbit polyclonal anti-GFP (Department of Cell Biology, Radboudumc Nijmegen, The Netherlands)[59] after antigen retrieval. Imaging was performed using a Leica DM6000B microscope.

Protein gelelectrophoresis and Western Blot

β1 integrin knockdown efficiency in HT-1080 cells was detected by protein gel electrophoresis and Western blot analysis using complete cell lysates. β1 integrin was detected with mouse anti-β1 integrin (clone 18/CD29, BD Biosciences) and α-tubulin, as loading control with mouse anti-α-tubulin (clone DM1A; Millipore). All protein samples were separated under reducing conditions on 8% SDS-PAGE and transferred onto a nitrocellulose membrane, blocked with 2% milk–PBST (1h, RT) incubated with primary antibody (~18h, 4°C), washed with PBST, and incubated with HRP-conjugated anti-mouse antibody (Jackson Immunoresearch; 1 h, RT). Protein bands were detected using Luminol/H_2O_2. To detect multiple proteins on the same membrane, membranes were stripped using Restore Western Blot Stripping buffer (Thermo Scientific), blocked again and labeled with primary and secondary antibody.

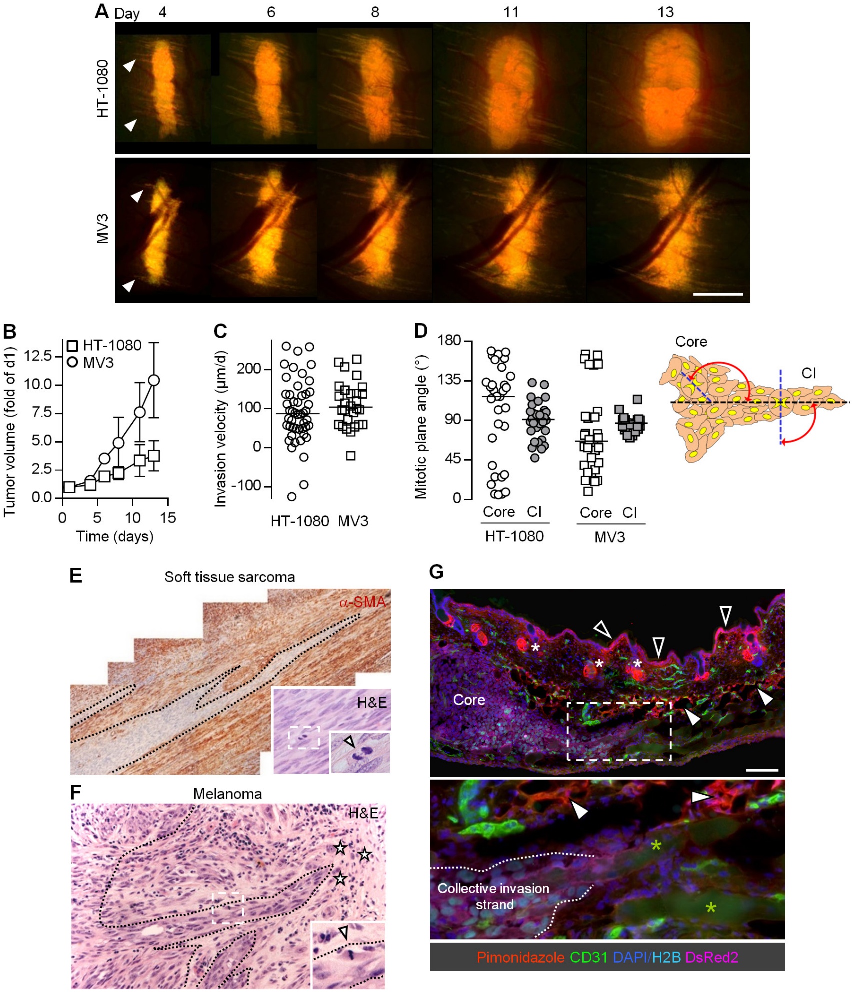

Supplementary Figure 1. Kinetics and organization of collective invasion in mouse dermis and comparison to human samples.

(A,B) Time-dependent whole-tumor morphology **(A)** and tumor volume **(B)** of HT-1080 and MV3 xenografts in the skin window. Arrowheads, onset of collective invasion. Scale bar, 1 mm. **C)** Median velocity of collective invasion into the dermis. Data represent distance migrated per day from day 4 to day 6 of individual collective strands. Negative values originate from occasional rearward orientation or retraction of strand tips. **D)** Orientation of mitotic planes in the core or collective invasion (CI) strands relative to the direction of migration. A median angle of ~90° reflects mitotic planes aligned perpendicular to the invasion direction. **E)** Collective invasion pattern in human adult primary soft tissue sarcoma in sub-diaphragmal location. Multicellular strands bordered by reactive α-smooth muscle actin (SMA) positive stromal cells. Inset, mitotic planes (arrowhead) orientated perpendicularly to the invasion direction. Dashed lines, border between invasion zone and stroma. **F)** Collective invasion pattern in human primary melanoma lesion during vertical growth phase with deep dermal invasion. Inset, mitotic plane (arrowhead) perpendicular to invasion direction. Dashed lines, border stroma to invasion zone. Asterisks, individual tumor cells. **G)** Absence of hypoxic areas in HT-1080 xenograft after 7 days of growth in the skin window. Hypoxic regions detected by pimonidazole staining (red) include the upper epidermis (black arrowheads), sebaceous glands (white asterisks) and dermal fat tissue (white arrowheads), but not the tumor core. Green asterisks, autofluorescent myofibers. Scale bar, 1 mm.

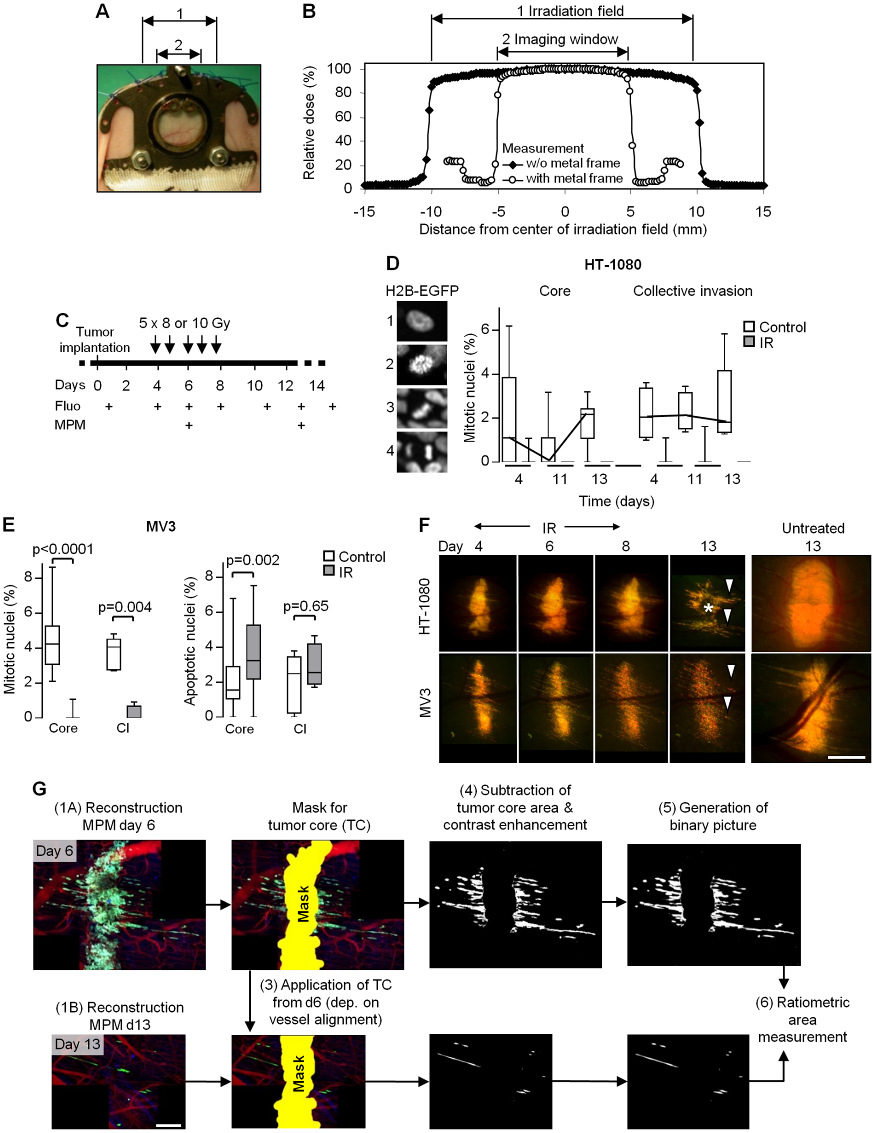

Supplementary Figure 2. Work flow and quantitative analysis of the radiation response of sarcoma and melanoma tumor sub-regions monitored by intravital microscopy.
(A,B) Dimensions and uniform dosing of irradiation across the visible field of the skin window using focal-beam irradiation (2 cm beam diameter). **(A)** Topography of the irradiation field (1) and skin window (2). **(B)** Dosimetry of irradiation measured across the irradiation field (1). Due to the metal frame of the imaging window only the window itself (2) is exposed to irradiation. **C)** Experimental procedure for sequential intravital imaging of the tumor response to fractionated irradiation. Fluo, epifluorescence overview microscopy. MPM, subcellular-resolved multiphoton microscopy. **D)** Frequency of mitotic planes in HT-1080 tumor core and collective invasion strands, by scoring the H2B-EGFP pattern (1, interphase nucleus; 2-4, mitotic nuclei (2, prometaphase, 3; metaphase; 4, anaphase). Data show the median fraction, 25th/75th (box) and 5th/95th percentiles (whiskers) from 5-20 different microscopic fields representing 3

to 4 tumors. **E)** Frequency of mitotic and apoptotic nuclear pattern in tumor core or collective invasion (CI) zone of MV3 tumors (day 6). Data show the median fraction, 25th/75th (box) and 5th/95th percentiles (whiskers) from 9-28 different microscopic fields representing 4 to 5 tumors. Statistics, Mann-Whitney test. **F)** Time course of radiation response in representative lesions, compared to non-irradiated control tumors (day 13). Arrowheads, invasion zone. Asterisks, regression zone. Scale bar, 1 mm. **G)** Sequence of images to quantify the residual tumor mass in tumor sub-regions (example lesion, regression after irradiation combined with anti-b1b3 integrin treatment). The area covered by invading cells measured at day 13 was normalized to the area at day 6 and expressed as relative fraction for each tumor. The same procedure was used to determine the area of the tumor core. Scale bar, 250 μm.

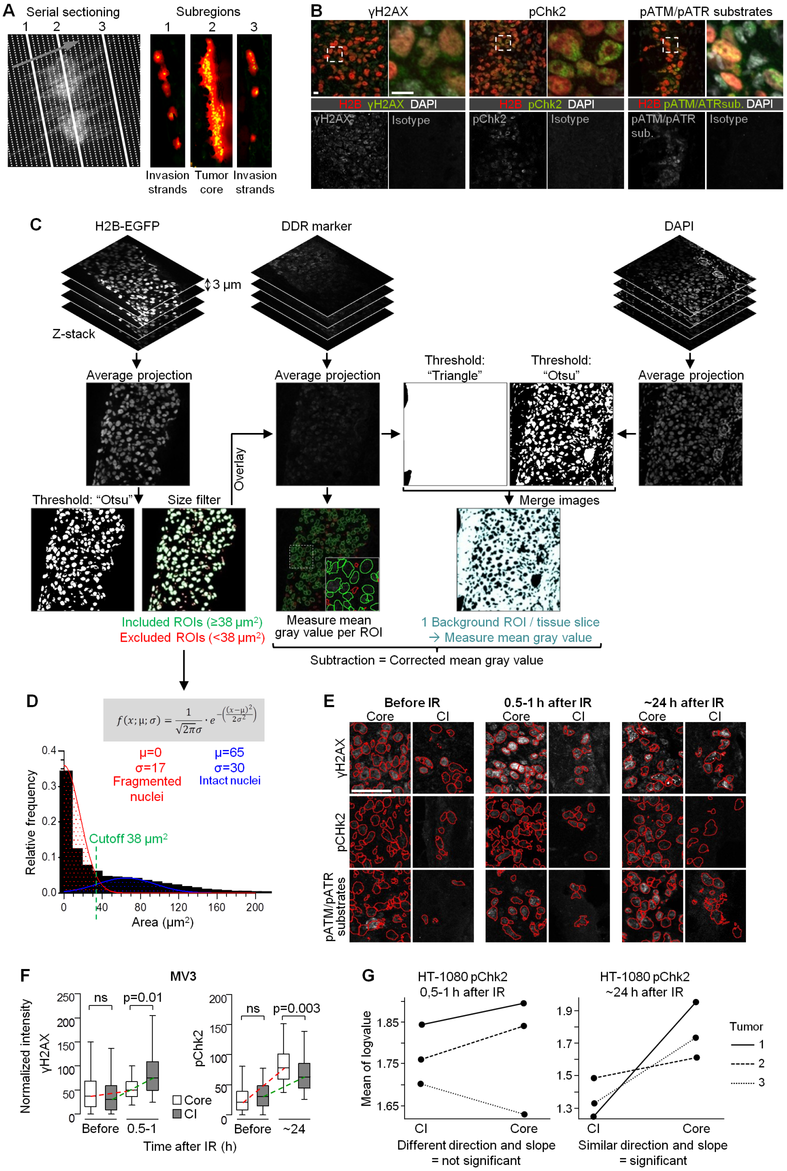

Supplementary Figure 3. Tumor sub-region analysis of the DNA damage response by serial sectioning and image cytometry.
A) Principle of serial vertical tumor sectioning and morphology mapping to annotate serial samples from tumor core (region 2) and invasion zone (regions 1 and 3). Arrow, direction of sectioning. **B)** Specific and isotype-controlled background staining for DNA damage response (DDR) markers (irradiated samples). Dashed rectangles, region of detail images. Scale bar, 10 µm. **C)** Work-flow for image segmentation and single cell cytometry. ROI, region of interest. **D)** Histogram analysis of nuclear size distribution to determine the cutoff for exclusion of nuclear fragments (i.e. apoptotic nuclei). Indicated variables and formula were used for Gaussian distribution fitting to define the intersection and separate fragmented from intact nuclei. Area binning of ~18,000 nuclear ROIs from 3 independent HT-1080 tumors including cores and invasion

zones. Similar distributions and curves were obtained for MV3 tumors resulting in the same cutoff (data not shown). **E)** Representative γH2AX, pChk2 and pATM/ATR substrate signal in sub-regions of HT-1080 tumors before or shortly and 1 day after a single-dose irradiation. Representative maximum intensity projections from confocal 3D stacks. Red selections, ROIs of tumor nuclei. CI, collective invasion. Scale bar, 50 µm. **F)** Quantification of γH2AX and pChk2 signal intensity in MV3 tumors before and after a single-dose irradiation. Data originate from ~150-600 nuclei per invasion zone and tumor and ~1,000-6,000 nuclei per core and tumor from 2 independent tumors, represented as medians, 25th/75th (box) and 5th/95th percentiles (whiskers). Dashed lines visualize approximate dynamics of DNA damage response. Statistics, mixed model ANOVA (see methods section for details). **G)** Identification of biologically relevant effects from large datasets. Example plots derived from the lmer function after performing a mixed model ANOVA showing the distribution of mean of logvalues for different tumor sub-regions and tumors. Only data sets revealing similar directions and slopes were included for statistical analysis (right plot), whereas samples with disparate or noise-like behaviors (left plot) were considered not significant.

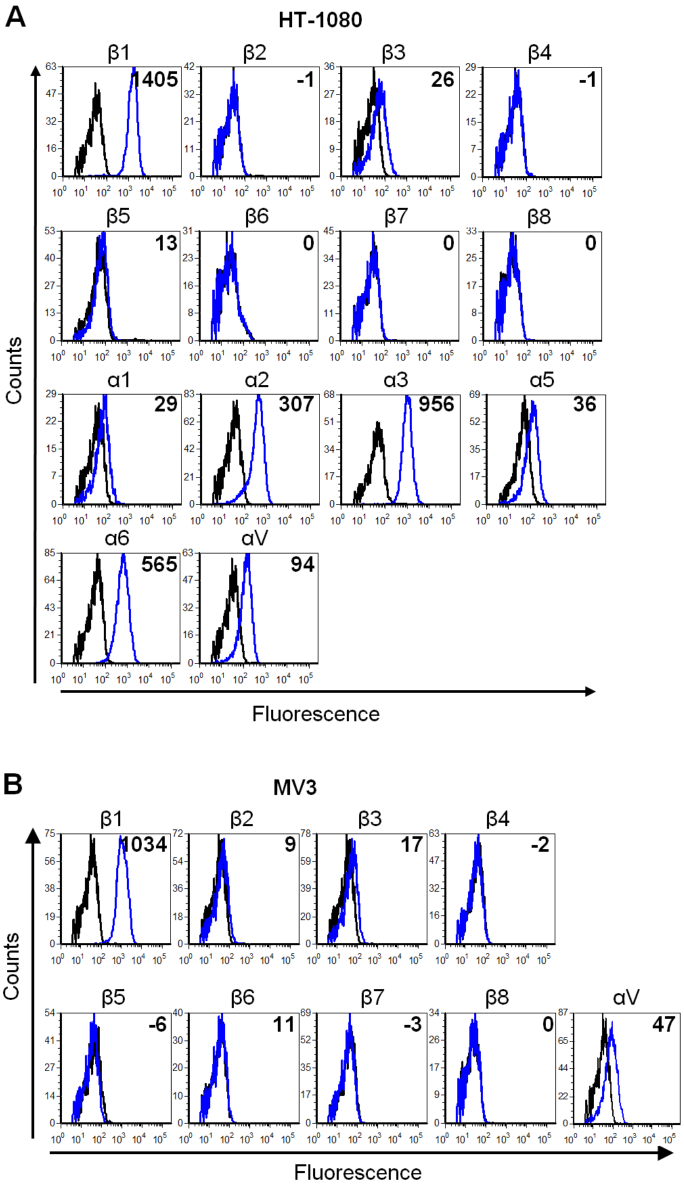

Supplementary Figure 4. Integrin expression profiles in HT-1080 and MV3 cells.
(A,B) Surface expression pattern of integrin β and α chains on HT-1080 **(A)** and β chains on MV3 **(B)** cells determined by flow-cytometry. Black line, isotype control. Values, mean fluorescence (minus isotype values).

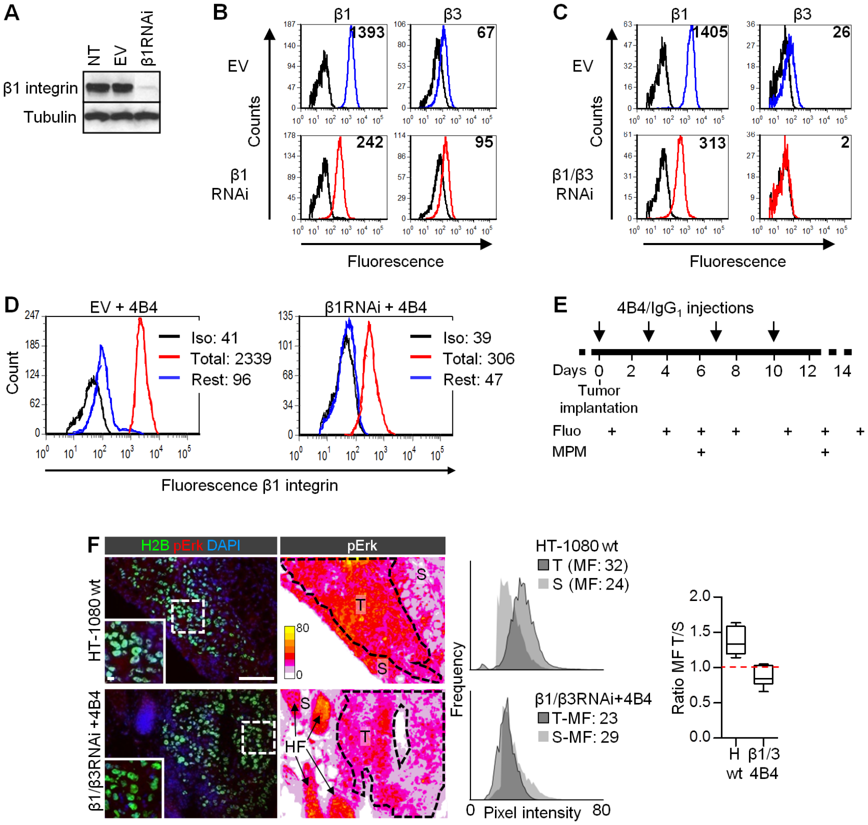

Supplementary Figure 5. RNAi based integrin targeting in HT-1080 cells.

(A-C) Downregulation of β1 and β3 integrins in HT-1080 cells by shRNA. **A)** Knockdown efficiency of β1 integrin in dual-color HT-1080 cells (Western Blot), compared to non-transduced (NT) and empty vector (EV) transduced cells. β-tubulin, loading control. **(B,C)** Upregulation of β3 integrins after downregulation of β1 integrin **(B)** and efficient downregulation of both β1 and β3 integrins after β1/β3RNAi **(C)** determined by flow cytometry. Surface expression pattern of β1 and β3 integrins on β1RNAi cells or β1/β3RNAi cells (red lines) compared to cells transfected with empty vector (EV, blue lines). Black line, isotype control. Values, mean fluorescence (minus isotype values). Stability of β1/β3 downregulation was routinely verified, and no outlier behavior or drift of expression to other integrin β-chains was noted (data not shown). **D)** Reduction of β1 integrin adhesion epitope detected by FITC-conjugated mAb 4B4 on vector control (EV; left) and β1RNAi cells (right) after epitope saturation with unconjugated mAb 4B4 (3 µg/ml; blue line showing residual epitopes) compared with unspecific IgG1 (red line; total epitopes). Black line, isotype control staining (Iso). Values indicate mean fluorescence intensities. **E)** Experimental procedure for administration of anti-β1 integrin mAb 4B4 or IgG1 and sequential intravital imaging of the tumor response to integrin interference. Fluo, epifluorescence overview microscopy. MPM, subcellular-resolved multiphoton microscopy. **F)** Diminished phosphoErk signal (MAPK signaling) after β1/β3 integrin targeting (day 7). Histograms show the mean pixel fluorescence (MF) intensity of pErk from control (HT-1080 wildtype) and β1/β3 integrin targeted tumors (T, dotted lines, identified by H2B-EGFP label) compared to pErk signal in the surrounding stroma (S), which further contained hair follicles (HF) with strong endogenous pErk expression. Ratio of tumor- and stroma-derived pErk intensity is displayed as medians, 25th/75th (box) and 5th/95th percentiles (whiskers) determined from 10 independent regions of the according stroma region after exclusion of HF, with a ratio of 1.0 (red dashed line) when signal intensity of both regions was equal. Calibration bar, pixel intensity. Scale bars, 100 µm (overview), 10 µm (inset).

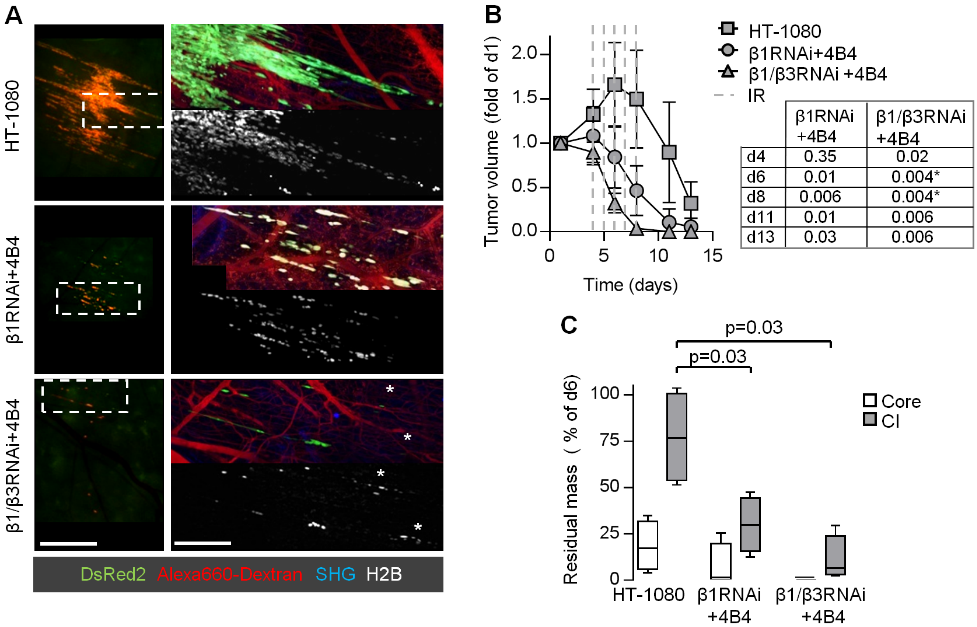

Supplementary Figure 6. Radiosensitization of HT-1080 tumor lesions by β1/β3 integrin RNA interference combined with antibody-based β1 integrin targeting.
A) Topology and extent of the invasion zone in response to fractionated irradiation combined with single-integrin (β1) or dual β1/β3 integrin interference. Epifluorescence (left) and 3D reconstructed z-projections from regions marked by dashed boxed using multiphoton microscopy (right) (day 13). White asterisks, apoptotic nuclei. Scale bars, 1 mm (left), 250 µm (right). **B)** Time-dependent tumor volume. Data show the means ± standard deviation from 3 to 4 independent tumors, with p-values for comparing irradiated integrin-targeted tumors to irradiated control tumors. *, significant p-value after Bonferroni correction for multiple comparisons (Bonferroni-corrected threshold was p=0.005). Statistics, Mann-Whitney test. **C)** Regression of tumor core and collective invasion (CI) zone after irradiation with or without integrin mono- or dual-interference. Data show the median, 25th/75th (box) and 5th/95th percentiles (whiskers) of day 13 normalized to day 6 (Bonferroni-corrected threshold was p=0.025). Statistics, Mann-Whitney test.

Supplementary Figure 7. Radiosensitization of sarcoma and melanoma tumors by dual antibody-based integrin interference. ▸
A) Protocol for administration of anti-β1 (4B4) and αV integrin (17E6) mAbs or IgG1 combined with fractionated irradiation and sequential intravital imaging of the tumor response. Fluo, epifluorescence overview microscopy. MPM, subcellular-resolved multiphoton microscopy. **(B-H)** Tumor morphology and quantification of radiosensitization assessed by intravital microscopy. **(B,E)** Time-dependent growth or regression of HT-1080 or MV3 lesions in response to the indicated treatment conditions. n.a., not analyzed due to humane endpoint after day 13 (tumor > 2cm^3). Asterisks, regression tumor core. Arrowheads, tumor remnants. Scale bars, 1 mm. **(C,F)** Time-dependent tumor volume during and after treatment with IgG1 or mAb 4B4+17E6 with or without irradiation. Data show the means ± standard deviation from 3 to 4 (HT-1080) or 3 to 5 (MV3) independent lesions. The indicated p-value compares IgG1/IR control with 4B4/17E6 and IR (day 15). Statistics, Mann-Whitney test. **(D,G)** Mitotic frequencies in non-irradiated and irradiated tumor core and collective invasion (CI) zone. Data show the medians, 25th/75th (box) and 5th/95th percentiles (whiskers) from 7 to 23 independent fields from 4 (HT-1080) or 3-5 (MV3) independent tumors. Statistics, Mann-Whitney test. **H)** Long-term follow-up (day 26) after treatment with 4B4 and 17E6 and irradiation, revealing minimal residual disease. Dotted grey line, position of former tumor. Box, position of right panel. Zoom shows surviving cells without mitotic activity (arrowheads) and cytoplasm-free, condensed nuclei of disintegrated cells (asterisks).

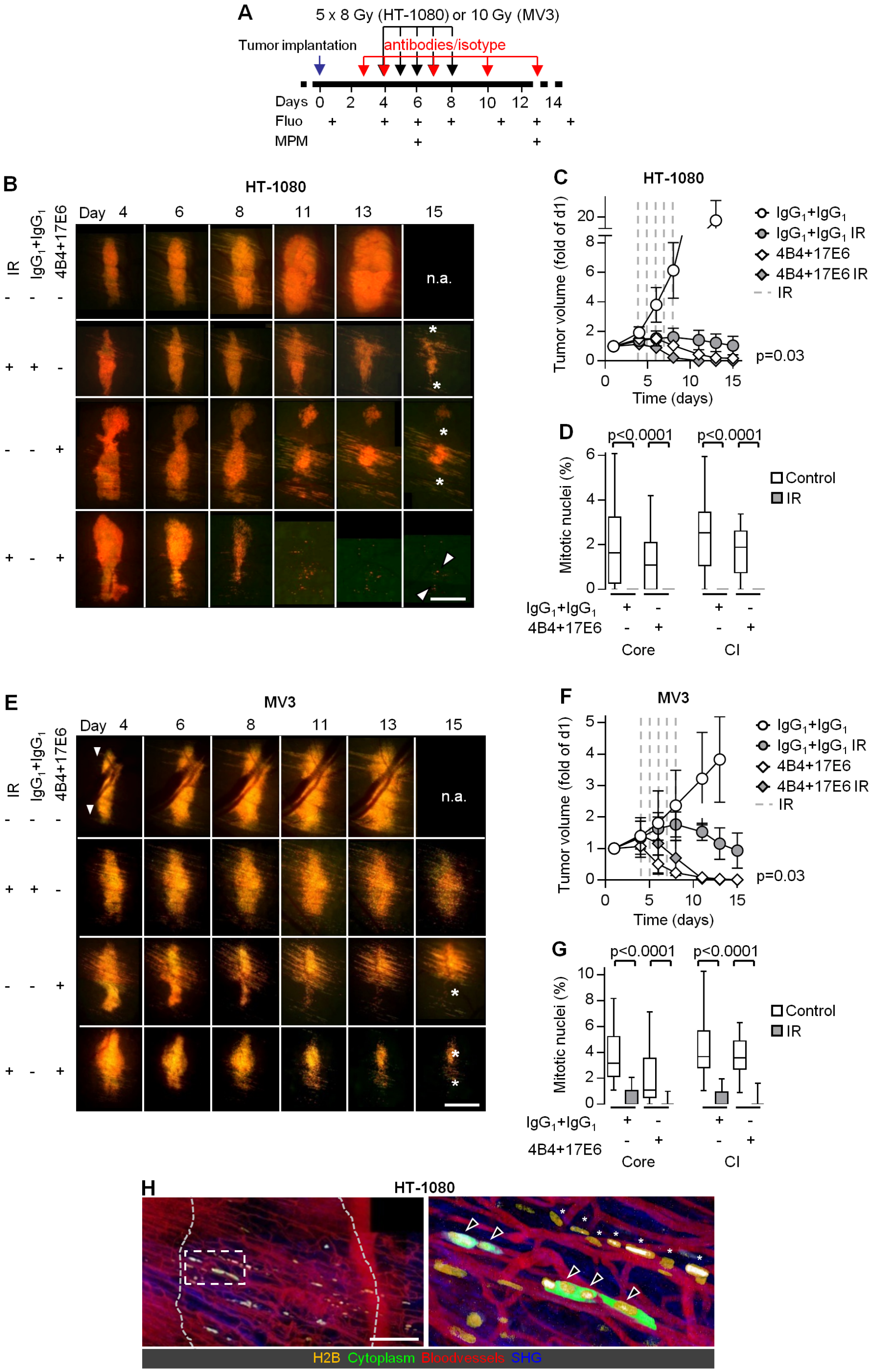
A
5 x 8 Gy (HT-1080) or 10 Gy (MV3)
Tumor implantation
antibodies/isotype
Days 0 2 4 6 8 10 12 14
Fluo + + + + + + +
MPM + +
B
HT-1080
IR
IgG1+IgG1
4B4+17E6
Day 4 6 8 11 13 15
n.a.
C
HT-1080
Tumor volume (fold of d1)
Time (days)
IgG1+IgG1
IgG1+IgG1 IR
4B4+17E6
4B4+17E6 IR
IR
p=0.03
D
Mitotic nuclei (%)
p<0.0001
p<0.0001
Control
IR
IgG1+IgG1
4B4+17E6
Core
CI
E
MV3
IR
IgG1+IgG1
4B4+17E6
Day 4 6 8 11 13 15
n.a.
F
MV3
Tumor volume (fold of d1)
Time (days)
IgG1+IgG1
IgG1+IgG1 IR
4B4+17E6
4B4+17E6 IR
IR
p=0.03
G
Mitotic nuclei (%)
p<0.0001
p<0.0001
Control
IR
IgG1+IgG1
4B4+17E6
Core
CI
H
HT-1080
H2B Cytoplasm Bloodvessels SHG

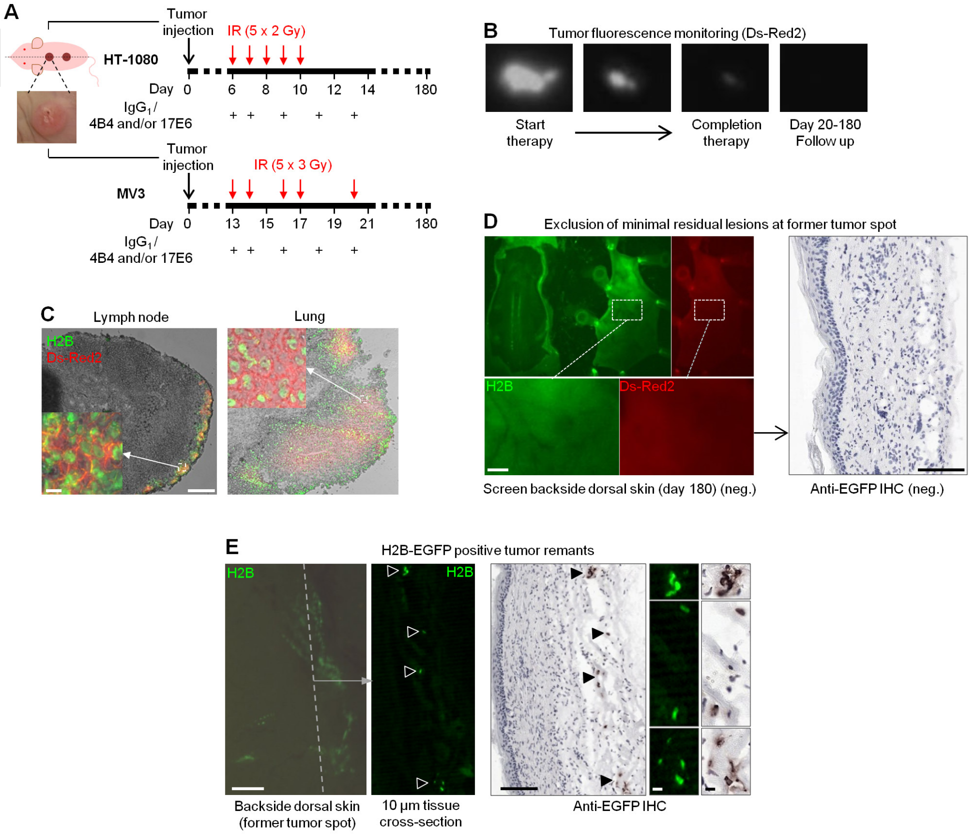

Supplementary Figure 8. Procedures and outcome of long-term therapy response monitoring after combining irradiation with single- or dual-targeted anti-integrin therapy.
A) Treatment schemes for HT-1080 and MV3 tumors. Tumor cells were injected at day 0 resulting in an intradermally growing tumor located along the dorsal midline (dashed line). Example image, intradermal HT-1080 lesion. Time points of irradiation and antibody administration are indicated. **B)** Example tumor undergoing complete regression after therapy monitored longitudinally by whole-body fluorescence imaging. **C)** Dual-color detection of lung and lymph node metastases. Microscopic whole-organ screen (not shown) was followed by analysis of cryosections (shown). Scale bars, 100 µm (overview) and 10 µm (inset). **D)** Identification of minimal residual disease at the endpoint. The dorsal skin was screened from the deep fascia for presence or absence of fluorescent tumor remnants (left panel). In case of doubt sub-regions were additionally sectioned for analysis by anti-EGFP immunohistochemistry (IHC) (right panel). Images show typical tumor-negative outcome. Scale bar, 100 µm. **E)** Examples of minimal residual lesions present at the tumor implantation site at the end point (day 180).Tumor remnants with strand-like pattern of green-fluorescent tumor nuclei (H2B-EGFP) followed by tissue sectioning and validation by anti-EGFP IHC. Dashed line, approximate position of tissue cross-section. Arrowheads, intact H2B-EGFP positive tumor nuclei. Right panel, validation of EGFP positive tumor remnants and positive anti-EGFP IHC side by side. Scale bars, 100 µm (overview) and 10 µm (details).

References

1. Nieto, M. A., Huang, R. Y.-J., Jackson, R. A. & Thiery, J. P. EMT: 2016. *Cell* **166,** 21–45 (2016).
2. Alexander, S. & Friedl, P. Cancer invasion and resistance: Interconnected processes of disease progression and therapy failure. *Trends Mol. Med.* **18,** 13–26 (2012).
3. Hirata, E. *et al.* Intravital imaging reveals how BRAF inhibition generates drug-tolerant microenvironments with high integrin beta1/FAK Signaling. *Cancer Cell* **27,** 574–588 (2015).
4. Pickup, M. W., Mouw, J. K. & Weaver, V. M. The extracellular matrix modulates the hallmarks of cancer. *EMBO Rep.* **15,** 1243–53 (2014).
5. Verduzco, D. *et al.* Intermittent hypoxia selects for genotypes and phenotypes that increase survival, invasion, and therapy resistance. *PLoS One* **10,** e0120958 (2015).
6. Rahbari, N. N. *et al.* Anti-VEGF therapy induces ECM remodeling and mechanical barriers to therapy in colorectal cancer liver metastases. *Sci. Transl. Med.* **8,** 360ra135 (2016).
7. Domoto, T. *et al.* Glycogen synthase kinase-3β is a pivotal mediator of cancer invasion and resistance to therapy. *Cancer Sci.* **107,** 1363–1372 (2016).
8. Friedl, P., Locker, J., Sahai, E. & Segall, J. E. Classifying collective cancer cell invasion. *Nat. Cell Biol.* **14,** 777–83 (2012).
9. Smerage, J. B. *et al.* Monitoring apoptosis and Bcl-2 on circulating tumor cells in patients with metastatic breast cancer. *Mol. Oncol.* **7,** 680–92 (2013).
10. Cheung, K. J. *et al.* Polyclonal breast cancer metastases arise from collective dissemination of keratin 14-expressing tumor cell clusters. *Proc. Natl. Acad. Sci.* **113,** 201508541 (2016).
11. Aceto, N. *et al.* Circulating Tumor Cell Clusters Are Oligoclonal Precursors of Breast Cancer Metastasis. *Cell* **158,** 1110–1122 (2014).
12. Yamaguchi, N., Mizutani, T., Kawabata, K. & Haga, H. Leader cells regulate collective cell migration via Rac activation in the downstream signaling of integrin β1 and PI3K. *Sci. Rep.* **5,** 7656 (2015).
13. Paoli, P., Giannoni, E. & Chiarugi, P. Anoikis molecular pathways and its role in cancer progression. *Biochim. Biophys. Acta - Mol. Cell Res.* **1833,** 3481–3498 (2013).
14. Park, C. C., Zhang, H. J., Yao, E. S., Park, C. J. & Bissell, M. J. Beta1 integrin inhibition dramatically enhances radiotherapy efficacy in human breast cancer xenografts. *Cancer Res.* **68,** 4398–405 (2008).
15. Monferran, S. *et al.* Alphavbeta3 and alphavbeta5 integrins control glioma cell response to ionising radiation through ILK and RhoB. *Int. J. Cancer* **123,** 357–64 (2008).
16. Eke, I. *et al.* β1 Integrin / FAK / cortactin signaling is essential for human head and neck cancer resistance to radiotherapy. *J. Clin. Invest.* **122,** 1529–1540 (2012).
17. Vehlow, A., Storch, K., Matzke, D. & Cordes, N. Molecular Targeting of Integrins and Integrin-Associated Signaling Networks in Radiation Oncology. *Mol. Radio-Oncology, Recent results cancer Res.* **198,** 89–106 (2016).
18. Élez, E. *et al.* Abituzumab combined with cetuximab plus irinotecan versus cetuximab plus irinotecan alone for patients with *KRAS* wild-type metastatic colorectal cancer: the randomised phase I/II POSEIDON trial. *Ann. Oncol.* **26,** 132–140 (2015).
19. Winograd-Katz, S. E., Fässler, R., Geiger, B. & Legate, K. R. The integrin adhesome: from genes and proteins to human disease. *Nat. Rev. Mol. Cell Biol.* **15,** 273–288 (2014).
20. Eke, I. & Cordes, N. Focal adhesion signaling and therapy resistance in cancer. *Semin. Cancer Biol.* **31,** 65–75 (2015).
21. Janes, S. M. & Watt, F. M. Switch from αvβ5 to αvβ6 integrin expression protects squamous cell carcinomas from anoikis. *J. Cell Biol.* **166,** 419–31 (2004).

22. Hodkinson, P. S. *et al.* ECM overrides DNA damage-induced cell cycle arrest and apoptosis in small-cell lung cancer cells through beta1 integrin-dependent activation of PI3-kinase. *Cell Death Differ.* **13,** 1776–1788 (2006).
23. Seguin, L., Desgrosellier, J. S., Weis, S. M. & Cheresh, D. A. Integrins and cancer: regulators of cancer stemness, metastasis, and drug resistance. *Trends Cell Biol.* **25,** 234–240 (2015).
24. Rasheed, S., Nelson-Rees, W. A., Toth, E. M., Arnstein, P. & Gardner, M. B. Characterization of a newly derived human sarcoma cell line (HT-1080). *Cancer* **33,** 1027–33 (1974).
25. van Muijen, G. N. *et al.* Establishment and characterization of a human melanoma cell line (MV3) which is highly metastatic in nude mice. *Int. J. cancer.* **48,** 85–91 (1991).
26. Yamamoto, N. *et al.* Cellular dynamics visualized in live cells in vitro and in vivo by differential dual-color nuclear-cytoplasmic fluorescent-protein expression. *Cancer Res.* **64,** 4251–6 (2004).
27. Kissler, S. *et al.* In vivo RNA interference demonstrates a role for Nramp1 in modifying susceptibility to type 1 diabetes. *Nat. Genet.* **38,** 479–83 (2006).
28. Alexander, S., Koehl, G. E., Hirschberg, M., Geissler, E. K. & Friedl, P. Dynamic imaging of cancer growth and invasion: a modified skin-fold chamber model. *Histochem. Cell Biol.* **130,** 1147–54 (2008).
29. Andresen, V. *et al.* Infrared multiphoton microscopy: subcellular-resolved deep tissue imaging. *Curr. Opin. Biotechnol.* **20,** 54–62 (2009).
30. Weigelin, B. *et al.* Focusing and sustaining the antitumor CTL effector killer response by agonist anti-CD137 mAb. *Proc. Natl. Acad. Sci. U. S. A.* **112,** 7551–6 (2015).
31. Chapman, M. E., Hu, L., Plato, C. F. & Kohan, D. E. Bioimpedance spectroscopy for the estimation of body fluid volumes in mice. *Am. J. Physiol. Renal Physiol.* **299,** F280-3 (2010).
32. Vieira, P. & Rajewsky, K. The half-lives of serum immunoglobulins in adult mice. *Eur. J. Immunol.* **18,** 313–316 (1988).
33. Nelissen, J. M. D. T., Peters, I. M., de Grooth, B. G., van Kooyk, Y. & Figdor, C. G. Dynamic Regulation of Activated Leukocyte Cell Adhesion Molecule-mediated Homotypic Cell Adhesion through the Actin Cytoskeleton. *Mol. Biol. Cell* **11,** 2057–2068 (2000).
34. Schindelin, J. *et al.* Fiji: an open-source platform for biological-image analysis. *Nat. Methods* **9,** 676–82 (2012).
35. Bates, D., Mächler, M., Bolker, B. & Walker, S. Fitting Linear Mixed-Effects Models Using lme4. *J. Stat. Softw.* **67,** 1–48 (2015).
36. Weigelin, B., Bakker, G.-J. & Friedl, P. Intravital third harmonic generation microscopy of collective melanoma cell invasion: Principles of interface guidance and microvesicle dynamics. *IntraVital* **1,** 32–43 (2012).
37. Eyden, B. P., Manson, C., Banerjee, S. S., Roberts, I. S. & Harris, M. Sclerosing epithelioid fibrosarcoma: a study of five cases emphasizing diagnostic criteria. *Histopathology* **33,** 354–60 (1998).
38. Clark, W. H., From, L., Bernardino, E. A. & Mihm, M. C. The histogenesis and biologic behavior of primary human malignant melanomas of the skin. *Cancer Res.* **29,** 705–27 (1969).
39. Gorayski, P., Burmeister, B. & Foote, M. Radiotherapy for cutaneous melanoma: current and future applications. *Future Oncol.* **11,** 525–34 (2015).
40. Hoefkens, F., Dehandschutter, C., Somville, J., Meijnders, P. & Van Gestel, D. Soft tissue sarcoma of the extremities: pending questions on surgery and radiotherapy. *Radiat. Oncol.* **11,** 136-1–12 (2016).
41. Tolaney, S. M. *et al.* Role of vascular density and normalization in response to neoadjuvant bevacizumab and chemotherapy in breast cancer patients. *Proc. Natl. Acad. Sci.* **112,** 14325–14330 (2015).

42. Ciccia, A. & Elledge, S. J. The DNA Damage Response: Making It Safe to Play with Knives. *Mol. Cell* **40,** 179–204 (2010).

43. Zannini, L., Delia, D. & Buscemi, G. CHK 2 kinase in the DNA damage response and beyond. *J Mol Cell Biol.* **6,** 442–457 (2014).

44. Tarunina, M. & Jenkins, J. R. Human p53 binds DNA as a protein homodimer but monomeric variants retain full transcription transactivation activity. *Oncogene* **8,** 3165–73 (1993).

45. Houben, R. *et al.* High-level expression of wild-type p53 in melanoma cells is frequently associated with inactivity in p53 reporter gene assays. *PLoS One* **6,** e22096-1–7 (2011).

46. Rogakou, E. P., Pilch, D. R., Orr, A. H., Ivanova, V. S. & Bonner, W. M. DNA double-stranded breaks induce histone H2AX phosphorylation on serine 139. *J. Biol. Chem.* **273,** 5858–68 (1998).

47. Denais, C. M. *et al.* Nuclear envelope rupture and repair during cancer cell migration. *Science* **352,** 353–8 (2016).

48. Cerezo, A. *et al.* The absence of caveolin-1 increases proliferation and anchorage- independent growth by a Rac-dependent, Erk-independent mechanism. *Mol. Cell. Biol.* **29,** 5046–59 (2009).

49. Gibert, B. & Mehlen, P. Dependence Receptors and Cancer: Addiction to Trophic Ligands. *Cancer Res.* **75,** 5171–5 (2015).

50. Hodivala-Dilke, K. M. *et al.* Beta3-integrin-deficient mice are a model for Glanzmann thrombasthenia showing placental defects and reduced survival. *J. Clin. Invest.* **103,** 229–38 (1999).

51. Mitjans, F. *et al.* An anti-alpha v-integrin antibody that blocks integrin function inhibits the development of a human melanoma in nude mice. *J. cell Sci.* **108,** 2825–38 (1995).

52. Sunyer, R. *et al.* Collective cell durotaxis emerges from long-range intercellular force transmission. *Science* **353,** 1157–61 (2016).

53. Varennes, J., Han, B. & Mugler, A. Collective Chemotaxis through Noisy Multicellular Gradient Sensing. *Biophys. J.* **111,** 640–9 (2016).

54. Mauger, A., Emonard, H., Hartmann, D. J., Foidart, J. M. & Sengel, P. Immunofluorescent localization of collagen types I, III and IV, fibronectin, laminin, and basement membrane proteoglycan in developing mouse skin. *Roux's Arch. Dev. Biol.* **196,** 295–302 (1987).

55. Dickreuter, E. *et al.* Targeting of β1 integrins impairs DNA repair for radiosensitization of head and neck cancer cells. *Oncogene* **35,** 1353–62 (2016).

56. Plessner, M., Melak, M., Chinchilla, P., Baarlink, C. & Grosse, R. Nuclear F-actin formation and reorganization upon cell spreading. *J. Biol. Chem.* **290,** 11209–11216 (2015).

57. Wellbrock, C. & Arozarena, I. The Complexity of the ERK/MAP-Kinase Pathway and the Treatment of Melanoma Skin Cancer. *Front. Cell Dev. Biol.* **4,** 33-1–9 (2016).

58. Koivisto, L., Heino, J., Häkkinen, L. & Larjava, H. Integrins in Wound Healing. *Adv. wound care* **3,** 762–783 (2014).

59. Cuppen, E. *Characterization of the molecular environment of the protein tyrosine phosphatase PTP-BL*. (Radboud University Nijmegen, 1999).

Chapter 6

Microdissection and RNA Expression Profiling of Tumor Core vs. Invasion Zone

Anna Haeger*, Nader Atlasy, Henk Stunnenberg
and Peter Friedl

Manuscript in preparation

*A.H. developed the strategy, established and performed the microdissection and RNA isolation, prepared all figures and wrote this manuscript.

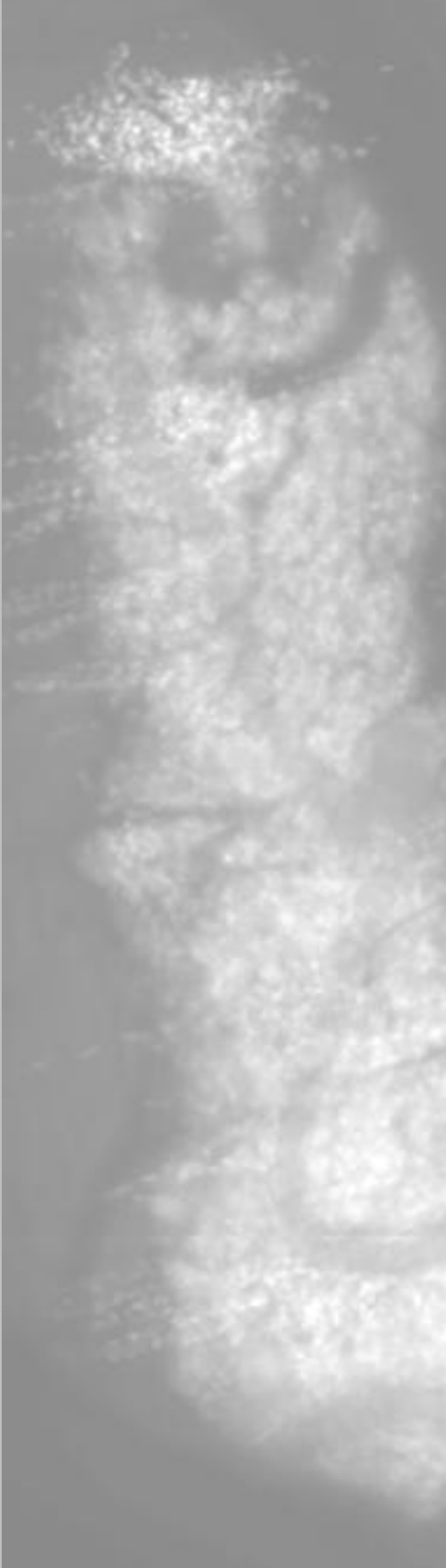

Genomic profiling of tumor material and sub-regional differences in therapy response revealed that a single lesion might suffer from intratumor heterogeneity. Human sarcoma xenografts grown in an imaging window in mice show clear compartmentalization, with a distinct tumor core and collective invasion zone, both exposed to differential environmental context and exhibiting diverging therapy response, thus displaying clear intratumor heterogeneity. To identify target genes in the invasion zone driving this heterogeneity, this chapter describes the establishment of intravital microscopy-based 3D microdissection to isolate tumor core and invasion zone as separate fraction from live tumors, followed by RNA extraction and expression profiling through RNAseq. While tumor cores and invasion zones with a size range of 1 mm to <100 µm were successfully isolated and high-quality RNA was obtained from both tumor sub-regions, initial downstream analysis of RNAseq results suffered from the contained mixture of human tumor and stromal, murine RNA. However, upon further technical optimization of RNAseq performance and analysis, intravital microscopy-guided microdissection will become a valuable tool to analyze heterogeneity of spatially and functionally annotated tumor sub-regions.

Introduction

Tumor lesions usually appear as physical entity, however, histological analyses and emerging cancer genomics approaches combined with cancer research settings showed that cancerous lesions consist of distinct morphological, molecular and functional sub-regions[1–4]. By enabling adaptation responses, such intratumor heterogeneity may impact the biology and therapy response of cancer disease[5–10]. Several converging mechanisms can contribute to intratumor heterogeneity: Genetic diversity where distinct tumor sub-clones obtain additional private mutations compared to the initial tumor lesion, which might confer a survival advantage in selective environments, including contribution to therapeutic resistance, dissemination and metastasis formation[5,6,11]. Genetic heterogeneity can be identified by genome sequencing approaches and evaluation of tumor sub-clonality and is used to identify resistance mechanisms and, if possible, select suitable combinations of (targeted) therapy[3,5,6,11,12]. In addition, epigenetic heterogeneity such as differences in chromatin conformation, histone modifications and DNA methylation, can exist which originates either from genetic mutations that affect epigenetic regulators or is mediated by signals derived from the tumor microenvironment, including chromatin changes associated with cancer cell migration[13–18]. In contrast to genetic heterogeneity, epigenetic heterogeneity is modifiable and can occur transiently[13]. Furthermore, environment-derived signals reaching only tumor sub-regions may activate signaling cascades in cancer cells which contribute to intratumor heterogeneity without epigenetic reprogramming[7,9,19–22].

The invasion zone of tumor lesions contains migrating tumor cells which enter a microenvironment rich in extracellular matrix (ECM) components and various stromal cell types[10,23,24]. Compared to the tumor core, invading cancer cells thus receive distinct environmental input including mechanical and chemical stimuli, which together with chromatin changes to facilitate motility contribute to the development of intratumor heterogeneity and the distinction of two tumor sub-regions, i.e the tumor core and the invasion zone[7,10,14,25,26]. As shown in chapter 4 and 5 of this thesis for sarcoma and melanoma xenografts, this spatial heterogeneity of tumor core and invasion zone can be associated with functional heterogeneity shown by a differential response to integrin-targeting and radiotherapy with the invasion zone being radioresistant and capable to invade and survive independent of integrins (Fig. 1A). However, the molecular targets driving such invasion-associated heterogeneity and therapy failure remain to be dissected, which is necessary to identify new therapeutic targets and strategies to target the entire tumor lesion.

Characterization of the environmental stimuli and downstream effects in the cancer cell population requires separation of both entities, followed by the employment of various techniques including gene expression profiling, investigation of epigenetic changes covering both, DNA and histone modification, or proteomic analyses[21,27,28]. But, as each method depends upon distinct primary material, i.e. RNA, DNA or proteins, such multi-parametric analyses of sub-regions from the same lesion remain a technical challenge. However, since both, activation of signaling cascades and epigenetic modifications eventually converge in gene expression changes, which might be similarly reflected on protein level, gene expression analysis through RNAseq is a widely used, quantitative entry point to analyze intratumor heterogeneity and identify downstream modulators. Likewise the RNA sequence may reveal potential genetic mutations contributing to intratumor heterogeneity.[29,30]

Current experimental approaches to dissect intratumor heterogeneity and identify differences in the disseminating cell fraction include expression profiling of tumor and/or metastatic specimens which are analyzed either directly or after dissolution and/or short-term culture using bulk or single-cell analyses[31–33]. However, thus far neither of these approaches addressed spatial and functional annotations of defined tumor-sub-regions. In contrast, the combination of orthotopic xenograft models, imaging windows and preclinical intravital microscopy constitutes an ideal setting to longitudinally monitor tumor growth and invasion, with the option for controlled interference or therapy application to observe effects at single-cell resolution, such as invasion associated radioresistance described in chapter 5[23,24,34,35]. Expression of fluorescent markers allows clear identification of a tumor core and collective invasion zone in this model system. Therefore, combined with obvious heterogeneity between both sub-regions, the intradermal invasion model was selected to establish a microscopy-guided microdissection approach for differential isolation and profiling of both sub-compartments, with the aim to identify mechanisms underlying the heterogeneity between tumor main mass and invading tumor cells, and the potential impact of the peritumor microenvironment.

This chapter describes the technical establishment of the image-based microdissection approach followed by optimization of tissue preservation and RNA isolation procedure for subsequent expression profiling using RNAseq. Separated isolation of tumor main mass and invasion zones from untreated human HT-1080 sarcoma xenografts including subsequent RNA isolation were successfully achieved, introducing intravital microdissection for studies of intratumor heterogeneity.

Material and Methods

Cells and cell culture

Dual-color variants of human HT-1080 sarcoma cells[36], expressing cytoplasmic DsRed2 and nuclear histone 2B (H2B)-EGFP[37], were cultured in DMEM (Invitrogen) supplemented with 10% fetal calf serum (Sigma Aldrich), penicillin and streptomycin (both 100 µg/mL; PAA), Hygromycin B (Invitrogen, 0.2 mg/mL) and G418 sulfate (Calbiochem, 0.2 mg/mL) at 37°C in a humidified 5% CO_2 atmosphere.

Animal experiments

Animal procedures were approved by the Ethical Committee on Animal Experiments of the Radboud University, Nijmegen (The Netherlands) (RU-DEC 2011-040) and performed in the Central Animal Laboratory of the Radboud University Nijmegen, in accordance with the Dutch Animal Experimentation Act and the European FELASA protocol.

Skin window model

Titanium dorsal skin imaging windows were transplanted onto 10 to 14 week-old male athymic Balb/c nude mice (CANN.CG-FOXN1NU/CRL, Charles River), as described[23]. One day post-surgery tumor cells (~5x10^5 cells in 4 µL PBS) were implanted into the dermis by image-guided microinjection. To monitor tumor progression live mice were anesthetized with isofluorane and stably mounted onto a temperature-controlled platform (37°C). Subsequently epifluorescence overviews of dual-color tumors were generated with a 4x objective (NA 0.3, Olympus).

Microscopy-based microdissection and tissue collection

Microscopy-guided microdissction was applied at day 6 after tumor implantation to intradermal xenograft lesions showing a well-developed invasion zone originating from the tumor core. As inclusion criteria, the tumor core showed volume increase compared to day 1 and a well-developed neovascular network consistent with an established lesion. Mice were anesthetized by i.p. injection of 0.0875 mg/kg body weight (BW) atropine, 0.35 mg/kg BW xylacine and 7 mg/kg BW ketamine. For reliable tumor dissection, mice were immobilized in a plastic tube with the skin-fold window exposed through a slit, fixed onto a metal holder which was placed onto a heating pad. To warm the mouse, the plastic tube was further surrounded by small bags containing warm water (~40°C). A coverslip was placed underneath the epidermal site of the imaging window as a stable support facilitating the microdissection. After removal of the imaging coverslip the exposed tissue was moisturized with 0.9% NaCl solution (Braun).

Intravital microdissection was performed using a fluorescence stereomicroscope (Leica MZFLIII, 0125 N.A., EL6000external light source, GFP Plus and DsRed filter sets) at up to 800x magnification to reach oligocellular resolution. Tumor lesions were dissected with a micro-knife (Micro-Knife 20° (0.120mm), #62091-08) and micro-hook (Micro-Hook 90° (0.25mm), #62091-18) connected to handle (#62090-00, Electron Microscopy Sciences). Subsequently dissected tissue was harvested and transferred using watchmaker tweezers (length 110mm, tip 0.06mm by 0.10mm, Aesculap).

Tissue samples were either collected in with RNA*later* stabilization reagent (Qiagen) or snap-frozen. For preservation in RNA*later* stabilization reagent, prior to starting the dissection process DNase/RNase-free 1.5 ml reaction tubes (Thermo Fisher Scientific) were filled with the reagent (100 µL for tumor cores, 60 µL for invasion zones) and placed at room temperature. Microdissection was performed as quickly as possible to minimize surgery-imposed perturbation and gene expression alteration. Immediately after isolation tissue pieces were submerged in the respective amount of RNA*later* stabilization reagent (one piece per reaction tube) and left at room temperature till microdissection was completed. After o/n incubation at 4°C samples were stored at -20°C until RNA isolation was performed. For snap-frozen samples tissue pieces were put into an empty DNase/RNase-free 1.5 mL reaction tube and subsequently snap-frozen using a liquid nitrogen cooled mini mortar (Calpaclab). Frozen samples were stored in liquid nitrogen (short-term)/at -80°C (long-term).

RNA isolation

RNA isolation was performed using the RNeasy Miro kit (Qiagen). In brief, RNA*later* stabilization reagent was aspirated and tissue pieces were lysed in freshly prepared RLT lysisbuffer containing β-mercaptoethanol (β-ME, Merck Millipore, 10 μL of 14.3 M β-ME per mL RLT buffer). Snap-frozen samples were thawed on ice prior to lysis. Tissue pieces larger than 1 mm^3, including the tumor core, were lysed in 350 μL, and smaller tissue pieces, including the invasion zone, in 70 μL lysisbuffer. Tissue was disrupted and homogenized by repetitive resuspension, vortexing and mashing (using a 20-200 μL pipette tip). Subsequently non-homogenized debris was removed by centrifugation (3min, full-speed (21,130 x g)) and transfer of the supernatant to a new DNase/RNase-free 1.5 mL reaction tube, containing 1 volume of 70% EtOH. Lysate and EtOH were carefully mixed and transfered, including any potential precipitate, to a RNeasy spin column placed in a 2 mL collection tube and processed according to the manufacturer's instruction until RNA elution (RNeasy Micro Handbook (version 12/2007) protocol "Purification of total RNA from animal and human tissues" steps 5-12). After placing the spin column into a new 1.5 ml collection tube, RNA from tumor core samples was eluted using 14 μL DNase/RNase-free water, while invasion zone samples were eluted with a volume of 7 μL. Following application of nuclease-free water onto the filter of the column, collection tubes containing the column were incubated at 37°C for 1 min. After 1 min centrifugation at full speed (21,130 x g) for elution, RNA samples were immediately put on ice. Subsequently for invasion zone samples elution was repeated by re-using the column and applying another 7 μL of nuclease-free water. Eventually RNA collected in both elution steps was pooled in one tube. Immediately after RNA extraction, RNA concentration was determined (NanoDrop 1000, Thermo Fisher Scientific) and samples to measure RNA quality (2100 Bioanalyzer, Agilent) were prepared. RNA samples were stored at -80°C.

RNAsequencing

RNAseq was performed using the the SMART-seqII protocol, as described[38]. cDNA was synthesized according to the manufacturer’s protocol using the ultra low input RNA SMART-seq v4 kit (Clontech) and subsequently sheared using a Biorupter Pico sonication system (Diagenode). To evaluate sonication efficiency, cDNA was analyzed on a 2100 Bioanalyzer.

To prepare the libraries for next generation sequencing the KAPA Hyper Prep Kit (KAPA Biosystems) was used applying the standard Illumina library preparation protocol. In brief, end-repair and A-tailing of the sonicated cDNA were performed in one reaction (30 min, 20°C) followed by heat-inactivation of the enzyme (30 min, 65°C). For barcoding, end-repaired and A-tailed samples were incubated with NEXTflex ChIP-seq adapters (Bioo Scientific) (15 min, 20°C) followed by clean-up to remove remaining enzymes and adapters using AMPure XP beads (Beckman Coulter) with a sample to bead ratio of 1 : 0.8. cDNA libraries were amplified running 10 PCR cycles with the KAPA HIFI HotStart Kit (KAPA Biosystems) and subsequently cleaned using the Qiaquick PCR purification kit (QIAGEN). Selection of 300 bp fragments was achieved by an E-Gel electrophoresis system size selection approach (Thermo Fisher Scientific). After vacuum centrifugation (Savant DNA SpeedVac, Thermo Fisher Scientific), library concentration was determined fluorometrically (Qubit 2.0, Thermo Fisher Scientific) and average size of fragments was analyzed by automated electrophoresis (2100 Bioanalyzer). Next generation sequencing was performed on a NextSeq 500 platform (Illumina) with paired-end reads, a medium sequencing depth of 30 million reads per end and 75 bp read length.

Raw RNAseq data were cleaned from ribosomal RNA contamination using the Bowtie software package[39] and reads with a quality score >15 were further analyzed. Processed reads were aligned to the human genome (hg19) using GSNAP[40] with default options. Subsequently reads mapping uniquely to the human genome were re-aligned to the mouse genome (mm9) followed by removal of reads mapping to the mouse genome. Through application of the Xenome algorithm[41] already cleaned reads derived from the previous step were assigned to the human and mouse genome k-mers (24 nt) to further remove contaminating mouse-derived reads. This additional processing step further improved selectivity for human and mouse mapping reads by 10%. Human-specific reads selected after the previous clean-up steps were counted and annotated to the human genome using Htseq-count[42], followed by analysis of differential gene expression applying DESeq[43] and using the R software environment. Cut-offs to determine differentially expressed genes were as follows: i) expression threshold of minimum 20 counted reads per gene (corresponds to 0.6 mRNA molecules), ii) p value and FDR <0.05, and iii) fold change ≥1.5. Gene ontology (GO)-term analysis was performed using the DAVID online platform[44,45].

Results

To enable image-guided microdisscetion, cancer cells stably expressed fluorescent markers (H2B-EGFP and DsRed2), which allowed precise isolation of the cancer cell fraction by 3D fluorescence microscopy during dissection. HT-1080 sarcoma xenografts grown intradermally in the dorsal imaging window initiated deep tissue invasion by 2-3 days after implantation

(Fig. 1B). Initiation of the angiogenic switch in the tumor core, visible through the formation of new blood vessels occurred by day 5 to 6, coinciding with exponential growth (Fig. 1B). This resulted in a well defined tumor core of ~1.5 x 2 mm with lateral invasion zones of up to 1mm length.

Cuts to perform the actual microdissection were made with so-called micro-knives having a blade width of 0.12 mm, while a micro-hook with a thickness of ≤0.25 mm was used to lift up the tumor tissue and separate it from the underlying epidermis (Fig. 1C). First, to physically separate both tumor sub-regions and minimize contamination of core cells in the invasion zone, occurring through physical perturbation onto the tumor core, two lateral incisions were made next to the core that approximately 1/8 to maximally 1/4 of an invasion strand became retained in the core fraction, including the critical transition zone (Fig. 1D, red dashed line). Due to the relative abundance of the tumor core volume, cross-contamination with invading cells was considered negligible. Subsequently, the invasion zone was separated from the surrounding tumor-free dermis by further circumferential incisions in parallel and orthogonal direction (Fig. 1D, yellow and blue dashed lines). To isolate the tumor core, further incisions were positioned at the lower and upper poles to retrieve the samples as a single tissue piece (Fig. 1D, green dashed lines). Overall, the combination of fluorescence microscopy-based guidance and employment of the micro-tools made it possible to separately isolate tumor core and invasion zones with minimal cross-contamination by dermal structures, as the lateral dermis and the underlying epidermis remained intact (Fig. 1E,F).

As standard procedure, maximum preservation of isolated tissue including integrity of nucleic acids was achieved by fast dissection (within ~10 min from initial cut perturbing blood circulation to isolation of final tissue piece) and direct sample transfer to RNA stabilization reagent. For both tumor sub-regions this yielded RNA with a quality index approximating the maximum score and hardly RNA degradation (Fig. 2A). In contrast, other preservation strategies, such as snap-freezing in liquid nitrogen, yielded inferior RNA quality (Fig. 2A). Concordant with size of the tissue chunks, amounts of RNA isolated per invasion zone sample were by 9-fold lower compared to the tumor core (Fig. 2B), though still sufficient to perform subsequent RNAseq (minimum amount ≥ 10ng), which was done for cores and invasion zones obtained from three human HT-1080 xenografts grown in three different mice.

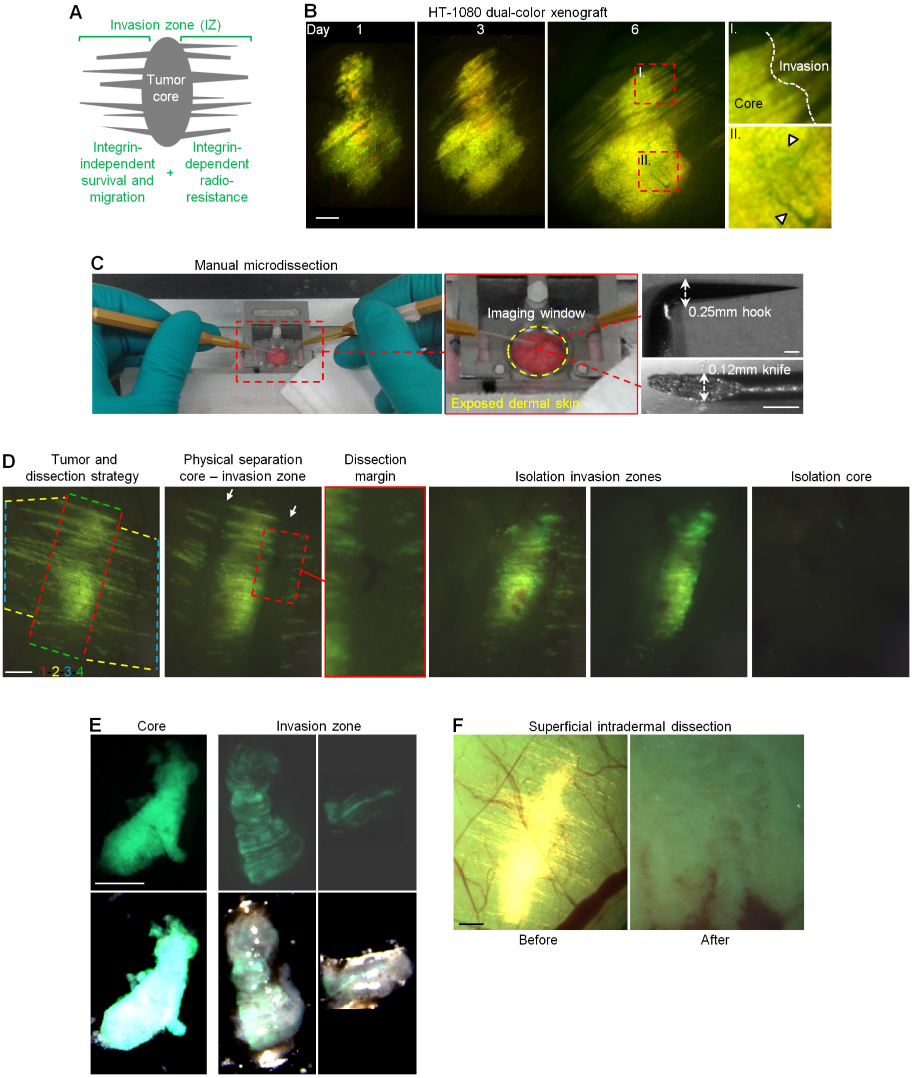

Figure 1. Microscopy-guided microdissection of fluorescent human sarcoma xenografts in the mouse dermis.
A) Differential topology and functional heterogeneity of tumor core and invasion zone in sarcoma xenografts. **B)** Epifluorescence intravital microscopy of a HT-1080 sacroma xenograft in the mouse dermis, expressing H2B-EGFP and DsRed2, monitored through an imaging window. Arrowheads, neovessels. Scale bar, 100 µm. **C)** Setup and micro-tools to perform manual microdisscetion in the dermal imaging window. Scale bar, 200 µm. **D)** Step-wise xenograft dissection and removal of invasion zone and tumor core. Coloured, dashed lines and numbers in the first panel represent (order of) performed incisions. Arrows, location of incisions post-surgery. Zoom, clean dissection margin. Scale bar, 100 µm. **E)** Isolated tissue pieces containing tumor core or invasion zone. Upper panels, xenograft-derived H2B-EGFP signal. Lower panels, overlay brightfield and H2B-EGFP signal. Scale bar, 1 mm. **F)** Microdissection and tissue isolation are confined to the dermal tissue, leaving the deeper dermis and epidermis intact. Scale bar, 100 µm.

To minimize perturbation of RNA expression by disruption of the tumor microenvironment, isolated tumor-sub-regions were not subjected to any tissue digestion or cell sorting prior to preservation. Therefore, raw sequencing reads contained both, human (xenograft-derived) and murine (stromal) RNA. To separate human from murine sequences, data processing included steps to remove contaminating reads mapping to the mouse genome (see methods section for details). Eventually, the fraction of human-specific reads retrieved from the tumor core or invasion zone was 40% and 10%, respectively, while the remaining amount of reads mapped to both, the mouse and the human reference (Fig. 2C). The fraction of reads mapping uniquely to the mouse genome, which were excluded from further analyses, was negligible small (data not shown). Because fractions of human-specific reads differed for both sub-regions, which would have biased further analyses, differential gene expression was analyzed using both, unique human and human/mouse mapped reads. The according principal component analysis (PCA) plot, did not show any co-clustering of samples derived from the same tumor sub-region (Fig. 2D). However, two paired invasion zones from the same lesion mapped closer together, as expected based on their common origin (Fig. 2D). This indicated that not exclusively the factor “tumor sub-region” accounted for inter-sample differences but independent tumor samples generally exhibited significant differences in differentially expressed genes.

As consequence of high variability observed in the PCA plot, differentially expressed genes in the respective sub-region were only obtained after lowering the expression cutoff from 50 down to 20 minimum reads in at least one of the samples and fold-change from 2 to 1.5. Six genes were identified as commonly upregulated in the invasion zone compared to the tumor core, and three genes as consistently downregulated (Fig. 2E). Gene ontology (GO) analysis for the obtained hits revealed, that except for β3 integrin which becomes (among others) associated with the GO terms “cell migration” and “cell-matrix adhesion”, all differentially expressed genes have major functions in either endothelial or muscle tissue or the blood compartment and thus, very likely, originate from the mouse stroma.

These preliminary RNAseq data obtained from human cancer cells in a mouse background using a medium sequencing depths (~30 million reads), revealed major shortcomings in identifying cancer-cell specific hits, likely caused by cross-contamination with mouse-derived RNA. However, the identification of downregulated β3 integrin in the invasion zone, which is probably xenograft-derived, was consistent between all samples indicating general feasibility of differential dissection and RNAseq analysis of tumor sub-regions.

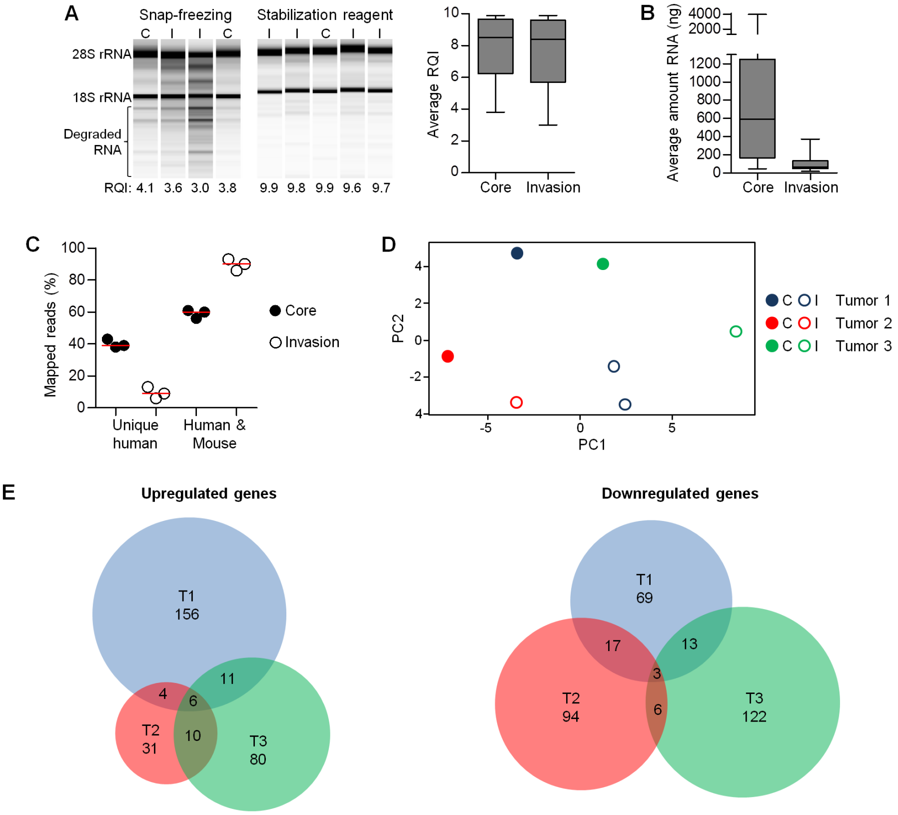

Gene ID	Gene name	Log2 Fold change (range)
ANKRD1	Ankyrin repeat domain 1	**2.8** (1.8 - 4.3)
CAV3	Caveolin 3	**3.7** (1.2 - 6.2)
DES	Desmin	**3.0** (1.0 - 5.1)
MYH1	Myosin 1	**1.3** (1.2 - 1.5)
NEB	Nebulin	**2.9** (1.2 - 4.2)
XIRP1	Xin actin-binding repaet-containing protein 1	**2.3** (1.3 - 3.2)

Gene ID	Gene name	Log2 Fold change (range)
FLVCR2	Feline leukemia virus subgroup C receptor-related protein 2	**-1.7** (-1.2 - -2.2)
ITGB3	Integrin beta 3	**-1.4** (-1.1 - -1.6)
SERPINF2	Alpha-2-antiplasmin	**-1.8** (-1.5 - -2.3)

Figure 2. Extraction of high-quality RNA from tumor sub-regions and subsequent analysis of differentially regulated genes through RNAseq.

A) Measurement of RNA degradation to estimate RNA quality. Average RNA quality index (RQI) displayed as minimum to maximum plot from 17 core and 23 invasion zone samples. C, tumor core. I, invasion zone. RQI, 1=low quality, 10=high quality. **B)** Average amount of RNA obtained per isolated tumor sub-region displayed as minimum to maximum plot from individual samples (27 cores, 34 invasion zones). **C)** Distribution of mapped reads among the mouse and human genome for each tumor sub-region derived from 3 independent xenografts. **D)** Principal component (PC) analysis of differentially regulated genes in tumor sub-regions from 3 independent xenografts. C, core. I, invasion zone. **E)** Differentially expressed (DE) genes in the invasion zone of 3 independent xenografts, displayed as Venn diagrams (top) and gene list with common DE genes and level of differential expression (bottom tables). T, tumor.

Discussion

The here developed image-based microdissection approach allows to separately isolate small sub-regions of fluorescent human xenografts, here the tumor core and the invasion zone. In contrast to other strategies, including laser dissection microscopy, fine-needle aspiration or isolation of cancer cell sub-populations through *in vitro* and *in vivo* sub-culture of surgical specimens[46–51], fluorescence-guided dissection using micro-tools enables i) isolation of clearly annotated sub-regions, through combination with intravital imaging[23,24] also with known environmental context, ii) rapid collection of live tissue followed by immediate fixation and iii) avoids cellular reprogramming events caused by loss of the native environment upon tissue digestion or cell culture conditions[52,53].

Eventual aim of this study was to perform differential gene expression profiling of both sub-regions to determine targets driving microenvironmental-induced intratumor heterogeneity. However, the preliminary transcriptome profiling by RNAseq shown here suffered from limited sensitivity and delivered largely inconclusive data. Only the downregulation of β3 integrin in the HT-1080 invasion zone can possibly be linked to a biological phenotype: as shown in chapter 5 blocking of αVβ3 integrin has no effect on the radiation-response of HT-1080 tumors in the long-term observation setting (Chapter 5, Fig. 4C), which would make sense if the target is intrinsically downregulated. Additionally, down-regulation of β3 integrin in the invasion zone of HT-1080 tumors might partially explain ongoing dissemination after integrin-targeting described in chapter 4, as invading cells might intrinsically adapt additional integrin-independent migration modes.

Since *in vitro* experiments using 3D spheroid-based invasion models resulted in almost 20 differentially expressed and functionally validated hits when performing RNAseq of samples derived from the spheroid body vs. invading cells (data not shown), *in vivo* data most likely suffer from technical limitations precluding conclusive results rather than lack of differential gene expression patterns. A major confounding factor for the *in vivo* analysis is the contained mixture of human cancer cell RNA and contaminating stroma-derived murine RNA. Although processed reads of both tumor sub-regions could be separated into two categories, i.e. uniquely mapping to the human genome and mapping to both, human and mouse genome, reads belonging to the latter category could not be neglected: the fraction of mapped human reads and thus potential target genes was >30% smaller for invasion zone samples, which would have prohibited meaningful comparative expression profiling. To overcome these limitations, technical refinements need to be implemented. First, enhancing the sequencing depth by increasing the read length might allow more specific mapping of reads to either genome thereby cleaning the human RNA-derived reads from the murine RNA-derived reads. Although a first attempt including a switch from 43bp to 75bp length (maximum of the sequencing platform used here) did not affect the specificity (data not shown), switching to another platform allowing reads up to 300bp still remains an option[54]. Second, the relative enrichment of fluorescent marker-derived RNA could be retrieved, to estimate the relative amount of human cancer cells in either isolated fraction. Prerequisite would be a standard generated by mixing defined proportions of digested stromal tissue and fluorescent tumor cells, followed by RNAseq to determine the amount of reads mapping to fluorescent markers for each defined stroma:tumor ratio. Eventually, reads mapping to both the human and mouse genome could be redivided, with the amount correlating with a certain number of fluoresecent marker reads being counted as human, while the remaining reads would be regarded as mouse-derived.

Third, if bioinformatic strategies fail to reach further exclusion of contaminating murine RNA-derived reads, physical removal of mouse-derived cells before RNA isolation would allow to increase specificity. The possibilities include enzymatic tissue digestion followed by fluorescence-activated cell sorting (FACS) of fluorescent and non-fluorescent cells[31] or, in case of very small specimens, single cell aspiration of fluorescent tumor cells cells[55] or single-cell sequencing approaches combined with image-based selection of each individual cell[56]. However, as tissue digestion would introduce a delay between cell isolation and fixation, expression profiling after physical separation of human and murine cells may include artifacts caused by gene expression changes associated with tissue dissolution[52]. To overcome this, RNA polymerase inhibitors like α-amanitin & actinomycin D could be added to enzymatic solutions and sorting buffers[31], delivering a valuable opportunity to physically separate mouse and human tissue while preserving the native expression profiles of tumor core and invasion zone immediately after tissue dissection for subsequent expression profiling including only human-specific reads. Apart from focusing on the tumor lesion, clear separation of human and mouse-derived hits would also enable in depth profiling of the according stroma, possibly combined with antibody-based enrichment for stromal cell subsets like endothelial cells (e.g CD31)[57] or cancer associated fibroblasts (e.g. α-SMA)[58]. Eventually, independent of the final approach to resolve confounding similarity between human and mouse-derived reads, analysis of both, tumor sub-regions and the according stroma, will help to understand development of microenvironmentally- induced intratumor heterogeneity.

Besides the spatial factor, another factor co-determining (the extent of) intratumor heterogeneity has not been investigated here, i.e. tumor progression over time. Although the incipient lesions used to establish the image-guided microdissection approach had undergone the angiogenic switch and onset of invasion, exponential growth had just initiated and invasion may persist till day 9 and thereafter[23]. Thus, as both sub-regions independently progress further, the level of heterogeneity in older lesions probably differs from incipient lesions. However, to investigate this, the microdissection of progressed xenografts requires further refinement: The internal pressure of the tumor core increases the larger it grows, and therefore passive drift of core cells into the invasion zone or rupture of the tumor main mass needs to be prevented, e.g.

through puncture of the tumor main mass followed by aspiration of tumor cells. Apart from that, additional optimization of the microscopy-based microdissection approach might allow to isolate sub-regions within the invasion zone, including leader and follower cells of a collective strand, individually detached cells or the transition zone between tumor core and invasion zone. As technically limiting factors the available microscopic magnification, size of the micro-tools and the possibility to aspirate (single) cells will determine whether subsets of the invasion zone can be reliably isolated from defined niches intravitally.

Beyond RNAseq, the isolation strategy described here may also be suitable for assessing epigenetic or proteome changes in tumor sub-regions, and thereby derive multi-scale information on differences in invasion-associated reprogramming and therapy response of cancer cells[47,59–62]. As the invasion zone maximally consists of a few thousand cells, the applicability will depend upon the sensitivity of the detection strategy[63–65].

In summary differential gene expression analysis of tumor sub-regions including both the tumor and stromal cell fraction will eventually contribute to the identification of targets driving tumor cell reprogramming, dissemination or therapeutic resistance. Although technical shortcomings currently constitute relative bottlenecks, improved sensitivity of gene expression profiling and single-cell approaches will eventually help to resolve these issues to enable the identification of mechanisms underlying intratumor heterogeneity[66–69].

Acknowledgments

This work was supported by NWO-Vici (918.11.626), the European Research Council (617430-DEEPINSIGHT), and the Cancer Genomics Center (CGC.nl) to PF. Work of AH was supported by the PhD fellowship program of the Radboudumc, Nijmegen, The Netherlands.

We gratefully acknowledge Manon Vullings, Huib Croes and Gert-Jan Bakker for expert experimental and logistic support.

References

1. Swanton, C. Intratumor Heterogeneity: Evolution through Space and Time. *Cancer Res.* **72,** 4875–4882 (2012).
2. Nowell, P. C. The clonal evolution of tumor cell populations. *Science* **194,** 23–8 (1976).
3. McGranahan, N. & Swanton, C. Clonal Heterogeneity and Tumor Evolution: Past, Present, and the Future. *Cell* **168,** 613–628 (2017).
4. O'Connor, J. P. B. *et al.* Imaging Intratumor Heterogeneity: Role in Therapy Response, Resistance, and Clinical Outcome. *Clin. Cancer Res.* **21,** 249–257 (2015).
5. Gerlinger, M. *et al.* Intratumor Heterogeneity and Branched Evolution Revealed by Multiregion Sequencing. *N. Engl. J. Med.* **366,** 883–892 (2012).
6. Szerlip, N. J. *et al.* Intratumoral heterogeneity of receptor tyrosine kinases EGFR and PDGFRA amplification in glioblastoma defines subpopulations with distinct growth factor response. *Proc. Natl. Acad. Sci.* **109,** 3041–3046 (2012).
7. Hirata, E. *et al.* Intravital imaging reveals how BRAF inhibition generates drug-tolerant microenvironments with high integrin beta1/FAK Signaling. *Cancer Cell* **27,** 574–588 (2015).
8. Burrell, R. A., McGranahan, N., Bartek, J. & Swanton, C. The causes and consequences of genetic heterogeneity in cancer evolution. *Nature* **501,** 338–345 (2013).
9. Junttila, M. R. & de Sauvage, F. J. Influence of tumour micro-environment heterogeneity on therapeutic response. *Nature* **501,** 346–54 (2013).
10. Friedl, P. & Alexander, S. Cancer invasion and the microenvironment: plasticity and reciprocity. *Cell* **147,** 992–1009 (2011).
11. Yancovitz, M. *et al.* Intra- and Inter-Tumor Heterogeneity of BRAFV600EMutations in Primary and Metastatic Melanoma. *PLoS One* **7,** e29336 (2012).
12. Navin, N. *et al.* Tumour evolution inferred by single-cell sequencing. *Nature* **472,** 90–94 (2011).
13. Mazor, T., Pankov, A., Song, J. S. & Costello, J. F. Intratumoral Heterogeneity of the Epigenome. *Cancer Cell* **29,** 440–451 (2016).
14. Gerlitz, G. & Bustin, M. The role of chromatin structure in cell migration. *Trends Cell Biol.* **21,** 6–11 (2011).
15. Taddei, M. L., Giannoni, E., Comito, G. & Chiarugi, P. Microenvironment and tumor cell plasticity: An easy way out. *Cancer Lett.* **341,** 80–96 (2013).
16. Ell, B. & Kang, Y. Transcriptional control of cancer metastasis. *Trends Cell Biol.* **23,** 603–611 (2013).
17. Gerlitz, G. & Bustin, M. Efficient cell migration requires global chromatin condensation. *J. Cell Sci.* **123,** 2207–2217 (2010).
18. Zhang, X. *et al.* Integrin α4β1 controls G9a activity that regulates epigenetic changes and nuclear properties required for lymphocyte migration. *Nucleic Acids Res.* **44,** 3031–3044 (2016).
19. Heinecke, J. L. *et al.* Tumor microenvironment-based feed-forward regulation of NOS2 in breast cancer progression. *Proc. Natl. Acad. Sci.* **111,** 6323–6328 (2014).
20. Smith, M. P. *et al.* The Immune Microenvironment Confers Resistance to MAPK Pathway Inhibitors through Macrophage-Derived TNF. *Cancer Discov.* **4,** 1214–1229 (2014).
21. Sun, Y. *et al.* Treatment-induced damage to the tumor microenvironment promotes prostate cancer therapy resistance through WNT16B. *Nat. Med.* **18,** 1359–1368 (2012).
22. Barker, H. E., Paget, J. T. E., Khan, A. A. & Harrington, K. J. The tumour microenvironment after radiotherapy: mechanisms of resistance and recurrence. *Nat. Rev. Cancer* **15,** 409–425 (2015).
23. Alexander, S., Koehl, G. E., Hirschberg, M., Geissler, E. K. & Friedl, P. Dynamic imaging of cancer growth and invasion: a modified skin-fold chamber model. *Histochem. Cell Biol.* **130,** 1147–54 (2008).

24. Weigelin, B., Bakker, G.-J. & Friedl, P. Intravital third harmonic generation microscopy of collective melanoma cell invasion: Principles of interface guidance and microvesicle dynamics. *IntraVital* **1,** 32–43 (2012).

25. Yeung, T.-L. *et al.* TGF-Beta Modulates Ovarian Cancer Invasion by Upregulating CAF-Derived Versican in the Tumor Microenvironment. *Cancer Res.* **73,** 5016–5028 (2013).

26. Odenthal, J., Takes, R. & Friedl, P. Plasticity of tumor cell invasion: governance by growth factors and cytokines. *Carcinogenesis* **37,** 1117–1128 (2016).

27. Holton, S. E., Bergamaschi, A., Katzenellenbogen, B. S. & Bhargava, R. Integration of Molecular Profiling and Chemical Imaging to Elucidate Fibroblast-Microenvironment Impact on Cancer Cell Phenotype and Endocrine Resistance in Breast Cancer. *PLoS One* **9,** e96878 (2014).

28. Hu, M. *et al.* Distinct epigenetic changes in the stromal cells of breast cancers. *Nat. Genet.* **37,** 899–905 (2005).

29. Byron, S. A., Van Keuren-Jensen, K. R., Engelthaler, D. M., Carpten, J. D. & Craig, D. W. Translating RNA sequencing into clinical diagnostics: opportunities and challenges. *Nat. Rev. Genet.* **17,** 257–271 (2016).

30. Wang, Z., Gerstein, M. & Snyder, M. RNA-Seq: a revolutionary tool for transcriptomics. *Nat. Rev. Genet.* **10,** 57–63 (2009).

31. Chuang, C.-H. *et al.* Molecular definition of a metastatic lung cancer state reveals a targetable CD109–Janus kinase–Stat axis. *Nat. Med.* **23,** 291–300 (2017).

32. Gerber, T. *et al.* Mapping heterogeneity in patient-derived melanoma cultures by single-cell RNA-seq. *Oncotarget* **8,** 846–862 (2016).

33. Le Pennec, S. *et al.* Intratumor heterogeneity and clonal evolution in an aggressive papillary thyroid cancer and matched metastases. *Endocr. Relat. Cancer* **22,** 205–216 (2015).

34. Alexander, S., Weigelin, B., Winkler, F. & Friedl, P. Preclinical intravital microscopy of the tumour-stroma interface: invasion, metastasis, and therapy response. *Curr. Opin. Cell Biol.* **25,** 659–71 (2013).

35. Weigelin, B., Bakker, G.-J. & Friedl, P. Third harmonic generation microscopy of cells and tissue organization. *J. Cell Sci.* **129,** 245–55 (2016).

36. Rasheed, S., Nelson-Rees, W. A., Toth, E. M., Arnstein, P. & Gardner, M. B. Characterization of a newly derived human sarcoma cell line (HT-1080). *Cancer* **33,** 1027–33 (1974).

37. Yamamoto, N. *et al.* Cellular dynamics visualized in live cells in vitro and in vivo by differential dual-color nuclear-cytoplasmic fluorescent-protein expression. *Cancer Res.* **64,** 4251–6 (2004).

38. Picelli, S. *et al.* Full-length RNA-seq from single cells using Smart-seq2. *Nat. Protoc.* **9,** 171–181 (2014).

39. Langmead, B. & Salzberg, S. L. Fast gapped-read alignment with Bowtie 2. *Nat. Methods* **9,** 357–9 (2012).

40. Wu, T. D. & Nacu, S. Fast and SNP-tolerant detection of complex variants and splicing in short reads. *Bioinformatics* **26,** 873–81 (2010).

41. Conway, T. *et al.* Xenome--a tool for classifying reads from xenograft samples. *Bioinformatics* **28,** i172-8 (2012).

42. Anders, S., Pyl, P. T. & Huber, W. HTSeq--a Python framework to work with high-throughput sequencing data. *Bioinformatics* **31,** 166–9 (2015).

43. Anders, S. & Huber, W. Differential expression analysis for sequence count data. *Genome Biol.* **11,** R106 (2010).

44. Huang, D. W., Sherman, B. T. & Lempicki, R. A. Bioinformatics enrichment tools: paths toward the comprehensive functional analysis of large gene lists. *Nucleic Acids Res.* **37,** 1–13 (2009).

45. Huang, D. W., Sherman, B. T. & Lempicki, R. A. Systematic and integrative analysis of large gene lists using DAVID bioinformatics resources. *Nat. Protoc.* **4,** 44–57 (2009).

46. Tomonaga, N. *et al.* Analysis of Intratumor Heterogeneity of EGFR Mutations in Mixed Type Lung Adenocarcinoma. *Clin. Lung Cancer* **14,** 521–526 (2013).

47. Sugihara, Y. *et al.* Laser microdissection and two-dimensional difference gel electrophoresis reveal proteomic intra-tumor heterogeneity in colorectal cancer. *J. Proteomics* **78,** 134–147 (2013).

48. Roussos, E. T. *et al.* Mena invasive (Mena(INV)) and Mena11a isoforms play distinct roles in breast cancer cell cohesion and association with TMEM. *Clin. Exp. Metastasis* **28,** 515–27 (2011).

49. Galli, R. *et al.* Isolation and Characterization of Tumorigenic, Stem-like Neural Precursors from Human Glioblastoma. *Cancer Res.* **64,** 7011–21 (2004).

50. Morikawa, K., Walker, S. M., Jessup, J. M. & Fidler, I. J. In Vivo Selection of Highly Metastatic Cells from Surgical Specimens of Different Primary Human Colon Carcinomas Implanted into Nude Mice. *Cancer Res.* **48,** 1943–8 (1988).

51. Nagasawa, T., Sugai, T., Shoji, T., Habano, W. & Sugiyama, T. Molecular Analysis of Single Tumor Glands Using the Crypt Isolation Method in Endometrial Carcinomas. *Int. J. Gynecol. Cancer* **26,** 1658–1666 (2016).

52. Richardson, G. M., Lannigan, J. & Macara, I. G. Does FACS perturb gene expression? *Cytom. Part A* **87,** 166–175 (2015).

53. Daniel, V. C. *et al.* A Primary Xenograft Model of Small-Cell Lung Cancer Reveals Irreversible Changes in Gene Expression Imposed by Culture In vitro. *Cancer Res.* **69,** 3364–3373 (2009).

54. Metzker, M. L. Sequencing technologies — the next generation. *Nat. Rev. Genet.* **11,** 31–46 (2010).

55. Möhlendick, B. *et al.* A robust method to analyze copy number alterations of less than 100 kb in single cells using oligonucleotide array CGH. *PLoS One* **8,** e67031 (2013).

56. Chung, W. *et al.* Single-cell RNA-seq enables comprehensive tumour and immune cell profiling in primary breast cancer. *Nat. Commun.* **8,** 15081 (2017).

57. Carmeliet, P. & Jain, R. K. Angiogenesis in cancer and other diseases. *Nature* **407,** 249–257 (2000).

58. Shiga, K. *et al.* Cancer-Associated Fibroblasts: Their Characteristics and Their Roles in Tumor Growth. *Cancers (Basel).* **7,** 2443–58 (2015).

59. Brocks, D. *et al.* Intratumor DNA Methylation Heterogeneity Reflects Clonal Evolution in Aggressive Prostate Cancer. *Cell Rep.* **8,** 798–806 (2014).

60. Torres, C. M. *et al.* The linker histone H1.0 generates epigenetic and functional intratumor heterogeneity. *Science (80-.).* **353,** aaf1644-aaf1644 (2016).

61. Spagnolo, D. *et al.* Pointwise mutual information quantifies intratumor heterogeneity in tissue sections labeled with multiple fluorescent biomarkers. *J. Pathol. Inform.* **7,** 47 (2016).

62. Varley, K. E., Mutch, D. G., Edmonston, T. B., Goodfellow, P. J. & Mitra, R. D. Intra-tumor heterogeneity of MLH1 promoter methylation revealed by deep single molecule bisulfite sequencing. *Nucleic Acids Res.* **37,** 4603–4612 (2009).

63. Pisanic, T. R. *et al.* DREAMing: a simple and ultrasensitive method for assessing intratumor epigenetic heterogeneity directly from liquid biopsies. *Nucleic Acids Res.* **43,** e154–e154 (2015).

64. Balluff, B., Hanselmann, M. & Heeren, R. Mass Spectrometry Imaging for the Investigation of Intratumor Heterogeneity. *Adv. Cancer Res.* **134,** 201–230 (2017).

65. Bolduc, N., Lehman, A. P. & Farmer, A. Preparation of Low-Input and Ligation-Free ChIP-seq Libraries Using Template-Switching Technology. *Curr. Protoc. Mol. Biol.* **116,** 7.28.1-7.28.26 (2016).

66. Tirosh, I. *et al.* Dissecting the multicellular ecosystem of metastatic melanoma by single-cell RNA-seq. *Science (80-.).* **352,** 189–196 (2016).

67. Han, L. *et al.* Co-detection and sequencing of genes and transcripts from the same single cells facilitated by a microfluidics platform. *Sci. Rep.* **4,** 6485 (2015).

68. Tellez-Gabriel, M., Ory, B., Lamoureux, F., Heymann, M.-F. & Heymann, D. Tumour Heterogeneity: The Key Advantages of Single-Cell Analysis. *Int. J. Mol. Sci.* **17,** E2142 (2016).

69. Alizadeh, A. A. *et al.* Toward understanding and exploiting tumor heterogeneity. *Nat. Med.* **21,** 846–53 (2015).

Chapter 7

Summary, Discussion and Implications

Anna Haeger, Stephanie Alexander and Peter Friedl

Partially published in modified form in:
EJC Suppl. 2013 Sep;11(2):291-3

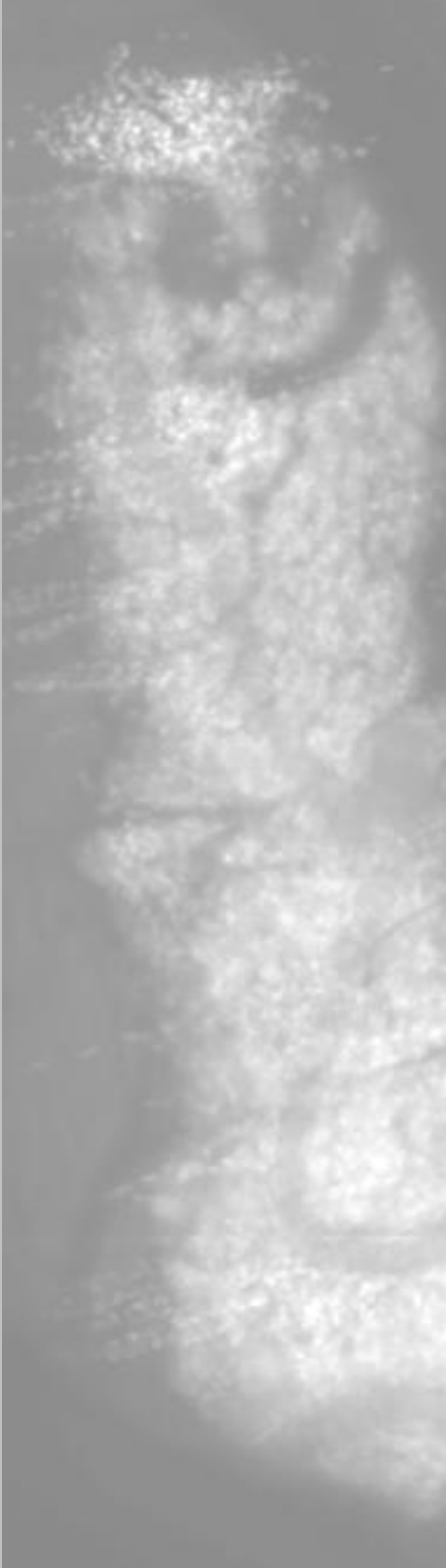

Metastatic cancer progression is mediated by both single-cell and/or collective mechanisms, including local tissue invasion, entry into blood and/or lymph vessels, circulation, exit at distant sites and finally outgrowth of a metastatic lesion[1]. Simultaneously, with each step of the metastatic cascade, cancer cells enter and reciprocally interact with distinct micro-environments, undergo adaptation, and likely adopt differential behavior, despite the fact that they usually derive from a single mutant cell clone[2,3]. Focusing on mesenchymal tumor types, in this thesis mechanisms of tumor cell dissemination and therapeutic resistance were investigated, using *in vitro* spheroid and *in vivo* xenograft models.

Besides cancer invasion and metastasis, collective cell movement contributes to cell migration in morphogenesis and tissue repair[4]. **Chapter 2** addresses guidance mechanisms in collective migration, which comprise a fundamental feature to coordinate and maintain joint translocation of the moving cell groups with retained cell–cell contacts. Guidance principles employed during collective migration include the topography and/or stiffness of the environment (contact guidance), physical cues like fluid-flow induced shear stress or passive drift as well as chemical cytokine-based and electrical ion-channel stimulating cues, which are often present as a gradient. Subsequently migrating cell groups needs to integrate and prioritize guidance signals, which act in parallel and, combined with cell-intrinsic migration programs, steer and determine plasticity of (collective) migration.

In **chapter 3** *in* vitro experiments in 3D tissue cultures addressed whether and how topographic cues including matrix density and stiffness control single-cell and collective migration modes of mesenchymal sarcoma and melanoma cells. The data show that with increasing matrix density cells switched from individual to collective movement. Collective invasion is established for cells of epithelial origin but remains controversial for mesenchymal cell types which usually lack strong cell-cell cohesion and rather migrate individually in loose extracellular matrix (ECM). However, in confining ECM which forces leader cells to proteolytically cleave the dense matrix and generate tracks of least resistance, mesenchymal cells become “jammed” which subsequently promotes cell-cell junction formation and the acquisition of collective polarity. Thus, topographic confinement underlies a collective invasion phenotype of mesenchymal tumor cells. Accordingly, unconfined conditions (i.e. a loose matrix) support single cell migration, identifying matrix density as critical determinant for migration plasticity of mesenchymal cell types, which is further not affected by matrix rigidity.

Apparently, the concept of confinement-induced collectivity overlaps with the concept of cell jamming: But, whereas the jamming concept describes the transition from a collectively mobile to a stable, non-moving state[5,6], the results from 3D culture in mesenchymal cells indicate that confinement-induced collective movement still represents a partially jammed state, which is abandoned once cells fully individualize. Jammed rather than fluidized states in confinement-induced collective migration include the initial phase prior to onset of migration, when leader cells have to cleave tracks which are not preexisting in randomly polymerized high-density 3D collagen matrices. Likewise, follower cells which pile up behind track-forming leader cells and experience lateral geometric confinement resemble a jammed state. Accordingly, confinement-induced collective migration of both leader and follower cells should be appreciated as consequence of partial cell jamming.

In **chapter 4** the collective invasion phenotype of mesenchymal tumor cells observed *in vitro* was confirmed *in vivo* when studying the process of sarcoma and melanoma invasion in the orthotopic dermal environment using single-cell resolved multiphoton microscopy. Accordingly, the interfaces present *in vivo* between tissue structures such as muscle fibers and blood vessels enabled the cells to maintain collective movement even in the absence of β1 and αVβ3 integrin-mediated cell-matrix anchorage, although integrin depletion generally went along with an increased probability towards single cell migration. This identifies integrin availability in cooperation with matrix density, as independent determinant of migration plasticity in mesenchymal cell types. Contradicting the common assumption that integrins are indispensable for metastatic dissemination[7], integrin-independent individual and collective migration of sarcoma and melanoma cells further contributed to the formation of distant lung metastases and an even enhanced seeding frequency. However, as integrin-mediated anchorage comprises an essential source of pro-survival signals, similar to the primary tumor lesion disseminated cancer cells failed to grow out and develop macrometastases when integrins were not available. These findings suggest that collective migration represents an invasion mode of high cellular and molecular order that, after loss of integrin function, interconverts to single-cell dissemination and metastasis, similar to previous evidence from tumor explant models[8]. Therefore, application of integrin-targeted cancer therapies, which were designed based on established growth-and dissemination promoting properties of various integrin sub-types[7], may be confounded by cell release and enhanced systemic dissemination, at least in mesenchymal tumor types.

In **chapter 5** the collective invasion niche of sarcoma and melanoma xenografts was further characterized by mapping its sensitivity towards genotoxic radiotherapy. Remarkably collective invasion strands were identified as radioresistant, whereas cells in the tumor core underwent apoptosis upon application of fractionated high-dose irradiation. Analysis of the DNA damage response (DDR) in both tumor sub-regions revealed similar amounts of irradiation-induced DNA double-strand breaks which were however cleared more rapidly and efficiently in the collective invasion zone. By comparison, persisting DDR signals in the tumor core indicated ill-fated attempts of DNA repair eventually followed by apoptosis induction. As mediators of anchorage-dependent pro-survival signals integrins have been implicated in mediating radiation resistance[9–12]. As detailed in **chapter 4**, the emergence and survival of the invasion zones of sarcoma and melanoma xenografts were largely insensitive to β1 and αVβ3 depletion, which accounts for the only integrin β subtypes expressed by the tumor models used. However, upon additional radiotherapy both the tumor core and the invading cell fraction underwent apoptosis followed by regression of the entire lesion, indicating that therapeutic resistance in the collective niche depends upon integrin-dependent pro-survival signaling and stimulation of DNA repair. Notably, single-chain integrin-targeting strategies to overcome radioresistance in (pre)clinical settings were reported as incompletely effective thus far[13], which may result from compensation by other integrin family members. In contrast, dual-integrin targeting addressing all available β integrin sub-types as described in **chapter 5** effectively ablated invasion-associated radioresistance and successfully eradicated ≥ 80% of tumor lesions in a preclinical long-term study, hence introducing multiple integrin-targeting as successful strategy to (re)consider application of integrin-based anti-cancer therapy.

Whereas **chapter 3** identified the mechanism of confinement-induced collective invasion of mesenchymal sarcoma and melanoma tumors, **chapter 4 and 5** subsequently revealed that, compared to the tumor core, this collective invasion zone exhibits remarkable differences regarding the dependency on integrin-mediated pro-survival signals as well as sensitivity to genotoxic treatment. Obviously, both tumor sub-regions differ in their organization and perception of the microenvironment and their cellular state (motile vs. static); however, which of these differences drive this sub-regional tumor heterogeneity and by which mechanism remains unresolved thus far. To address the molecular profiles of tumor sub-regions identified by intravital microscopy, **chapter 6** describes the establishment of an image-based microdissection approach to separately isolate in live tissue tumor core and invasion zone of human sarcoma and melanoma xenografts grown in the mouse dermis for subsequent expression profiling by RNAseq. Whereas the separation and isolation of tumor sub-regions was technically successful, meaningful interpretation of global expression profiling data still suffered from the rather large amount of mouse stromal background contaminating the human cancer cell fraction. Thus further technical improvement of RNAseq procedures and in particular data processing is needed to better delineate gene candidates driving integrin dependency of radiation resistance and other oncogenic processes in the collective invasion zone.

Plasticity of migration – mechanisms and implications for metastasis formation

Similar to actomyosin-based single-cell migration, collective migration is plastic, i.e. it undergoes modification with altered intracellular signaling or an altered environment[14]. Accordingly, in this thesis (**chapter 3 and 4**) for two mesenchymal cancer cell models matrix density and integrin availability were identified as important modulators of migration plasticity, stimulating either individual or collective migration. A similar range of migration mode plasticity has thus far primarily been reported for epithelial models: single-cell migration emerging after dissolution of cell-cell junctions follows two types of conversions that are currently known – the epithelial–mesenchymal transition (EMT) and the collective–amoeboid transition (CAT)[15–19]. EMT is a well established molecular process that leads to the down-modulation of cell–cell adhesion, whereby the migration machinery remains intact, which induces single-cell detachment and scattering from multicellular groups[2,16,20]. For mesenchymal cells, based on their intrinsic characteristics, the direction of migration mode conversion is actually reversed: they typically migrate as individualized cells but, as shown in **chapter 3**, switch to collective migration if they enter a confined matrix. Furthermore, as they readily switch back to single-cell migration modes in unconfined environments, conversions happen rather instantaneous and are likely not regulated by cellular reprogramming events like EMT[16]. Beyond this, integrin depletion in confined conditions is another factor stimulating a conversion from collective movement to single cell detachment, which even broadens the range of migrational plasticity in mesenchymal cells. Whereas in epithelial models single-cell detachment is enabled by reduced cadherin expression, loss-of-function mutations in cadherin and catenin signaling pathways, or deregulated function of proteases degrading cadherins and other cell–cell adhesion molecules[21–23], mechanisms regulating the switch towards single-cell migration after integrin loss in mesenchymal cells require further investigation. Fitting the broad range of implications of integrin-mediated downstream signaling[24–26] it has been shown that via so-called "adhesive cross-talk" integrins mediate upregulation of cadherins and thus stimulate formation of cadherin-based cell-cell adhesion[27–29]. Accordingly, loss of integrin function may promote the dissolution of cadherin-based junctions. Furthermore, integrins must be considered as further, direct or indirect, junctional gatekeepers. Thus far they have been shown to contribute to cell-cell attachment indirectly via intercellular deposits of the matrix components fibronectin or laminin[30–32], or through interaction with laminins and the tetraspanin CD151[33]. Direct integrin-integrin-based cellular junctions have not been revealed yet but nevertheless numerous possibilities account for the interplay between integrin availability and switch between single-cell and collective migration modes in mesenchymal cells.

CAT is the transition from collective invasion to amoeboid single-cell crawling after simultaneous weakening of cell–cell and cell–matrix interactions in epithelial and mesenchymal tumor cells *in vitro*[8,18,19]. The observation described in **chapter 4**, that decreased cellular elongation after integrin targeting in sarcoma and melanoma cells *in vitro* and *in vivo* follows the above-mentioned switch from collective to single-cell migration, and consecutive cell rounding after detachment from the group, validates the presence of similar CAT mechanisms for mesenchymal models *in vivo*. Importantly, this intgrin-low to integrin-independent movement is still sufficient to execute the entire metastatic cascade, for which integrins were thus far described as indispensable[7]. Apart from ECM, the tumor micro-environment contains various stromal cells[34], which are able to form homo- and heterotypic junctions with cancer cells like N-cadherin-mediated interactions between cancer and endothelial cells or cadherin-23-based adhesion between cancer cells and fibroblasts[35,36]. These interactions together with the cellular glycocalix may support friction-based force transmission as mechanism underlying integrin-independent movement[37]. Additionally, CD44 and discoidin domain receptors (DDRs) constitute alternative adhesion systems enabling migrating cells to interact with matrix components like collagens or hyaloronic acid[38–41], potentially promoting integrin-independent migration. Via selectins expressed on endothelial cells, leukocytes and platelets cancer cells have numerous integrin-independent possibilities of interaction when crossing the endothelial barrier and entering the hematogeneous phase of the metastatic cascade[7,42]. Cluster formation with leukocytes and/or platelets not only protects disseminating cancer cells from shear stress but also promotes arrest in small capillaries of distant organs[1,43–45], followed by extravasation. Granulae-release by platelets and selectin-based interactions between cancer cells and the endothelium might activate inflammatory pathways which increase permeability of the endothelial wall and thus facilitate extravasation[46,47]. Eventually, these mechanisms may coexist with integrin-dependent migration and dissemination, and gain dominance once integrin expression and function are downregulated. In aggregate, the results in this thesis indicate an important anchorage function for integrins, which limits cell dissemination and metastatic progression, consistent with enhanced dissemination after integrin targeting in certain other models[48–50].

Overall, both epithelial and mesenchymal models thus exhibit a broad range of migration plasticity and basically every described migration mode might contribute to metastatic dissemination. But, whereas collective migration increases efficiency with regard to metastatic outgrowth[51–53], single cell migration and especially integrin-independent migration rather promote the seeding frequency with single cells persisting for weeks without dividing (dormancy phenotype)[50,54]. Beyond this, understanding of the signals maintained by simultaneous cell–cell and cell–matrix communication during cancer cell invasion and secondary plasticity will be important in defining the cross-talk between strategies of invasion and resistance signaling[55].

Joint mechanisms of cancer invasion and resistance

Based on the multiple inputs from the tumor microenvironment and their overlapping signaling pathways, invasive tumor-cell migration and survival stimulation can be considered as interconnected cell functions. As a particular challenge, in collective invasion the joint signaling from tissue structures and cell–cell junctions may activate survival pathways not engaged in quiescent, non-invading tumor regions, eventually supporting resistance as shown in **chapter 5**. Thereby, the residual niches that withstand targeting of conventional therapy can consist of a limited number of cells which, after surviving cycles of therapies, re-grow, initiate migration and thereby re-establish an invasive tumor. The signals required for both single-cell and collective cancer invasion include the activation of integrins, cadherins, small GTPases Rac and Rho, as well as Ras pathways, and the engagement of intracellular signaling networks that include phosphatidylinositide 3-kinase (PI3K), mechanistic Target of Rapamycin (mTOR), Src- and mitogen-activated protein (MAP)- kinases[55–61] (Fig. 1). Simultaneously, these pathways also control cell growth and survival[24,55,60,62,63].

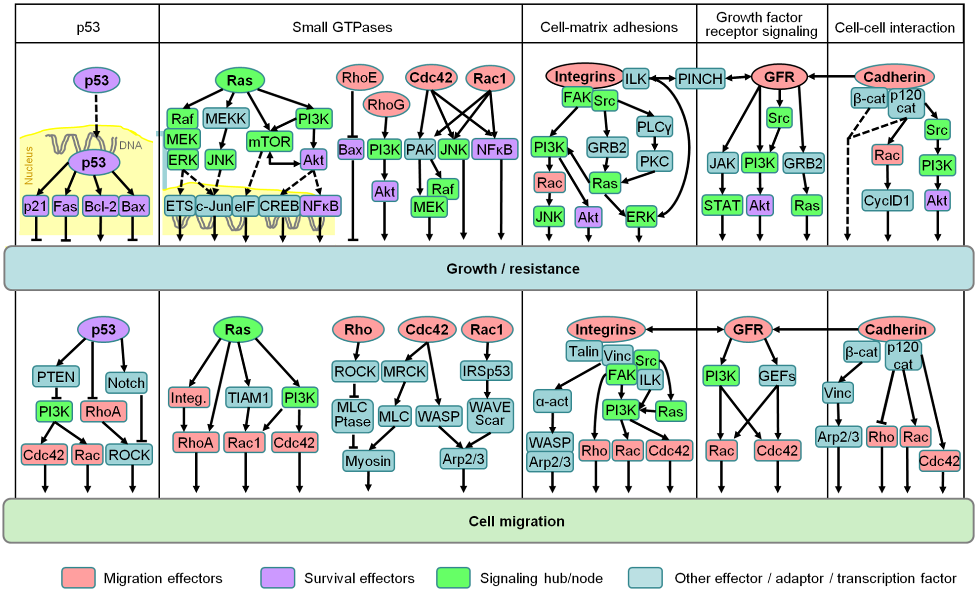

Figure 1. Signaling pathways controlling tumour cell growth, survival and invasion.
Example pathways of p53, Ras GTPase, small Rho GTPases, integrins, growth factor receptors and cadherins with a dual role in controlling cell growth (upper row) and survival as well as cell migration and invasion (lower row). Migration effectors are marked in pink, survival effectors in purple, signaling hubs in bright green. Arrows indicate signaling direction. Bound to DNA, transcription factors. a-Act., a-actinin; cat, catenin; Cdc42, cell division cycle 42; CREB, cAMP response element-binding; CyclD1, cyclin D1; eIF, eukaryotic initiation factor; ERK, extracellular signal-related kinase; ETS, erythroblast transformation specific (transcription factor); FAK, focal adhesion kinase; GEF, guanine nucleotide exchange factor; GFR, growth factor receptor; GRB2, growth factor receptor-bound protein 2; ILK, integrin-linked kinase; Integ., integrin; JNK, Janus-kinase; MEK, mitogen-activated protein kinase/extracellular signal-regulated kinase kinase; MEKK, MEK kinase; MLC, myosin light chain; MLCPtase, MLC phosphatase; MRCK, myotonic dystrophy kinase-related Cdc42-binding kinase; NFκB, nuclear factor ‘kappa-light-chain-enhance’ of activated B cells; PAK, p21-activated kinase; PINCH, particularly interesting Cys–His-rich protein; PKC, protein kinase C; PLCγ, phospholipase γ; PTEN, phosphatase and tensin homologue; ROCK, Rho-activated kinase; STAT, signal tranducer and activator of transcription; TIAM1, T-cell lymphoma invasion and metastasis 1; Vinc, vinculin; WASP, Wiskott–Aldrich syndrome protein; WAVE, WASPfamily Verprolin-homologous protein.
Figure also displayed and discussed in detail in: Alexander, S. & Friedl, P. Cancer invasion and resistance: Interconnected processes of disease progression and therapy failure. Trends Mol. Med. ***18,*** *13–26 (2012).*

Consequently, druggable signaling hubs that may serve to target both tumor invasion and resistance include growth factor and chemokine signaling, integrin engagement, as well as downstream Ras/MAPKs, PI3K and mTOR signaling[12,60,64–68]. The effects of integrin-targeted therapy on metastatic dissemination and resistance in sarcoma and melanoma models have been investigated in **chapter 4 and 5** of this thesis, however with increased dissemination after integrin targeting on the one hand but otherwise integrin-dependent radioresistance, responses were differential, requiring further elaboration of targeting strategies.

Intratumor sub-regional heterogeneity – implications for (integrin-targeted) therapy

In a progressing tumor undergoing metastatic dissemination essentially each step of the metastatic cascade represents an anatomic and molecular "sub-compartment", i.e. the primary tumor core, the invasion zone, circulating tumor cells (CTCs) and the metastatic lesion [1,2,69,70]. The *in vivo* results in **chapter 4 and 5** indicate that radiation and integrin-targeted therapy reach different efficacy for tumor sub-regions: radiotherapy causes regression of the tumor main mass while the invading cells survive with dissemination unaffected (Fig. 2). Similarly, upon integrin mono-targeting the tumor core and metastatic colonies in the lung have a major growth deficit and even may regress whereas the invasion zone remains largely intact but dissemination rate even increases (Fig. 2). These findings emphasize the need for preclinical therapy approaches, which dissect the therapy response for each step of the metastatic cascade, e.g. by using a combination of intravital imaging, blood sampling and microscopic metastasis screens. Conclusions about therapy efficiency based on the sole interpretation of effects observed for the primary lesion could lead to detrimental outcome in a patient: both the radiotherapy and integrin-targeting approach would have been interpreted as "successful" due to regressing bulk lesions, however applied in the patient resistant cell clones present in the invasive tumor margin or therapy-induced dormant, disseminated cells which may grow out after therapy completion may negatively impact prognosis.

Beyond the joint mechanisms of cancer invasion and resistance, differences in the microenvironment of each tumor sub-region further account for differential therapeutic responses[2,34,55,71–73]. For tumors growing in the deep dermis or at the metastatic site, the core mainly consists of densely packed tumor cells interspersed with (neo)vessels and likely tumor associated fibroblasts[74,75]. Invading tumor cells may interact with stromal fibroblasts but additionally co-opt preexisting tissue structures including muscle fibers, blood vessel or nerve bundles, enclosed by a ligand-rich ECM[74,76]. In the blood stream cancer cells either interact with each other in CTC clusters or with platelets and/or immune cells, which also might facilitate intravascular arrest and extravasation at a distant site[1,45,77]. Support for improved cancer cell survival from the stroma, especially experienced by the disseminating cancer cell fraction, may result from differentially engaged receptor systems, e.g. integrins or DDRs in collagen-rich environments or CD44 interacting with selectins on endothelial cells or

leukocytes[78,79]. Eventually, the exposure to an increased ligand diversity and higher amount of engaged extracellular receptors with subsequent activation of downstream survival signaling cascades likely underlies increased survival of invading cancer cells compared to the tumor core and might also explain anoikis resistance observed after integrin-targeted therapy[2,3,55].
To unravel the exact mechanisms driving intratumor heterogeneity and differential therapy responses in sarcoma and melanoma lesions **chapter 6** describes a microscopy-guided microdissection approach to intravitally isolate different tumor and stromal sub-compartments for subsequent molecular profiling including gene expression or analysis of epigenetic modifications. To identify new therapeutic targets to overcome metastatic tumor cell dissemination, performing the profiling under therapeutic pressure might help to obtain local resistance mechanisms. Most likely this will result in combined approaches such as the combination of radiotherapy and dual (β1 and αVβ3) integrin targeting investigated in **chapter 5.** To eliminate the invasion niche and prevent seeding to distant organs, combining DNA damage induction (irradiation) and anoikis-based mechanisms (integrin-targeting) reaches a level of apoptosis induction sufficient to eradicate the entire tumor lesion, including tumor main mass and invasion zone and further prevents lung metastasis (Fig.2). To further address compensatory upregulation by other integrins as resistance mechanism, which may contribute to the limited efficacy of clinical application of single-integrin targeting in cancer[13,65,80], targeting approaches described in **chapter 4 and 5** preceded generation of an integrin expression profile to subsequently target all expressed integrin β chains. Correspondingly, similar screens become included into innovative cancer therapy regimens, including multi-targeted kinase inhibition and immunotherapy, moving towards personalized treatment options[65,81,82].

Conclusion

The findings described in this thesis, employing 3D organotypic tissue culture and preclinical intravital microscopy, contribute to the mechanistic understanding of cancer invasion and metastasis. The results emphasize the contribution of the tumor microenvironment to metastatic progression and intratumor heterogeneity, and how invasion and the microenvironment jointly support cancer cell survival and resistance in mesenchymal tumor types. The here developed treatment strategy of combined radiotherapy and dual/multiple-integrin targeting should be considered as option to address radioresistance in the clinics, replacing approaches applying mono integrin-targeting.

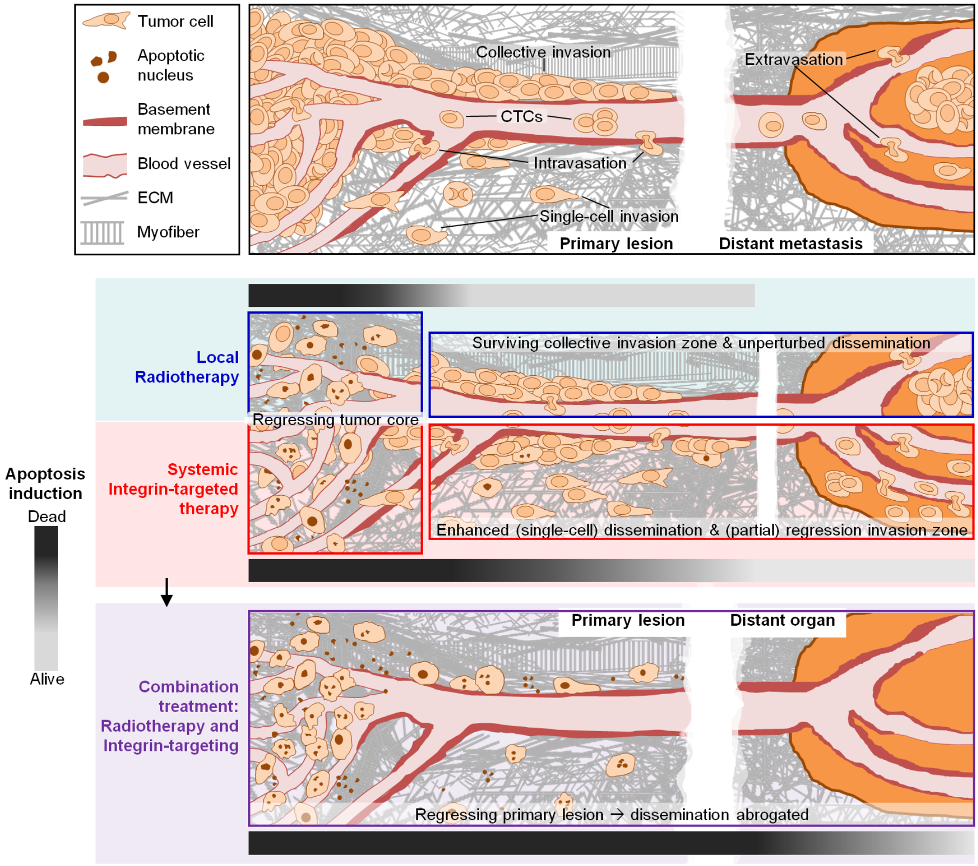

Figure 2. Sub-regional tumor heterogeneity during metastatic cancer progression accounting for differential treatment response and the need for combination therapies.
Effects of local irradiation and integrin-targeted therapy on a tumor lesion undergoing metastatic dissemination. Tumor core, invasion zone, disseminating tumor cells and metastatic lesions respond differentially to the applied treatment, underlying therapy failure due to resistance development or enhanced dissemination. Only the combination of both therapeutic approaches reaches a level of apoptosis induction sufficient to kill the primary tumor and overcome metastatic dissemination.

References

1. Valastyan, S. & Weinberg, R. A. Tumor metastasis: Molecular insights and evolving paradigms. *Cell* **147,** 275–292 (2011).
2. Friedl, P. & Alexander, S. Cancer invasion and the microenvironment: plasticity and reciprocity. *Cell* **147,** 992–1009 (2011).
3. Pickup, M. W., Mouw, J. K. & Weaver, V. M. The extracellular matrix modulates the hallmarks of cancer. *EMBO Rep.* **15,** 1243–53 (2014).
4. Friedl, P. & Gilmour, D. Collective cell migration in morphogenesis, regeneration and cancer. *Nat. Rev. Mol. Cell Biol.* **10,** 445–57 (2009).
5. Pegoraro, A. F., Fredberg, J. J. & Park, J.-A. Problems in biology with many scales of length: Cell–cell adhesion and cell jamming in collective cellular migration. *Exp. Cell Res.* **343,** 54–59 (2016).
6. Sadati, M., Taheri Qazvini, N., Krishnan, R., Park, C. Y. & Fredberg, J. J. Collective migration and cell jamming. *Differentiation.* **86,** 121–5 (2013).
7. Ganguly, K. K., Pal, S., Moulik, S. & Chatterjee, A. Integrins and metastasis. *Cell Adh. Migr.* **7,** 251–61 (2013).
8. Hegerfeldt, Y., Tusch, M., Bröcker, E. B. & Friedl, P. Collective Cell Movement in Primary Melanoma Explants: Plasticity of Cell-Cell Interaction, Beta1-Integrin Function, and Migration Strategies. *Cancer Res.* **62,** 2125–2130 (2002).
9. Eke, I. *et al.* β1 Integrin / FAK / cortactin signaling is essential for human head and neck cancer resistance to radiotherapy. *J. Clin. Invest.* **122,** 1529–1540 (2012).
10. Monferran, S. *et al.* Alphavbeta3 and alphavbeta5 integrins control glioma cell response to ionising radiation through ILK and RhoB. *Int. J. Cancer* **123,** 357–64 (2008).
11. Park, C. C., Zhang, H. J., Yao, E. S., Park, C. J. & Bissell, M. J. Beta1 integrin inhibition dramatically enhances radiotherapy efficacy in human breast cancer xenografts. *Cancer Res.* **68,** 4398–405 (2008).
12. Dickreuter, E. & Cordes, N. The cancer cell adhesion resistome: mechanisms, targeting and translational approaches. *Biol. Chem.* **398,** 721–735 (2017).
13. Vehlow, A., Storch, K., Matzke, D. & Cordes, N. Molecular Targeting of Integrins and Integrin-Associated Signaling Networks in Radiation Oncology. *Mol. Radio-Oncology, Recent results cancer Res.* **198,** 89–106 (2016).
14. Friedl, P. & Wolf, K. Plasticity of cell migration: a multiscale tuning model. *J. Cell Biol.* **188,** 11–9 (2010).
15. Nieto, M. A. Epithelial plasticity: a common theme in embryonic and cancer cells. *Science* **342,** 1234850 (2013).
16. Nieto, M. A., Huang, R. Y.-J., Jackson, R. A. & Thiery, J. P. EMT: 2016. *Cell* **166,** 21–45 (2016).
17. Hegerfeldt, Y., Tusch, M., Bröcker, E.-B. & Friedl, P. Collective Cell Movement in Primary Melanoma Explants. *Cancer Res.* **62,** 2125–2130 (2002).
18. Lehmann, S. *et al.* Hypoxia Induces a HIF-1-Dependent Transition from Collective-to-Amoeboid Dissemination in Epithelial Cancer Cells. *Curr. Biol.* **27,** 392–400 (2017).
19. te Boekhorst, V. & Friedl, P. Plasticity of Cancer Cell Invasion-Mechanisms and Implications for Therapy. *Adv. Cancer Res.* **132,** 209–264 (2016).
20. Thiery, J. P. Epithelial-mesenchymal transitions in tumour progression. *Nat. Rev. Cancer* **2,** 442–454 (2002).
21. Kurley, S. J. *et al.* p120-catenin is essential for terminal end bud function and mammary morphogenesis. *Development* **139,** 1754–1764 (2012).

22. Ewald, A. J., Brenot, A., Duong, M., Chan, B. S. & Werb, Z. Collective epithelial migration and cell rearrangements drive mammary branching morphogenesis. *Dev. Cell* **14,** 570–81 (2008).

23. Friedl, P., Locker, J., Sahai, E. & Segall, J. E. Classifying collective cancer cell invasion. *Nat. Cell Biol.* **14,** 777–83 (2012).

24. Giancotti, F. G. & Ruoslahti, E. Integrin signaling. *Science (80-.).* **285,** 1028–1033 (1999).

25. Morse, E. M., Brahme, N. N. & Calderwood, D. A. Integrin Cytoplasmic Tail Interactions. *Biochemistry* **53,** 810–820 (2014).

26. Seguin, L., Desgrosellier, J. S., Weis, S. M. & Cheresh, D. A. Integrins and cancer: regulators of cancer stemness, metastasis, and drug resistance. *Trends Cell Biol.* **25,** 234–240 (2015).

27. Weber, G. F., Bjerke, M. A. & DeSimone, D. W. Integrins and cadherins join forces to form adhesive networks. *J. Cell Sci.* **124,** 1183–1193 (2011).

28. Mui, K. L., Chen, C. S. & Assoian, R. K. The mechanical regulation of integrin-cadherin crosstalk organizes cells, signaling and forces. *J. Cell Sci.* **129,** 1093–100 (2016).

29. Epifano, C. & Perez-Moreno, M. Crossroads of integrins and cadherins in epithelia and stroma remodeling. *Cell Adh. Migr.* **6,** 261–73 (2012).

30. Salmenperä, P. *et al.* Formation and activation of fibroblast spheroids depend on fibronectin–integrin interaction. *Exp. Cell Res.* **314,** 3444–3452 (2008).

31. Belvindrah, R., Hankel, S., Walker, J., Patton, B. L. & Muller, U. Beta 1 Integrins Control the Formation of Cell Chains in the Adult Rostral Migratory Stream. *J. Neurosci.* **27,** 2704–2717 (2007).

32. Blandin, A.-F. *et al.* Glioma cell dispersion is driven by α5 integrin-mediated cell–matrix and cell–cell interactions. *Cancer Lett.* **376,** 328–338 (2016).

33. Zevian, S. C. *et al.* CD151 promotes α3β1 integrin-dependent organization of carcinoma cell junctions and restrains collective cell invasion. *Cancer Biol. Ther.* **16,** 1626–40 (2015).

34. Hui, L. & Chen, Y. Tumor microenvironment: Sanctuary of the devil. *Cancer Lett.* **368,** 7–13 (2015).

35. Li, G., Satyamoorthy, K. & Herlyn, M. N-cadherin-mediated intercellular interactions promote survival and migration of melanoma cells. *Cancer Res.* **61,** 3819–25 (2001).

36. Apostolopoulou, M. & Ligon, L. Cadherin-23 Mediates Heterotypic Cell-Cell Adhesion between Breast Cancer Epithelial Cells and Fibroblasts. *PLoS One* **7,** e33289 (2012).

37. Paluch, E. K., Aspalter, I. M. & Sixt, M. Focal Adhesion-Independent Cell Migration. *Annu. Rev. Cell Dev. Biol.* **32,** 469–490 (2016).

38. Schmidt, S. & Friedl, P. Interstitial cell migration: integrin-dependent and alternative adhesion mechanisms. *Cell Tissue Res.* **339,** 83–92 (2010).

39. Ponta, H., Sherman, L. & Herrlich, P. A. CD44: From adhesion molecules to signalling regulators. *Nat. Rev. Mol. Cell Biol.* **4,** 33–45 (2003).

40. Leitinger, B. Discoidin domain receptor functions in physiological and pathological conditions. *Int. Rev. Cell Mol. Biol.* **310,** 39–87 (2014).

41. Fu, H.-L. *et al.* Discoidin Domain Receptors: Unique Receptor Tyrosine Kinases in Collagen-mediated Signaling. *J. Biol. Chem.* **288,** 7430–7437 (2013).

42. Bendas, G. & Borsig, L. Cancer cell adhesion and metastasis: Selectins, integrins, and the inhibitory potential of heparins. *Int. J. Cell Biol.* **2012,** 676731 (2012).

43. Chambers, A. F., Groom, A. C. & MacDonald, I. C. Dissemination and growth of cancer cells in metastatic sites. *Nat. Rev. Cancer* **2,** 563–72 (2002).

44. Au, S. H. *et al.* Clusters of circulating tumor cells traverse capillary-sized vessels. *Proc. Natl. Acad. Sci.* **113,** 4947–4952 (2016).

45. Li, J. & King, M. R. Adhesion receptors as therapeutic targets for circulating tumor cells. *Front. Oncol.* **2,** 79 (2012).

46. Weber, M. R. *et al.* Activated tumor cell integrin alphaVbeta3 cooperates with platelets to promote extravasation and metastasis from the blood stream. *Thromb. Res.* **140,** S27–S36 (2016).
47. Laubli, H., Spanaus, K.-S. & Borsig, L. Selectin-mediated activation of endothelial cells induces expression of CCL5 and promotes metastasis through recruitment of monocytes. *Blood* **114,** 4583–4591 (2009).
48. Ramirez, N. E. *et al.* The α2β1 integrin is a metastasis suppressor in mouse models and human cancer. *J. Clin. Invest.* **121,** 226–237 (2011).
49. Qian, F., Vaux, D. L. & Weissman, I. L. Expression of the integrin alpha4beta1 on melanoma cells can inhibit the invasive stage of metastasis formation. *Cell* **77,** 335–347 (1994).
50. Truong, H. H. *et al.* β1 integrin inhibition elicits a prometastatic switch through the TGFβ-miR-200-ZEB network in E-cadherin-positive triple-negative breast cancer. *Sci. Signal.* **7,** ra15 (2014).
51. Aceto, N. *et al.* Circulating Tumor Cell Clusters Are Oligoclonal Precursors of Breast Cancer Metastasis. *Cell* **158,** 1110–1122 (2014).
52. Cheung, K. J. & Ewald, A. J. A collective route to metastasis: Seeding by tumor cell clusters. *Science (80-.).* **352,** 167–169 (2016).
53. Cheung, K. J. *et al.* Polyclonal breast cancer metastases arise from collective dissemination of keratin 14-expressing tumor cell clusters. *Proc. Natl. Acad. Sci.* **113,** 201508541 (2016).
54. Sosa, M. S., Bragado, P. & Aguirre-Ghiso, J. A. Mechanisms of disseminated cancer cell dormancy: an awakening field. *Nat. Rev. Cancer* **14,** 611–622 (2014).
55. Alexander, S. & Friedl, P. Cancer invasion and resistance: Interconnected processes of disease progression and therapy failure. *Trends Mol. Med.* **18,** 13–26 (2012).
56. Huttenlocher, A. & Horwitz, A. R. Integrins in Cell Migration. *Cold Spring Harb. Perspect. Biol.* **3,** a005074–a005074 (2011).
57. Theveneau, E. & Mayor, R. Cadherins in collective cell migration of mesenchymal cells. *Curr. Opin. Cell Biol.* **24,** 677–84 (2012).
58. Zegers, M. M. & Friedl, P. Rho GTPases in collective cell migration. *Small GTPases* **5,** e28997-1–10 (2014).
59. Devreotes, P. & Horwitz, A. R. Signaling Networks that Regulate Cell Migration. *Cold Spring Harb. Perspect. Biol.* **7,** a005959 (2015).
60. Lien, E. C., Dibble, C. C. & Toker, A. PI3K signaling in cancer: beyond AKT. *Curr. Opin. Cell Biol.* **45,** 62–71 (2017).
61. Huang, C., Jacobson, K. & Schaller, M. D. MAP kinases and cell migration. *J. Cell Sci.* **117,** 4619–4628 (2004).
62. Mendoza, M. C., Er, E. E. & Blenis, J. The Ras-ERK and PI3K-mTOR pathways: cross-talk and compensation. *Trends Biochem. Sci.* **36,** 320–8 (2011).
63. Zhong, X. & Rescorla, F. J. Cell surface adhesion molecules and adhesion-initiated signaling: Understanding of anoikis resistance mechanisms and therapeutic opportunities. *Cell. Signal.* **24,** 393–401 (2012).
64. Ley, K., Rivera-Nieves, J., Sandborn, W. J. & Shattil, S. Integrin-based therapeutics: biological basis, clinical use and new drugs. *Nat. Rev. Drug Discov.* **15,** 173–183 (2016).
65. Sheldrake, H. M. & Patterson, L. H. Strategies To Inhibit Tumor Associated Integrin Receptors: Rationale for Dual and Multi-Antagonists. *J. Med. Chem.* **57,** 6301–6315 (2014).
66. Thorpe, L. M., Yuzugullu, H. & Zhao, J. J. PI3K in cancer: divergent roles of isoforms, modes of activation and therapeutic targeting. *Nat. Rev. Cancer* **15,** 7–24 (2014).
67. Santarpia, L., Lippman, S. M. & El-Naggar, A. K. Targeting the MAPK–RAS–RAF signaling pathway in cancer therapy. *Expert Opin. Ther. Targets* **16,** 103–119 (2012).
68. Polivka, J. & Janku, F. Molecular targets for cancer therapy in the PI3K/AKT/mTOR pathway. *Pharmacol. Ther.* **142,** 164–175 (2014).

69. Neelakantan, D., Drasin, D. J. & Ford, H. L. Intratumoral heterogeneity: Clonal cooperation in epithelial-to-mesenchymal transition and metastasis. *Cell Adh. Migr.* **9,** 265–276 (2015).

70. Kim, T.-M. *et al.* Subclonal Genomic Architectures of Primary and Metastatic Colorectal Cancer Based on Intratumoral Genetic Heterogeneity. *Clin. Cancer Res.* **21,** 4461–4472 (2015).

71. Barker, H. E., Paget, J. T. E., Khan, A. A. & Harrington, K. J. The tumour microenvironment after radiotherapy: mechanisms of resistance and recurrence. *Nat. Rev. Cancer* **15,** 409–425 (2015).

72. Nakasone, E. S. *et al.* Imaging Tumor-Stroma Interactions during Chemotherapy Reveals Contributions of the Microenvironment to Resistance. *Cancer Cell* **21,** 488–503 (2012).

73. Hirata, E. *et al.* Intravital imaging reveals how BRAF inhibition generates drug-tolerant microenvironments with high integrin beta1/FAK Signaling. *Cancer Cell* **27,** 574–588 (2015).

74. Alexander, S., Koehl, G. E., Hirschberg, M., Geissler, E. K. & Friedl, P. Dynamic imaging of cancer growth and invasion: a modified skin-fold chamber model. *Histochem. Cell Biol.* **130,** 1147–54 (2008).

75. Kalluri, R. The biology and function of fibroblasts in cancer. *Nat. Rev. Cancer* **16,** 582–598 (2016).

76. Weigelin, B., Bakker, G.-J. & Friedl, P. Intravital third harmonic generation microscopy of collective melanoma cell invasion: Principles of interface guidance and microvesicle dynamics. *IntraVital* **1,** 32–43 (2012).

77. Labelle, M. & Hynes, R. O. The initial hours of metastasis: the importance of cooperative host-tumor cell interactions during hematogenous dissemination. *Cancer Discov.* **2,** 1091–9 (2012).

78. Leitinger, B. & Hohenester, E. Mammalian collagen receptors. *Matrix Biol.* **26,** 146–155 (2007).

79. Napier, S. L., Healy, Z. R., Schnaar, R. L. & Konstantopoulos, K. Selectin Ligand Expression Regulates the Initial Vascular Interactions of Colon Carcinoma Cells: The Roles of CD44v and Alternative Sialfucosylated Selectin Ligands. *J. Biol. Chem.* **282,** 3433–3441 (2006).

80. Bianconi, D., Unseld, M. & Prager, G. Integrins in the Spotlight of Cancer. *Int. J. Mol. Sci.* **17,** 2037 (2016).

81. Gibney, G. T., Weiner, L. M. & Atkins, M. B. Predictive biomarkers for checkpoint inhibitor-based immunotherapy. *Lancet Oncol.* **17,** e542–e551 (2016).

82. McDermott, U. & Settleman, J. Personalized Cancer Therapy With Selective Kinase Inhibitors: An Emerging Paradigm in Medical Oncology. *J. Clin. Oncol.* **27,** 5650–5659 (2009).

Nederlandse **S**amenvatting

Acknowledgements

Curriculum **V**itae

List of **P**ublications

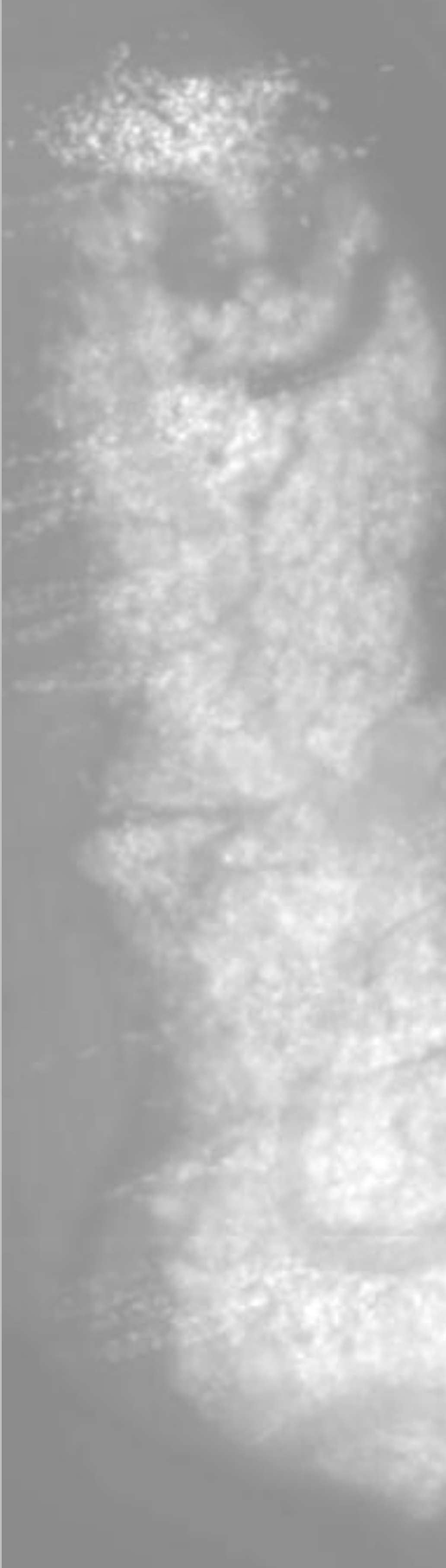

Nederlandse Samenvatting

Kanker behoort wereldwijd tot de grootste doodsoorzaken, en is voornamelijk dodelijk door het vermogen van kankercellen om uitzaaiingen (metastasen) te vormen of door resistentie tegen therapieën te ontwikkelen. De progressie van een groeiende naar een metastaserende kanker verloopt via verschillende stappen: 1) de lokale invasie van migrerende kankercellen in het weefsel rondom de primaire tumor, 2) het binnendringen van tumorcellen in bloed en/of lymfevaten, 3) het verlaten van de bloed en lymfevaten elders in het lichaam, en 4) de kolonisatie en de vorming van afstandsmetastasen in andere organen. Ondanks het feit dat metastaserende cellen waarschijnlijk allemaal afkomstig zijn van een enkele gemuteerde cel kloon, gedragen metastaserende kankercellen zich vaak anders dan de cellen in de primaire tumor. Deze verschillen kunnen worden veroorzaakt door variatie in cellulaire mechanismen die cellen gebruiken om de verschillende stappen van metastasen te bewerkstelligen. Een belangrijk verschil hierbij is de manier van celmigratie, waarbij cellen of als individuele cellen migreren, of als groepje cellen, ook wel genoemd collectieve celmigratie. Gedurende metastasering worden cellen bovendien blootgesteld aan verschillende milieus, waaraan ze zich zullen aanpassen, en hierdoor verdere veranderingen ondergaan. De focus van dit proefschrift is het gedrag van mesenchymale soorten kanker, die gekarakteriseerd worden door migratie als individuele cellen. In dit proefschrift wordt bestudeerd hoe deze tumorcellen zich uitzaaien en hoe zij resistentie tegen bestaande kanker therapieën ontwikkelen. Hiervoor werd gebruik gemaakt van zowel *in vitro* spheroid als *in vivo* xenograft modellen.

Collectieve cel migratie draagt bij aan het ontstaan van metastasen, maar is ook van belang tijdens embryonale ontwikkeling of bij het herstel van beschadigd weefsel. **Hoofdstuk 2** geeft een samenvatting van de mechanismes waarmee collectieve cel migratie de richting van migratie reguleert. Sturing van de celgroepen, waarbij de cellen met cel-cel bindingen contact houden, is essentieel om collectieve beweging van cellen onderling te coördineren. Mechanismes om migrerende celgroepen te sturen zijn onder ander afhankelijk van de topografie en/of stijfheid van de omgeving (sturing door middel van omgevingscontact) en van fysieke parameters zoals stroming van vloeistof. Vloeistofstromen kunnen actief cellen sturen via signalen afkomstig van frictiekrachten, of passief, door cellen mee te voeren. Voorts kunnen signalen van oplosbare moleculen of elektrische signalen, die ionkanalen stimuleren, betrokken zijn. Sturing door deze factoren wordt vaak bewerkstelligd doordat ze als gradiënt aanwezig zijn en op deze manier celgroepen heterogeen stimuleren en hierdoor sturen. Als een celgroep meerdere sturingssignalen tegelijk ontvangt, is het belangrijk deze te integreren en te prioriteren. Samen met de intrinsieke migratie programma's van de cellen zal dit uiteindelijk het karakter en de richting van collectieve migratie bepalen.

In **hoofdstuk 3** wordt met *in vitro* experimenten met 3D celkweek methoden onderzocht of en hoe de topografie van de omgeving, in het bijzonder de dichtheid en stijfheid, invloed heeft op de individuele of collectieve migratie van mesenchymale sarcoom- en melanoom cellen. De resultaten laten zien dat toenemende dichtheid van de omgeving zorgt voor een switch van individuele naar collectieve migratie. Deze resultaten waren verrassend omdat collectieve migratie mechanismes een karakteristieke eigenschap is van kankercellen met een epitheliale oorsprong, terwijl individuele cel migratie typerend is voor mesenchymale cellen. Mesenchymale cellen vormen geen sterke cel-cel contacten en migreren dus in een omgeving met lage dichtheid als individuele cellen. Echter, zodra de dichtheid van de omgeving hoog is, en dus ruimte beperkt is, moeten cellen ruimte genereren via proteolyse waardoor er paden ontstaan, waarlangs vervolgens ook andere cellen migreren. Omdat alleen de voorste cellen van een celcollectief, genaamd "leider cellen" deze paden kunnen maken, en "volger cellen" hier achteraan bewegen, zullen er files ontstaan. Als gevolg hiervan vormen de cellen onderlinge cel-cel contacten, waardoor een collectieve polariteit opgebouwd wordt. Samenvattend laat dit hoofdstuk zien, dat topografische beperking ten grondslag ligt aan collectieve migratie van mesenchymale kankercellen terwijl een omgeving zonder ruimtelijke beperking individuele cel migratie bevordert. De dichtheid van de omgeving is daarom een bepalende factor om de migratie mechanisme van mesenchymale cellen te beïnvloeden. Stijfheid van de omgeving heeft echter geen effect op de manier van migratie van mesenchymale cellen.

Hoofdstuk 4 laat zien dat de *in vitro* bevindingen uit hoofdstuk 3 ook *in vivo* worden waargenomen. Dit hoofdstuk beschrijft de implantatie van humane sarcoma en melanoom cellijnen als xenograft tumor in de dermis van een muis. Met behulp van multifotonen microscopie is de invasie van de kankercellen uit de primaire tumor in de orthotrope omgeving bestudeerd, waarbij ook collectieve migratie wordt waargenomen. Dit komt omdat de grensvlakken tussen weefselstructuren, die *in vivo* aanwezig zijn, zoals spiervezels of bloedvaten, ruimtelijk begrensde omgevingen vormen welke collectieve migratie mogelijk maken. Celmigratie is in veel gevallen afhankelijk van het vermogen van cellen om met behulp van bindingseiwitten, genaamd integrines, te binden aan de omliggende matrix. **Hoofdstuk 4** laat echter zien dat collectieve invasie van sarcoom en melanoom cellen *in vivo* ook onafhankelijk van β1- en αVβ3 integrines kan plaatsvinden. De afwezigheid van deze integrines veroorzaakt wel een switch naar individuele migratie. Dus, naast dichtheid van de omgeving is ook de aanwezigheid van integrines een bepalende factor voor de migratie patroon van mesenchymale cel types. Omdat sarcoom en melanoom cellen *in vivo* blijkbaar zonder integrines het weefsel kunnen binnendringen, werd vervolgens onderzocht of de cellen ook metastasen kunnen vormen in afwezigheid van integrines. Hiervoor was de hypothese dat integrines absoluut noodzakelijk zijn voor de uitzaaiing van kankercellen. Het blijkt echter dat integrine-onafhankelijke individuele en collectieve invasie nog steeds tot uitzaaiing kan leiden en dat de frequentie van uitzaaiing zelfs verhoogd is vergeleken met cellen waarbij integrines nog aanwezig zijn. Omdat integrines ook van belang zijn voor de overleving van cellen, zijn de primaire tumor en de metastasen wel geremd in hun groei. Gezien het belang van integrines voor overleving en groei, zijn voorheen kanker therapieën ontwikkeld, die integrines blokkeren en dus groei van de tumor remmen. Echter, zoals **hoofdstuk 4** laat zien, is het mogelijk dat dergelijke therapieën, tenminste voor mesenchymale soorten kanker, leiden tot verhoogde uitzaaiing van enkele kankercellen, welke na voltooien van de therapie, kunnen uitgroeien tot makroskopische metastasen.

In **hoofstuk 5** is onderzocht of collectieve migratie van sarcoom en melanoom cellen *in vivo* leidt tot een veranderde gevoeligheid voor radiotherapie. Opmerkelijk was dat het deel van de tumor dat collectieve invasie ondergaat resistent is tegen de bestraling, terwijl cellen in de tumorkern apoptose ondergaan na een hoge dosis gefractioneerde bestraling. De hoeveelheid DNA schade na bestraling was vergelijkbaar in beide tumor fracties. Echter, analyse van de reactie op DNA-schade liet zien dat herstel van de DNA schade sneller en efficiënter is in de cellen uit de collectieve migratie zone. In de tumorkern waren tekenen te zien van een verstoorde DNA-schade respons, leidend tot celdood via apoptose. Omdat integrines belangrijk zijn voor adhesieafhankelijke overleving kunnen ze een rol spelen bij de resistentie tegen bestraling. In **hoofdstuk 4**, is al laten zien dat collectieve migratie en de overleving van migrerende sarcoom en melanoom cellen grotendeels onafhankelijk van β1 en αVβ3 integrines is. Echter, als remming van integrines wordt gecombineerd met bestraling leidt dit tot apoptose van zowel de tumor kern als het collectief-invasieve deel, waardoor uiteindelijk regressie van de hele tumor optreedt. Samenvattend laat dit zien dat resistentie tegen bestraling in collectief-invasieve cellen, afhankelijk is van integrine-gemedieerde overlevingssignalen en stimulatie van herstel van DNA schade. Pogingen om resistentie tegen bestraling door middel van integrine interferentie als therapie te bestrijden, zijn tot nu toe onsuccesvol gebleken. Een mogelijke verklaring is dat de therapie was gericht tegen maar een integrine keten, welke door verhoogde expressie van een andere integrine keten gecompenseerd kon worden. De therapie beschreven in **hoofdstuk 5** is gericht tegen twee integrine ketens, welke ook de enige zijn die in de gebruikte sarkoom en melanoom cel lijnen tot expressie komen. De remming van alle beschikbare integrines lijkt een effectieve strategie om resistentie tegen bestraling in collectief migrerende kankercellen aan te gaan. In overeenstemming hiermee werden in een lange-termijn studie ≥ 80% van de tumoren volledig geëlimineerd, wat een goede aanwijzing is om kanker therapiën, die tegen integrines zijn gericht, weer in overweging te nemen.

Terwijl in **hoofdstuk 3** ruimtelijke beperking als mechanisme werd geïdentificeerd om mesenchymale sarkoom en melanoom cellen collectief te laten migreren, laten **hoofdstuk 4 en 5** vervolgens zien, dat vergeleken met de tumorkern, de cellen die collectief invaderen, verschillend zijn wat betreft afhankelijkheid van integrine-gemedieerde overlevingssignalen en gevoeligheid voor bestraling. Blijkbaar zijn zowel organisatie als de waarneming van de omgeving verschillend voor beide tumor regio's. Bovendien hebben ze een verschillende status, namelijk bewegend vs. statisch. Welke van deze verschillen verantwoordelijk zijn voor de intra-tumor heterogeniteit is tot nu toe niet bekend. Een manier om dit uit te vinden, is het opstellen van een moleculair profiel van beide tumor regio's (kern vs. collectieve invasie). Om deze reden beschrijft **hoofdstuk 6** de ontwikkeling van een methode om de tumorkern en de invasie zone van sarkoom en melanoom xenografts in de muis dermis van elkaar te scheiden, en vervolgens te analyseren met behulp van RNA sequencing (RNAseq). Hoewel deze methode succesvol is opgezet, waren de verkregen resultaten moeilijk te interpreteren vanwege de hoge aanwezigheid van RNA uit het omliggend muisweefsel wat tot hoge achtergrond waarden leidde. Een technische verbetering van de zowel de RNAseq procedure en data analyse is daarom noodzakelijk om kandidaat genen te identificeren die de afhankelijkheid van integrines en resistentie tegen bestraling en andere oncologische processen in de collectieve migratie zone van melanoom en sarkoom cellen bepalen. Het uiteindelijke doel is om op deze manier nieuwe targets voor kanker therapiën te vinden en/of al bestaande therapiën door middel van combinaties te verbeteren.

Acknowledgements

Finally, Finally, Finally, I am writing this last part of my thesis. Seven years ago I started this PhD project, including moments where I thought that completion of this project and thesis will never happen… But luckily there were many people along my PhD track who supported me in manifold ways. Finally reaching this point would have been impossible without them.

Peter, my promotor, your are the first one who I want to thank. The first time I got in touch with your work was the NCMLS forum evening organized by your group in december 2008, leaving me very impressed by colorful in vivo images and very interesting data. During my internship in Bé's group I virtually fell in love with cell biology – looking through a microscope, seeing cells migrating, dividing or dying, simply amazing. As your group was in the same department I also had the opportunity to learn more about your work and I felt, that I wanted to become a part of this fascinating piece of science. When I had the chance to participate in the PhD proposal competition I ask you if you wanted to be my supervisor – you answered within minutes and we met a few days later. With your help I eventually wrote and got granted a research proposal containing my own ideas, which just felt great back then and I am still very thankful for that. We both know, that eventually this proposal got not completely implemented in my thesis. However, "just a few revision experiments" and unexpected research findings resulted in challenging projects, which you steered such, that in the end I still had a story with a common thread. Thank you for being always reachable when I ran into problems, your optimism when I thought all the data were crap, your criticism when I sent you a text containing "weiße Schimmel" und "schwarze Rappen" and the opportunity to represent our group at several international conferences. With your help my scientific skills definitely got improved!

Kata, although you were surprised to see you announced as my co-promotor, for me it was actually quite obvious. Next to Peter you accompanied me along my entire PhD track, you were always there when I had questions and eventually you became co-author of two of my thesis chapters. Not to forget the chapter about “Metastasering” that we wrote together with Peter for the “Canon van de Oncologie”, a nice experience and exercise to once write for a non-scientific public.

Mirjam, I should have announced you as additional co-promotor but unfortunately I found it out too late. Sorry for that. Although you joined our group when I had already started my PhD you were of great help to me: for either experimental or scientific questions I could always reach you sitting in your “corner”. Without you I would have been despaired of the “cryptic lamellipodia” in the TCB review. And finally, without you, this thesis would also lack a proper

Dutch summary. Thank you for turning my try of a Duch translation into a nice, well-to-read and correct version.

Bé, you were my lecturer, my internship supervisor and head of the department while I performed my PhD. But apart from that, all the time, you also acted as a mentor to me. I want to thank you for all your cordial, sometimes critical but always encouraging words. Your lectures and the internship in your group inflamed my passion for cell biology.

Joris, my official PhD mentor. Although we just met four times I don`t want to have missed these meetings and I know, that if it had been necessary we could have met more often. I enjoyed to talk to you about success and frustrations (which were usually the major part), with your comments giving me recognition, relief and new motivation.

Manon, without you this thesis, as it is now, would probably not exist. The DDR analysis and long-term study – impossible without you. Your accuracy, reliability and persistence was amazing. The way you took care of the long-term mice, never giving up to do everything that they reached the end of the study – incredible. If I needed help, you were there: coming early in the morning, staying late or doing mouse work in the weekend when I didn't have time, it was never a problem for you. Unfortunately it didn't work out that you joined me in Cologne for a while, but I am glad that you are back in Nijmegen now and that you will be my paranymph. And I hope that eventually the day will come that you can put the picture of the stained strand cross-section above your bed ;-).

Esther, our first encounter was not really a good one - I forgot to clean up a counting chamber in the cell culture… But luckily you soon realized that this was actually an exception and I got to know you as a very nice colleague :-). You became my mate in the cell culture and in PRIME and also spent lots of your breaks joining me in the Olympus room. I really enjoyed our chats in the early morning when no one else was there yet or just working next to you while having the radio as loud as possible (thank you for also listening to my favorite German radio station ;-)). I don't know whether I would have made it without your mental and procedural support and I hope that you can once overcome the trauma that you have with doing surgeries on "my" nudes. Sorry that I left you, but at least for my defense we will be re-united having you as paranymph at my side. And as I already told you, coming back to Nijmegen is still an option…

Samuel, **Bettina** and **Marina**, my German colleagues that joined me from the very beginning in the Friedl lab and made me feel welcome. I remember long, fruitful and funny discussions in the kitchen, "your" first lab unit or in PRIME. **Samuel**, I will never forget the almost-heart-attack moment when we met late at night in the dark lab, me coming back from the microscope and you entering the cell culture room… **Bettina**, always there to help out with almost every question, especially mouse- and microscopy-related stuff, many thanks for all your support and sharing your fascinating data with me. **Marina**, my MMD and PhD-retreat mate, I enjoyed to have you as a very close colleague at my side. In contrast to me you managed to get familiar with the AFM (also many thanks to **Joost** at this point) and were of big help getting my collagen stiffness measurements done and analyzed.

Sjoerd, time is running: when I asked you for help with getting the sandwich migration experiments completed you had just started your PhD. When I will have my thesis defense your official PhD time will be almost completed (within the last two years, now and then I feared that you will even “overtake” me ;-)). I liked your critical and precise way to plan and perform experiments and thanks to you we got the in vivo – in vitro analogy for the integrins and metastasis chapter nicely completed. I wish you all the best for the completion of your PhD!

Sarah, in Houston I took over your apartment and your bike, in Nijmegen you took over the responsibility to finish the remaining mouse-CTC experiments when I had already left. I have to admit, that this was not really a fair deal… Therefore I am deeply grateful for all your help and support to get the valuable CTC part for the integrins and metastasis chapter finished. Also for you: all the best for the completion of your PhD!

Mariska, **Olga**, **Pavel**, **Antoine**, **Jan Hendrik**, **Gert-Jan**, **Cornelia**, **Julia**, **Cindy**, **Lianne**, **Steffi L**, **Angela**, **Harsha** and **Jessica**, current and former Friedl lab members and nice colleagues. Thank you for all your answers and help when I was in need! I really enjoyed the friendly and helpful atmosphere we had in the lab.

Linda en **Magda**, heel erg bedankt voor jullie hulp rondom administratieve zaken! **Linda**, vooral toen ik al weg was uit Nijmegen heb jij ervoor gezorgd dat mijn “aanstelling” bij het Radboudumc verder soepel door kon lopen. **Magda**, jij stond altijd open voor vragen en problemen, bedankt voor je ondersteuning!

Furthermore I also would like to thank all other (former) Cell Biology colleagues: **Marieke**, **Remco vH**, **Ad**, **Rinske**, **Mietske**, **Michiel**, **Mirthe**, **Susan**, **Lieke**, **Rick**, **Walther**, **Ineke**, **Huib**, **Gerda**, **Frank**, **Jan✝**, **Irene**, **Jack**, **Wiljan** and **Monique** – I met you during my internship in Bé's group and you made me feel home in the Cell Biology department. I hope you forgave me for leaving to the Friedl site. Before and after I started my PhD **Anchel**, **Claire**, **Anke**, **Annika**, **Ellen**, **Laurène**, **Ingeborg**, **Remco vC** and **Leontien** joined the department – I want to thank all of you for the friendly and supportive atmosphere, with special thanks to **Huib** (there are hardly problems you don’t have a solution for), **Marieke** and **Jack** for solving all microscope-related issues. And last but not least, **Louis**, thanks to your macros data analysis got a lot easier.

Essential parts of the 6th floor are also the departments of **Animal Physiology** and **Biochemistry**. I enjoyed that it always felt like one big community rather than three different departments and even more different research groups. Paaslunch, dagje-uit, sinterklaas and kerstdiner were celebrated together and I remember them as lot of fun. Thank you for that!

During my PhD I had the opportunity to supervise three students – **Bob**, **Niro** and **Lilian**. Many thanks for all your input and especially **Lilian**, thanks a lot for staying with me as student assistant after having your internship completed. Your work saved me a lot of time and I wish you all the best for your future career!

A major part of this thesis is based on mouse experiments: **Bianca**, **Iris**, **Henk** en **Kitty**, heel erg bedankt voor jullie hulp en inzet om “mijn” muizen zo goed mogelijk te verzorgen.

In my final PhD year I finally got the microdissection running and thanks to the help of **Henk** and especially **Nader** I made it to also include some RNAseq experiments into this thesis. **Nader**, I am very grateful for the effort you made to help me extracting as much RNA as possible from my tiny tissue samples, analyze the quality of my RNA, find a suitable way to prepare a library from my little amounts of RNA and actually do the library prep for me and eventually, to analyze the “mouse-human RNA mess” as good as possible. Chapter 6 would probably not exist without you.

In 2012 the Houston lab was started and I even had the chance to spent four months there, which was a great time. **Steffi A.**, I kind of took over your PhD project and we both know what “just a few revision experiments” ended like… Thank you for becoming my friend, for sharing frustrations and success and for making me enjoying my 2nd long-term stay in the USA. I am very much looking forward to the next big fire ;-). **Steve**, thanks to you I survived the first weeks in Houston, when Steffi was in Australia: Joining you for spinning classes, picking up your bike with me driving your car home, preparing apple pie for thanksgiving or shocking American people when asking for more food at Olive Garden – there are many funny memories. **Micheal**, we only briefly met personally when I was in Houston but had a lot of contact via Skype. Thank you for finding a way to analyze the in vivo migration data and to actually do the analysis. I really appreciate that you kept tracking “my” cells while running the Houston lab, focusing on your own experiments and having your growing family at home. **Veronika**, **Liying**, **Eleonora** and of course all the other Houston lab members, thank you for a great time in the Houston lab and the numerous scientific input we shared during our joint labmeetings.

End of 2015 I moved to the University Hospital of Cologne where I met new colleagues and friends who joined and (mentally) supported me for the “final analysis and writing part” of my thesis. First of all I want to thank **Roman**, my new boss. Thanks to your courtesy and patience I was able to get my thesis finished, and I am sorry that it still took me almost two years… All **Thomas**, **Sos**, and **Peifer** lab members, and especially **Steffie** and **Johannes**, thank you for the warm welcome in the lab and the nice atmosphere, for statistical support and for having open ears for thesis-related frustrations.

Ein ganz besonderer Dank, gilt meinen Freunden, besonders **Nina** und **Ines**, und meiner Familie, besonders euch, **Mama** und **Papa**. Ihr habt mich den Weg einschlagen lassen, den ich einschlagen wollte, mir vertraut und immer an mich geglaubt, auch wenn es gedauert und gedauert hat und ihr mich manchmal monatelang nicht zu Gesicht bekommen habt (außer über Skype ;-)).

Matthias, mein Ehemann und bester Freund. Ohne dich hätte ich es wahrscheinlich nicht bis hierhin geschafft. Danke für dein unendliches Verständnis, wenn die Arbeit doch mal wieder länger gedauert hat und ich Abende und Wochenenden der Arbeit anstatt dir gewidmet habe. Danke, dass du und Tiger mich immer wieder angestupst haben, wenn ich nicht mehr weiter wusste oder wollte. Danke, wenn du meine Arbeit einfach mal aus einem anderen Blickwinkel angeschaut hast und das zur Lösung von Problemen geführt hat. Danke, dass ich mich immer auf dich verlassen kann! Ich liebe dich.

Curriculum Vitae

Anna Haeger was born on January 13th, 1986 in Bonn-Duisdorf, Germany. In 2005 she started to study (medical) Biology at the Radboud University Nijmegen, The Netherlands and finished in 2008 with the degree Bachelor of Science. Afterwards she participated in the highly selective Master program Molecular Mechanisms of Disease and graduated in 2010 as Master of Science. As part of her Master education she performed a 6 months internship at the Radboud Institute for Molecular Life Sciences (RIMLS) Department of Cell Biology in the group of Bé Wieringa followed by a 7 months internship at the Department of Biochemistry and Molecular Biology, Mayo Clinic Rochester (MN, USA) under the supervision of Jan van Deursen. During these internships Anna got attracted by the research field of cancer cell biology and microscopy and decided to continue her career with a PhD in this direction. With Peter Friedl as supervisor and future promoter she participated in the RadboudUMC PhD proposal competition and successfully developed and defended a research proposal to investigate the mechanisms underlying invasion, metastasis formation and therapy response in mesenchymal cancer cells at the RIMLS Department of Cell Biology. The results of this PhD project, which Anna started in October 2010, are described in this thesis. A part of the experiments were performed during a 4 months stay as guest researcher at the Department of Genitourinary Medical Oncology-Research, UT MD Anderson Cancer Center (TX, USA) in 2012. In 2015, after completion of her practical PhD work, Anna decided to stay in the area of cancer biology but to switch to projects closer related to the clinics and genomics field. Since October 2015 she is working as a Postdoc in the group of Roman Thomas at the Department of Translational Genomics, University of Cologne (Germany), investigating the cellular consequences of genomic alterations in Small Cell Lung Cancer.

List of Publications

Hamada M, **Haeger A**, Jeganathan KB, van Ree JH, Malureanu L, Wälde S, Joseph J, Kehlenbach RH, van Deursen JM. Ran-dependent docking of importin-beta to RanBP2/Nup358 filaments is essential for protein import and cell viability. ***J Cell Biol.*** *2011 Aug 22;194(4):597-612.*

van Horssen R, Willemse M, **Haeger A**, Attanasio F, Güneri T, Schwab A, Stock CM, Buccione R, Fransen JA, Wieringa B. Intracellular NAD(H) levels control motility and invasion of glioma cells. ***Cell Mol Life Sci.*** *2013 Jun;70(12):2175-90.*

Friedl P, **Haeger A**, Wolf K. Metastasering (book chapter in Dutch). ***Canon van de oncologie****; DCHG medische communicatie; 2012.*

Haeger A, Alexander S, Friedl P. Cancer invasion and resistance. ***EJC Suppl.*** *Sep 2013; 11(2): 291–293.*

Haeger A, Krause M, Wolf K, Friedl P. Cell jamming: collective invasion of mesenchymal tumor cells imposed by tissue confinement. ***Biochim Biophys Acta.*** *2014 Aug;1840(8):2386-95.*

Haeger A, Wolf K, Zegers M, Friedl P. Collective Cell Migration: Guidance Principles and Hierarchies. ***Trends Cell Biol.*** *2015 Sep; 25(9):556-66*

Submitted or in preparation:

Haeger A (shared first author), Alexander S, Vullings M, Kaiser FMP, Veelken C, Flucke U, Koehl GE, Hirschberg M, Flentje M, Hoffman RM, Geissler EK, Kissler S, FriedlP. Collective cancer invasion: an integrin-dependent radioresistant niche. ***In revision.***

Haeger A, Alexander S, van Helvert S, Weischer S, Vullings M, Kaiser FMP, Kissler S, Weiger M, Friedl P. Integrin-independent migration and metastasis formation of fibrosarcoma and melanoma tumor cells. ***In preparation.***

Weigelin B, de Beer M, Fransen J, **Haeger A**, Bakker GJ & Friedl P. Guided cell migration along tissue highways. ***In preparation.***